2013-8

Multimodal Wearable Sensors for Human-Machine Interfaces

Mark Nolan
Technological University Dublin, mark.nolan@tudublin.ie

Recommended Citation

Nolan, M. (2013) *Multimodal Wearable Sensors for Human-Machine Interfaces.*Doctoral Thesis, Technological University Dublin. doi:10.21427/D79903

2013-08-23

Multimodal Wearable Sensors for Human-Machine Interfaces

Mark Nolan

Multimodal Wearable Sensors for Human-Machine Interfaces

by

Mark Nolan

A thesis submitted to the Dublin Institute of Technology for the degree of Doctor of Philosophy (Ph.D.)

Supervisors: Dr. Ted Burke, Mr. Frank Duignan, Prof. Eugene Coyle

School of Electrical and Electronic Engineering

August 2013

Abstract

Certain areas of the body, such as the hands, eyes and organs of speech production, provide high-bandwidth information channels from the conscious mind to the outside world. The objective of this research was to develop an innovative wearable sensor device that records signals from these areas more conveniently than has previously been possible, so that they can be harnessed for communication. A novel bioelectrical and biomechanical sensing device, the *wearable endogenous biosignal sensor* (*WEBS*), was developed and tested in various communication and clinical measurement applications.

One ground-breaking feature of the *WEBS* system is that it digitises biopotentials almost at the point of measurement. Its electrode connects *directly* to a high-resolution analog-to-digital converter. A second major advance is that, unlike previous active biopotential electrodes, the *WEBS* electrode connects to a shared data bus, allowing a large or small number of them to work together with relatively few physical interconnections. Another unique feature is its ability to switch dynamically between recording and signal source modes. An accelerometer within the device captures real-time information about its physical movement, not only facilitating the measurement of biomechanical signals of interest, but also allowing motion artefacts in the bioelectrical signal to be detected. Each of these innovative features has potentially far-reaching implications in biopotential measurement, both in clinical recording and in other applications.

Weighing under 0.45 g and being remarkably low-cost, the *WEBS* is ideally suited for integration into disposable electrodes. Several such devices can be combined

to form an inexpensive digital body sensor network, with shorter set-up time than conventional equipment, more flexible topology, and fewer physical interconnections.

One phase of this study evaluated areas of the body as communication channels. The throat was selected for detailed study since it yields a range of voluntarily controllable signals, including laryngeal vibrations and gross movements associated with vocal tract articulation. A *WEBS* device recorded these signals and several novel methods of human-to-machine communication were demonstrated. To evaluate the performance of the *WEBS* system, recordings were validated against a high-end biopotential recording system for a number of biopotential signal types. To demonstrate an application for use by a clinician, the *WEBS* system was used to record 12-lead electrocardiogram with augmented mechanical movement information.

Declaration

I certify that this thesis which I now submit for examination for the award of Ph.D., is entirely my own work and has not been taken from the work of others, save and to the extent that such work has been cited and acknowledged within the text of my work.

This thesis was prepared according to the regulations for postgraduate study by research of the Dublin Institute of Technology and has not been submitted in whole or in part for another award in any other third level institution.

The work reported on in this thesis conforms to the principles and requirements of the DIT's guidelines for ethics in research.

DIT has permission to keep, lend or copy this thesis in whole or in part, on condition that any such use of the material of the thesis be duly acknowledged.

Signature of Author: *Mark I. Nolan*

Mark I. Nolan

Friday, 20th December 2013

Acknowledgements

I would like to express my deep gratitude to my supervisor, Dr. Ted Burke, for giving me the opportunity to undertake this research and for his continuous guidance and assistance throughout this experience.

I would like to extend my thanks to all of the tPOT research group members who have helped me over the years. My advisory supervisor Frank Duignan, for his valuable support. Dr. Damon Berry, for the highly motivational conversations we had and his unending enthusiasm for the project. The assistance provided by Dr. Richard Hayes was also greatly appreciated. Recognition is due to the technicians in the School of Electrical and Electronic Engineering for their patience and advice in sourcing equipment.

I am indebted to DIT for providing me with the opportunity to work my way up through the educational ladder. Choosing to study at DIT has been one of the best decisions that I could have made.

For their friendship and support on a daily basis, I am very grateful to the people of the Biomedical and Environmental Sensing lab - Brian Madden, Sheng Yu, Johnalan Keegan, James Condron and Louise Cannon to name but a few.

Finally, I would like to dedicate this thesis to those closest to me: my parents, for their support and encouragement during my Ph.D. and throughout my education at all levels; and my significant other, Elaine, for her patience, love and counsellor services.

Publications Arising from this Thesis (all peer reviewed).

M. Nolan, T. Burke, E. Coyle. (2012) A Wireless and Digital Electrode Bus Topology for Biopotential Measurement. *23rd IET Irish Signals and Systems Conference*. Maynooth, Ireland. 70-73.

M. Nolan, T. Burke, E. Coyle. (2011) Novel Bioelectrical Measurement using a Digital Biopotential Monode. *Bioengineering in Ireland*. Galway, Ireland. 100.

B. Madden, **M. Nolan**, T. Burke, J. Condron, E. Coyle. (2011) Intelligibility of Electrolarynx Speech using a Novel Hands-Free Actuator. *4th International Joint Conference on Biomedical Engineering Systems and Technologies*. Rome, Italy. 265-269.

B. Madden, **M. Nolan**, T. Burke, J. Condron, E. Coyle. (2010) Intelligibility of Electrolarynx Speech using a Novel Actuator. *21st IET Irish Signals and Systems Conference*. Cork, Ireland. 158-162.

M. Nolan, B. Madden, T. Burke. (2009) Accelerometer based Measurement for the Mapping of Neck Surface Vibrations during Vocalized Speech. *IEEE Engineering in Medicine and Biology Society, EMBC*. Minneapolis, Minnesota, USA. 4453-4456.

M. Nolan, T. Burke, F. Duignan. (2009) Accelerometer based Measurement of Body Movement for Communication, Play, and Creative Expression. *4th European Conference of the International Federation for Medical and Biological Engineering*. Antwerp, Belgium. 1835-1838.

Table of Contents

List of Acronyms and Abbreviations

3-D	Three-dimensional
AC	Alternating current
ACh	Acetylcholine
AChE	Acetylcholinesterase
ADC	Analog-to-digital converter
AFE	Analog front end
Ag/AgCl	Silver/silver chloride
AMR	Anisotropic magnetoresistance
AT	Assistive technology
BAN	Body area network
BLE	Bluetooth low energy
CMRR	Common-mode rejection ratio
CNS	Central nervous system
CPU	Central processing unit
DAC	Digital-to-analog converter
DC	Direct current
DCO	Digitally controlled oscillator
DLP	Digital Light Processing™
DMP™	Digital Motion Processor™
ECG	Electrocardiogram
EEG	Electroencephalogram
EMG	Electromyogram
EOG	Electrooculogram
FIFO	First in, first out
GPIO	General purpose input/output
GSR	Galvanic skin response
GUI	Graphical user interface
HMI	Human-machine interface
I^2C	Inter-integrated circuit
IEEE	Institute of Electrical and Electronic Engineers

IMU	Inertial measurement unit
LFSR	Linear feedback shift register
LSBACC	Least significant bits access
M1	Primary motor cortex
MEG	Magnetoencephalogram
MEMS	Microelectromechanical systems
MMG	Mechanomyogram
op-amp	Operational amplifier
OSR	Over-sampling rate
PCB	Printed circuit board
PGA	Programmable gain amplifier
PMA	Pre-motor area
PNS	Peripheral nervous system
PRBS	Pseudo-random binary sequence
RFID	Radio-frequency identification
SA	Slave address select pin
SD16_A	Texas Instruments sigma-delta 16-bit analog-to-digital converter
SINC	$\mathrm{sinc}(x) = \frac{\sin(x)}{x}$
SMA	Supplementary motor area
SoC	System-on-chip
SPI	Serial peripheral interface bus
TI	Texas Instruments
UART	Universal asynchronous receiver transmitter
UD	Universal Design
VEP	Visual evoked potential
VI	Virtual instrument
WEBS	Wireless biosignal sensor
ΣΔ	Sigma-delta
ΣΔ ADC	Sigma-delta analog-to-digital converter

Index of Tables

Index of Figures

Chapter 1 Introduction

An extraordinary amount of information can be gleaned from biosignals, including bioelectrical and biomechanical signals, originating in the human body. Biosignals which are under some degree of voluntary control provide excellent opportunities for channelling communication and control information from the conscious brain to the outside world. Examples include: control of powered prostheses (Velliste *et al.* 2008, Collinger *et al.* 2013), motion-based control (Esquenazi *et al.* 2012) and brain-computer interfaces (Emotiv 2012). Biosignals which are not under direct voluntary control (*e.g.* bioelectrical signals emanating from the heart) are also highly informative and are widely used in applications such as health monitoring and biofeedback (Holter 1961).

Advances in sensor technology have opened up new avenues in biosignal measurement (Pantelopoulos and Bourbakis 2010). In particular, integrated-circuit motion sensors such as accelerometers and gyroscopes have decreased in size and cost to the point that they are now routinely incorporated into everyday consumer devices like smartphones and tablet computers. Concurrently, newer generations of analog-to-digital converters incorporate more features specific to biopotential measurement with increased resolution, smaller physical footprint and lower cost. These new technologies provide users with more communication channels through which they can interact with technology than previously existed. Consumer products such as motion-based controllers (Nintendo 2006, Sony Computer Entertainment 2010), activity level indicators (Nike Inc. 2012, Jawbone 2011) and heart rate monitors (Polar Electro 2013, Samsung Group 2013) are becoming commonplace and the scope of these technologies will continue to expand in the future. According to industry research, the market for

consumer and healthcare wearable sensing devices is expected to grow exponentially over the coming years - up from 14 million units in 2011 to between 100 - 171 million units annually by the year 2016 (ABI Research 2011, IMS Research 2012). A significant motivation for this research was that by further integrating bioelectrical and biomechanical sensing into wearable, discreet and low-cost sensors, new and exciting possibilities for future modes of human-machine interaction can be realised.

1.1 Research aim

The aim of this research is to facilitate the use of information-rich channels from the human body for augmented communication and control in novel human-machine interfaces (primarily human-to-machine rather than vice versa).

In later chapters, I will show that I have achieved this aim by designing tiny wearable sensors that facilitate novel biomedical instrumentation configurations, wide area biomechanical measurement and advanced body sensor networking. I have identified various information-rich channels on the body and have demonstrated their practicality as a conduit for communication and control. In order to harness some of the human body's channels of voluntary communication and control in new ways, I have utilised several existing biosignal measurement technologies while also making some advances in biomedical instrumentation and biopotential data interpretation to address specific problems in augmented communication.

Beyond applications of communication and control, the importance of technology that facilitates recording and analysis of personal health data is growing (Dishman 2012). Personal health monitoring is an increasingly important tool within human-machine interfaces (Intel 2011). The augmentation of biopotential measurement

with real-time biomechanical information can facilitate a more complete understanding of personal health data. For this reason, I have also developed innovative user interfaces for use by clinicians in health monitoring which facilitate informed analysis of the bioelectrical signals under investigation.

1.2 Specific objectives

1. *The principal objective of this research was to develop a novel system, titled the wireless endogenous biosignal sensor (WEBS), incorporating both novel bioelectrical measurement and biomechanical signal measurement.*

By combining bioelectrical and biomechanical recordings from a single tiny device, it is possible to tap into two types of information-rich channels originating in the body in a non-invasive and unobtrusive manor. Furthermore, the signals should be seen as complementary. To take a simple example, information about the physical movement of a biopotential electrode can provide a timely warning of the presence of motion artefacts in the recorded electrical signal. Similarly, the monitoring of a user's physical movement can contextualise recorded biopotential signals (*e.g.*, changes in heart rate could be associated with changes in a wearer's activity level). A system like the *WEBS* increases information mobility between the wearer's body and everyday digital devices. Through its design, the *WEBS* can serve multiple functions simultaneously (*e.g.*, human-machine interaction and health monitoring).

The development of the *WEBS* device and its practical applications were informed by the principles of universal design (UD) (North Carolina State University 1997). The principles of UD suggest that designers should create products that are accessible to people with the broadest range of abilities, in ways that avoid segregating

users with disabilities (National Disability Authority 2013) (discussed further in Section 2.4.1). In the context of this project, the UD principles translate into an aspiration that the technology developed is useful and appealing to people *with and without* disabilities. With this in mind, it was intended that the *WEBS* system should be:

- Simple
- Reliable
- Very low-cost
- Very small
- Non-invasive
- Unobtrusive
- Convenient

The desired technical specifications for the *WEBS* system were that it should have:

- One or more high-sensitivity accelerometers
- A low-power design utilising a battery power supply
- An analog-to-digital converter with high resolution and high sampling rate
- The ability to communicate wirelessly with a computer
- Real-time data processing capability
- A modular design

The *WEBS* device design, incorporating the characteristics and technical specifications listed above, is described in detail in Chapter 3 and a thorough validation of this design is the topic of Chapter 4.

2. *An additional objective of this project was to demonstrate the operation of the WEBS prototype in one or more working augmented communication systems.*

A full chapter of this thesis (Chapter 5) provides a detailed description of the implementation and testing of the *WEBS* prototype in the following applications:

- Human-machine interfaces for communication, play and creative expression.
- Mapping of laryngeal vibrations on the surface of the skin to explore their potential use as a channel of communication and control.
- Gesture recognition for configurable human-machine interfaces which can be adapted to the needs of individual users.
- Enhanced biopotential recording with richer contextual data.

1.3 Project deliverables

Before reviewing the original knowledge contributions arising from this project, it is worthwhile describing some of the specific project deliverables including both hardware and software designs.

1.3.1 The *WEBS* device – a wearable biosignal sensor system

The primary project deliverable is the design of the final *WEBS* system (together with a fully operational prototype). 3-D models illustrating the design of the final *WEBS* components are shown in Figure 1.1. The *WEBS* system is a discreet, versatile, and accessible device that provides an intuitive interface for facilitating communication and control. The *WEBS* system has been designed from the outset as a digitally controllable

body sensor network with multiple slave sensors sharing a single digital data bus. A master device coordinates communication between itself and each of the *WEBS* slaves.

Each *WEBS* slave incorporates an industry standard biopotential recording button-clip, which attaches onto the majority of commercially available biopotential electrodes. A single *WEBS* slave is less than 0.55 cm^3 in volume and weighs less than 0.45 g. The recording of bioelectrical signals is achieved using a novel bioinstrumentation arrangement (described in Section 3.2.2) and a high-resolution analog-to-digital converter. Biomechanical signal measurement is performed using a tri-axial accelerometer.

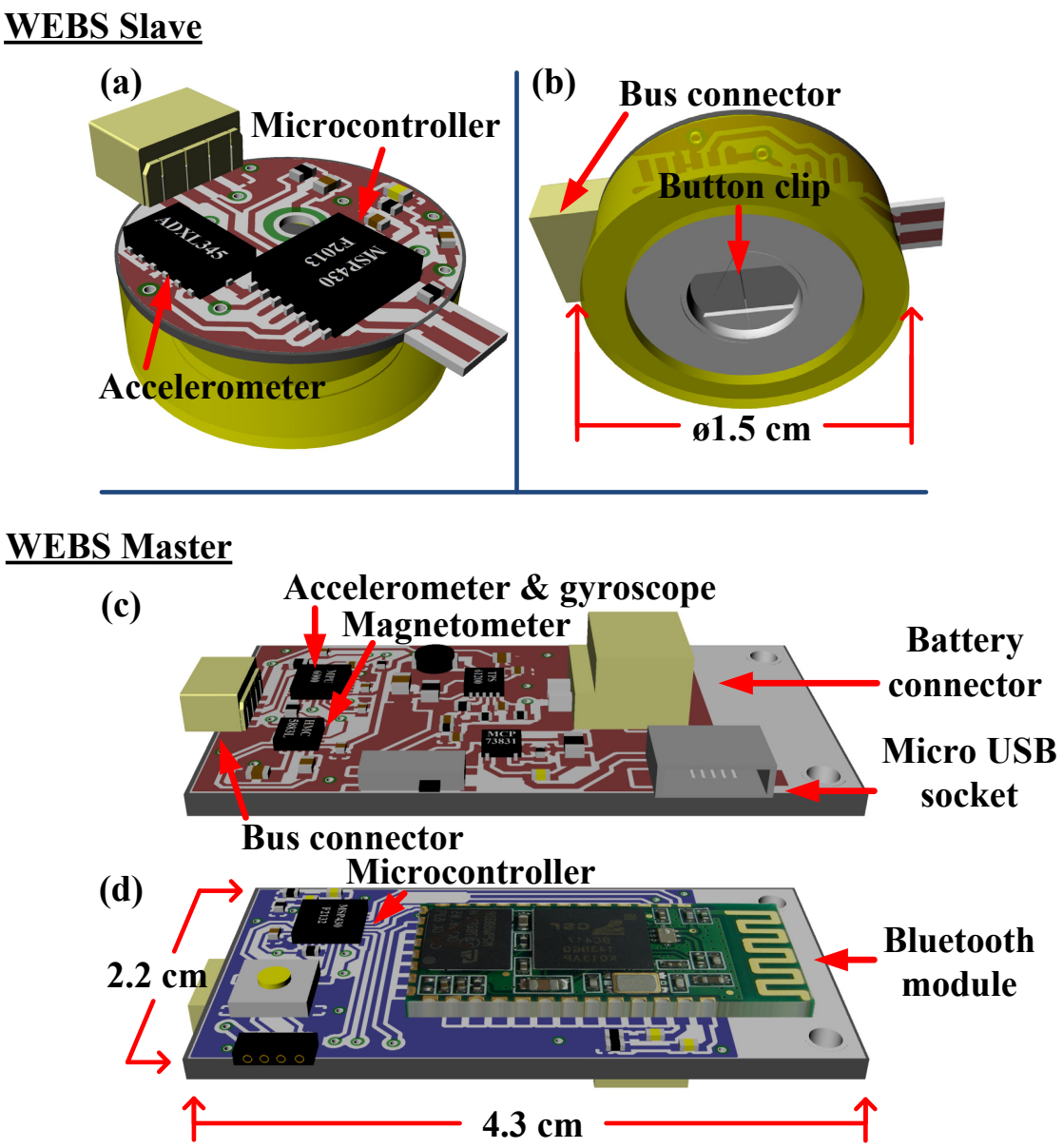

Figure 1.1: 3-D illustrations of the: *WEBS* slave from (a) top and (b) bottom view; and the *WEBS* master (c) top and (d) bottom view. The main features of each device are also highlighted. Note that the *WEBS* slaves' plastic body has been rendered as partially transparent to make the internal structure visible. One *WEBS* master is connected to up to 25 slave devices via a configurable and shared digital data bus that plugs into their on-board bus connector sockets.

The master device also contains a tri-axial accelerometer, gyroscope and magnetometer to provide information about the user's absolute orientation and movement. The master communicates wirelessly with a Bluetooth-enabled computer base station or mobile phone, which allows interaction in real time through a user interface. The design of the device is intended to support additional optional modules

that can share the same digital data bus. For example, in daily health and activity monitoring, the *WEBS* system also has the ability to record data to a bus-connected storage device.

The arrangement and number of slaves can be dynamically configured to suit a wide variety of applications without the need to re-program the system. The master is pre-programmed to detect all slaves connected to the bus on power-up (or when requested to do so by a base station). It achieves this by polling each possible address and compiling a table of those addresses from which it receives a response. The design of the *WEBS* topology allows, for the first time, the low-impedance connection (between human and electronic circuit) required in almost all biopotential recording configurations to be dynamically assigned to a different electrode (or electrodes) at any time. These multi-purpose digital electrodes facilitate a number of highly novel approaches for biological signal measurement - an example of which is discussed later in Section 5.5.

Figure 1.2 illustrates two possible configurations in which the prototype *WEBS* can be used to measure (a) the electrooculogram and (b) 12-lead electrocardiogram (explored in Section 4.3 and Section 5.4 respectively). In each scenario, both the bioelectrical and biomechanical signals can be analysed to provide a clearer perspective on the physiological activity under observation.

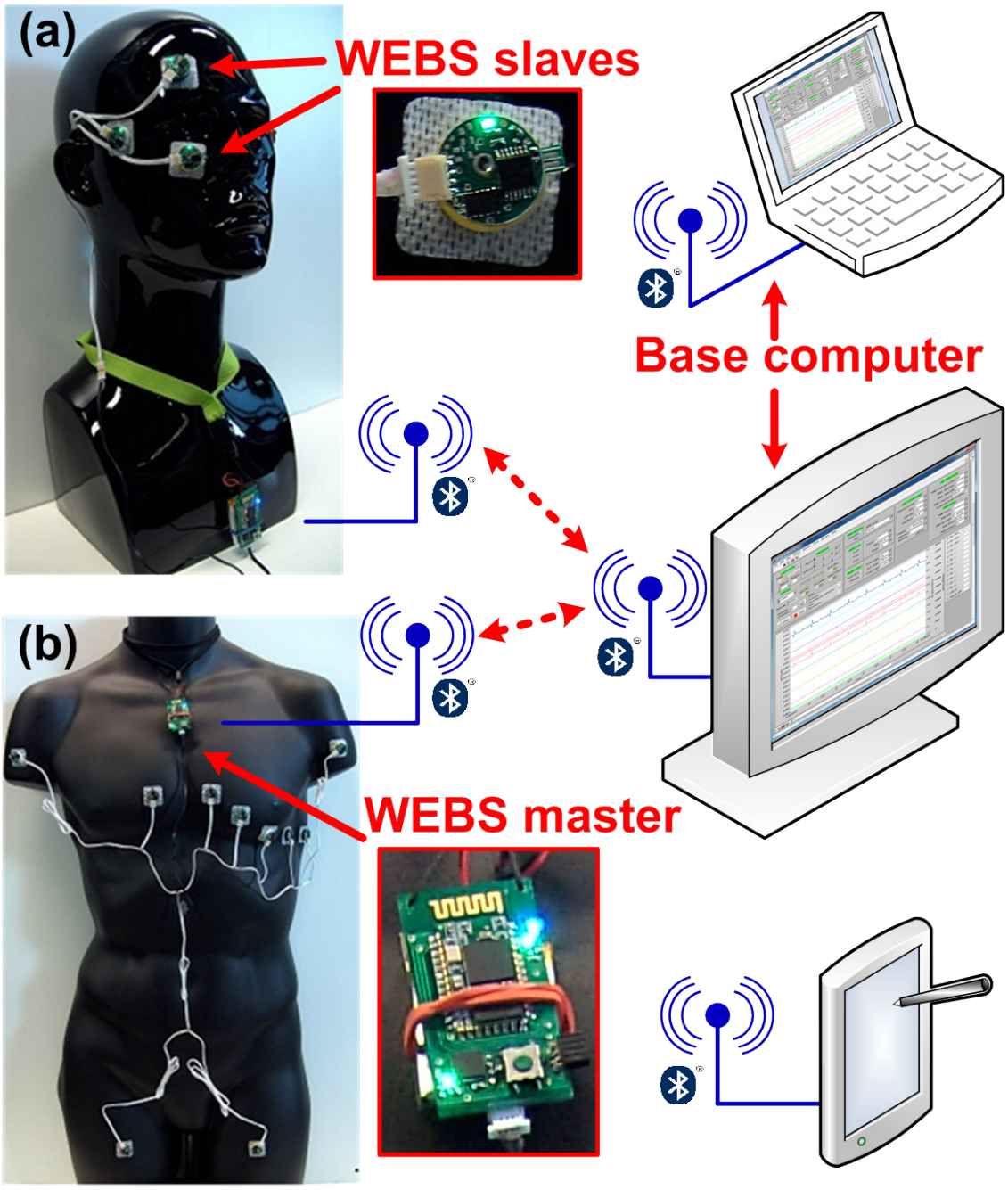

Figure 1.2: An illustration of two example *WEBS* wiring configurations for: (a) electrooculogram and (b) 12-lead electrocardiogram measurement. Several *WEBS* slave electrodes and a single *WEBS* master are connected together via a shared digital bus. The master can communicate wirelessly to any Bluetooth-enabled base computer. A PC-based graphical user interface has been developed so that a user can easily configure and record data from the *WEBS* system.

1.3.2 Applications

Although this project makes a fundamentally novel contribution to biopotential instrumentation technology, the motivation for seeking new designs in this area was to make the use of bioelectrical and biomechanical signals more practical in everyday applications. Therefore, the approach taken here has intentionally been application-led, with a consistent focus on usable systems. With this in mind, during the course of this research several applications have been designed that demonstrate the use of the *WEBS* device in complete gesture-based user interface systems. These applications allow users, whether able-bodied or not, to interact with a computer system such as a PC or laptop using biopotential and/or biomechanical signals that are under some degree of voluntary control. The design of the *WEBS* allows it to be adapted not just to use a single set of gestures, but to be configurable to a specific user's requirements, such that it can be seen as constituting something akin to a generic user interface.

In addition to demonstrating the ability of an able-bodied person to use the device for communication and control with a computer system, specific assistive technology interfaces that build on the initial system are also described. For example, I have demonstrated the use of gross and subtle body movements as a modality of control for a remote-controlled toy car (described in Section 5.1.2). In that application, a gross body movement, head tilting, controlled the steering while a subtle body movement, laryngeal vibrations, controls the car's speed. This configuration of the *WEBS* system also suggests how the system could be used to control a powered wheelchair. For control of a powered prosthesis, a combination of muscle activation, as measured by an accelerometer and the digital electrode, can form the basis of real-time control. A related example is demonstrated in Section 5.2 in which electromyogram signals, as recorded by the *WEBS* system, are used as control inputs to a computer game.

1.4 Contributions to knowledge

As illustrated in Figure 1.3, the primary contributions of this research lie at the intersection of biomedical instrumentation and augmented communication and control (highlighted in green). Whilst assistive technology is perhaps the first application that comes to mind, the approach taken here is not to focus solely on communication and control by disabled people but to provide solutions that are useful to a broader range of people.

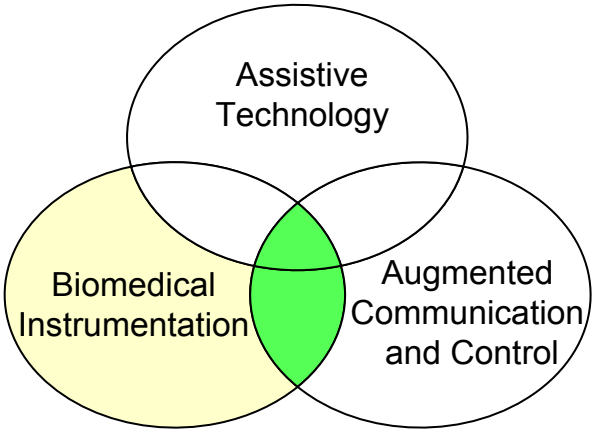

Figure 1.3: A Venn diagram highlighting the area in which the primary contributions of this project lie (shaded in green). This research also makes novel contributions to area of biomedical instrumentation, which have applications in their own right (shaded in yellow).

Although the objectives of this project were clearly defined and reasonably focused, the decision to focus on real world applications in parallel with the development of novel instrumentation technology has led the work down a wide variety of fruitful avenues. I have identified seven specific contributions to knowledge that I believe are particularly significant. The first category of contributions relate to the physical *WEBS* device:

1. The design, fabrication and testing of a multimodal biosignal sensor network that has several advantages over existing measurement topologies (Section 3.2.1).

2. The design of a novel bioinstrumentation configuration in which digitisation occurs at the point of measurement within the electrode (Section 3.2.2).

3. The augmentation of biopotential measurement with biomechanical movement sensing - as measured within each electrode (Section 3.2.3).

The second category of knowledge contributions relates to the example applications (described in Chapter 5) that show how this novel measurement technology can be applied to real world problems.

4. The design of multiple human-to-machine interfaces that transform software-definable user gestures into generic control input signals (Section 5.1.2, Section 5.2 and Section 5.4).

5. The design of a computer interface that presents the biopotential and biomechanical signals recorded by the *WEBS* in a manner that is useful and accessible for clinical analysis. By way of example, the application of the *WEBS* system to recording a 12-lead electrocardiogram with augmented biomechanical information is demonstrated in Section 5.4.

The groundbreaking design of the *WEBS* system provides unique opportunities for novel biopotential recording configurations that go far beyond the straightforward measurement of time-varying differences in endogenous voltage between points on the surface of the body. A third category of knowledge contributions arising from this project concerns these avenues of investigation.

6. The discovery and investigation of the complex three-dimensional characteristics of neck skin surface vibrations during vocalisation at different phonation frequencies (Section 5.1).

7. The development of a novel method of electrode-skin impedance analysis incorporating pseudo-random binary sequence system identification into the designed multimodal sensor network (Section 3.2.6 and Section 5.5).

This list of contributions is reviewed again in Chapter 6, with additional references to the evidence supporting each contribution from the intervening chapters.

1.5 Thesis preview

This research followed a coherent methodology involving four partially overlapping research phases: (1) literature review; (2) design and implementation of the *WEBS* device; (3) performance testing; and (4) design of user applications for the final system. These phases are reflected in the chapter structure of this thesis.

Chapter 2 reviews of the state of the art in the relevant areas of biomedical instrumentation and augmented communication. Some background knowledge of relevant human physiology, which is required to understand the bioelectrical and biomechanical signals of interest, is reviewed here. The initial emphasis is on the origin of these signals, including information about the relevant parts of the neurological infrastructure of the brain and body. Chapter 2 also reviews various biopotential and biomechanical signals (voluntary and involuntary), together with the electrical circuits and sensors conventionally used to measure them. Also described are several issues associated with the use of conventional biopotential measurement approaches in tiny

integrated sensors designed for use in practical communication, control or clinical measurement technologies.

Chapter 3 describes the design and implementation of the *WEBS* device which has been conceived as an evolution of the conventional biosignal measurement systems described in Chapter 2. This device provides key benefits over existing designs while posing several design challenges – all of which are described here. Also presented in Chapter 3 is the graphical user interface that has been designed to allow a user to easily configure *WEBS* device and capture biosignal data recorded by it. This graphical user interface facilitates custom-built software interfaces that cater to specific biosignal and/or application requirements. This chapter also contains a description of how it is envisaged the device can be used in a daily context; for example, by a therapist or family member attaching it to a user with physical disabilities.

Chapter 4 describes the extensive testing that has been undertaken on the *WEBS* system in order to gauge its performance in biopotential and biomechanical signal measurement. This chapter also provides a detailed comparison of the *WEBS* system's capabilities to those of a high-end, commercially available, biopotential measurement system (the BioSemi ActiveTwo). This comparison includes a detailed comparative analysis of various biopotential signals recorded using both systems.

Chapter 5 focuses on applications, exploring examples of new and exciting possibilities that become feasible when using these novel low-cost *WEBS* sensors (including some that were investigated using earlier iterations of the device). The initial emphasis in Chapter 5 is on harnessing information hotspots in the human body (as bioelectrical and/or biomechanical signal sources) for specific applications in communication, control and creative expression. In this chapter it is shown how a combination of bioelectrical and biomechanical signals which are under some degree of

voluntary control can be utilised as a multimodal input to a broader based control system. A novel 12-lead electrocardiogram computer interface is also described, which displays bioelectrical signal information with augmented biomechanical motion activity, facilitating easier interpretation of physiological phenomena. Chapter 5 concludes with an investigation into the use of the *WEBS* network to analyse the impedance between pairs of electrodes using pseudo-random binary sequence system identification.

Chapter 6 presents discussion of the work, suggestions for future research and conclusions. This chapter begins by evaluating whether the research aims and objectives have been satisfied by this research. The original contributions to knowledge are reviewed by assessing relevant examples. The limitations of the device's design are critically assessed and a list of suggested design modifications that could be incorporated into future iterations of the *WEBS* design is included. Interesting future applications of the *WEBS* system are also proposed. This chapter closes with the conclusions that have been garnered from carrying out this research.

Chapter 2 Literature Review

The ultimate aspiration of this research is to create new technology that facilitates communication and control in human-machine interfaces. With this in mind, a useful starting point is to reflect on how information originating in the body is channelled to the outside world. When a human communicates, their body transduces thoughts, ideas or emotions from within the brain into observable outward manifestations that another human or machine can interpret. Typically, the transduction of information from thought into an observable signal occurs via the action of muscles, under the control of the nervous system.

As explained in this chapter, different motor functions (and likewise sensory receptors) have various quantities of brain cells devoted to their operation (*i.e.*, their movements or sensations). This means that certain parts of the body are served by a higher bandwidth neurological infrastructure. Conspicuous examples of high-bandwidth motor function include the hands, facial features and speech production. In the context of this research, it is important to review the normal flow of information between the brain and the outside world because, ideally, any new technology for human-to-machine communication should utilise existing body communication infrastructure in a way that is suitable and convenient for a user. This can be most effectively achieved by targeting the anatomical features that are served by a higher bandwidth information infrastructure.

This chapter begins by describing the body's neurological infrastructure with specific regard to how it handles sensory and motor information. The information channels that are most relevant to this research are two types of biological signals (or biosignals) which emanate from the body: bioelectrical and biomechanical signals.

These, and the instrumentation typically used to measure them, are described in detail in this chapter. This chapter also reviews the current literature in the area, guided by what I see as the overlapping fields to which this work applies. This research does not solely concern bioinstrumentation; there is also an intention here to focus on augmented communication and control. From that point of view, not only will relevant literature in biosignal measurement be reviewed, but also existing methods of harnessing relevant biosignals as channels of communication and control.

2.1 Relevant physiology

The nervous system is the body's fast information communication infrastructure. It allows the transfer of sensory information and motor control signals between the brain and the rest of the body. The other information system in the body, which is not the focus of this discussion, is the endocrine system. It utilises hormones to regulate functions such as growth and development, reproduction and metabolism (Marieb and Hoehn 2012: 308).

The nervous system is divided into two main parts, the Central Nervous System (CNS) (made up of the brain and spinal cord) and the Peripheral Nervous System (PNS) (consisting of the all nervous tissue that exists outside of the central nervous system and connects it to limbs and organs) (Tortora and Derrickson 2011: 448). Some of the constituent components of the nervous system will be described in this section. In addition, the operation of muscle tissue (especially in cardiac muscles and consciously controllable skeletal muscles) is of particular interest to this research and this will also be described.

2.1.1 Nervous tissue

As mentioned previously, the nervous system network comprises nervous tissue (also known as neural tissue). Nervous tissue is the information transport medium that conducts and transfers electrical impulses (or nerve impulses) between the brain and other parts of the body (*i.e.*, sensory organs and muscles). Nervous tissue contains two basic cell types, glial cells and neurons. The term glial cells (or neuroglia cells) is a collective name for a number of cell types that have several functions in nervous tissue. They help maintain the physical structure of nervous tissue, provide nutrients to neurons, and repair tissue framework after injury. Approximately half of the volume of the nervous system consists of glial cells (Martini *et al.* 2011: 380).

Neurons are core to the functioning of the nervous system. Neurons are excitable cells which process and transmit nerve impulses (also known as action potentials) around the body by electrochemical signalling. This electrochemical signalling is in the form of moving ions (principally sodium (Na^+), potassium (K^+), and chloride (Cl^-). It is estimated that there are approximately 86 billion neurons in the human brain (Azevedo *et al.* 2009). Neurons are generally considered to be amitotic as they apparently undergo no further mitosis after adolescence (Saladin 2011: 442); meaning that if a neuron is destroyed it cannot be replaced.

There are four major structurally distinct types of neuron: anaxonic, bipolar, unipolar and multipolar (Martini *et al.* 2011: 378-379) - as illustrated in Figure 2.1. An anaxonic neuron has no anatomical features that would allow a distinction between its axons and dendrites. Bipolar neurons have two separate branches (or processes) that emanate from the cell body - one dendritic process and one axon. In a unipolar neuron, a single process emanates from the cell body on which the dendrites and axon co-exist.

The point at which the dendrites meet the axon is called the initial segment. In a multipolar neuron, two or more dendrites are attached to the cell body to which a single axon is connected. The separate pseudounipolar neuron is unique in that it is classed as a unipolar neuron but it starts of as a bipolar neuron during development in the embryo. Pseudounipolar neurons have one axon coming out of the cell body that splits into two process (or branches), a central process and a peripheral process. The most common neuron in the human nervous system is the multipolar neuron (Martini *et al.* 2011: 379).

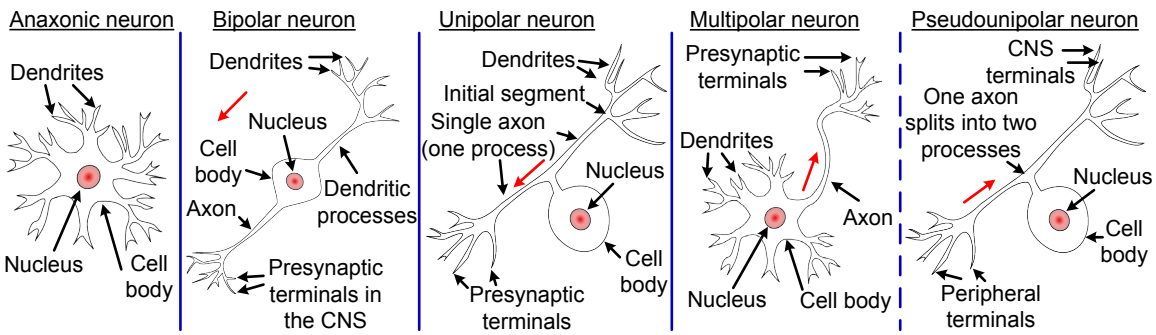

Figure 2.1: An overview of different neuron types. Note that the relative size difference between the illustrated neurons is not accurate. A red arrow denotes the direction of nerve impulse in each neuron. The images are modified from (Haas 2012).

As illustrated in Figure 2.1, the soma, or cell body, contains the nucleus and is the control centre of the neuron. Dendrites receive information - in the form of a synaptic potential - from sensory receptors and/or other neurons. Some neurons can have over a thousand dendritic branches and this allows for connections to tens of thousands of other cells. The arriving synaptic potential triggers an action potential, which travels down the axon using an electrical impulse whereby the polarity across the axon membrane rapidly changes. In the axon, voltage-gated ion channels control the balance between the amount of either sodium (Na^+) or potassium (K^+) ions that are present on the inside or outside of the axon membrane (Hodgkin and Huxley 1952). Depolarisation occurs when there is an influx of Na^+ ions into the axon followed by repolarisation when there is an outward flow of K^+ ions. The axon connects to the

neuron's presynaptic terminals, which relay a synaptic potential to other neurons and other types of cells. In the human nervous system, axons vary in length from less than 1 mm (found in interneurons) to over 1 m (found in the sciatic nerve which connects the big toe to the spinal cord) (Debanne *et al.* 2011).

Neurons can also be classified on the basis of function into motor neurons, sensory neurons and interneurons (Martini *et al.* 2011: 379). Motor neurons link the brain to muscles by extending their axons outside of the CNS to control muscles. Sensory neurons are pseudounipolar neurons where the soma and central process are located in the spine and the peripheral process extends out into the peripheral nervous system to sensory receptors. Sensory neurons are activated by external stimuli such as light and touch in contrast to other neurons in the CNS that are activated by each other. The extended axons from motor neurons and the peripheral process from sensory neurons are called peripheral axons. A nerve is just an enclosed cable-like bundle of these peripheral axons. An interneuron is a multipolar neuron that acts like a relay junction for sensory and motor neurons in the CNS. Technically, all neurons in the CNS are interneurons but the term is often used with specific reference to those neurons that relay information locally rather than over large distances in the CNS.

The end of each neuron's axon branches out into an array of presynaptic terminals that relay information to other neurons, muscle cells, glands, *etc*. The presynaptic terminals of one cell and the dendrites of a second cell, to which the first is connected, do not physically connect with each other. Rather, there is a small gap between them called a synapse. Figure 2.2 illustrates an example of a synapse at a neuromuscular junction. The presynaptic terminal sends information from one side of this gap to the receiving postsynaptic cell (*e.g.*, a muscle cell in Figure 2.2) on the other

side. Each neuron has between 1,000 and 10,000 synaptic connections to other neurons (Ikezu and Gendelman 2008).

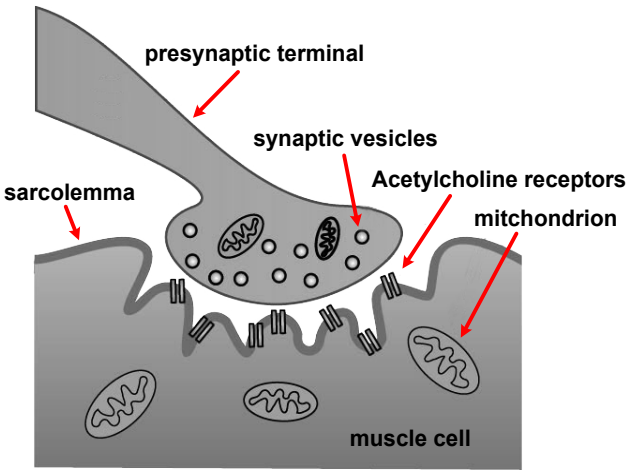

Figure 2.2: An illustration of a chemical synapse at a neuromuscular junction. The presynaptic terminal from a neuron in an efferent nerve fibre is connected to a muscle cell via a small gap. A chemical reaction occurs between acetylcholine released from the neuron and an enzyme called acetylcholinesterase at the other side of the junction when a nerve impulse is sent down the nerve fibre. The image is modified from (Dake 2005).

The synapse can be either an electrical synapse or a chemical synapse (Martini *et al.* 2011: 400-401). In an electrical synapse, the presynaptic terminal and postsynaptic cell membranes are connected by channels that are capable of passing electrical current in the form of moving ions (principally sodium (Na^+), potassium (K^+), and chloride (Cl^-)). In a chemical synapse, the terminal contains mitochondria and vesicles filled with molecules of acetylcholine (ACh). ACh is a neurotransmitter which is released by the neuron to change the membrane properties of another cell. The release of ACh is triggered by the arrival of an action potential which has propagated down the axon from the soma to the presynaptic terminal. ACh is broken down by an enzyme called acetylcholinesterase (AChE). It is this release of ACh and breaking down by AChE in the synapse that controls a flow of sodium ions and results in the generation of an electrical impulse.

2.1.2 The central nervous system

The CNS consists of the brain and spinal cord. In the human body, 98 % of the neural tissue is located in the CNS (Martini *et al.* 2011: 137). Because of its critical functions, the human body provides protection from damage to the CNS by enclosing it in the skull and vertebrae. Groups of neurons in the CNS are called nuclei and constitute the grey matter. White matter in the CNS is mostly made up of myelinated axon tracts (Tortora and Derrickson 2011: 458).

One of the components of the CNS that is a key focus of this discussion is the cerebral cortex region of the brain. The cerebral cortex supports many functions, such as intelligence and personality, which help determine an individual's character. Two important functions of the cerebral cortex, which are of primary interest here, are the interpretation of sensory input and motor control. The sensory areas receive and process information from the body's senses. The senses by which we perceive stimuli from the outside world are called the exteroceptive senses. Traditionally we think of these as being the five primary senses of sight, hearing, taste, smell and touch (Aristotle ca. 350 BC). Additional sensory modalities like the sense of pain, balance, proprioception, time, temperature difference and direction could also be considered (Jacobson 2009). The five primary sensory modalities have long been recognised to be associated with specific groups of brain cells (*i.e.*, regions of the cerebral cortex) – as described in Table 2.1.

Table 2.1: A table listing the regions of the cerebral cortex that are associated with the primary sensory modalities. The approximate location for each region is described and the corresponding sensory modality is listed (Marieb and Hoehn 2012: 242-243).

	Name	Location	Sense
1	Primary visual cortex	Located on the occipital lobes	Sight
2	Primary auditory cortex	Located on the temporal lobes	Hearing
3	Primary gustatory area	Located on the insular cortex	Taste
4	Primary olfactory cortex	Located on the uncus of the piriform region of the temporal lobes	Smell
5	Primary somatosenory cortex	Located on the anterior parietal lobes (*i.e.*, the post-central gyrus)	Touch

Of even more relevance to the work carried out in this research are the motor areas of the cerebral cortex. The motor areas plan and control voluntary movement of the body. The main motor areas of interest are the primary motor area (or primary motor cortex), Broca's speech area and a third associated area, the pre-motor area (Tortora and Derrickson 2011: 553-554) - as described in Table 2.2.

Table 2.2: A table listing the principal motor areas of the cerebral cortex. For each region, the approximate location in the cerebral cortex and the role played in the planning and control of motor movement are also described (Tortora and Derrickson 2011: 552-554, Marieb and Hoehn 2012: 241-243).

	Name	Location	Responsibility
1	Primary motor cortex	Located in the posterior portion of the frontal lobe (*i.e.*, the pre-central gyrus)	Controls the execution of motor movement
2	Broca's speech area	Located in the frontal lobe, close to the lateral cerebral sulcus	Directs the muscles involved in speech
3	Pre-motor area	Located in the frontal lobe, anterior to the primary motor cortex	Plans motor movement

In 1954, a neurosurgeon, Dr. Wilder Penfield, and a neurologist, Dr. Herbert Jasper, published their work regarding the mapping of the sensory and motor cortices of the brain (Penfield and Jasper 1954). Their work was principally focused on treating patients with severe epilepsy by identifying and neutralising the area of the brain where each patient's seizures were triggered. While their patients were conscious and under local anaesthesia, they would electrically stimulate different areas of the brain in an effort to locate the seizure's point-of-origin. Resulting from their experiments, they were able to create a map of the primary somatosensory cortex and the primary motor cortex. These maps illustrate that these cortices are divided into different areas, each associated with a different part of the body - as illustrated in Figure 2.3.

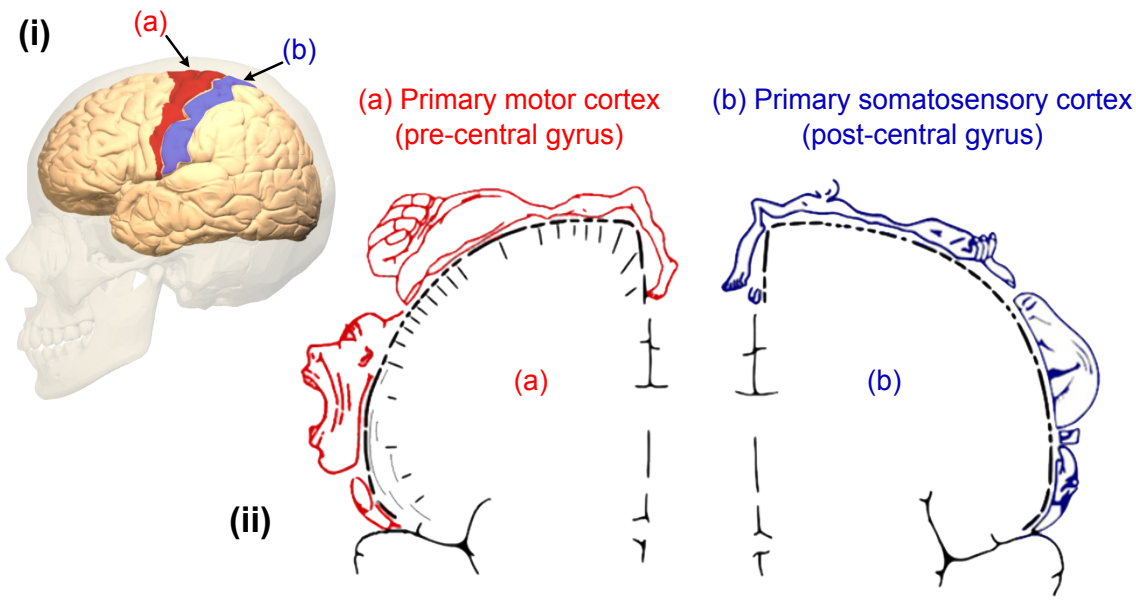

Figure 2.3: Illustrations of: (i) the lateral surface of the human cerebral cortex with the (a) pre-central (*i.e.*, the primary motor cortex) and (b) post-central (*i.e.*, primary somatosensory cortex) regions highlighted in red and blue; and (ii) splices of these regions overlaid with representations from Penfield's Homunculus. The images are modified from (i) - (Ministry of Education Culture Sports and Technology - Japan 2011) and (ii) - (Maquesta 2007).

Once these disproportionately sized body parts are assembled into two separate figures, a pair of disfigured humans is produced with disproportionately large hands, lips and face in comparison to the rest of the body. This is called Penfield's Cortical

Homunculus and it is a vivid representation of the fact that the size of the area of the brain associated with a body part depends on the amount of neurological resources associated with that body part – both for information processing and information transfer. For example, because our hands require fine motor skills for manipulating objects, a much larger area of the motor cortex (and in turn more brain cells) is devoted to them then there is for other parts of the body like the knee or elbow.

2.1.3 The peripheral nervous system

The PNS connects the CNS to muscles, glands and sensory receptors. Nerve impulses travelling away from the CNS to effector organs (*i.e.*, muscles and glands) propagate through efferent nerves (Marieb and Hoehn 2012: 228). Nerve impulses travelling from sensory receptors towards the CNS propagate through afferent nerves. Groups of neurons in the PNS are called ganglia. An area of skin that is mainly supplied by a single sensory nerve is called a dermatome. A group of muscles served by a single motor nerve is called a myotome.

There are two types of nerves in the PNS, spinal nerves and cranial nerves. Spinal nerves originate in the spinal cord from the neck down. There are 31 pairs (*i.e.*, left-hand side and right-hand side) of spinal nerves in the human body and these are categorised according to their corresponding location on the vertebral column (*i.e.*, spine). In descending order on the spine there are eight cervical nerve pairs (C1 to C8), twelve thoracic nerve pairs (T1 to T12), five lumbar nerve pairs (L1 to L5), five sacral nerve pairs (S1 to S5) and one coccygeal nerve pair (Marieb and Hoehn 2012: 257-262, Martini *et al.* 2011: 425-434). Each spinal nerve serves motor, sensory and autonomic (*i.e.*, heart rate, digestion *etc.*) functions in various parts of the torso and limbs.

Cranial nerves come directly from the brain and serve functions predominantly in the head and neck. A list of the twelve pairs of cranial nerves (one for each side of the brain) is shown in Table 2.3.

Table 2.3: A table listing the twelve cranial nerve pairs. The nerves are categorised into having a sensory and/or motor role and their primary function is described (Gray 1918: 748, Marieb and Hoehn 2012: 258-259). This list is ordered according to the nerves' respective locations from the front of the brain to the back.

Order	Nerve	Sensory/Motor	Example of Function
1st	Olfactory	Purely sensory	Sense of smell
2nd	Optic	Purely sensory	Visual information
3rd	Oculomotor	Mainly motor	Eye movement
4th	Trochlear	Mainly motor	Eye movement
5th	Trigeminal	Both	Facial sensation
6th	Abducens	Mainly motor	Eye movement
7th	Facial	Both	Facial expression and taste
8th	Vestibulocochlear	Mainly sensory	Senses sound, rotation and gravity
9th	Glossophyaryngeal	Both	Taste
10th	Vagus	Both	Speech
11th	Accessory	Mainly motor	Neck and trapezius movement
12th	Hypoglossal	Mainly motor	Primarily tongue movement

The efferent nerves that are responsible for motor movement and, in particular, those that form the highest bandwidth information channel out of the brain and into the outside world, are most relevant to this research. For example, with regard to the cranial nerves listed in Table 2.3, the nerves associated with speech (vagus), the tongue (hypoglossal) and neck and trapezius (accessory) movement are indirectly utilised (through the measurement of laryngeal vibrations and head orientation) in a human-to-machine communication application demonstrated in Section 5.1.

2.1.4 Muscle tissue

Up to this point, the discussion has been focused on the transmission medium in the human body (*i.e.*, the nervous system) for information flow (*i.e.*, nerve impulses). This section describes one type of organ in the body that is affected by nerves impulses, muscles. The primary function of a muscle is to produce force and they operate by the contraction of muscle tissue. There are three types of muscle tissue in the human body: skeletal muscle, cardiac muscle and smooth muscle (Tortora and Derrickson 2011: 328). The structure and operation of each type of muscle tissue is different in each case - as will be explained in this section.

Skeletal muscles allow us to voluntarily manipulate the bones in our bodies that are attached by joints, for example, our limbs, fingers or toes. They also: protect the entrances and exits of the digestive, respiratory and urinary tracts; generate heat; and protect internal organs. The activation of skeletal muscles is voluntary and depends on efferent nerve activity from the CNS to operate. Skeletal muscle tissue typically comprises thousands of cylindrical muscle cells (also known as muscle fibres) (Martini *et al.* 2011: 301). These muscle fibres are long, striated (*i.e.*, having a visible repeating pattern of red and white lines) and can contain several hundred nuclei. A single motor neuron can control from less than ten to thousands of muscle fibres - depending on the level of fine motor control required by a specific part of the body. When a muscle contracts, the activation of individual motor neurons (and therefore the muscle fibres under its control, *i.e.* a motor unit) do not occur simultaneously (Denny-Brown and Pennybacker 1938, Henneman *et al.* 1965b). Instead, motor neurons are generally recruited in order of size (*i.e.*, motor unit recruitment) from smallest to largest in relation to the applied load on the muscle (Henneman and Olson 1965, Henneman *et al.* 1965a).

Cardiac muscle cells (also known as cardiocytes) are solely located within the heart. Unlike skeletal muscles, cardiac muscles do not depend on activation via nerve signalling from the CNS. Special cells called autorhythmic cells, located in the heart's sinoatrial node, generate an electrical impulse that keeps the heart beating in a regular rhythm (*i.e.*, they act as the heart's pacemaker) (Saladin 2011: 726). The effect of neural activity on the muscle is to speed up or slow down the rate at which the autorhythmic cells activate. Furthermore, this limited control is involuntary. The electrical impulse begins when one autorhythmic cell activates which triggers a chain reaction in the neighbouring autorhythmic cells. The generated electrical impulse propagates through cardiac muscle cells causing them to contract. Cardiac muscles cells are short, branched and striated. They usually contain a single nucleus and the cells are interconnected together (Martini *et al.* 2011: 136).

Smooth muscles are found in several locations around the body such as the walls of arteries and veins where they control the diameter of the blood vessel, helping to control the flow of blood. They make up layers of the gastrointestinal tract where they move food and urine and in the respiratory tracts where they control the diameter of the passageways. Like cardiac muscle, contractile control of smooth muscles is involuntary. However, like skeletal muscles, smooth muscle cells are controlled by the nervous system. Smooth muscle cells are short, spindle-shaped and non-striated (Martini *et al.* 2011: 136). Unlike skeletal and cardiac muscle cells, smooth muscle cells have only one central nucleus.

2.2 Biopotential measurement

Biosensors are devices that can analyse substances which are produced or consumed in a biochemical process (Eggins 1997). A wide variety of biosensors is

available for different uses. A biosensor has three parts. The first is biological component under measurement. The second is the transducer, which converts the measured component of the biological component into a signal that can be recorded and analysed. The third part consists of any electrical circuitry that connects to the sensor and processes the signal from the transducer. Different types of biosensors can be used to measure many biological substances like sugars, urea, and cholesterol. The term biosensor can also refer to certain biopotential sensing devices that are used to measure bioelectrical signals originating in the human body. The following section describes: various biopotentials used in control systems and clinical diagnosis; sensors and bioinstrumentation conventionally used to capture the signals; several issues involved in biopotential recording; and finally some state-of-the-art systems.

2.2.1 Biopotentials

A biopotential is a time-varying electrical potential at a point on or in a living organism. Biopotentials arise primarily due to movement of charge carriers (in the form of moving ions – Section 2.1.1) travelling throughout our bodies in nerves and muscles. Conventionally, the term biopotential refers to those components of the recorded signal that originate within the organism rather than due to external influences. When measured on the skin surface, these small electrical voltages are typically in the microvolt range. For example, the electrocardiogram (ECG) (electrical activity associated with the cardiac cycle of the heart) can range from 1 μV to 10 mV (Nagel 1995) - although it is normally at the lower end of that range during skin-surface measurement.

Although a biopotential can be measured at a single point, it is typically measured as a time-varying potential difference between two points on or in the

organism (or between one point and an average of several points). The distance between the electrodes on the human body has a large effect on the depth and extent of the region of sensitivity (as illustrated in Figure 2.4). The flow of charge carriers through the body is spread out in an electric field across the body tissue. The closer the electrodes, the smaller the region of sensitivity (diagram (a) in Figure 2.4). The further apart the electrodes, the greater the region of sensitivity (diagram (b) in Figure 2.4).

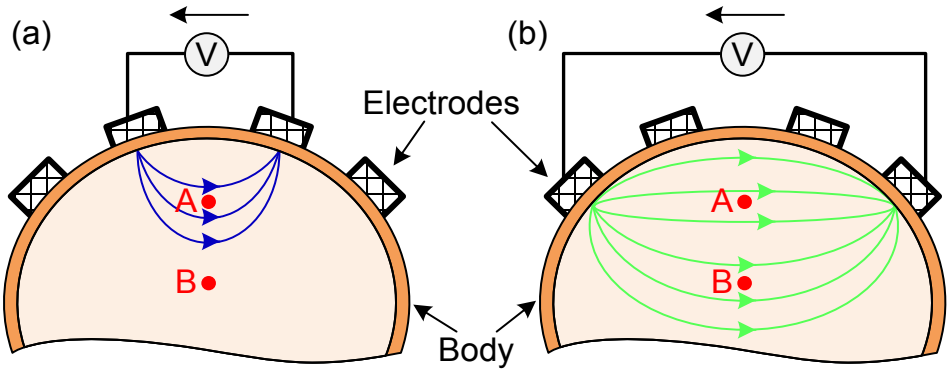

Figure 2.4: Multiple diagrams showing the position-dependent sensitivity for a pair of measurement electrodes. If, for example, point 'A' and point 'B' in Figure 2.4 were the locations of two different muscles in the body, the electrode configuration in (a) would be more sensitive to activity of 'muscle A' and less sensitive to 'muscle B' activity. In comparison, the electrode configuration in (b) would be sensitive to activity in both muscles.

A unipolar lead records the electrical potential at a single point relative to a reference potential (either at a specific point, or sometimes the average of a number of electrode potentials). By contrast, a bipolar lead configuration, as illustrated in Figure 2.4, records the electrical potential difference between two points, both relative to a reference potential.

Different electrode positions on the human body also give very different perspectives on the same underlying electrical activity. For example, the electrical activity from the heart (*i.e.*, the ECG) has a distinctly different appearance depending on the point of measurement on the body (as shown in Figure 2.5). In Einthoven's

electrocardiographic model (1908), the heart can be represented as a two-dimensional dipole (as viewed from the frontal plane) at a fixed location in the body (Malmivuo and Plonsey 1995: 193). The magnitude and direction of this dipole varies due to the electrical activity of different regions of the heart during the course of a cardiac cycle. In Figure 2.5, the heart dipole is viewed from the bipolar limb leads of Einthoven's triangle. Einthoven's triangle (as shown by the blue arrows) is an approximate representation of the lead vectors associated with the bipolar limb leads (Malmivuo and Plonsey 1995: 277).

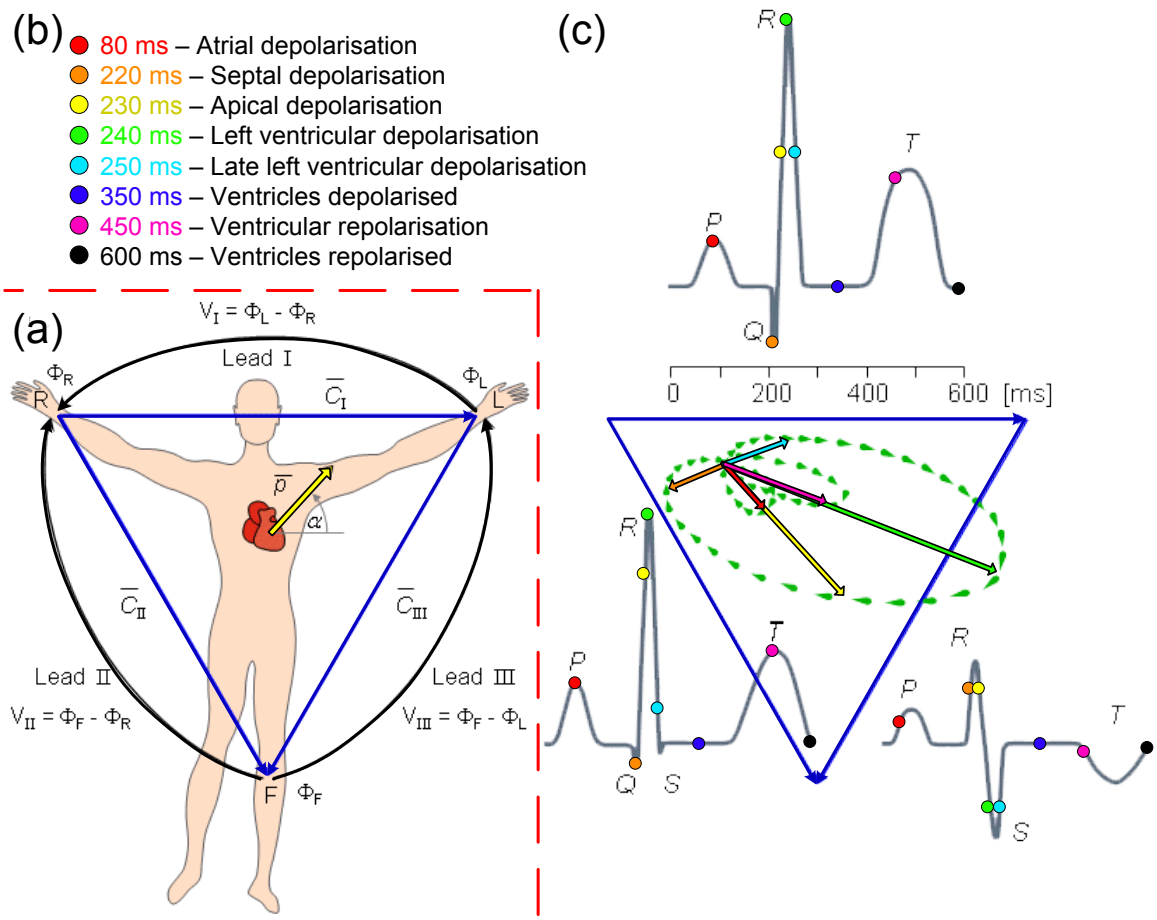

Figure 2.5: Diagrams showing how a biopotential voltage can vary depending on the electrode location (*i.e.*, viewpoint) on the human body. (a) The lead vectors of Einthoven's triangle (blue arrows), the bipolar limb leads (black curved arrows) and the representative dipole of the heart (yellow arrow). (b) The heart's electrical activity sequence during a cardiac cycle. (c) The change in orientation and magnitude of the dipole during a cardiac cycle and the corresponding effect it has on the bipolar lead signals. Note that the three bipolar limb leads require a separate low-impedance

connection between the measurement circuitry and the body (usually on the right leg) that is not shown on this diagram. These images are modified from (Malmivuo and Plonsey 1995: 278-283).

Several ECG measurement topologies are widely used in clinical measurement, which range from a basic 3-lead ECG (as illustrated in Figure 2.5) to a more detailed 15-lead ECG. The common 12-lead model involves 10 physical electrodes connected onto predefined points on the body from which 12 different electrical signals are recorded, each providing a different view of the electrical activity of the heart (Malmivuo and Plonsey 1995: 286-289). A deviation in an ECG from an expected norm can aid in the diagnosis of cardiac problems such as a myocardial infarction (heart attack) or ischemia (poor blood flow) or certain heart abnormalities such as hypertrophic cardiomyopathy (abnormal enlargement of the heart) or aortic regurgitation (failure of the aortic valve to close completely causing a leak of blood back into the heart) (Andreoli *et al.* 1997: 46-55). A 12-lead ECG can be recorded by a clinician in the hospital or, in order to obtain an immediate measurement of a patient in distress, by an ambulance medic using a portable electrocardiograph. If a patient has a suspected heart condition, a doctor can prescribe a Holter (1961) monitor that records heart activity over a period of time. On accumulation of the data, the doctor can examine possible ECG abnormalities as the patient went about their daily activities.

In all cases listed above, the ECG is typically recorded in isolation from other physiological phenomena. Although the primary focus of this research is the facilitation of communication and control, the novel sensor technology developed for that purpose has obvious applications in clinical biopotential measurement, such as the augmenting ECG with information regarding the subject's motion activity and gait or the detection of motion artefacts in ECG, which are both discussed further in Section 5.4.

Another biopotential commonly used in clinical measurement and research is the electroencephalogram (EEG) (electrical signals associated with brain activity). The measurement of EEG is typically used to study three types of activity: spontaneous activity, evoked potentials and single-neuron bioelectrical events (Malmivuo and Plonsey 1995: 257). The spontaneous electrical activity is the brain's ongoing activity when not undertaking a specific task (*e.g.*, processing sensory input or motor control). Evoked potentials are components of EEG that are used to gauge the brain's response to an external stimulus (*e.g.*, visual, auditory or sensory). The electrical activity of single neurons can be measured by isolating individual neurons using an array of needle-sized electrodes (*i.e.*, a microelectrode array) (Hoogerwerf and Wise 1994). Whereas the spontaneous activity and evoked potentials can be measured across the scalp's skin surface, the measurement of single neuron behaviour requires invasive methods.

As our understanding of the EEG improves, avenues are beginning to open up for using these signals to control human-to-machine interfaces (*e.g.*, control of powered prostheses (Velliste *et al.* 2008, Collinger *et al.* 2013)). Computer game controllers are currently available that allow a user to interact with a computer through EEG activity (Emotiv 2012, Neurosky 2012). A disadvantage to using EEG equipment is that it can be time consuming to attach and cumbersome to use. A full EEG cap used to record skin-surface potentials typically contains 128 individual electrodes, each with a separate wire connecting it to signal conditioning circuitry.

A biopotential with conspicuous ability to be used in the conscious control of human-to-machine interfaces is the electrooculogram (EOG) (electrical potential variations that occur in the vicinity of the eyes when they are moving, due to a standing electric field around each eye) (Malmivuo and Plonsey 1995: 440-442). The EOG is an easily interpreted set of biopotential signals that represents movement of the eyes in the

vertical and horizontal plane, with respect to the orientation of the head, *i.e.*, gaze position. The EOG is assumed linear over a high dynamic range of approximately ± 70º with an accuracy of approximately 1º to 2º (Augustyniak *et al.* 2010). The horizontal and vertical components of the EOG are conventionally recorded using two pairs of skin surface electrodes (one pair above and below the eye and a second pair located either side of the eyes) and one reference electrode (typically placed behind an ear). The principal impediment to harnessing the EOG as a control signal is the continuous presence of drift in the measured electrical potential, even when the eyes remain in a stationary position.

The electromyogram (EMG) is another biopotential that is an obvious candidate for use in the conscious control of human-to-machine interfaces. EMG is produced during activation of muscles (typically measured from skeletal muscles) and can be measured on the surface of the skin (using skin surface electrodes) or intramuscularly (using more invasive needle electrodes which are inserted into the subject). Excluding possible induced electromagnetic interference, the resting potential of a healthy skeletal muscle fibre is $-85\,mV$ (Martini *et al.* 2011: 96). Upon conscious activation of a skeletal muscle, action potentials begin to appear across the muscle, which contribute to the EMG. As the level of muscle exertion increases, more active muscle fibres produce action potentials (see Section 2.1.4). Upon full exertion, the EMG appears as a disorderly group of action potentials with varying rates and amplitudes (Andreoli *et al.* 1997). A disadvantage of recording EMG with conventional skin surface electrodes is that only activity from superficial muscles is accessible. Also, since the EMG has characteristics similar to band-limited noise, electrical interference from the surrounding environment can obscure the original EMG signal (Clark 2009).

Some of the biopotentials that are frequently measured from the human body are listed in Table 2.4.

Table 2.4: Examples of various biopotentials, basic description and frequency and voltage ranges (Olson 2009). The ranges given for ECG, EEG, EOG and ERG represent the detectable signals on the skin surface. The EMG ranges represent those detectable intramuscularly.

Abbr.	Title	Description	Freq. Range	Voltage Range
ECG	Electrocardiogram	Cardiac Monitoring	0.01 Hz to 250 Hz	0.5 mV to 4 mV
EEG	Electroencephalogram	Electrical activity produced by firing neurons in the brain	DC to 150 Hz	5 µV to 300 µV
EMG	Electromyogram	Muscle activity	DC to 10 kHz	0.1 mV to 5 mV
EOG	Electrooculogram	Eye movement	DC to 50 Hz	50 µV to 3.5 µV
ERG	Electroretinogram	Electrical activity in various cell types in the retina	DC to 50 Hz	0 V to 900 µV

2.2.2 Biopotential sensors

As described in Section 2.1.1, the nervous system uses a flow of ions, principally sodium (Na^+), potassium (K^+), and chloride (Cl^-), in and out of cells to communicate. An action potential, caused by fluctuations in ion concentrations, propagates along nerve cells and muscle fibres that spread throughout the body. The collective electrical activity of nerve cells and muscle fibres within the body can be measured as a biopotential (*i.e.*, a time-varying difference in electrical potential between points on the surface of the skin) using a transducer called a surface recording electrode. An electrode is an electrochemical sensor that converts the flow of ions within the body

into a flow of electrons which can then be measured by an electronic circuit (Neuman 2009b).

There are many different transducers available, ranging from the traditional wet silver-silver chloride electrodes to modern 3-D MEMS microelectrode arrays (Hoogerwerf and Wise 1994), each with its own advantages and disadvantages. For example, disposable hydrogel electrodes are flexible as they are constructed using a thin layer of silver foil (Neuman 2009b). The entire skin surface side adheres to the skin via a hydrogel film saturated with an electrolytic solution, both of which are manufactured from materials with adhesive properties. These attributes mean that hydrogel electrodes are useful for monitoring biopotentials in patients who are not in a stationary position. However, a disadvantage to this construction is that the ions in the skin-electrode junction are less mobile and in reduced concentration, resulting in an electrode that has higher source impedance compared to electrodes with a pure electrolyte gel layer. Selection of the correct transducer depends on different factors including: the signal under measurement; the desired surface resolution; whether a skin surface or implanted transducer is used; what size the device needs to be; *etc.*

2.2.2.1 Metal plate electrodes

The most frequently used form of electrode in biopotential measurement, and the one most pertinent to the present research, is the metal-plate electrode. Metal-plate electrodes are commonly manufactured using a silver/silver chloride (Ag/AgCl) combination. A layer of silver, which is connected by an insulated wire to a measuring circuit, is coated with a layer of silver chloride. Silver chloride is a slightly soluble ionic compound and acts as the electrode-electrolyte interface. The electrolyte, or gel in Figure 2.6, is an aqueous solution soaked in a sponge and is used to create a better

connection between the surface of the skin and the electrode. For an Ag/AgCl electrode, the electrolyte contains anions (negatively charged ions) of Cl^- and cations (positively charged ions) of the electrode metal, silver (Ag^+). Chemical reactions at the interface between the electrode and electrolyte allow charge to transfer from one to the other (Neuman 2009b).

2.2.2.2 The electrode-skin interface

Figure 2.6 illustrates a block diagram of a metal-plate electrode in contact with a layer of skin and an equivalent circuit model (Neuman 2009b). This model includes equivalent impedances for the electrode, Z_d, gel, R_s, skin (epidermis, Z_e, and sweat glands/ducts, Z_p) and tissue, R_u. The DC offset, E_{he}, is caused by the half-cell potential at the electrode-electrolyte interface and E_{se} (and E_p) by variances in ionic concentration across the epidermis.

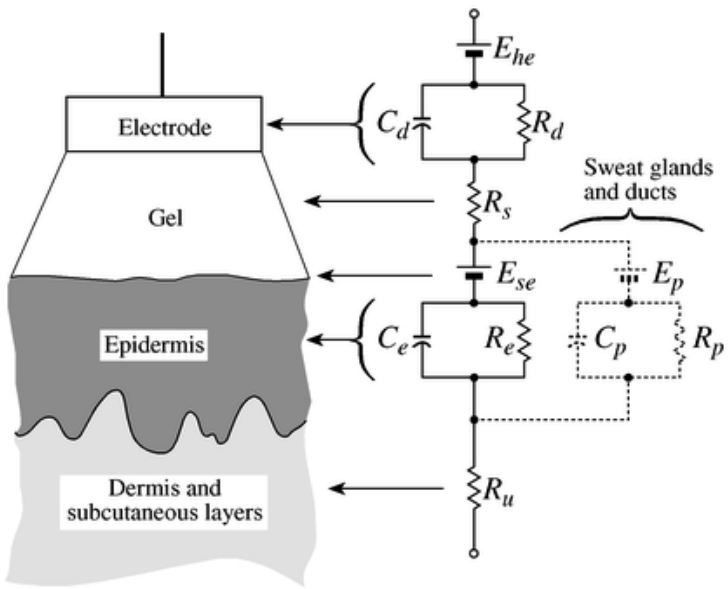

Figure 2.6: A block diagram of the electrode-skin interface and the equivalent circuit model. The image is referenced from (Stilson 1996) but based on (Neuman 2009b).

Improper connection at an electrode-skin junction (*i.e.*, failure to achieve a consistent low-impedance path from the skin, via electrolyte, to the electrode) can result

in large motion artefacts and erroneous recordings in biopotential measurements (see Section 2.2.4). In order to check the quality of an electrode-skin connection, an electrode impedance meter is sometimes used. This type of device is connected to electrodes that have been applied to the skin, prior to connection to bioinstrumentation circuitry. The cost of these devices can range up to €1500, making them prohibitive for everyday use (Grass Technologies 2013). Impedance meters conventionally operate by performing a frequency sweep on an unknown impedance network - in this case, between one electrode and another via the body. A sinusoidal test current at one or more frequencies (typically 10 Hz and 30 Hz) is used and, at each frequency, the impedance (magnitude and phase) is calculated. Commercial electrode impedance meters typically specify a maximum test current of less than 10 μA AC with no electrode DC polarising current (Grass Technologies 2013) (further discussion in Section 2.2.4).

Utilising a custom-built impedance meter, Grimnes (1983) has shown that the epidermis, dermis and subcutaneous impedance values vary widely at different measurement points on the body. For example, under specific experimental conditions, it was found that the impedance in the hand was 320 kΩcm^2 compared with the upper arm at 700 kΩcm^2 - both measured under a test signal at 10 Hz. The reactive component of tissue impedance is regarded as unimportant at a test signal frequency range of under 1 kHz (Malmivuo and Plonsey 1995: 407). It has been shown that the value of the skin's impedance has a non-linear relationship to the AC test signal from an impedance meter (Yamamoto and Yamamoto 1981, Lackermeier *et al.* 1996). Rosell *et al.* (1988) conducted a thorough investigation of this phenomenon by measuring the impedance values at various positions on the thorax, leg and forehead. They concluded that: at a high frequency of 1 MHz, the average impedance was approximately 120 Ω; at 100 kHz it was approximately 220 Ω; at a low frequency of 1 Hz it varied from 10 kΩ to 1 MΩ.

To simulate the worst case scenario, both Grimnes (1983) and Rosell *et al.* (1988) conducted their experiments using wet-gel electrodes on unprepared skin.

Over the course of ten days, Grimnes (1983) observed that the impedance of a pre-gelled ECG electrode placed on the upper arm, decreased from approximately 400 kΩ to approximately 1.5 kΩ. Huigen *et al.* (2002) corroborated these results by noticing a reduction in signal noise of up to 50 % 20 minutes after application. Grimnes (1982, cited in Grimnes 1983) attributed this impedance reduction to two reasons, firstly, the dispersion of electrolyte on the surface of the skin over time causes an increased effective electrode area. Secondly, electrolyte penetration into the skin increases the quality of the electrical connection to the body. Rosell *et al.* (1988) noted that, in some circumstances, they found an impedance increase of up to 20 % which they attributed to the closure of the sweat ducts after application of the cool electrolyte gel.

2.2.3 Evolution of bioinstrumentation technology

Bioinstrumentation technology has evolved considerably since the pioneering work of several early researchers. Augustus Waller (1887) was the first to publish graphs produced from the recording of electrical activity from the heart. Waller used a Lippmann capillary electrometer connected to zinc electrodes covered in brine dampened chamois leather. The Lippmann capillary electrometer, invented by Gabriel Lippmann (1873), consisted of a thin glass tube in which a volume of mercury lay beneath sulphuric acid. The height of the meniscus would vary depending on the amount of electrical potential subjected to it and the change could be observed using a microscope. Willem Einthoven (1895), using his own improved electrometer design, described the electrocardiogram and the deflection labels PQRST that remain in use to

this day. Einthoven went on to develop a string galvanometer (Einthoven 1901, cited in Rivera-Ruiz *et al.* 2008) and demonstrated its use for producing accurate electrocardiograms (Einthoven 1902, cited in Rivera-Ruiz *et al.* 2008). Einthoven's string galvanometer was similar to that independently developed previously by Clément Ader (1897) for use in telecommunications. However, Einthoven's apparatus achieved a significantly higher sensitivity, thus facilitating diagnostic quality electrocardiographs.

The next evolution in bioinstrumentation design began when Ernstene and Levine (1928) published the first incident of the amplification of an electrocardiogram through electrical means by way of a vacuum tube, rather than mechanical means as was the case with Einthoven's string galvanometer. With the advent of solid-state electronics and the invention of the transistor, amplifier design transitioned from vacuum tubes to semiconductor diodes and transistors. The classic design for the late 20th century became a three operational amplifier (op-amp) instrumentation amplifier configuration, as illustrated in Figure 2.7.

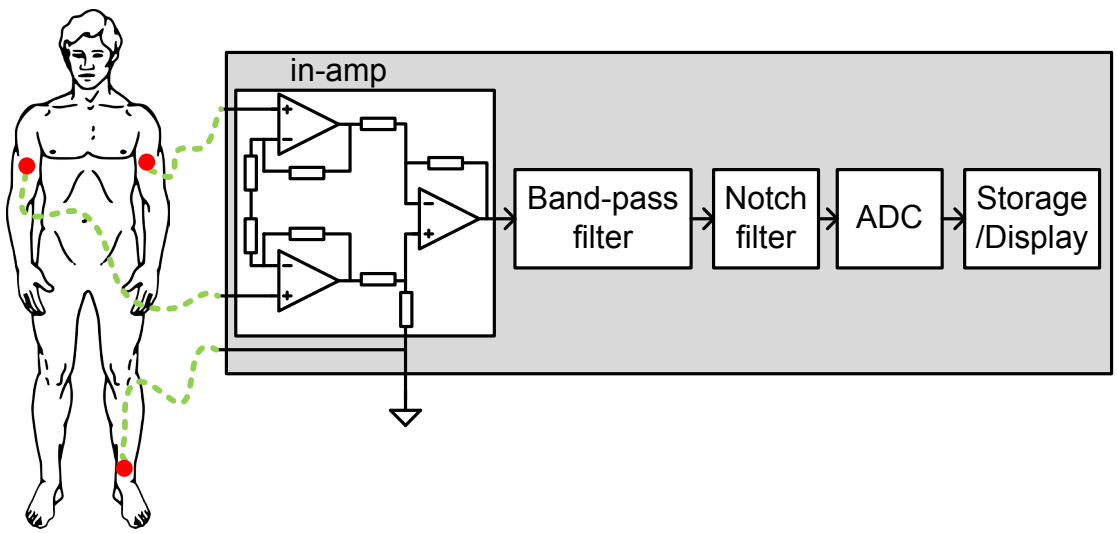

Figure 2.7: A diagram illustrating the late 20th century conventional bipolar biopotential recording topology - using 3-lead ECG as an example. This model utilises an instrumentation amplifier (comprising three operational amplifiers) that amplifies the difference signal between the two source electrodes. A low impedance connection to the body is used as a reference point.

In this conventional biopotential recording topology, three or more electrodes are placed on the body and a time-varying electrical potential between pairs of points is recorded. Figure 2.7 shows a bipolar lead configuration in which the signal electrodes are connected to high impedance amplifier inputs, while an additional electrode provides a low-impedance path between the amplifier and human subject. Bipolar leads are usually preferred since interference appearing at both signal electrodes can be mostly eliminated using an instrumentation amplifier with high common-mode rejection ratio (CMRR) as discussed in greater detail in Section 2.2.4.

Since the amplitude of a biopotential signal is typically in the microvolts range, multiple stages of voltage amplification are sometimes required so that the electrical signals can be examined and recorded. The biopotential voltage is typically amplified to suit the specified input voltage range of an analog-to-digital converter. Modern sigma-delta ($\Sigma\Delta$) analog-to-digital converters typically have up to 24-bit sampling resolution. As technological advances increase the maximum resolution of analog-to-digital converters, less gain is required before digitising small biopotential voltages.

After amplification, biopotential signals conventionally pass through one or more filter stages, as shown in Figure 2.7. In this example, a band-pass filter stage allows the biopotential frequency range of interest to pass through whilst rejecting DC and higher frequency interference. A second stage consisting of a notch filter facilitates reduction of mains interference. Alternatively (or additionally), digital filtering can be carried out subsequent to sampling.

As mentioned previously, signal conditioning systems typically utilise common-mode rejection by sending the inverse of the common-mode signal back into the body through a low impedance input connection to the body. Another evolution, as

illustrated in Figure 2.8, utilises a right-leg-driver (or driven-right-leg) within the feedback loop (the name is a convention, rather than a requirement that it be connected to the subject's right leg). In a driven right-leg system, the common-mode signal is inverted, amplified and sent back into the body in order to reduce the common-mode interference before it enters the bioinstrumentation circuitry (Winter and Webster 1983a). This negative feedback approach has the added benefit of providing a certain level of electrical protection (Neuman 2009a). If a large voltage appears between the patient and ground reference potential, the right-leg-driver operational amplifier would saturate, effectively un-grounding the subject. With the op-amp disabled, a parallel combination of the resistors in the right-leg-driver links the subject to ground. In order to limit the possible current going through the subject, these resistors can be in the several megohms range.

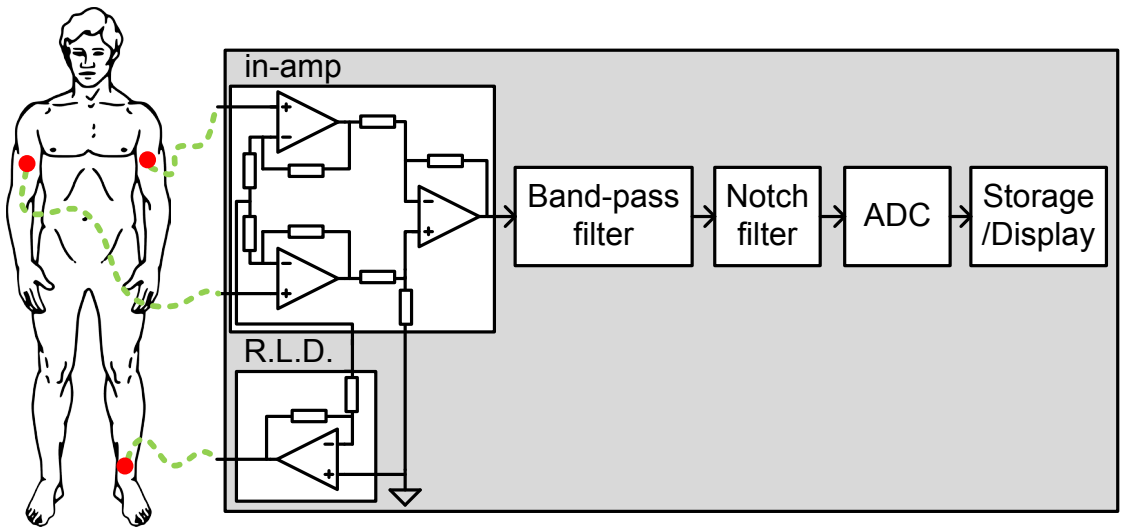

Figure 2.8: A diagram illustrating the late 20th century conventional bipolar biopotential recording topology incorporating a right-leg driver - using 3-lead ECG as an example. In this model the common-mode signal is inverted, amplified and sent back into the body.

A drawback of conventional unipolar and bipolar recording configurations is that wires (typically up to a meter long) must connect each electrode to the recording equipment. The majority of biopotentials have a tiny signal amplitude (5 µV to 5 mV

range) (Olson 2009). Consequently, any external electromagnetic interference that is induced in these passive electrode wires can have a corrupting effect on the original measured biopotential signal (Huhta and Webster 1973). In addition, these long electrode wires usually run in parallel, which can create an undesirable capacitance between the wires (*i.e.*, a parasitic capacitance) and lead to a disruption of the normal current flow system. High performance modern electrode systems, such as the BioSemi ActiveTwo (2002), go some way towards addressing this problem by incorporating an active element, *i.e.*, operational amplifier, into the electrode. These active electrodes increase the signal power at the point of measurement such that the relative effect of the induced noise on the wires is reduced significantly (*i.e.*, increasing the signal-to-noise ratio) (MettingVanRijn *et al.* 1996).

A novel example of active electrode design is by Tae-Ho *et al*. (2008) whereby a unity gain buffer was integrated into a fabric electrode. The electrode comprised a nonwoven fabric, Evolon, which provides a flexible, durable, washable, soft and smooth fabric that is also dimensionally non-stretchable. On one side of the fabric, a transducer layer was hand-printed using Ag/AgCl ink. On the other side, conductive wires and electrical components were attached using adhesive pastes. Testing was conducted by measuring ECG from a subject in a sitting position and while jogging using both an active and a non-active fabric electrode. Their results indicated that, even with hand-crafted electrodes, a significant improvement in signal quality can be obtained using the active electrodes, especially in a physically active environment such as jogging.

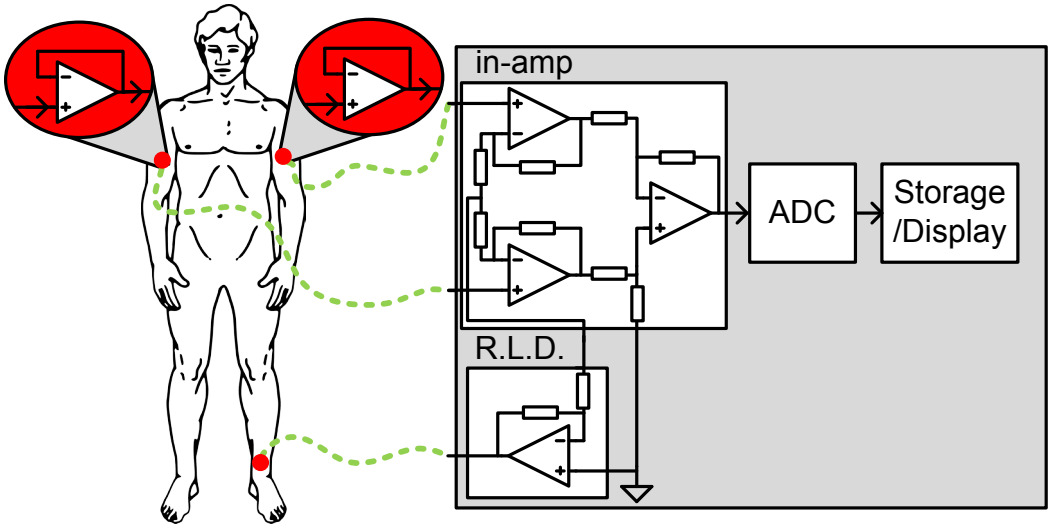

Figure 2.9: A diagram illustrating the biopotential recording topology similar to that used in many high-performance electrode systems. An active element (*i.e.*, an operational amplifier) is incorporated into each sensing electrode. Although it is configured as a unity gain buffer in this case, some gain or filtering can be also incorporated at this stage.

Due to the decrease in cost, size and power requirements of integrated circuits, there is a growing trend to shift the bioinstrumentation circuitry away from a base measurement system and into the electrode itself. Schnitz *et al*. (2004) and Fadem and Schnitz (2005) have designed a multi-electrode system for use in EEG measurement with on-electrode filtering, gain and analog-digital conversion stages. Their device utilised a serial peripheral interface bus (SPI) with high bus speeds that allow for a large number of electrodes to be employed, as is required with EEG. A disadvantage to their approach is that, in their system, electrode sampling can only be performed sequentially rather than synchronously. Jivet *et al.* (2009) and Jivet and Dragoi (2008) have investigated the use of on-electrode integrated circuitry for electrical impedance tomography applications. Their design incorporates on-electrode voltage measuring and constant current generation circuitry. It also uses an I^2C digital bus as the communication backbone between electrodes. Unlike the multi-purpose electrode system outlined in this research, their system has a single application and is not designed to also measure biopotential signals. The examples outlined above form part of

a wider body of research in the area of body area networks (BAN) with applications including health care monitoring and human-machine interfaces. The IEEE standard for BANs has been under development since 2007 (Institute of Electrical and Electronics Engineers 2007).

Harrison *et al.* (2007) have shown that, with the use of Microelectromechanical systems technology (MEMS), all active electrode data processing and wireless transmission circuits can be moved onto the electrode such that all external voltage carrying wires can be omitted from bioinstrumentation design. They describe a method to record neural activity with a low-power and wireless integrated circuit built on top of an implanted 100-electrode MEMS microelectrode array of surface area 3.6 mm^2. Of specific note in this context, they stated that the performance of their system was limited due to interference between the analog and digital subsystems caused by their proximity to each other. Another issue of note was their need to transmit large amounts of continuously streaming data over a wireless channel with limited bandwidth. To overcome this, the quantity of data was reduced by shifting the data processing on-board the integrated circuit such that only detected EEG spike information was transmitted.

Future biopotential recording systems might take the form of a single point of measurement from the body whereby the electrical circuit is completed via a capacitive coupling between the body/circuitry and earth. This topology of electrical potential measurement, which I have termed *monodal* measurement (Nolan *et al.* 2011), poses substantial circuit design challenges and has rarely been used in practice. However, examples of single-point biopotential measurement have occasionally appeared in the literature (Harland *et al.* 2002b, Song-Hee *et al.* 2004). In particular, Maruyama *et al.* (2007) outline an interesting progression from a conventional three-electrode design to a true unipolar (*monodal*) circuit design. Their design incorporated capacitive electrodes

into a seatbelt with the aim of measuring a driver's ECG. They demonstrated encouraging results in that their system was capable of measuring ECG through a single capacitive coupling electrode - without the need for a reference electrode.

2.2.4 Biopotential recording considerations

Biopotential measurement can be performed utilising basic equipment and knowledge. However, to obtain safe and accurate recordings that facilitate the correct interpretation of the underlying physiological phenomena, an in-depth awareness and understanding of the intricacies involved in biopotential instrumentation is required. The following section describes various causes of biopotential signal degradation and some related circuit design considerations.

2.2.4.1 Causes of signal degradation

As stated previously in Section 2.2.1, the majority of biopotentials have a tiny signal amplitude of between 5 μV and 5 mV. Consequently, signals under measurement are easily susceptible to corruption by external forces such as electromagnetic interference or physical body movement. A large body of research exists regarding the identification, description and quantification of noise in biopotential measurement, for example (Huigen *et al.* 2002, Fernández and Pallás-Areny 2000, Gondran *et al.* 1996, Webster 1984).

Huigen *et al.* (2002) attempted to identify and quantify the sources of noise in surface electrodes and found that at frequencies below 30 Hz, the majority of the noise originates in the electrode-skin interface and more specifically in the gel-skin interface. It can be gleaned from their results that, whilst mains interference is a dominant

interference feature in the spectrum of the signal, its predicable distribution in the frequency spectrum (at 50 Hz and its harmonics) makes it relatively straightforward to filter. In their experiments, other identifiable sources of interference were amplifier noise, thermal noise and noise from the metal-electrolyte interface. At frequencies above 30 Hz, the majority of interference was attributed to amplifier noise. Various common causes of signal degradation within the biosignal bandwidth are described in Table 2.5.

Table 2.5: A summary of the most common causes of signal degradation in biopotential measurement.

Region	Source	Description	References
Body	Motion artefacts	Physical movement of the electrode relative to the surface of the skin changes the electrode-skin interface.	(Tam and Webster 1977)
	Muscle contractions	Unwanted electrical activity from conscious/unconscious activation of muscles not under investigation. (*e.g.*, unwanted ECG while measuring EMG or vice versa).	(Tong *et al.* 2001, Akbary and Rabbani 2010)
	Respiration	Rhythmic or sporadic breathing activity manifested on top of a recorded biopotential signal. It can also be considered beneficial in ECG-derived respiration (EDR) signal analysis.	(Moody *et al.* 1985, Travaglini *et al.* 1998)
Common-mode interference	Electromagnetic interference	Including: – Power line interference – Radio-frequency interference – Static electricity – Interference from other electronic devices	(Webster 1984, Huhta and Webster 1973)
	DC bias	Removed in AC-coupled biopotential measurement systems. Often required for EOG or in very low frequency recording.	(Olson 2009, Nagel 1995)

	Parasitic / coupling capacitances	Parasitic capacitances (*e.g.*, between the subject/measurement equipment and ground) or coupling capacitance (*e.g.*, between measurement wires) can facilitate the flow of undesirable displacement currents.	(Metting van Rijn *et al.* 1991)
Measurement circuitry	Electrode-skin interface	Including: – High skin impedance due to location or inadequate skin preparation – Impedance imbalance between different electrode sites – Thermal noise	(Huigen *et al.* 2002, Tam and Webster 1977)
	Analog-to-digital converter introduced errors	Including: – Quantisation error – Aliasing	(Kester *et al.* 2005)
	Amplifier noise	Noise current and noise voltage sources are generated at the transistor input junction within operational amplifiers.	(Winter and Webster 1983b, Webster 1977, Horowitz and Hill 1989: 428)

Three causes of signal degradation that are particularly pertinent to this research - common-mode interference, impedance matching and motion artefacts - are examined greater detail in the following sections.

Common-mode interference

When recording a bipolar biopotential (*i.e.*, a differential voltage between two points on the body), the common-mode signal comprises two dominant components - 50 Hz AC interference from mains electricity (Huhta and Webster 1973) and a DC electrode offset potential. Some of the interference can be cancelled with a high input-impedance instrumentation amplifier, which removes the AC line noise common to both inputs and amplifies the differential signal present on the inputs. For example, in the

case of standard 3-lead ECG, since the measured electrical potentials originate at different points on the body, the left-arm and right-arm ECG signals are at different voltage levels and are amplified by the instrumentation amplifier. Choosing a differential amplifier with a high common-mode rejection ratio (≤ -120 dB) can reduce the common-mode interference to a satisfactory level (Winter and Webster 1983b). To further reject 50 Hz interference, an operational amplifier is used to amplify and invert the common-mode voltage and drive it back into the patient through another electrode (Winter and Webster 1983a). This technique, called a right-leg-driver, was described in Section 2.2.3.

Impedance matching

Matching the input impedance of the measurement circuit to that of the skin impedance is an important design factor. An impedance imbalance in the measurement circuitry can arise due to improperly connected electrodes or due to electrodes located at different points on the body. Unknown or variable skin/electrode impedances can cause offset and gain errors. An electrode-skin impedance mismatch also leads to a reduction in the common-mode rejection ratio of an amplifier (Winter and Webster 1983b).

Efforts have been made to reduce mismatching of electrode impedances. Silva *et al.* (2006) designed a model utilising a digitally controlled impedance compensation circuit. Their simulated model analysed the mains supply interference output from a differential amplifier connected to two electrodes. This signal was compared with a voltage reference and, if the amplitude of the two signals differed, a digitally controllable impedance connected in series with one of the electrodes was adjusted until the interference levels matched. Although simulated with ideal components, their model showed a best case interference reduction of 98.5 % after a brief settling time.

As described in Section 2.2.1, an electrolyte gel is typically used to lower the impedance of the skin-to-electrode interface. Skin preparation by exfoliating dead skin cells can also reduce skin impedance. By abrading the skin with fine sand paper, followed by cleaning with an alcohol wipe, a decrease in measured noise of up to 80 % can be achieved (Huigen *et al.* 2002). The abrasion of the skin exfoliates the stratum corneum, *i.e.*, the top dead layer of the epidermis.

Motion artefact

A double layer of charge forms at the intersection between an electrode and an electrolyte. If the electrode is moved with respect to the electrolyte, this interferes with the distribution of charge at the intersection between them and results in a momentary change of the half-cell potential until equilibrium can be re-established. If two electrodes are situated at different points on the body - both in contact with an electrolyte - and only one moves while the other remains stationary, a potential difference appears between the two electrodes. This potential difference is known as a motion artefact and can be a significant cause of interference in biopotential measurement (Khan and Greatbatch 1974, Valchinov and Pallikarakis 2004).

2.2.4.2 Circuit design considerations

One of the most important design criteria when designing a biopotential signal acquisition system is isolation from the mains power supply. Not only does this reduce the 50 Hz AC interference but it also removes the risk of potentially fatal electric shocks that could occur. Portable biosignal monitoring systems tend to utilise low, single-sided voltage supplies (*e.g.*, Holter monitors or blood pressure monitors). While bipolar supplies are still used, 5 V single-sided systems are now common and trending to a single-sided 3.3 V supply. The advantages of these power supplies are a decrease in

circuit complexity and battery size. Given the low-voltage power supplies typically used, precision signal conditioning integrated circuits are often favoured (or required) in biopotential recording.

Some types of medical equipment require an electrical current to be sent through the body to operate (*e.g.*, electrode impedance meters – discussed in Section 2.2.2). The International Electrotechnical Commission's (2005) safety requirements for medical electrical equipment (IEC 60601-1) defines patient auxiliary current as "*current flowing in the patient in normal use between any patient connection and all other patient connections and not intended to produce a physiological effect*". This international safety standard states that the maximum patient auxiliary current permissible for DC is 10 μA and for AC is 100 μA. Ideally, there should be zero net current through the body (*i.e.*, no DC) as a DC bias can result in polarisation of the electrode due to the accumulation of ions near electrode sites. Electrode polarisation can cause burns and/or tissue necrosis with long-term application (Greatbatch *et al.* 1969, Szocik *et al.* 2010). Commercial electrode impedance meters, for example, typically specify a maximum test current of less than 10 μA AC with no electrode DC polarising current (Grass Technologies 2013).

2.2.5 The state of the art in biopotential recording

Thus far, the discussion has focused on biopotential signals, the typical circuitry used to measure them and some of the issues involved in their measurement. This section explores the state of the art in biopotential recording that has a significant impact on the original research presented in this thesis. Advances in both integrated-circuit and biopotential sensor technology are opening up new avenues in biopotential measurement. Two significant advances in analog-to-digital converter design, sigma-

delta converters and analog-front-ends are discussed in the following section. An emerging technology that holds great potential for the future of biopotential sensor design, the capacitive-coupling electrode, is also described.

2.2.5.1 Advances in analog-to-digital converters

An analog-to-digital converter (ADC) is a key component in the majority of biopotential recording systems. Until recently, the most commonly used type of ADC has been the successive approximation register (SAR) ADC. As the name implies, SAR converters provide a successive approximation of a signal over a short period. For example, each conversion result of a 12-bit SAR is the result of twelve consecutive comparisons between the input signal voltage and a reference voltage, which is adjusted to match it incrementally. At each stage, the relative bit of the output data register is populated with the binary result of the comparison as the ADC homes in on the approximated result (Maxim Integrated Products Inc 2001).

Certain recent advances in ADCs relate to the maturing technology that is the sigma-delta (ΣΔ) ADC. A ΣΔ converter samples its input signal at a very high frequency and, after a predefined duration, the final digitised result is calculated based on the average of each of the conversion values. The exact operation of the ΣΔ modulator lies outside the scope of this research. However, excellent sources for further reading include (Boser and Wooley 1988, Candy and Temes 1992, cited in Kester and Bryant 2005). Some details regarding the internal features of a typical ΣΔ ADC are also outlined in Chapter 3. The ΣΔ topology facilitates high-resolution sampling (up to 31-bit resolution with current technology). However, depending on the ΣΔ modulator clock frequency, the ΣΔ converter sampling delay (*i.e.*, latency) is normally higher than with the SAR converter. There has traditionally been a trade-off between the resolution of a

ΣΔ converter and its sampling rate. In recent years however, the performance of ΣΔ converter technology has advanced such that the AC, DC and sampling rate characteristics are comparable to SAR converters whilst maintaining the benefit of high resolution.

The lower-frequency sampling clock of the SAR ADC means that an anti-aliasing filter is generally required. By contrast, ΣΔ converters have a much higher sampling clock relative to their effective bandwidth, so the digital filter within the ΣΔ ADC acts as an adequate anti-aliasing filter in many cases. A disadvantage of the ΣΔ converter's higher speed sampling clock is an increase in the current consumption of the circuit.

Another technological advance in the field of biosignal measurement is the *analog-front-end* (AFE), and more specifically medical AFEs. AFEs facilitate a significant reduction in size, power and overall cost of medical equipment by integrating the majority of required instrumentation and data conversion circuitry into a single integrated component. One company pioneering medical AFEs is Texas Instruments (2012). For example, the ADS1298R is an ECG front-end that features built-in circuitry for right-leg-driver, Wilson terminal output, respiration impedance measurement, and an internal oscillator, voltage reference and programmable gain controllers. It has eight independent ΣΔ analog input channels, each with 24-bit resolution at a simultaneous sampling rate of 32 kSa/s. All of this in an 8 mm by 8 mm package footprint. The ADS1298R communicates to a master device over an SPI bus and only requires twelve external capacitors to operate.

Combining various discrete components into a single integrated-chip also yields the benefit of a higher overall accuracy in the bioinstrumentation equipment. Individual components within the integrated circuit can be manufactured to a higher specification

using such methods as laser trimming of resistors and capacitors. The ADS1299 by Texas Instruments, for example, features 24-bit, 8-channel ΣΔ with simultaneous sampling and a reduction of 77 % in input-referred-noise to 1 μV_{pp} compared to existing AFEs. These features make this chip ideal for EEG recording where high accuracy is required.

The next evolution is a complete system-on-chip (SoC) whereby the analog front end is combined with a computer processor into a single integrated circuit. Examples in the literature include a SoC for 3-lead ECG (Galjan *et al.* 2008) and for 8-channel EEG with built-in seizure classification processor (Yoo *et al.* 2012).

2.2.5.2 Capacitive electrodes

In recent years, work has been carried out on developing various systems for the measurement of biopotentials through a capacitive medium. This technique involves measuring the displacement current, rather than the real current, originating in the human body. Displacement current is an electric current associated with a time-varying electric field rather than due to moving charges. The advantage for biopotential measurement is a non-contact, non-invasive measurement with no skin preparation. Since this method eliminates the need for direct electrical contact with the body, this reduces interference arising due to sources like motion artefacts and impedance matching issues.

Due to the advantages of biopotential measurement through fabric for health monitoring, capacitive electrodes have been implemented for contactless ECG recording in a car seat (Chamadiya *et al.* 2009), car seatbelt (Maruyama *et al.* 2007), a bed sheet (Kin-fai and Yuan-ting 2008), a toilet seat (Baek *et al.* 2008), a chair (Ko Keun *et al.* 2005), and for detecting the ECG of neonates and infants (Kato *et al.* 2006, Furusawa *et*

al. 2003). Although these systems signpost the future of biopotential recording, there are still technical challenges to overcome before these systems come into everyday use (*e.g.*, reducing the inherent susceptibility of these systems to electromagnetic interference). The following two sections describe two branches of capacitive coupling electrodes: MEMS-based electrodes and an electric potential sensor.

MEMS based electrometer

Hull (1932) and Gunn (1932) first highlighted the usefulness of a vibrating condenser acting as an electrostatic generator in the measurement of small DC voltages. This technique was later developed into a competent technique for measuring positive ions and became known as a vibrating reed electrometer. The principle of the vibrating reed electrometer is that amplification is more easily accomplished with AC rather than DC. The input DC potential, arising from the passage of the ion current through a large resistor is converted to AC by applying it through a series resistor to a capacitor whose capacitance is periodically varied with amplitude ΔC. The result is an AC voltage, of magnitude $\Delta V = V(\Delta C/C)$, which is proportional to the input DC voltage. The AC signals can then be amplified using a conventional AC amplifier and demodulated back to DC (Duckworth *et al.* 1986). The sensitivity of the vibrating reed electrometer can be improved by increasing the resonant frequency of the vibrating reed and decreasing its input capacitance. This type of electrometer was used widely throughout the 1970's but was replaced by solid-state electrometers due to ease of operation and maintenance.

MEMS-based electrometers combine the principle of the vibrating reed electrometer with modern microelectromechanical systems, resulting in electro-static detection that can be implemented on a micrometre scale with greater control over sensitivity and noise levels. In MEMS-based electrometers, a capacitor plate, made of silicon, is forced to oscillate sinusoidally, either by electrostatic or electromechanical

means, as illustrated in Figure 2.10. This capacitor plate, or shutter, oscillates in parallel to a static capacitor plate, both separated by a fixed distance. The result is that the shutter oscillation creates a modulating capacitance by varying the overlap between the fixed and oscillating capacitor plates. The amount of charge induced in the static capacitance plate is a function of the shutter displacement and the strength of the electric field. The shutter is biased at a constant reference potential (usually ground) and ideally has a resonant frequency which is higher than the flicker noise (or 1/f noise) corner frequency of the pre-amplifiers (*i.e.*, outside the range of the low-frequency noise introduced by the operational amplifier's electronic components).

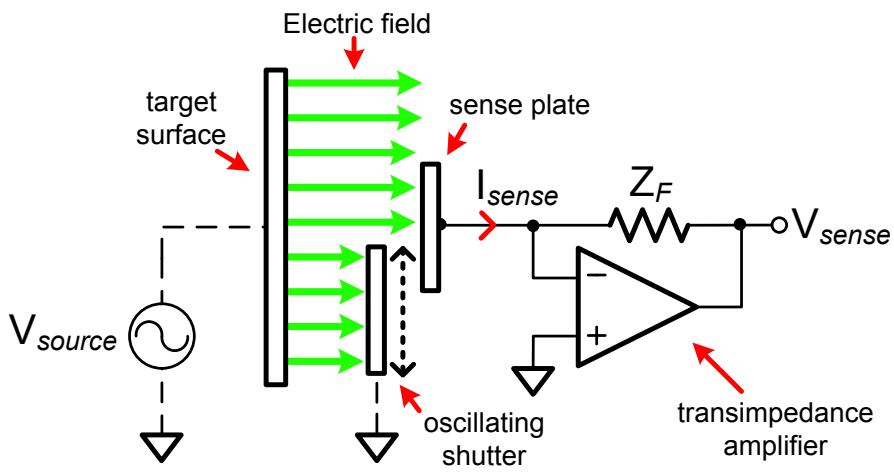

Figure 2.10: A schematic showing the sensing element of a MEMS-based electrometer. The amount of charge induced in the static sense plate is proportional to the oscillating shutter displacement and the strength of the electric field between the two static plates. A transimpedance amplifier can be used to convert the current across the plates into an output voltage. This diagram is based on (Denison *et al.* 2006b).

Song-Hee *et al.* (2004) describes a modification of this topology by incorporating two static plates into their design which results in the induced signal current on the oscillating plate being proportional to the difference between the voltages on the two static plates and thus allowing for differential input with common-mode rejection. Denison *et al.* (2006a, 2006b) and Lundberg *et al.* (2006) have developed various feedback techniques for Song-Hee's design, allowing for self-resonating control

of the shutter. More recently, Denison *et al.* have demonstrated the ability of their system to detect ECG (Denison *et al.* 2007b) and EEG (Denison *et al.* 2007a).

Zhuang *et al*. (2009) identify a problem with amplifying the AC voltage directly from the static capacitor plate as the input charges are quickly drained by the voltage preamplifier's bias current. Their solution is to couple the static capacitor plate to the preamplifier with a capacitor, which in principle creates a zero bias current but with some compromise in charge resolution. Additional problems with the MEMS-based electrometer include operating temperature range and bandwidth. However, in the latter, Denison *et al.* (2007a) have reported the ability to achieve a low-noise of 0.95 μV_{rms} in a 0.05 Hz to 100 Hz bandwidth.

Electric potential sensor

This technique has been developed by a team in the University of Sussex using a displacement current electrometer developed in-house (Prance *et al.* 2000). This device, which they term the electric potential sensor (EPS), works by utilising the ultra low input bias current properties of the INA116 instrumentation amplifier.

In an ideal operational amplifier, the input resistance is infinite. The input impedance of each field effect transistor (FET) at the front end of an ideal operational amplifier would therefore be purely capacitive. In reality, there is always a finite on-chip leakage current (*i.e.*, an undesirable current flow) that prevents this from being the case. In the absence of an input bias current, the gate of the FET will generally charge via the leakage current path, which leads to saturation of the amplifier in a short space of time. The early work of the group at the University of Sussex focused on optimising the input impedance and noise performance of an electrometer using an OPA111 op-amp, through a combination of guarding techniques and feedback circuits. The main

guarding technique, which they employed with the aim of stabilising the operating point of the op-amp at DC, involved a DC input bias current circuit comprising a 10 TΩ glass-encapsulated carbon-film type resistor connected between the input signal and ground. This type was chosen following a search for a commercially available resistor with very high resistance, small tolerance and stability between sampling. The effect was a reduction in noise level with the conclusion that the higher the resistance value in the input bias circuit, the higher the reduction.

Subsequently, the group developed their EPS based on the INA116, which has the added advantage of on-chip guarding facilities, as illustrated in Figure 2.11. Using these facilities, the group are able to operate their probe as an unconditionally stable charge amplifier for long periods without the provision of an input bias current circuit. With the removal of the input bias current circuit, their EPS system is now a charge amplifier (coulomb meter) rather than a voltmeter, as was the case in their previous design iterations.

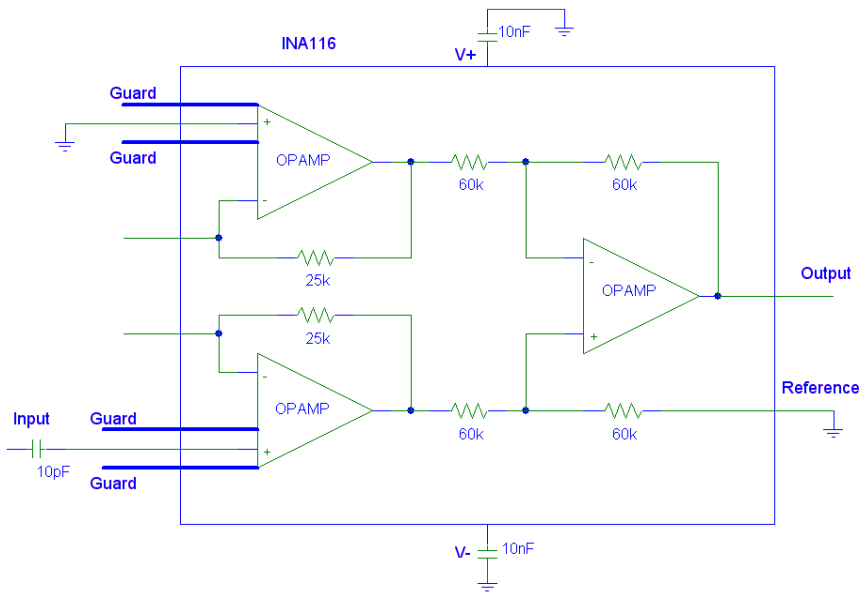

Figure 2.11: A schematic of the INA116 used in the electric potential sensor. The INA116 is configured as a charge amplifier with the guard connections extending out from the integrated circuit and surrounding the inverting and non-inverting input connections. The image is taken from (Prance *et al.* 2000).

Initially, the EPS device was developed to be used in close proximity with the skin. However, experiments have shown that the device is capable of recording recognisable ECG and breathing activity with an air gap of 40 cm between the sensor and the body (Prance *et al.* 2008). The EPS sensor has been applied to EEG monitoring (Harland *et al.* 2002b), basic ECG monitoring in a lab environment (Harland *et al.* 2002a) and on a portable wrist-mounted device (Harland *et al.* 2003). Harland *et al.* (2005) have also been able to reconstruct a 7-lead ECG using an array of electrodes configured in a small Einthoven triangle with diameter 15 cm.

A key advantage of the EPS is that it allows the biopotential measurement to be taken at one point on the body, eliminating the need for interconnected electrodes positioned at multiple points around the body.

2.3 Biomechanical signal measurement

In the previous section, one family of biosignals, biopotentials, was discussed. The other group of biosignals that are of primary interest to this research are biomechanical signals. The biomechanical signals of most immediate significance are those from gross or subtle body movement. The origin of these signals (*i.e.*, muscle tissue) was described previously in Section 2.1.4. This section initially describes one particular subtle body movement signal, the mechanomyogram (MMG), and then describes the sensors that can be used to measure body movement signals.

2.3.1 The mechanomyogram

The MMG is a signal that records the mechanical vibrations emanating from working muscles. The vibration of muscle at the onset of, and during, contraction can be

measured using sensors such as accelerometers or microphones placed on the surface of the skin over an active muscle. The useful bandwidth of MMG lies between approximately 3 Hz and 100 Hz. The MMG signal consists of three components (Smith *et al.* 1998);

1. Gross lateral movement at the initiation of a contraction generated by a non-simultaneous activation of muscle tissue (*i.e.*, motor unit recruitment).

2. Smaller subsequent lateral oscillations of the muscle fibres at the resonance frequency of the muscle.

3. Dimensional changes of the active fibres.

As a biomechanical signal, the MMG has several advantages over the corresponding electrical signal, the electromyogram (EMG) (see Section 2.2.1). One advantage is that there is no need for electrodes to be placed on the skin to record muscle activity, thus avoiding most of the practical problems associated with biopotential recording. Another advantage is that since the MMG has a higher signal-to-noise ratio than surface EMG, the MMG can be used to monitor muscles that are deeper in the human body, without the need for invasive measurement techniques. Furthermore, MMG can be used to detect muscle activation in the presence of very substantial electrical interference, such as would be the case during functional electrical stimulation of a muscle. A disadvantage of MMG is that the skin layers act as a low-pass filter on the original mechanical vibrations originating in the muscle. A second disadvantage is that MMG does not allows observation of, for example, neuronal firing, which is possible with EMG.

2.3.2 Biomechanical MEMS sensors

Biomechanical sensors measure mechanical movements and properties of an organism. Advances in sensor technology have created exciting opportunities in the area of human-machine interfaces (Trankler and Kanoun 2001). In particular, accelerometers, gyroscopes and magnetometers, created using microelectromechanical system (MEMS) technology, have decreased in size and cost to the extent that they are now routinely incorporated into portable consumer devices, including smartphones, game controllers, and tablet computers. Such sensors have numerous applications in biomedical engineering including measurement of a user's daily activity (*e.g.*, pedometer), gait analysis, and the detection of subtle body movement such as MMG (Nolan and dePaor 2004) and/or gross deformation of body parts (*e.g.*, a respiratory belt).

MEMS technology provides the ability to create integrated devices consisting of tiny components of between 1 µm and 100 µm (Beeby *et al.* 2004: 32). These devices typically include electronic components (*e.g.*, a central processing unit (CPU) and sensing circuitry) and a mechanical sensing or actuator element. The benefit of MEMS technology is that a significant reduction in the cost, power consumption and size of the devices can be achieved. Everyday MEMS sensor examples include accelerometers and gyroscopes, while an example of MEMS actuation is Digital Light Processing™ (DLP), which is used in some video projectors. DLP projectors have a microscopic adjustable mirror for every pixel displayed.

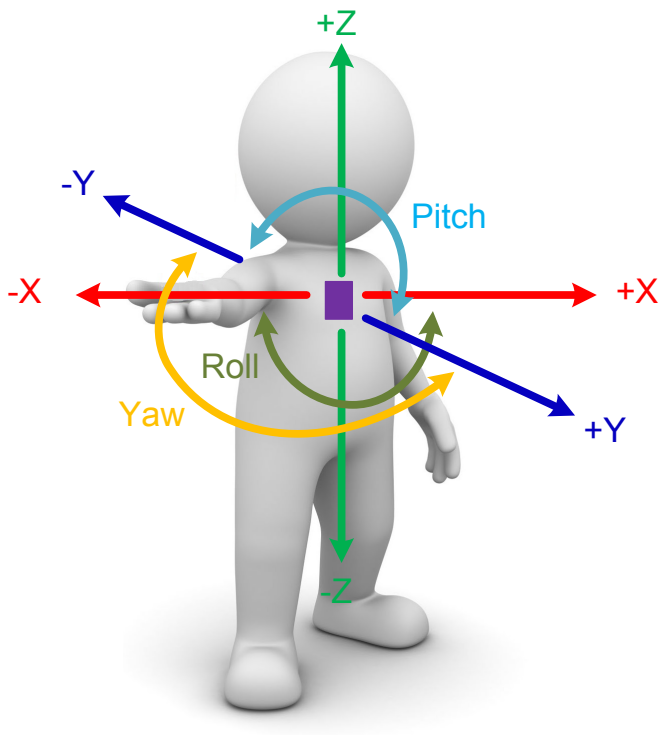

Figure 2.12: An illustration of the 3-D orientation and location motion tracking (*i.e.*, pitch, roll and yaw (absolute heading)) that can be obtained by combining accelerometer, gyroscope and magnetometer measurements from a single device worn on the chest. The image is modified from (Ganesh 2011).

Single-chip solutions exist which combine two or more types of MEMS motion sensors into a solitary integrated circuit called an inertial measurement unit (IMU) (InvenSense 2012, Analog Devices 2012). For example, the low-cost MPU-9150, manufactured by InvenSense, combines an accelerometer, gyroscope and magnetometer into a 4 mm x 4 mm x 1 mm package. The MPU-9150 also includes a Digital Motion Processor™ that offloads any required motion processing from a microcontroller and into the sensor itself to provide a 3-D view of motion activity (*i.e.*, pitch, roll and yaw (absolute heading)). The following sections introduce three of the most common types of MEMS sensors and the technology behind them.

2.3.2.1 Accelerometer

Accelerometers are electromechanical systems which are used to measure acceleration. The acceleration can be static (*e.g.*, measuring tilt with respect to gravity) or it can be dynamic (*e.g.*, measuring inertial force). Accelerometers can measure along one, two or three Euclidean geometric axes. They can be sensitive to a varying amount of inertial acceleration, for example ± 1 g, ± 2 g, ± 6 g, *etc.*, depending on the manufacturer's specifications.

The accelerometer's sensing element can be constructed in many ways. One method utilities a piezoelectric sensor. The piezoelectric effect describes the propensity for some materials to generate an electric field when they are subjected to a mechanical force. Another relatively new but rare example is a thermal bubble accelerometer (Ke-Min *et al.* 2005). A bubble of air is heated and the temperature is measured across the bubble. When a force is applied, due to the laws of thermal convection, a proportional temperature difference can be measured across the bubble.

The common accelerometer found in everyday devices such as mobile phones, step counters, and games consoles consists of a spring and a seismic mass. When acceleration is applied, the mass deviates from its neutral position and the amount of deviation is measured. This is accomplished either by measuring a capacitive difference between the mass and a fixed point or by measuring a resistive change on a piezoelectric resistance caused by spring deformation. Accelerometers have been around since 1783 when George Atwood invented them (reviewed in (Esposito and Schettino 2012)) but it is only in recent years, with the advent of MEMS technology, that the technology has become very widespread.

2.3.2.2 Gyroscope

A gyroscope is a device for measuring or maintaining orientation. A simple gyroscope consists of disk mounted on a base such that its axis can turn freely in one or all directions. The disk can then move independently of any external forces that are influencing the base. Gyroscopes are used in the aviation industry to detect roll, pitch and yaw. The Nintendo Wii MotionPlus incorporates a gyroscope and, when combined with the Wii Remote's accelerometer, can measure absolute rotational motion movements. Like the accelerometer, MEMS technology has made it possible for the size and cost of gyroscopes to be decreased dramatically.

2.3.2.3 Magnetometer

Magnetometers can measure the strength and/or direction of a magnetic field. Numerous approaches can be utilised in magnetometers for sensing magnetic fields. A common example used in devices manufactured by Honeywell and NXP Semiconductors is to use the magnetoresistance property of a conductive material. A Corbino disc is a conducting annulus with conducting inner and outer rims. DC current applied across the two rims drives a radial current in the area between the rims. Due to the Lorentz force, in the presence of a magnetic field along the same axis as the disc, a circular component of current also flows in the annulus. The extra current increases the resistance between the inner and outer rims and this effect is known as magnetoresistance. Anisotropic magnetoresistance (AMR) based magnetometers can sense the angle to which a magnetic field is applied to the sensor and are especially useful when measuring the Earth's magnetic field (*i.e.*, electronic compass).

2.4 Communication and control

As discussed in Chapter 1, this research aims to improve the capacity for communication and control through the use of information-rich channels on the human body. This research aspires to create technology that is useful to people with or without disabilities. For people with physical disabilities, those channels of information flow from the human body which would normally be of primary importance may be diminished or no longer usable. Therefore, in order to design devices for use by people with physical disabilities, it is important to have some understanding of the causes of communication impairment. This section will consider one common cause, neuromuscular disease, and two related concepts - assistive technology and universal design. This section also reviews some existing human-machine interfaces that utilise various biosignals as control inputs.

2.4.1 Impairment of voluntary movement due to disability

As described in Section 2.1, to cause movement of a muscle in the human body, an electrical signal propagates from the motor cortex in the brain along nerve fibres that connect to muscle fibres. A fault in any part of this transmission system can impair the function of the muscles and thus affect a person's mobility or ability to communicate. These faults in the nervous system are called neurological disorders and there are hundreds of such conditions (Hauser and Beal 2008). A particular group of neurological disorders called neuromuscular diseases cause communication and control impairment by affecting the functioning and control of muscles. Neuromuscular diseases, or disorders, include diseases affecting muscles, neuromuscular junctions, peripheral

nerves and their neuron bodies (Quan and Ringel 2010). Neuromuscular diseases are generally categorised as follows;

1. Upper motor neuron diseases
2. Lower motor neuron diseases
3. Diseases of the neuromuscular junction

Upper motor neuron diseases are characterised by a selective degeneration of the motor neurons of the spinal cord, brainstem or motor cortex. An example of an upper motor neuron disease is a stroke. A stroke, or cerebrovascular accident, occurs when the blood supply to part of the brain is interrupted, resulting in a loss in the supply of oxygen and nutrients to the nervous tissue and, ultimately, in the damage of nervous tissue. A stroke is caused by a blockage of an artery supplying blood to the brain (cerebral thrombosis) or a bleed into the brain from a burst blood vessel (cerebral haemorrhage). Strokes are the leading cause of acquired physical disability in Ireland. According to the Economic and Social Research Institute's HIPE report (2007), approximately 10,000 people are admitted to hospital each year in Ireland with stroke disease as the primary diagnosis. Other examples of upper motor neuron diseases are multiple sclerosis, tumours, spinal cord injury and Parkinson's disease.

Lower motor neuron diseases are characterised by a selective degeneration of the motor neurons of the peripheral nervous system where the body of the neuron is located in the spinal cord and the axon of the neuron connects to skeletal muscle through a peripheral nerve. Examples of lower motor neuron diseases are progressive muscular atrophy and progressive bulbar palsy. In Ireland, approximately one in 50,000 people, of which the majority are adults, will develop motor neuron disease in any year (Irish Motor Neurone Disease Association 2006).

Diseases of the neuromuscular junction are diseases that affect the synapse. As explained in Section 2.1.1, the synapse is the junction between the axon terminal of a neuron and the motor end plate of the muscle fibre. Examples of these types of diseases are myasthenia gravis and congenital disorders.

There are exceptions to these categories such as amyotrophic lateral sclerosis (ALS). ALS is one of the most common types of motor neuron disease and affects both the upper and lower motor neurons. Other medical conditions can also affect a person's voluntary movement without damage to the human nervous system such as osteoporosis and arthritis.

2.4.1.1 Assistive Technology

Assistive technology (AT) is technology designed to assist older people and people with physical disabilities in their everyday lives. The World Health Organisation (2012) defines disabilities as "*impairments, activity limitations, and participation restrictions*" and describes disability as a "*complex phenomenon, reflecting an interaction between features of a person's body and features of the society in which he or she lives*". The purpose of assistive technology is to restore independent living and mobility for people who would otherwise be limited in their daily activity by their physical condition.

The United Nations Convention on the Rights of Persons with Disabilities (2006), as ratified by 146 signatories worldwide, aims to promote, protect and ensure human rights for people with disabilities. The eight guiding principles of the Convention are:

1. Respect for inherent dignity, individual autonomy including the freedom to make one's own choices, and independence of persons

2. Non-discrimination

3. Full and effective participation and inclusion in society

4. Respect for difference and acceptance of persons with disabilities as part of human diversity and humanity

5. Equality of opportunity

6. Accessibility

7. Equality between men and women

8. Respect for the evolving capacities of children with disabilities and respect for the right of children with disabilities to preserve their identities

To facilitate access to machines for all people with physical disabilities, careful consideration should be given when designing any interface. Human-machine interfaces for people with physical disabilities can be either custom built for a specific user's needs and abilities or a general human-machine interface may be created for a common disability. Another technique, as promoted in articles 2 and 4 of the UN Convention on the Rights of Persons with Disabilities (2006), is to follow the principles of universal design (UD) which are outlined in the following section.

2.4.1.2 Universal design

The initiative of UD promotes the creation of products that are easily usable by the greatest range of people, regardless of their age or ability. The ambition of the

paradigm is that when a building, product or environment is in the process of planning, the designer should take into consideration the broad spectrum of people who might use the item or facility. The seven principles of UD (North Carolina State University 1997) are:

1. Equitable use
2. Flexibility in use
3. Simple and intuitive use
4. Perceptible information
5. Tolerance for error
6. Low physical effort
7. Size and space for approach and use

Consider as an example a wheelchair ramp at the entrance to a building. Often such a ramp is separate from pedestrian steps, creating two separate entrances to the building, one for able-bodied people and one for wheelchair users. To remove this segregation, a UD approach would be to remove the steps from the main entrance and replace it with a single ramp entering the building that all visitors can use. This approach not only benefits those with physical disabilities, but also many able-bodied people; for example, a parent with a buggy or a delivery person with a trolley.

2.4.2 Human-machine interfaces

A human-machine interface (HMI) is the medium through which a person communicates with a machine. The machine can be a computer or a mechanical system

or both. Common examples of HMIs include the computer keyboard, mouse and screen through which information is communicated from the user to the device and vice versa. An example in a mechanical system is the set of controls used when driving a car. These examples of human-machine interfaces are easily accessible by able-bodied people. However, in each of these cases, people with physical disabilities may require additional modes of access so that their ability to use the machine is not impaired.

2.4.2.1 Sensor-based HMI

With varying degrees of physical disability come different levels of access requirements. The more profound the physical impairment, the less options are available for HMIs. As the number of available channels of communication from a user's body decreases, the access time and the complexity of operation of a HMI device increases. The wheelchair, for example, has several means of operation. A paraplegic user can turn the wheels manually or operate a control joystick. A quadriplegic user might operate a wheelchair using switch inputs based on head movements or through voice recognition technology. In cases of profound physical impairment, a scanning mode selection system might be used, operated by a suck/blow switch or blink detection.

Another method is to use voluntarily controllable bioelectrical or biomechanical signals from the body as control inputs. Table 2.6 gives details of commonly used biosignals for sensor-based human-computer interaction. These biosignals can be used in isolation or in combination with other user inputs. It should be noted that these methods are not usable on a paralysed limb as the ability for voluntary control is lost. Other disadvantages of bioelectrical-signal based HMI are that they require the user to have knowledge of electrode placement and requires electrode/skin preparation before use.

Table 2.6: A table listing various biosignals, some human-computer interaction examples of each and their typical advantages and disadvantages.

Signal	Ref.	Function	Advantages	Disadvantages
EMG	(Goldstein *et al.* 2004, Heaton *et al.* 2004, Kubert *et al.* 2009)	Electromyogram (EMG) from neck muscles is used to control the activation of a hands-free electrolarynx	• Hands-free • Requires less strength from user compared with body-powered prosthesis	• Non-intuitive • Electrode needs placement on specific muscle nerves • Electrode/skin preparation
	(Boostani and Moradi 2003)	EMG from forearm is used to control an electrically-powered prosthetic hand		
MMG	(Shima and Tsuji 2009)	MMG from upper arm used to control an electrically-powered prosthetic forearm	• No need for electrode/skin preparation	• Need access to voluntarily controlled muscles • Tensing of muscles can have a tiring effect
EOG	(Karni *et al.* 1994)	Traditionally used for clinical purposes • Detection of rapid eye movement • Monitoring of optokinetic nystagmus	• Real-time • Low cost • Light independent • Non-invasive	• DC Drift and variable sensitivity • Sensitive to changes in head orientation. • EMG artefacts • Disturbed by blinks
	(Gips and Olivieri 1996, Kherlopian *et al.* 2006)	Human-computer interaction		
EEG	(Wolpaw *et al.* 2003)	Brain-computer interfaces	• Allows for some movement compared with MEG • Sensitive to tangential and radial dipoles (Longo 2007)	• Signal affected by skull, scalp *etc.* • Obtrusive • Sensitive to motion artefacts and other interference due to low signal level
	(Hammond 2005)	Neurofeedback		

MEG	(Mellinger *et al.* 2007)	Magnetoencephalography (MED), measurement of magnetic fields at the scalp used for controlling a cursor in a brain-computer interface	• Signal unaffected by skull, scalp *etc.*	• Very expensive • Needs significant magnetic shielding • Requires complete stillness • Not practical for everyday use • Sensitive only to tangential dipoles
GSR	(Strauss *et al.* 2005)	Galvanic skin response (GSR) used in biofeedback • Detection of anxiety levels • Detection of excessive sweating	• Cheap • Simple circuit implementation	• Susceptible to motion artefacts
	(Westeyn *et al.* 2006)	Measured in combination with an accelerometer to distinguish valid GSR signals from motion artefacts in children with autism		

2.4.2.2 Existing multimodal HMI devices

There are a number of novel examples of multimodal HMIs in commercially available products and in the literature. Several interesting and far-reaching examples are described below.

Shimmer

A commercially available device called *Shimmer* combines real-time physiological and kinematic measurement on a wearable device (Shimmer Research 2006). The current version of *Shimmer* has an on-board microcontroller, accelerometer, MicroSD card, Bluetooth and 802.15.4 radio communication. The design of *Shimmer*

allows for an external module to be connected to it such as an ECG, EMG, GSR or gyroscope module. This configuration limits measurement to a single biopotential with the need to reconfigure the hardware each time a different measurement set-up is required. *Shimmer* also uses the traditional three-electrode model of biopotential measurement.

Delsys - Trigno

The Trigno by Delsys is a commercially available product that combines differential EMG measurement and tri-axial accelerometer measurement into a single wireless device (Delsys 2012). The matchbox sized sensor (37 mm x 26 mm x 15 mm) has four electrodes (three measurement and one reference) situated on its base - at the point of contact with the body. A network of up to 16 individual Trigno sensors can be attached to the body wherein each device wirelessly communicates its sensor data back to a shared base station that is connected to a base computer or data acquisition device. The Trigno system features 16-bit ADC resolution and 2 kSa/s sampling rate for up to a total of 64-channels (16 EMG and 48 accelerometer channels) of biosignal data. Disadvantages to the system are that: the measurements from each Trigno sensor are slightly out of synchronisation (by less than 500 μs); the need for an intermediary base station increases overall device size; it uses the traditional electrode topology – increasing the size of each sensor; and that it is only configured to measure a single biopotential signal (*i.e.*, EMG).

Emotiv - EPOC

The *EPOC* by *Emotiv* (2012) is a commercially available brain-computer interface. It is a battery-powered wireless headset with sixteen electrodes placed in fixed positions across the surface of the cranium. The EPOC communicates wirelessly to a base computer via a proprietary communication protocol. When initially activated, the

software must undergo a training period during which the user is presented with an object on-screen and is requested to visualise performing a specific manipulation of the object, such as rotation or directional movement. The system captures, analyses and classifies a user's EEG activity, looking for signature patterns for each operation. According to the creators, the *Emotiv* can detect; twelve kinds of conscious movement thoughts; emotions; facial expressions; and head rotation (via a gyroscope). The initial target audience for the *EPOC Emotiv* is the gaming industry. However, several interesting applications have been demonstrated in assistive technology using the device including; phantom limb pain relief (Eleftheriadis *et al.* 2011); smartphone interfaces (Stopczynski *et al.* 2011, Petersen *et al.* 2011); and restoration of hand control following stroke (Fok *et al.* 2011).

NeuroSky - MindWave

The *MindWave* by *NeuroSky* (2012) is a simple headset with two electrodes, one for sensing placed on the forehead and a second for reference placed on the earlobe. The *MindWave* is wireless, battery powered and according to its creators produces research grade EEG. Although of basic construction, the *MindWave's* creators claim a powerful feature set including detecting the level of a user's attention and meditation while also being able to detect physical eye blinks. The *MindWave* has found many applications in brain-computer interfaces and medical diagnostics. A trivial brain-computer interface example is monitoring a subject's attention and/or meditation level (Crowley *et al.* 2010). A more profound example is its use in assessing cognitive load with potential applications such as the diagnosis and treatment of attention deficit and hyperactivity disorder in children or Alzheimer's disease in adults (Haapalainen *et al.* 2010).

NeuralWISP

A device called the *NeuralWISP*, created by Yeager *et al* (2009), is a wirelessly powered neural interface. This tiny (1.5 cm x 2.2 cm) device wirelessly harvests power from commercially available Radio-Frequency Identification (RFID) readers and they claim has an operating range of 1 m. Their circuit is designed to measure neural activity from a single electrode and to detect spikes that occur as tasks are performed by the user or as stimuli are presented to the user. Using a stimulated neural signal, they have demonstrated the ability of their device to record a certain quantity of neural data after a spike has been detected. The disadvantage to using RFID is that since the technology is typically designed to read many RFID tags only once, data throughput is limited when trying to read a single tag continuously. The maximum theoretical data throughput achieved by the *NeualWISP* system is approximately 100 kb/s.

Additional wearable devices

Gargiulo *et al.* (2008a, 2008b) have developed a Bluetooth-based biosignal monitoring system that is capable of measuring body movement, skin temperature and up to four biopotentials. Their design uses dry electrodes consisting of a conductive rubber connected to instrumentation circuitry via a double-shielded coaxial wire. A disadvantage of their system is that, due to the power demands of continuous transmission of data via Bluetooth over a period of time, a large power supply is required. In their case, a mobile phone battery was chosen which increased the space requirements greatly. Their design uses one electrode for measurement and another as a reference.

Mohseni at al. (2005) produced a wireless multichannel biopotential recording device consisting of an integrated circuit which was designed in-house to measure EEG

and transmit the recorded data over an FM link. Their final circuit design measured 1.7 cm x 1.2 cm x 0.16 cm and weighed 1.1 g with two miniature batteries attached.

2.5 Summary

This chapter has laid the foundation for this research by reviewing a large body of literature covering a wide range of relevant subject matter. This chapter commenced by describing, in detail, the physiological properties of various biosignals in the human body. As discussed, many of these bioelectrical and biomechanical signals (whether under conscious or unconscious control) are good candidates for use as high-bandwidth channels of communication in human-machine interfaces. With particular regard to this research, it is also necessary to understand the established technology in the field of biosignal measurement as well as some state-of-the-art measurement systems; both of which were reviewed in this chapter. This chapter concluded by exploring the relevance of various biosignals in real-world communication and control applications with an emphasis on usability by people with a broad range of abilities. A number of existing biosignal-based HMIs and assistive technology solutions were also reviewed.

The information presented in this chapter is a key knowledge prerequisite for the design of the multimodal wearable sensor discussed in the next chapter. This novel sensor design aspires to address some of the shortcomings of the existing technology described in this chapter.

Chapter 3 Design and Implementation of the Wireless Endogenous Biosignal Sensor

As described in the previous chapter, biopotential recording systems conventionally utilise multiple electrodes (either passive or active) to record a time-varying electrical potential from the body. Electrodes are usually connected in a bipolar or unipolar lead configuration. A potential difference is measured either between two electrodes (bipolar) or between one electrode and a reference (unipolar), possibly a low-impedance connection between the subject and the measurement equipment. Disadvantages of the conventional biopotential recording topology include the need for long wires to connect both signal and reference electrodes to instrumentation circuitry; the inevitability of electromagnetic interference being induced in these wires; and the inherently obtrusive nature of the measurement equipment.

The main focus of this chapter is the design and implementation of a new device, the *Wireless Endogenous Biosignal Sensor* (*WEBS*), which represents a topological evolution in bioinstrumentation, eliminating the need for analog current carrying electrode wires by digitising biopotentials as close as possible to the point of measurement in an electrode. Several electrodes can then be connected together, via a shared digital bus, to form a body sensor network with several significant advantages over conventional biopotential recording systems. The *WEBS* system delivers a significant reduction in wiring which facilitates less conspicuous biopotential recording.

By eliminating the analog current carrying wires altogether, a source of signal interference is removed from the system. This topology represents an evolutionary step in bioelectrical signal measurement. The following sections describe: the *WEBS* concept, benefits and challenges; a detailed description of the design of the device; the PC-based user interface; and the method of use of the system. Key aspects of this work on the *WEBS* system are described in (Nolan *et al.* 2012).

3.1 Concept, benefits and challenges

The *WEBS* system is a dynamic biosignal (bioelectrical and biomechanical) sensing platform that facilitates multimodal human-to-machine communication with applications in assistive technology and clinical measurement. The *WEBS* system comprises multiple layers of functionality and usability. At its core, as illustrated in Figure 3.1, the *WEBS* utilises a novel method of bioelectrical signal measurement. In an effort to reduce the number of components whilst also shifting the digitisation electronics as close to the point of measurement as possible, the electrode is directly connected to the input of a high-resolution analog-to-digital converter without any signal conditioning stage. When connected together on a digital data bus, a number of these sensors combine to form a body sensor network. This easily scalable network allows a large quantity of data to be recorded from the entire body surface area.

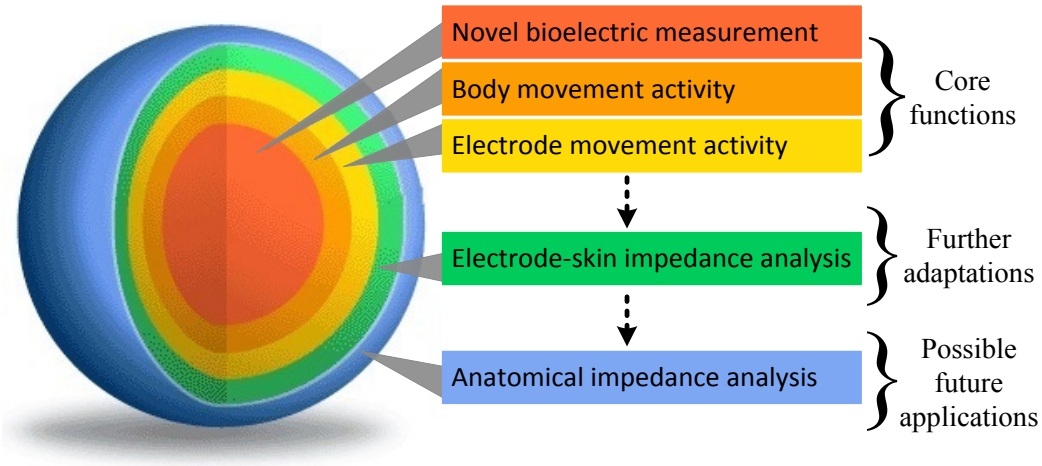

Figure 3.1: A diagram illustrating the multimodal nature of the Wireless Endogenous Biosignal Sensor. The core functions, as well two further adaptations, are highlighted.

As the electrode itself is transformed into a sensing node with a digital communication interface, additional sensors that share the same network infrastructure can also be incorporated into each electrode. By incorporating a tri-axial accelerometer into each *WEBS* node, gross and subtle biomechanical activity (second and third layers of the device) can be recorded. This configuration opens up new possibilities for human-to-machine communication and health monitoring. For example, if cardiac activity is under examination (as described in Section 2.2.1), the accelerometer allows the *WEBS* to monitor body movement and the activity level of a subject, which can then be considered alongside any variation in the observed electrocardiogram.

On a smaller scale, the accelerometer also provides information regarding movement of electrodes that are attached to the skin of a subject. This information can facilitate detection of motion artefacts in the recorded bioelectrical signal. By combining bioelectrical and biomechanical sensing into a tiny wearable device, the *WEBS* facilitates a more holistic approach to biosignal recording and analysis, in which more relevant contextual information is preserved.

The final two layers of the *WEBS* device, as shown in Figure 3.1, capitalise on the digitally controllable grid of electrodes by exploring the feasibility of integrated electrode-skin junction impedance analysis and, in the future, the possibility of anatomical impedance analysis. An electrical signal can be sent out from a selected source electrode through the body to a reference electrode. Comparing the original signal to the recorded output signal can yield information regarding the electrical properties of the transmission medium, *i.e.*, electrode-skin junction and the human body. It is envisaged that this measurement could be automatically performed between all of the electrodes on the *WEBS* system prior to biopotential recording so that an early indication of poor electrode-skin connection can be achieved. A novel approach to electrode and human-body impedance analysis, using existing system identification methods, is described later in this thesis (see Section 3.2.6 and Section 5.5).

The following is a list of the significant benefits of the *WEBS*:

1. The *WEBS* system reduces obtrusive bioinstrumentation circuitry and electrode wires by digitising biopotential signals very close to the point of measurement - thus reducing the susceptibility to electromagnetic interference that would degrade the biopotential being measured.

2. The *WEBS sys*tem facilitates measurement of the subtle and gross body movement, which can supplement biopotential signal measurement. For example, activity level can be estimated and valuable insights can be gained in the study of human motion.

3. The *WEBS* system provides the ability to detect subtle movement of individual electrodes on the skin surface. When combined with recorded biopotential

data, this can give an indication of possible instances of motion artefact that might occur in the recorded signal.

4. By combining both bioelectrical and biomechanical signal measurement onto an inconspicuous wearable device, the *WEBS* system facilitates new applications in human-to-machine communication and clinical measurement.

5. The *WEBS* system can harness a large quantity of biological data by attaching a very small number of sensors to the body, which make it practical in applications such as self-care and remote-care in connected health.

6. The *WEBS* system allows the choice of a reference electrode out of an array of electrodes to be software definable and altered at any time by the user.

7. The *WEBS* system provides an infrastructural backbone for future adaptations in dynamic electrode-skin impedance analysis.

The *WEBS* concept represents a considerable departure from conventional biopotential instrumentation designs and its realisation poses significant challenges including the following:

1. The integration of multiple biosignal sensors into a single tiny low-cost device.

2. The creation of an intelligent design that facilitates both current and future applications/adaptations.

3. The design of a novel bioinstrumentation topology combining multiple points of measurement on the human body.

4. The synchronisation of sampling between all of the electrodes.

5. The implementation of a communication protocol to facilitate a sufficiently high data rate for inter-electrode communication.

6. The choice of wireless transmission protocol for communication with a base computer/mobile phone.

7. The design of real-time computer interfaces to process and display the recorded data in a meaningful and useful manner.

8. The creation of an intuitive user interface for the system.

3.2 Hardware

Figure 3.2 illustrates the operational framework for the end-to-end system. The *WEBS* hardware consists of multiple identical slave electrode nodes connected (via wires) to a single master node, which communicates wirelessly to a base station. The desired number of nodes are connected via a common 4-wire digital bus made of flexible, light weight and durable wiring with standard JST-SH connector ends (JST Manufacturing Company Ltd. 1997). The connectors were chosen as they are robust, maintain a reliable connection and have a compact and low profile design. The master node relays information between the slave electrode nodes and a base computer interface via a wireless communication link (Bluetooth).

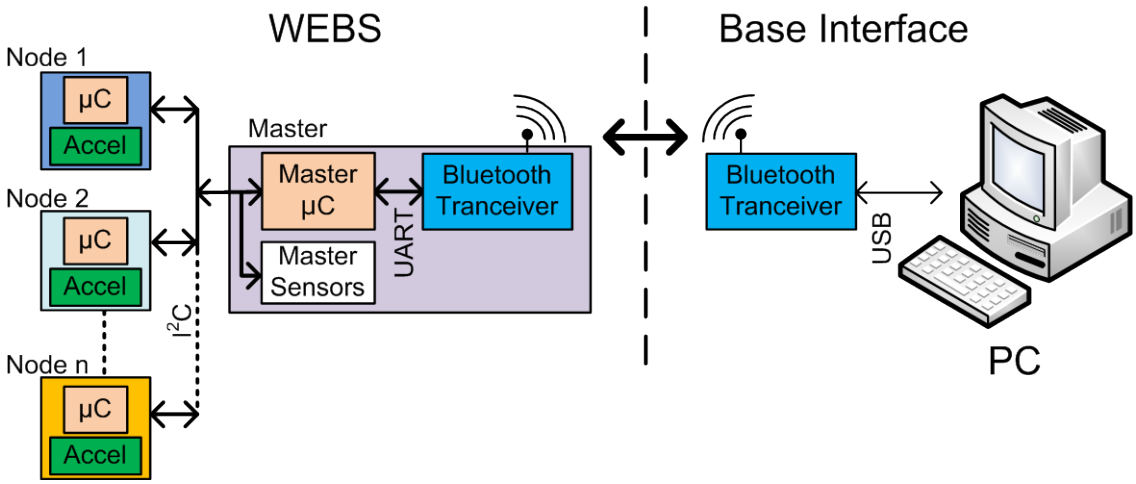

Figure 3.2: A block diagram of the end-to-end system. Note that for simplicity, single line connectors are shown for I^{2}C, UART and USB. In practice, each communication channel requires two digital wires two operate.

The following section expands on the technical capabilities of the *WEBS* master and slave devices and how they transform biosignals into useful diagnostic, communication and control information sources.

3.2.1 *WEBS* - slave and master

As illustrated in Figure 3.3, the *WEBS* slave electrode hardware is mounted on top of a standard snap-on clip that suits the commonly available button type disposable electrodes. Each *WEBS* slave contains a Texas Instruments (TI) MSP430F2013 microcontroller and an Analog Devices ADXL345 accelerometer. The MSP430F2013 has a built-in 16-bit, differential input, sigma-delta analog-to-digital converter (ΣΔ ADC). The metal of the snap-on clip is connected to the positive pin of the differential input via a short printed circuit board (PCB) track (3.5 mm x 0.3 mm). The negative input to the ADC is connected to the circuit ground. As all of the digital electrodes share a floating ground, all measurements are referred to this reference voltage.

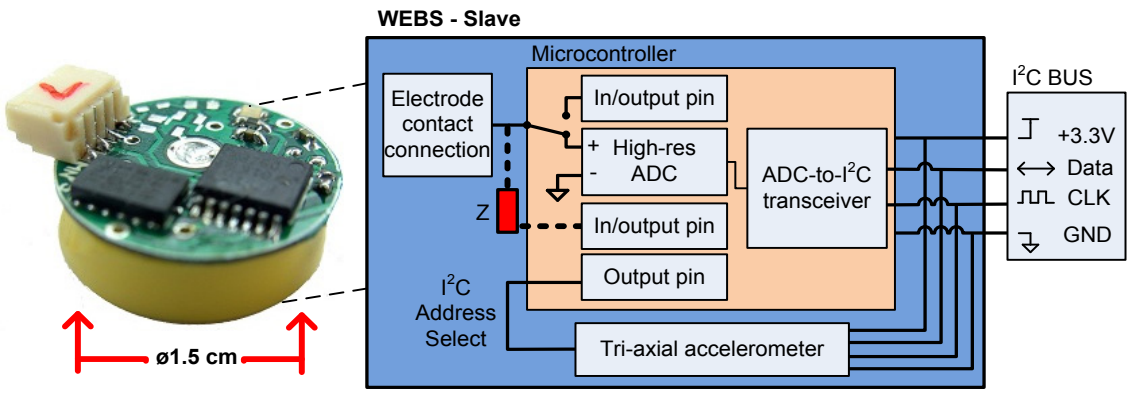

Figure 3.3: An image of a *WEBS* electrode and a block diagram showing the main features of the device. Each *WEBS* electrode acts as a pair of slaves (*i.e.*, the microcontroller and accelerometer) on a shared I²C digital bus. Note that the impedance Z (marked by the red box) forms part of signal source mode circuitry (see Section 3.2.6) and is not in included in all prototype devices.

A configurable register in the microcontroller allows for the electrode connection to be selected as either an analog input, as previously described, or a general purpose input/output pin (GPIO). Under control of the device's firmware, the pin can be set to be an output and driven low; this has the effect of setting the potential of the electrode in question to be the same as the floating ground. The location of the electrical reference point on the body is therefore digitally selectable.

The internal electrode configuration in Figure 3.3 also shows a secondary GPIO pin tied to the electrode via an impedance Z. This supplemental circuit, as indicated by a dashed line, forms part of a signal source mode that will be described in more detail in Section 3.2.6 and Section 5.5. During biopotential measurement, this secondary pin is set as an input (with high input impedance) and should have minimal effect on the measured signal.

The *WEBS* master, as shown in Figure 3.4, acts as a bridge between each of the slave sensors on the I²C bus and a base computer. Utilising a TI MSP430F2132 microcontroller, the master synchronises slave electrode sampling and manages communication on the I²C bus. All configuration settings and recorded data are relayed

between the *WEBS* system and a base computer via an on-board Bluetooth wireless transceiver module. When the configuration settings are transmitted from the base computer, the master sorts through the settings that belong to each device and then configures each device on the I^2C bus individually. The *WEBS* master also contains a combined tri-axial accelerometer and tri-axial gyroscope (the Invensense MPU-6000), and a tri-axial magnetometer (the Honeywell HMC5883L), which share the same I^2C bus. Together, these sensors provide 3-D orientation and location information about the *WEBS* master, from which the user's activity level can be estimated.

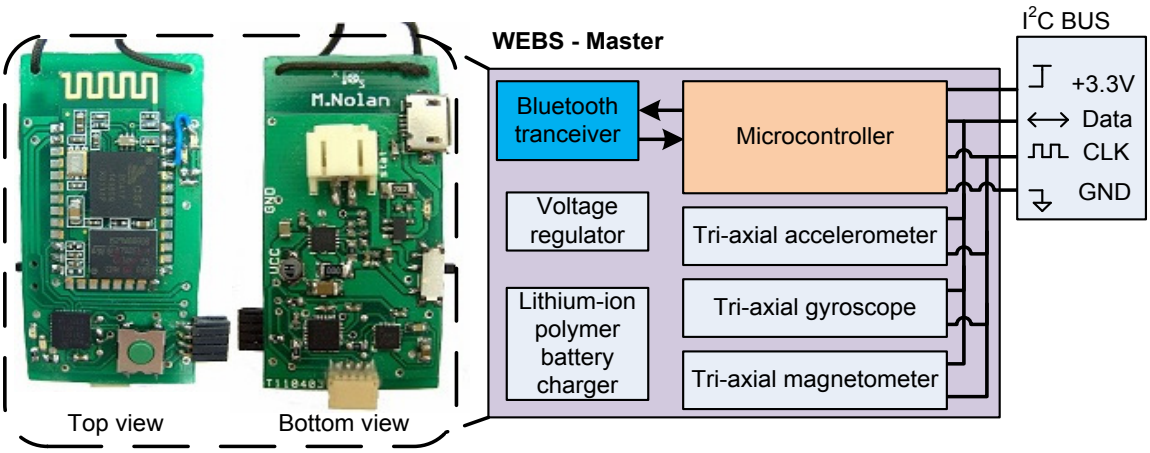

Figure 3.4: Images of the *WEBS* master device and block diagram showing the main features of the device. All devices within the master connected to the I^2C bus are powered from the on-board voltage regulator. The Bluetooth transceiver illustrated in top view of the *WEBS* master has since been replaced by the OBS421 (see Section 3.2.4).

During biopotential measurement, isolation from the mains power supply is essential due to safety and electrical interference concerns. Therefore, the entire *WEBS* system is powered via a single Lithium-ion polymer battery. Lithium-ion polymer battery technology provides batteries with higher energy density, low-weight, long-life and lower cost. The battery can be charged via an on-board micro USB connector and charging circuitry (MCP73831). A stable power supply is essential for ADC accuracy in

all *WEBS* sensors and this is achieved by means of a boost converter (TPS61200) that is also built into the *WEBS* master.

It was a conscious design decision for both the master and slave *WEBS* devices to keep their dimensions as small as possible. Consequently, both devices utilise dual-layer PCB. In order to reduce size and weight, the slave uses 0.4 mm thickness board (as opposed to the standard 1.6 mm). The slave PCB is only 1.5 cm in diameter and, when fully assembled, weighs less than 0.45 g with a volume of no more than 0.55 cm^3. This design reduces the likelihood of the weight and physical size of the measurement equipment negatively affecting the biosignals under investigation while also ensuring that the system is as unobtrusive as possible. Where feasible, the majority of the passive components were chosen to be a 0.4 mm x 0.2 mm footprint size (metric code 0402). The schematic and PCB layout for both *WEBS* devices can be found in Appendix A.

3.2.2 Bioinstrumentation configuration

As stated by Webster (1984), "*the goal of a biopotential recording system is the faithful reproduction of the signals that are generated in nerve and muscle*". With this in mind, careful consideration was given to the electrical properties of the proposed topology. This section reviews key characteristics of the equivalent circuit model and ΣΔ ADC that are fundamental to understanding the *WEBS* measurement topology.

3.2.2.1 Equivalent circuit model

Figure 3.5 illustrates the equivalent circuit model for a three *WEBS* electrode ECG recording, based on models by (Fricke and Morse 1925, Neuman 2009b, Texas

Instruments 2004). This model covers the equivalent impedances for the electrode, Z_d, gel, R_s, skin (epidermis, Z_e, and sweat glands/ducts, Z_p), and dermis and subcutaneous layers, R_u (as described in Section 2.2.1). The DC offset, E_{he}, is caused by the half-cell potential at the electrode-electrolyte interface and E_{se} by variation in ionic concentration across the epidermis. Z_t models the equivalent impedance of the tissue within a body where the membrane capacitance C_m, intracellular resistance R_{ic} and the extracellular resistance R_{ec} are shown.

As described in Chapter 2, the impedance of greatest magnitude in the equivalent circuit model is located at the electrode-skin junction. This value is highly dependent on skin preparation and electrolytic gel absorption. The model in Figure 3.5 covers the main components in the system. However, additional factors, such as nuances relating to different tissue types or electrode printed circuit board dynamics, are not represented.

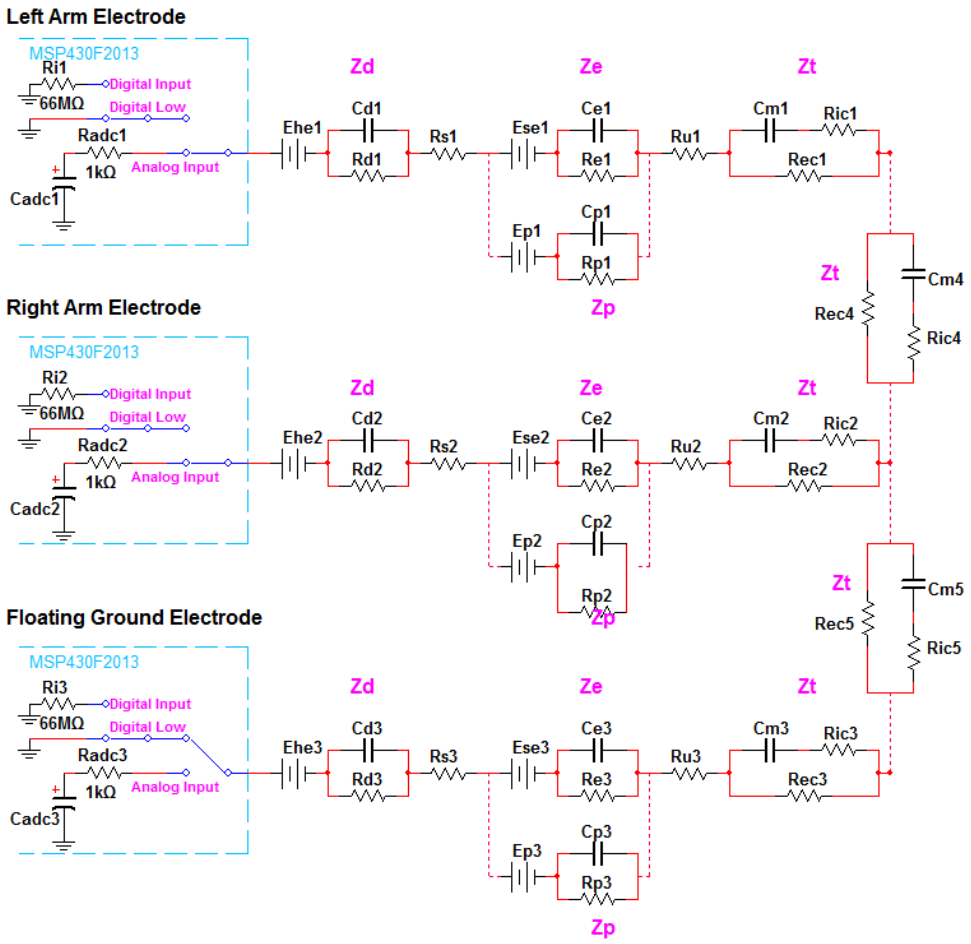

Figure 3.5: The equivalent circuit model for the instrumentation circuitry, Ag/AgCl electrode-skin junction and internal body tissue in the current topology. The sampling capacitance (C_{adc}) is dependent on the gain setting of the programmable-gain amplifier in the MSP430F2013 (see Section 3.2.2). Gains of 1, 2 & 4, 8, 16 & 32 correspond to sampling capacitance values of 1.25 pF, 2.5 pF, 5 pF and 10 pF respectively. This circuit is based on models by (Fricke and Morse 1925, Neuman 2009b, Texas Instruments 2004).

Most MSP430 microcontroller pins are multifunctional; each pin can be configured as a digital output, digital input or another selectable hardware function. The *WEBS* electrode connection pin utilises each of the following options at different times.

1. The pin can be configured as the input to a ΣΔ ADC for measuring bioelectrical phenomena. The values for the internal input impedance to the ΣΔ ADC, R_{adc} (set at 1 kΩ) and C_{adc} (set by the PGA), are provided in the manufacturer's specifications (Texas Instruments 2004).

2. The pin is used as a digital output, whereby the pin can be set to a digital low voltage - effectively turning that particular electrode into a reference electrode.

3. The pin is used as a digital input whereby it becomes a high-impedance input (66 MΩ at 3.3 V supply) (Texas Instruments 2005). In this state, negligible current flows into the pin, which effectively removes that particular electrode from the circuit topology.

3.2.2.2 Sigma-delta analog-to-digital converter (ΣΔ ADC)

The MSP430F2013 has a built-in high-resolution 16-bit ΣΔ ADC called the *SD16_A* (Texas Instruments 2004). At the core of the ΣΔ ADC is a 1-bit converter that functions like a comparator. To compensate for its low resolution, the ΣΔ ADC performs this comparison operation at a much higher frequency than the final output sampling frequency (f_S) of the ADC. The principle is that, by averaging out a stream of these 1-bit conversions, the magnitude of the input voltage can be calculated. The output rate of the 1-bit conversions is called the modulation frequency (f_M) and can be up to a maximum limit of 1.1 MHz in the case of the *SD16_A*. The rate at which the averaging calculation is performed is called the over-sampling rate (OSR). The OSR is essentially the ratio of the modulator frequency to the sampling frequency (*i.e.*, $OSR = f_M / f_S$). The higher the OSR, the more bits are included in the averaging calculation and so the magnitude of the input voltage can approximated with greater accuracy (*i.e.*, a higher ADC resolution).

In the *WEBS* electrode, the modulation frequency of the *SD16_A* is set to be directly proportional to the 16 MHz master microcontroller clock frequency and is therefore fixed at f_M = 1 MHz. The OSR setting of the *SD16_A* is user-selectable and ranges from 32 to 1024. The *SD16_A* has various features whose properties have a

significant bearing on biopotential recording. The following sections cover the SINC^3 comb filter, input voltage range, and the output data format.

SINC^3 comb filter

The 1-bit output stream of the ΣΔ modulator passes through an internal digital filter. The digital filter in the *SD16_A* is a SINC^3 comb filter and gets its name from its distinctive comb shaped frequency response. The SINC^3 comb filter decimates the input bit stream as a result of which aliasing from the modulation frequency is filtered out and a result is produced at the desired sampling frequency (based on the OSR). The manufacturer (Texas Instruments 2004) states that the filter transfer function is represented in the frequency domain by:

$$H(f) = \left[\frac{\operatorname{sinc}\left(OSR \,.\, \pi . \frac{f}{f_M} \right)}{\operatorname{sinc}\left(\pi . \frac{f}{f_M} \right)} \right]^3 = \left[\frac{1}{OSR} . \frac{\sin\left(OSR \,.\, \pi . \frac{f}{f_M} \right)}{\sin\left(\pi . \frac{f}{f_M} \right)} \right]^3 \tag{3.1}$$

where $\operatorname{sinc}(x) = \sin(x)/x$. Figure 3.6 illustrates the filter's frequency response based on the above equation for OSR values of 32 and 1024. With the ΣΔ ADC there is trade-off between the output resolution and the sampling frequency and this is represented in Figure 3.6. As can be seen, the higher the OSR value (and consequently ADC resolution), the narrower the range of input frequencies. The first filter notch for each plot is located at f_M / OSR.

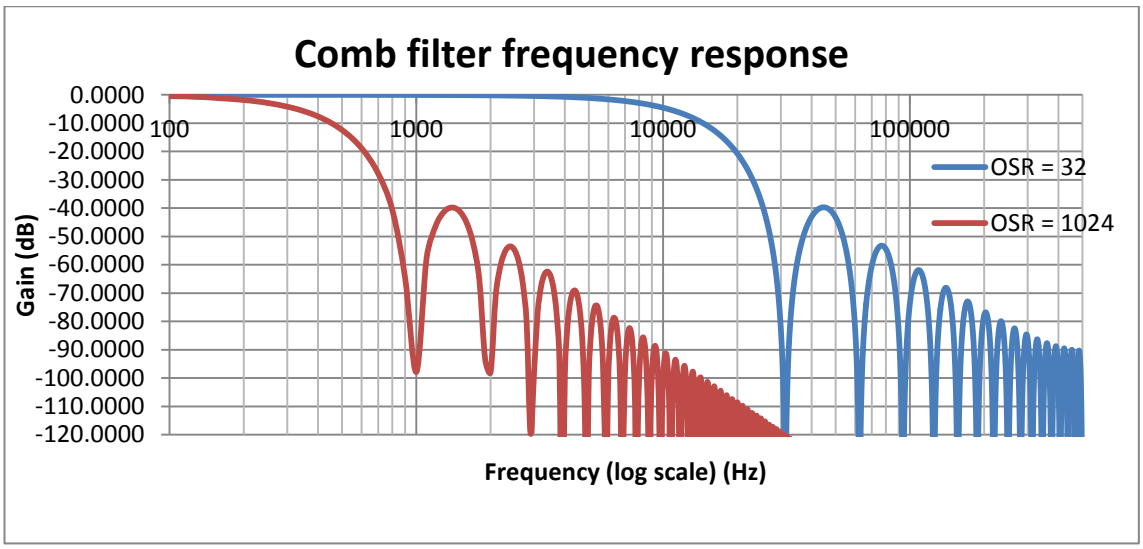

Figure 3.6: The frequency response of the SINC^3 comb filter in the SD16_A at OSR values of 32 and 1024. The graph is a magnified extract from a double-sided frequency response with a centre frequency of 500 kHz (where f_M = 1 MHz).

A disadvantage of the *SD16_A* ΣΔ ADC is that the SINC^3 comb filter requires a settling time before an accurate result is produced. The duration of the settling time depends on which of two *SD16_A* operating modes is in use, continuous conversion mode or single conversion mode. In continuous conversion mode, the first accurate sample is available on the fourth ADC conversion. Subsequent conversions are performed continuously and accurate samples are available after each conversion. In single conversion mode, only one accurate sample is requested which necessitates four ADC conversions per request.

The *WEBS* slaves are configured to perform an ADC conversion upon request from the master and not continuously. The primary reason for this choice is the ability to achieve synchronised sampling between all electrodes. The second, equally important reason is to maintain control over the initialisation of slave sampling so that it occurs during intervals when no I^{2}C bus activity is occurring – thus reducing the risk of induced electrical interference from the I^{2}C clock and data wires.

Figure 3.7 illustrates the settling time of the *SD16_A* to a 1 % step change in the full-scale input range. The *SD16_A* has a user configurable option to set number of ΣΔ ADC conversions performed before a result is produced and this ranges from one to four. This feature, along with the ability to set the OSR, provides the user with a high degree of sampling rate and output resolution flexibility.

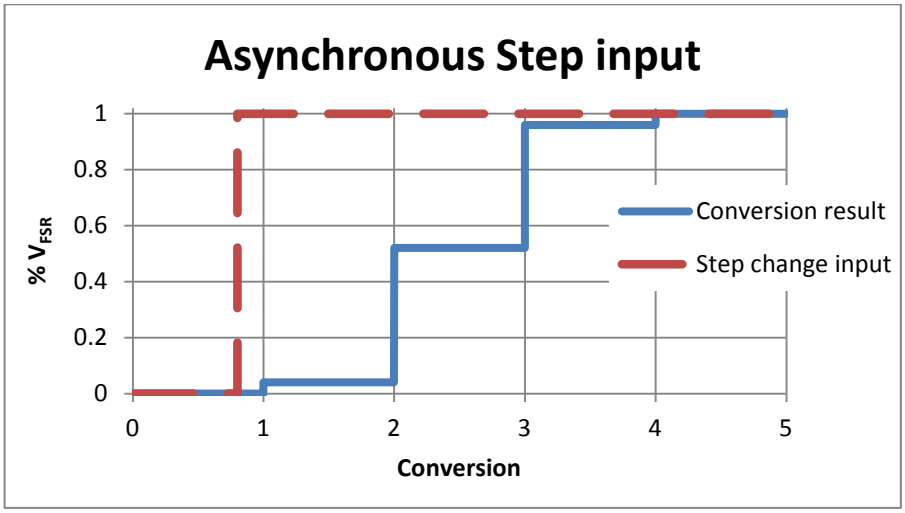

Figure 3.7: The digital filter step response and conversion points for a 1 % step change in full scale range voltage (V_{FSR}) that occurs asynchronously to the decimation rate of the $SINC^3$ comb filter. A valid result is produced after the fourth conversion (Texas Instruments 2004).

The minimum sampling time for the *WEBS* electrode can be calculated using the following equation (3.2), where there is a 40-cycle delay before the first conversion begins.

$$\text{Sampling time}_{\text{MIN}} = \frac{\text{No. of cycles per output result}}{\text{Modulator frequency}}$$
$$\text{Sampling time}_{\text{MIN}} = \frac{40 + (\text{No. of conversions} \times \text{OSR})}{1\ \text{MHz}} \tag{3.2}$$

In reality, although factory-calibrated, the accuracy of the MSP430's internal master clock frequency depends on the supply voltage and operating temperature and varies from one device to another. In the case of the *WEBS* slave's microcontroller, the MSP430F2013, this can typically vary by ± 1 % but can reach up to ± 6 % under

extreme conditions (Texas Instruments 2005). The *WEBS* system compensates for this by incorporating a 6 % tolerance into the sampling time. A list of the sampling times for each OSR and conversion number combination, similar to the lookup table pre-programmed into the *WEBS* slave and master, can be found in Table B.4 (Appendix B).

Input-voltage range

The *SD16_A* features a built-in programmable-gain amplifier (PGA), which provides a configurable gain feature that can be controlled by the *WEBS* user. The gain settings range between 1 and 32 and an increase in gain effectively reduces the input voltage range of the *SD16_A*. As biopotentials have a tiny signal amplitude, this feature is useful because it focuses the full resolution of the ADC over just the voltage range of interest. The *WEBS* electrode utilises the *SD16_A*'s built-in 1.2 V reference voltage (V_{REF}) and all ADC measurements are made relative to this. For the *WEBS* electrode's bipolar input, the full-scale input-voltage range (V_{FSR}) can be calculated by the following equation (Texas Instruments 2004):

$$\pm V_{FSR} = \pm \frac{V_{REF}/2}{PGA\ Gain} \tag{3.3}$$

Table 3.1 lists the input-voltage ranges for each of the PGA settings. The PGA value can be configured to suit the application. For example, in EOG measurement, where there can be a substantial DC offset, a lower value of gain might be required to expand the ADC input range to accommodate the biopotential signal. TI specify that the analog input range to the *SD16_A* should not exceed 80 % of V_{FSR} and this calculation is incorporated here. The last two right-hand columns indicate the *SD16_A* output values for each of the voltage range limits at two OSR settings.

Table 3.1: ***SD16_A*'s input-voltage range for various PGA settings. The voltage range values incorporate a manufacturer's input limit of 80 % of V_{FSR}. The range of the two's complement digital filter output are also shown (represented in hexadecimal) at example OSR values of 32 (15-bit ADC output) and 1024 (30-bit ADC output).**

PGA	1	2	4	8	16	32	Digital filter output	
							OSR = 32	OSR = 1024
$+V_{FSR}$	0.48	0.24	0.12	0.06	0.03	0.015	0x3FFF	0x1FFFFFFF
0 V	0	0	0	0	0	0	0x0000	0x00000000
$-V_{FSR}$	-0.48	-0.24	-0.12	-0.06	-0.03	-0.015	0x4000	0x20000000

A disadvantage to increasing the PGA is its effect on the sampling capacitance and consequently the minimum ADC sampling time. As described previously in this section, the input to the ΣΔ ADC can be modelled as a capacitance in series with a resistance (C_{adc} and R_{adc} in Figure 3.5). This sampling capacitance is dependent on the gain of the PGA as given by Table 3.2.

Table 3.2: **The sampling capacitance values for various programmable-gain amplifier gain settings (Texas Instruments 2004). Also listed are the typical gain values produced by the SD16_A PGA. The actual value can vary by up to ± 5 % (Texas Instruments 2005).**

PGA stated gain	Sampling capacitance, C_{ADC}	PGA actual gain (± 2 % to ± 5 %)
1	1.25 pF	1.00
2, 4	2.5 pF	1.96, 3.86
8	5 pF	7.62
16, 32	10 pF	15.04, 28.35

Other disadvantages of using the PGA are that the stated gain values are not always accurate and that it can introduce an offset voltage in the measurement (Texas Instruments 2005). Each *WEBS* slave electrode therefore requires a once-off internal calibration before each measurement session to counteract these undesirable aspects. It

is important to note that the PGA cannot be utilised as an input buffer stage to the ADC as it operates by means of switched capacitors rather than an operational amplifier and resistors (Davies 2008: 373).

Output data format

Within the context of the *WEBS*, the output data format from the *SD16_A* is dependent on two factors, the OSR and the least significant bits access flag (LSBACC) (Texas Instruments 2004). The *SD16_A* can normally be configured to generate either a bipolar offset binary, bipolar two's complement or unipolar output data format. However, the *WEBS* is pre-programmed to generate only a bipolar two's complement output. As explained previously in this section, the OSR setting ranges from 32 to 1024 and, the higher this number is, the greater the resolution of the ADC output. Table 3.3 highlights that, for the *WEBS* electrode bipolar ADC input, the number of possible digital-filter output bits ranges from 15-bits to 30-bits over an OSR range of 32 to 1024. As the *WEBS* I^2C data bus uses 8-bit data bytes, the number of bits to be transmitted is rounded up to the nearest 8-bit multiple.

Table 3.3: The number of digital filter output bits for each of the OSR settings on the bipolar ADC input. The actual number of bytes that needs to be transmitted by the *WEBS* are also shown for each OSR setting. The theoretical volts per least significant bit of ADC conversion is also listed at a gain setting of 1.

OSR	**32**	**64**	**128**	**256**	**512**	**1024**
Digital filter output bits	15	18	21	24	27	30
Number of output bytes	2	3	3	3	4	4
Theoretical Volt/LSB (At gain = 1)	36.6 µV	4.57 µV	572 nV	71.5 nV	8.94 nV	1.12 nV

The LSBACC is a configuration register flag of the *SD16_A* in the *WEBS* slave's microcontroller. The LSBACC flag allows access to the full range resolution of

the digital filter's output (depending the OSR setting as given by Table 3.3). When the LSBACC bit is low, the output register of the *SD16_A* contains the most significant 16-bits of the ADC conversion and, when high, the least significant 16-bits. This property of the *SD16_A* can be utilised by a *WEBS* user via an on-screen toggle switch in the *WEBS* user interface (Section 3.3) that decides between one of two *WEBS* sampling modes. In the first mode, the *WEBS* slave automatically toggles the LSBACC bit to read the full number of output bits that are produced from the *SD16_A* for each OSR setting. A look-up table, similar to Table 3.3, is pre-programmed into the *WEBS* master and slave devices so that each device knows the quantity of bytes to transmit. The *WEBS* master requests this quantity of bytes and transmits back to the base computer. In this mode, the full resolution of the digital-filter output is achievable. The principal advantage of this method is that, for lower OSR values, less information needs to be transmitted and therefore processing time is freed up and a faster sampling rate is achievable.

In the second mode, the LSBACC bit is permanently low. For each of the OSR settings the *WEBS* slave only produces the most significant 16-bits of the digital-filter output result. This approach results in a constant 16-bit output (*i.e.*, 2 transmitted bytes) independent of the OSR setting. The advantage of this method is that, by abandoning the least significant bits altogether from transmission, a higher sampling rate can be achieved, even at a higher accuracy measurement setting (*i.e.*, at an OSR of 1024).

3.2.3 Mechanical movement measurement

The *WEBS* system incorporates multiple mechanical movement sensors that provide a multitude of biomechanical measurement opportunities. As mentioned previously, the *WEBS* master features a 6-axis combined accelerometer and gyroscope -

the MPU-6000 (InvenSense 2011) - and a 3-axis magnetometer - the HMC5883L (Honeywell 2011). The accelerometer in the MPU-6000 features a selectable full scale range of ± 2 g, ± 4 g, ± 8 g or ± 16 g up to a maximum sampling rate of 1 kHz while its gyroscope has a full scale of ± 250°/s, ± 500°/s, ± 1000°/s, ± 2000°/s up to a maximum sampling rate of 8 kHz. The HMC5883L is capable of a 1° to 2° accuracy up to a maximum sampling rate of 160 Hz. When a user wears the *WEBS* master, a combination of the measurements from each of these sensors (angular rotation from the gyroscope, linear acceleration from the accelerometer and orientation relative to magnetic field intensity) can facilitate a view of the user's orientation and location in 3-D over time.

Each of the *WEBS* slaves contains a 3-axis accelerometer, the ADXL345 (Analog Devices 2013), which is capable of measuring linear acceleration over a full-scale range of ± 2 g, ± 4 g, ± 8 g or ± 16 g up to a maximum sampling rate of 3.2 kHz. Utilising the highest sensitivity setting (± 2 g), subtle movement signals such as the mechanomyogram can be measured. An array of *WEBS* electrodes could be placed across the full skin-surface area of a muscle under examination. Subtle movement of the electrode relative to the skin could also be detected which might indicate instances of motion artefact in a biopotential recording. At a lower sensitivity setting (± 8 g or ± 16 g), gross body movement information can be detected. When the *WEBS* slaves are spread across the body (*e.g.*, during 12-lead ECG measurement), each node can provide a unique vantage point for tracking body movement.

In the *WEBS* system, sensitivity settings for all sensors are user configurable through the *WEBS* user interface (see Section 3.3). Another feature that is user configurable is the sampling rate. In normal operation, the sampling rate is limited by the overall maximum sampling rate of the *WEBS* system. However, the *WEBS* user interface allows the user to disable specific axes of each sensor – thus freeing bandwidth

to focus on movement in a specific direction. An example of when this feature is useful is in the measurement of laryngeal vibrations (as measured on the skin-surface during speech), which are typically most intense along the axes normal to the skin (explored later in Section 5.1). A list of *WEBS* sampling rates for biomechanical measurement can be found in Table C.1 (Appendix C).

The MPU-6000 also contains a Digital Motion Processing (DMP^{TM}) engine that can perform complex calculations on the raw data from each sensor (the internal accelerometer and gyroscope and the external magnetometer) and return motion activity information in rotation matrix, quaternion or Euler angle format. This facility would offload processing power from the master and/or base computer. However, configuration of the DMP^{TM} requires up to 27 kB of microcontroller flash memory and the current master microcontroller, the MSP430F2132, is limited to 8 kB. Future iterations of the master device could capitalise on this feature, which would open the door to exciting new applications for the *WEBS*.

3.2.4 Inter-device communication

Several desirable features have been incorporated into the design of the *WEBS* digital electrode bus. Two design priorities were; to connect the *WEBS* and base computer wirelessly; and to minimise the number of wires shared between all electrodes. Another desired attribute was that the data bus and wireless transmission protocol would have sufficient bandwidth to be capable of fast data transmission rate, thus facilitating an adequate sampling rate from each sensor. For both of these reasons, the Inter-Integrated Circuit (I^2C) data bus topology (NXP Semiconductors 2012) combined with the Bluetooth wireless transmission protocol were chosen as the basis for the *WEBS* system.

3.2.4.1 *The Inter-Integrated Circuit bus (I^2C)*

Figure 3.8 illustrates a block diagram of the *WEBS* I^2C sensor network. Each electrode node is connected to a four-wire bus that comprises a shared clock, data and power supply connections (positive and ground). One microcontroller, a Texas Instruments (TI) MSP430F2132, acts as a master, coordinating communication between it and multiple slave TI MSP430F2013 microcontrollers.

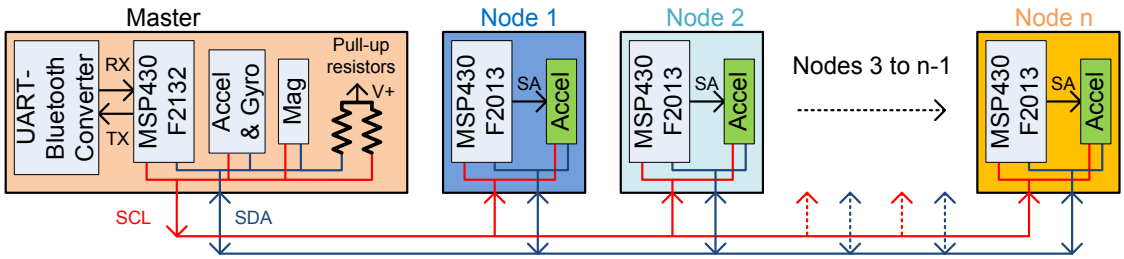

Figure 3.8: A block diagram of a master and *n WEBS* slave nodes connected to the I^2C bus. The I^2C data and clock lines are illustrated. Also illustrated within the master are the UART TX/RX lines which are connected to a UART-Bluetooth converter. The slave address select input line of the accelerometer is also shown.

As the current system uses 7-bit addressing, where the eighth bit is used as a read/write indicator, a theoretical maximum of 112 nodes (128 – 16 reserved addresses) could be connected onto the bus. In practice however, since the I^2C specification limits the bus capacitance to 400 pF (NXP Semiconductors 2012), the maximum number of devices is reduced to 25 nodes after taking into account the bus capacitance of: the master and slave microcontrollers; other sensors on the network; and the physical transmission medium. A table of the bus capacitances for individual *WEBS* I^2C components can be found in Table B.3 (Appendix B). Given the capacitance on the bus, the I^2C protocol necessitates the addition of pull-up resistors on the data and clock lines. The value for these pull-up resistors was carefully chosen at 1 kΩ with the aim of complementing the value of the bus capacitance and the possible variation between different recording topologies.

The I^2C data bus is set to run at a 400 kHz (I^2C Fast-mode) clock speed. However, the master microcontroller (MSP430F2132) has an output current limit of 1.5 mA before the output voltage level is overly compromised (*i.e.*, lower than supply voltage - 0.25 V). Due to increased loading, this current limit is only sufficient to maintain a 400 kHz clock speed for a certain bus wire length and number of nodes. Therefore, the actual clock frequency can vary depending different *WEBS* configurations. Table C.1 lists the maximum I^2C clock frequency for various *WEBS* wiring configurations (Appendix C).

The *WEBS* master has the ability to perform slave discovery whereby each possible address on the I^2C bus is polled and, if a response is received, the associated address is stored in a slave look-up table. Therefore, *WEBS* slave devices can be dynamically connected to the shared digital bus without the need for pre-programming the master or cycling the power. Slave detection occurs automatically at master power-up and upon request from the *WEBS* user interface (see Section 3.3).

The timing diagram in Figure 3.9 shows the transmission protocol used in the *WEBS* system. Note that in this example the master sensors are disabled and only a 2-byte ADC and single axis 2-byte accelerometer are enabled. At the start of each transmission, the master sends out a broadcast address. This signal synchronises the slaves so that all recording nodes sample their analog-to-digital converters simultaneously. Upon reception of this signal by each of the slaves, all activity on the I^2C bus goes silent for a set delay to allow for slave ΣΔ ADC sampling. The ΣΔ ADC resolution and mode settings (see Section 3.2.2) - configurable through the *WEBS* user interface (see Section 3.3) - determine the length of this delay (between 133.81 μs and 4.14 ms) and the number of resulting ADC bytes (between 1 and 4 bytes). The master then polls each of the nodes individually for their respective data. Due to a possible

propagation delay of the I^2C broadcast message, there may be a difference in the sampling initialisation time on each of the *WEBS* slaves, although this effect is assumed to be negligible.

The ADXL345 accelerometer in each of the slave nodes has a facility that allows its I^2C address to be one of two addresses, depending on whether an external slave address select pin (SA) is set high or low. Usually, this factor limits use of these accelerometers to a maximum of two per I^2C bus. A unique feature of the *WEBS* system that removes this limitation is that control of the SA pin is the responsibility of the microcontroller in the individual slave nodes (as illustrated previously in Figure 3.8). Taking the timing diagram in Figure 3.9 as an example, when Node 1's microcontroller is polled for data, it sets the SA pin of the Node 1's accelerometer low, *i.e.*, 'active' mode (accelerometer address = 0x53). The other nodes' microcontrollers recognise that they are not being addressed and set their corresponding SA pins high (accelerometer address = 0x1D). After Node 1's microcontroller has transmitted its data, the master then polls the 'active' accelerometer address for data. The process is repeated for each node during which the master addresses the corresponding 'active' accelerometer each time.

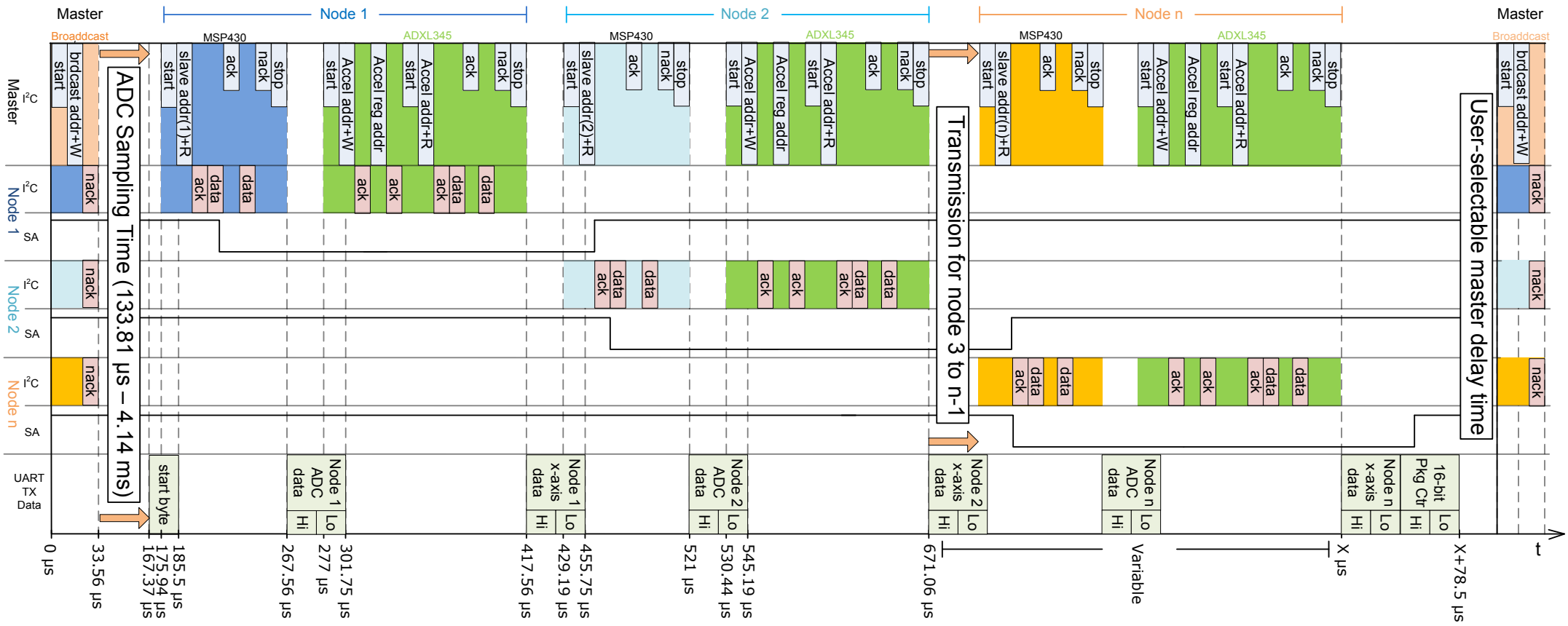

Figure 3.9: A timing diagram of data transmission on the *WEBS* system. In this example, the *WEBS* system is running at maximum sampling frequency for an *n* node system with 2 bytes of ADC data and 2 bytes of single-axis accelerometer data for each node. No communication activity occurs during analog-to-digital conversion time to reduce interference induced in the signal being measured. The activity on each accelerometer slave address select pin (SA) is also shown. I^2C clock rate = 380 kHz and UART rate = 500 kbps. (Note: background colours correspond to devices in Figure 3.8 and the time axis is not to scale)

3.2.4.2 Wireless communication

During the design of the *WEBS* master device, it was realised that, due to power requirements, the size of the device would be principally determined by the choice of wireless transmission protocol; and consequent battery requirement. There is a trade-off between battery consumption and data transmission rate, distance and reliability. Bluetooth was chosen as it is widely used, fast and reliable. Bluetooth typically has a high current demand and therefore requires a larger battery for extended operation. However, with the advent of newer generations of Bluetooth, integrated circuits and protocols have significantly improved on earlier designs. Bluetooth V4.0 introduced a Bluetooth low energy (BLE) profile which provides a lower power means of data transmission at a reasonably high data rate (approximately 200 kbps).

The *WEBS* master utilises a Bluetooth-to-serial transceiver module, the OBS421 manufactured by connectBlue (2012). The OBS421 appears on the base computer as a virtual COM port and acts as a seamless UART connection between the *WEBS* master and a user interface. The OBS421 runs the Bluetooth V2.1+EDR protocol which facilitates high-speed UART with a sustainable data throughput of up to 1.3 Mbps (maximum is 1.5 Mbps). The OBS421 has a stated 300 m range at an average transmission current consumption of 40 mA (at 3.3 V supply). A key benefit of the OBS421 is that it is firmware upgradeable to Bluetooth V4.0 with support for BLE. The OBS421 is also interchangeable with the OBS411 for lower power consumption (but also lower speed and range).

The UART rate for the *WEBS* master is set at 500 kbps. This is not a standard serial baud rate. However, as the *WEBS* master is operating from a 16 MHz clock frequency, this UART rate is an even divisor of the clock frequency, reducing possible

transmission errors. Furthermore, the defined rate is less than half of the stated maximum data throughput for the OBS421, which ensures that the system does not operate near the transceiver's limits while still leaving room for an increase in bit rate if required for future applications.

As the master receives the slave data samples from the I^2C bus, it simultaneously transfers this data to an internal Universal Asynchronous Receiver/Transmitter (UART) that is connected to a serial-to-Bluetooth converter. As shown in Figure 3.9, the data samples, separated into their high and low bytes, form the core of a UART data packet. A start byte is sent at the beginning of each packet to assist data parsing at the base computer. A 16-bit package counter is attached to the end of each packet to facilitate identification of missing data packets and ensure correct ordering of received packets.

3.2.5 Sampling frequency factors

The *WEBS* master utilises one of its integrated 16-bit hardware timers in order to maintain a constant sampling frequency. The timer clock is based on a divisor of the master clock frequency, and is set at 1 MHz. Each time the master initiates slave sampling, the timer counter is reset to zero. Throughout the duration of one complete packet of data (*i.e.*, during slave sampling, I^2C communication with the slaves and transmission of data back to the base computer), the timer counter continues to count up. If the timer has not yet counted up to a final count value (as specified by the user) before a complete packet of data has been processed, the master pauses until the count is equal and subsequently proceeds to the next data packet. If, at the end of the data packet, the timer is greater than or equal to the predefined count, the master instead proceeds directly onto processing the next data packet.

The sampling frequency of the *WEBS* can be defined through its user interface in which a list of achievable sampling rates populates a selectable drop-down box (see Section 3.3). Each sampling frequency listed in the user interface corresponds to a counter value that is sent to the master. In order to reduce the number of configuration bits sent to the master, a single 8-bit byte is sent which the master then bit shifts left by 5 to obtain the final count value. The sampling frequency is calculated by dividing the timer clock rate by the final count value. For example, to obtain a sampling rate of 128 Sa/s, the decimal number 244 must be sent from the *WEBS* user interface to the *WEBS* master. The *WEBS* master bit shifts this left by 5 to become the decimal number 7808 and this is stored as the final count value. At a rate of 1 MHz, this results in a theoretical sampling rate of 128.0738 Sa/s (*i.e.*, *1 MHz / 7808 = 128.0738 Sa/s*). A bit shift left of 5 on an 8-bit number facilitates 255 different sampling rates between 122.549 Sa/s and 31,250 Sa/s; although the latter is not feasible with the current *WEBS* design. Future iterations of the *WEBS* system could simply send a 16-bit counter value that would facilitate configurable sampling rates between 15.26 Sa/s and 1 MSa/s.

The method described above works sufficiently well to maintain a set sampling frequency. However, a number of factors in the *WEBS* system limit its maximum achievable sampling rate. The principal governing factors are listed below in order of decreasing impact.

1. **ADC sampling time.** The predominant limiting factor on the sampling rate of the *WEBS* digital electrode grid is a hardware property of the ΣΔ ADC. To make use of the full resolution of the ADC, a long sampling time is required (≤ 4.12 ms - equation (3.2)).

2. **Number of nodes.** Due to the polling nature of the I^2C data bus, each sensor takes it in turn to transmit its data to the master. Therefore, the greater the

number of nodes, the larger the overall data packet length and the longer the transmission time per sample (across all nodes).

3. **I^2C clock speed.** The current *WEBS* system has a hardware-limited clock speed of 400 kHz for I^2C. Future iterations of the *WEBS* could feature newer versions of the I^2C protocol, such as version 4.0, which would enable up to 5 MHz clock speed (NXP Semiconductors 2012).

4. **UART rate.** Although the OBS421 Bluetooth serial port module is capable of up to 1.3 Mbps data throughput, because of relatively low clock frequency of the master microcontroller, the UART speed in the current *WEBS* system is fixed at 500 kbps for increased stability. A master microcontroller with a faster clock frequency could utilise the full capabilities of the OBS421.

5. **Internal MSP430 ΣΔ ADC gain setting.** The settling time of the ΣΔ ADC's internal resistor-capacitor network (as illustrated previously in Figure 3.5) also places a limit on the sampling frequency. The capacitance value is determined by the ΣΔ ADC gain setting (see Table 3.2). As the *WEBS* slaves do not feature an input buffer stage, the effective impedance of the source must also be taken into account when calculating the settling time. The limit imposed by this aspect is considered less significant than those previously discussed. The equation for calculating the settling time is given by (Texas Instruments 2004).

Because the master needs to go through a sequence of steps involving multiple hardware interfaces in order to process a packet of data, a single aspect alone cannot determine the overall sampling rate. Even adding the time taken for each operation is

insufficient because, as previously illustrated in Figure 3.9, there can sometimes be an overlap between different operations.

A list of *WEBS* sampling rates for several *WEBS* wiring configurations and sampling settings can be found in Table C.1 (Appendix C). A summary of this table is listed below in Table 3.4. As shown, in order to be capable of measuring the full bandwidth of certain biopotential signals with the *WEBS* system (for example ECG and EEG, as listed previously in Table 2.4), it is necessary to choose a lower resolution setting. For example, the highest frequency of ECG can be up to 250 Hz (Table 2.4). In 3-lead ECG measurement with the *WEBS*, by setting the ΣΔ ADC resolution to be 24-bit (*i.e.*, at OSR = 256 with LSBACC), the sampling rate become 625 Sa/s (*i.e.*, satisfying the Nyquist-Shannon sampling theorem).

Table 3.4: A summary of Table C.1 in Appendix C listing the maximum sampling rate of the *WEBS* for various measurement configurations. Note that the third recording electrode listed for VEP is used to measure the VEP trigger state.

Signal	No. of recording electrodes	*WEBS* ΣΔ ADC and/or accelerometer	*WEBS* ΣΔ ADC Resolution	
			30-bit (OSR = 1024 with LSBACC)	15-bit (OSR = 32)
ECG (12-lead)	9	ADC	163.13 Sa/s	806.45 Sa/s
		ADC and XYZ	107.30 Sa/s	225.23 Sa/s
EOG	4	ADC	199.20 Sa/s	1545.74 Sa/s
		ADC and XYZ	157.23 Sa/s	505.05 Sa/s
ECG (3-lead)	3	ADC	207.04 Sa/s	1807.70 Sa/s
		ADC and XYZ	170.36 Sa/s	628.93 Sa/s
EEG (VEP)	3	ADC	207.04 Sa/s	1836.95 Sa/s

3.2.6 Signal-source mode

As shown previously in Figure 3.3 and Figure 3.5, the multifunctional microcontroller pin that is electrically connected to electrode connection in each *WEBS* slave (via a PCB track and button clip connector) can be set as either an ADC input, a digital input or a digital output. It has been stated previously that by setting this pin in a *WEBS* slave electrode to digital low output, this effectively turns that particular electrode into a reference electrode for the *WEBS* biopotential measurement system (Section 3.2.2.1). Another intriguing way in which this feature can be exploited is to output not just a constant digital value, but a digital sequence - namely a pseudo-random binary sequence (PRBS) - that can be utilised as a system identification test signal between pairs of *WEBS* electrodes on the human body.

A PRBS is a repeatable binary sequence of ones and zeros which appears random, but is deterministically generated (Horowitz and Hill 1989: 655). One advantage of using a PRBS signal as a system identification test signal is that its energy is distributed predictably over a wide frequency band and can be considered as a band-limited white noise signal (Davies 1970: 36-39). Therefore, performing PRBS system identification yields a large amount of information about a system from a relatively simple input signal. The application of PRBS excitation signals in system identification is well established (Davies 1970, Goodwin and Payne 1977, Eykhoff 1974: 386-394).

Although PRBS signals have been utilised to generate stimulus signals in the study of certain biopotentials (*e.g.*, visually evoked potentials (Srebro and Wright 1980), vestibulo-ocular relex (Furman *et al.* 1979)), references to the application of a PRBS signal to impedance analysis in a bioelectrical measurement context are scarce in the literature. Seong-Jun *et al.* (2007) briefly mention the use of PRBS system

identification to evaluate the use of the body as a medium for high-speed data transmission between wearable devices. However, they make no reference in the description of their design to the required safety aspects (discussed previously in Section 2.2.2.2). Their design seems to inject a DC current, which would not be acceptable over prolonged periods.

Here, a method is explored which capitalises on the *WEBS* as a body area network by transmitting a PRBS signal from one source electrode to another reference electrode through the body. Cross-correlating the input PRBS with the measured output voltage signal yields information about the impedance of the medium. As described in Section 2.2.2.2, this impedance is dominated by that which appears at the electrode-skin junction. Before a biopotential measurement (*e.g.*, ECG or EMG) is performed, the *WEBS* PRBS feature could be used to dynamically assess the quality of each electrode's connection to the human body. Such a feature would be of such tremendous practical benefit in real biopotential recording applications, that it is easy to imagine how it might become a standard feature of such systems in the future.

In this case, the test signal is a binary sequence. However, the *WEBS* measurement topology could also be adapted to other, more conventional, body-impedance measurement methods by the addition of a digital-to-analog converter (DAC) and associated circuitry within each *WEBS* slave. It is debatable whether such a feature would impart any significant benefit over the PRBS approach.

3.2.6.1 Circuitry

A number of circuit design aspects need to be considered when implementing PRBS system identification on the human body. Along with the safety concerns

associated with conventional impedance meters (Section 2.2.2.2), the following is a list of desirable circuit design requirements with specific regard to the *WEBS* system:

1. The ability to disable and electrically isolate any additional PRBS circuitry from the existing biopotential measurement circuitry such that its presence does not influence the normal measurement of biopotential activity.

2. The PRBS circuitry should utilise a minimal number of components so that it can be integrated into the existing *WEBS* slave device without increasing the current dimensions of the circuit board.

3. The voltage range of the PRBS signal needs to be within the limits of the *WEBS* ADC's input voltage range (within ± 0.48 V – see Table 3.1).

Figure 3.10 shows a circuit diagram of the *WEBS* with additional prototype PRBS circuitry. In this example, a pair of *WEBS* electrodes are separated across the body. The first stage of the PRBS circuit consists of a potential divider which steps down the digital output voltage from the microcontroller (0 V to 3.3 V) to within range of the *WEBS* ADC (in this case down to the range 0 V to 0.1 V). The second stage consists of a TI OPA334 operational amplifier (Texas Instruments 2003) configured as a unity gain buffer to isolate the source impedance (*i.e.*, the potential divider) from the loading impedance (*i.e.*, the human body and ADC). The benefit of the OPA334 is that it has an enable pin which, when disabled, places the output of the OPA334 in a high impedance state – ensuring that the impact of the PRBS circuitry during normal potential measurement mode is negligible. The third stage is a current limiting resistor, R_O, which limits the current flowing into the body (in this case at a maximum of 10 µA assuming the maximum signal voltage of 0.1 V). The final stage between the PRBS circuitry and the electrode terminal is a capacitor, C_{HP}. This capacitor has two functions.

Firstly, it acts as a DC blocker such that its output is a bipolar digital signal. Secondly, the combined impedance of R_O and C_{HP} along with the combined impedance of the electrode-skin junctions and the body form a potential divider - the output of which is a function of the fixed values of R_O and C_{HP} and the variable impedance between the PRBS source and reference electrodes. The frequency response of the system can be obtained by cross-correlating the voltage measured at the electrode terminal with the original stepped down PRBS signal.

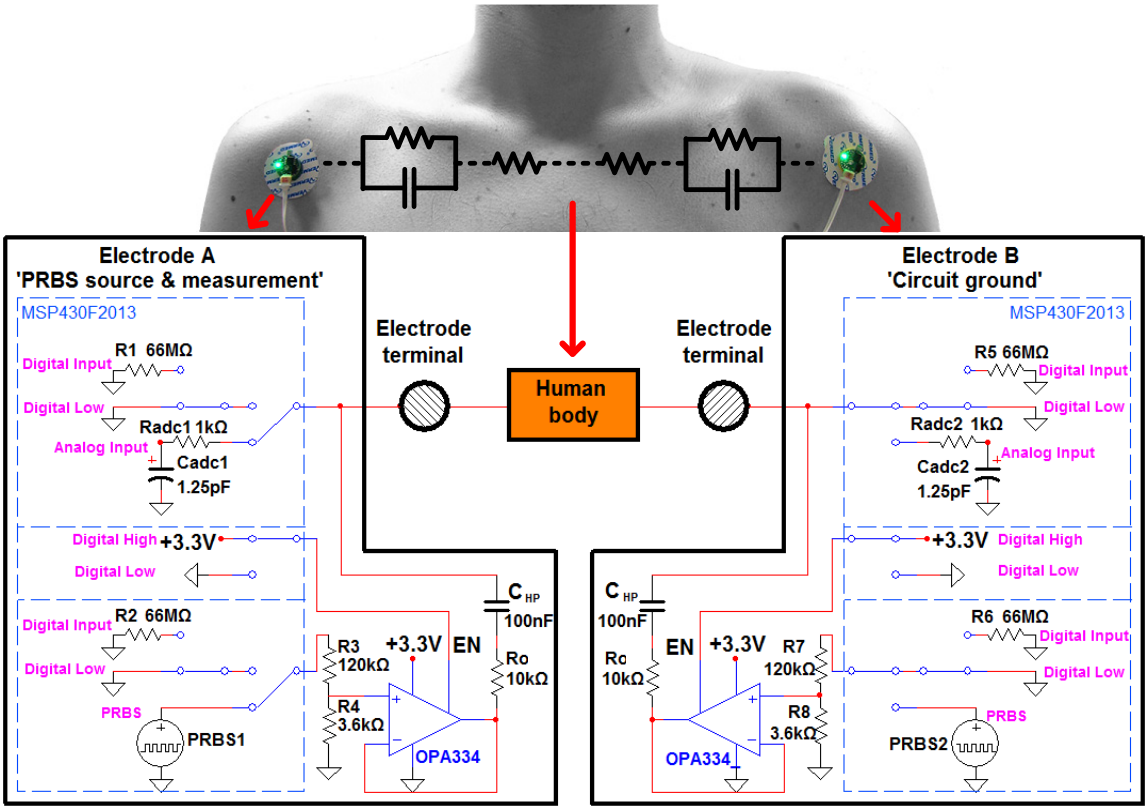

Figure 3.10: A schematic of a *WEBS* slave illustrating one variation of the PRBS system identification circuitry. A second pin on the MSP430 is connected to the electrode terminal via signal conditioning circuitry, a current limiting resistor (R_O) and a capacitor (C_{HP}). In this configuration, when two *WEBS* slaves are connected to the body (*i.e.*, 'Electrode A' generating a PRBS output and measuring the input to the body, and 'Electrode B' set to output a digital low voltage). A passive high-pass filter is formed between R_O, C_{HP} and the impedance of the body and electrode-skin junctions. The measured voltage is a function of this high-pass filter.

During PRBS system identification, it is desirable that only two *WEBS* electrodes are active (*i.e.*, one PRBS source with voltage measurement and one

configured to output a digital low voltage). Therefore, in PRBS mode, other electrodes are automatically configured to set their electrode-connected pins as digital inputs (*i.e.*, a high input impedance state), effectively removing them from the circuit. Similarly, it was an important design consideration that the PRBS circuitry would not introduce a permanent low impedance connection, direct or otherwise, to the circuit ground. Therefore, when the *WEBS* switches back to normal biopotential measurement mode, the OPA334 in each electrode is disabled, ensuring that the effect on the recorded biopotential signal is negligible.

The construction of each *WEBS* PRBS electrode is identical. Consequently, once several electrodes are connected across the body, only a software setting is required to select specific PRBS source, circuit ground and inactive electrodes. As the *WEBS* PRBS circuitry is at a prototype stage, it has not been included in the current model of the *WEBS* slave, as shown previously in Figure 3.3. Instead, two sample *WEBS* electrodes have been modified with additional circuit boards containing the described circuitry. Detailed testing of this circuit design is discussed in Section 5.5

3.2.6.2 Software implementation

A PRBS sequence can be generated in software using a linear feedback shift register (LFSR) (Horowitz and Hill 1989: 655). A LFSR is a shift register (SR) where the input bit is a predefined linear function of the register's previous state. In a conventional LFSR (*e.g.*, a Fibonacci LFSR), the feedback is determined by shifting all of the SR bits down by one, tapping the SR at various locations, performing an operation on the output bits and placing the result into the SR's most significant bit. The Galois LFSR produces the same output as a conventional LFSR but it uses a different structure. Instead, the least significant bit is put through XOR logic operations

interjected at various tap locations within the SR (as illustrated in Figure 3.11). The location of the tap positions, for both types of LFSR, can be represented as a polynomial equation. The maximum number of shift register possibilities is obtained by tapping the SR at certain locations given by maximal-length polynomials (listed in Table D.1 in Appendix D) (Davies 1970: 44-88). It is important to note that the maximum number of SR possibilities is $2^{SR\,bit\,length} - 1$ as the state where all SR bits are zero does not appear in the maximal-length sequence.

A Galois LFSR was used in the *WEBS* microcontroller due to its efficient software implementation and speed of execution (Goresky and Klapper 2002). An example of a 16-bit Galois LFSR is shown in Figure 3.11. In this example, the current shift register state is 0xAB95 (hexadecimal) and the feedback taps are located at bit numbers 16, 14, 13, 11 and 1 (these tap locations produce a maximal-length LFSR for a 16-bit shift register). The contents of the register shift to the right such that the least significant bit is fed back and undergoes a set number of XOR logic operations at predefined feedback tap positions. In this case the subsequent value of the LFSR is 0xE1CA (hexadecimal). An extract from the *WEBS* source code for Galois LFSR implementation can be found in Table D.2 in Appendix D.

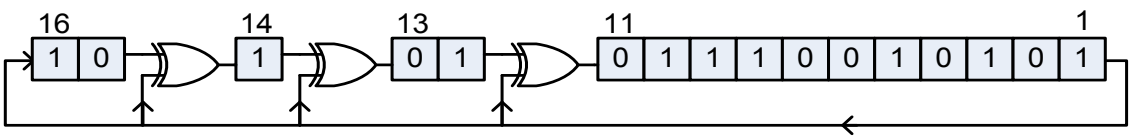

Figure 3.11: A block diagram illustrating a 16-bit Galois LFSR. To achieve the maximum number of LFSR states for a 16-bit shift register ($2^{SR\,bit\,length} - 1$) the feedback taps are located at 16, 14, 13, 11 and 1. The subsequent value of the LFSR in this example is 0xE1CA (hexadecimal).

The period of the PRBS sequence is determined by three factors:

1. The shift register size, and thus the maximum number of unique shift register states that are possible.

2. The feedback tap positions (as described previously).

3. The PRBS sequence chip rate (*i.e.,* duration of each bit).

The period is typically altered to suit the nature of the system under analysis (*e.g.*, a slower responding system might suit a lower shift register size and/or chip rate). The entire PRBS sequence can also be repeated a number of times in order to increase the statistical sample size on which to perform cross-correlation analysis.

Through the use of the *WEBS* GUI (Section 3.3), the user has the ability to set: the PRBS shift register size, start sequence and tap positions; the number of sequence iterations; and the chip rate. In the *WEBS*, the PRBS chip rate is synchronised with the ADC sampling rate and is therefore limited by the maximum sampling frequency of the *WEBS*. To achieve a high PRBS rate (approximately 2 kbps), the lowest resolution ΣΔ ADC setting (at OSR = 32) must be used.

In PRBS mode, each time the *WEBS* master transmits a broadcast message on the I^2C bus (to signify the initialisation of *WEBS* slave sampling), the PRBS source electrode outputs the least significant bit of the PRBS shift register and then samples the ADC channel. After a set sampling delay, the master polls the PRBS source electrode and the ADC result is returned. At this point, the Galois LFSR operation is performed to compute the new value of the PRBS SR bit and analog sampling begins again. This process is repeated until the end of the PRBS sequence.

Both the *WEBS* master and slave devices generate the same PRBS sequence - the slave so that it knows which bit of the PRBS sequence to output, and the master so that it can keep track of how far along in the sequence the slave is. Upon completion of the PRBS sequence, an iteration counter is incremented in the master and, once the count equals a user-defined value, the master issues a configuration command to the slaves to disable the PRBS mode. The recorded data stream is stored in the base computer for subsequent analysis.

3.3 WEBS user interface

Most of the backend signal processing and analysis is undertaken on a base computer for three main reasons. Firstly, transmitting the raw sensor data across the wireless network actually reduces the number of packet bytes needed compared with ADC values that have been converted into specific units with floating point numbers. Secondly, it frees up microcontroller resources so that the main role of the *WEBS* system is to get sensor data from point A (the signal source) to point B (the base computer) as fast as possible, thus increasing the maximum sampling frequency of the system. Finally, having the raw data provides a degree of signal processing freedom that would not exist with, for example, pre-filtered data. The following are desirable features which were decided upon before embarking on the design of the backend software and graphical user interface (GUI):

1. **Reliable.** To be usable in a real world environment, the *WEBS* system needs to operate correctly and consistently each time it is turned on.

2. **Intuitive.** So that the device can be used by the greatest range of people, both the hardware and software interface need to be user-friendly with a meaningful representation of sensor data.

3. **Capable of real-time and offline data processing, analysis and display.** This requires efficient code to perform in real time.

4. **Multi-threaded application.** To separate data acquisition, processing and displaying. This ensures that all data is taken from the serial port buffer in a timely manner while also capitalising on newer computer processor capabilities.

5. **Packet management.** Ability to keep track of packets so that the order and integrity is preserved.

6. **Dynamic configuration management.** Intelligent design to handle the multitude of configuration options available for the *WEBS* and supplemental sensors.

Figure 3.12 illustrates a block diagram for the base computer's internal operations when communicating with the *WEBS*. Utilising a Bluetooth enabled computer, the *WEBS* sensor network appears as a virtual serial port through which the *WEBS* is configured and the stream of recorded data is received. The *WEBS* system is controlled via a series of command bytes. A description of each *WEBS* command and their respective options can be found in Appendix B. A virtual instrument (VI) was created in LabVIEW as the primary GUI. This primary GUI is a multi-threaded program that can acquire, parse, store and graphically display the data stream. The primary GUI contains three separate threads that run in loops until either commanded to stop by the user or the master fails to respond.

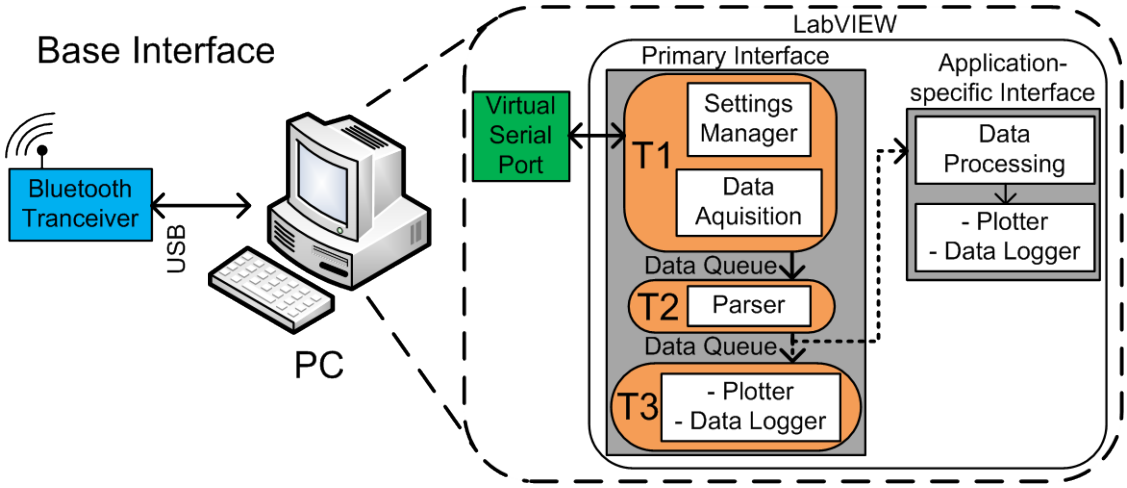

Figure 3.12: A block diagram of the internal operations of the graphical user interfaces. T1, T2 and T3 denote the separate thread operations in the primary GUI. A secondary application-specific interface that can replace thread 3 is also shown.

As indicated in Figure 3.12, information is passed from one thread to another via first in, first out (FIFO) data queues. When thread loops 1 and 2 each come to their loop end-point, their output data is placed in a queue for the next thread to remove. The benefit of this approach is that all data is buffered at each stage until it is read so that no data is lost. Each thread is free to continue running without having to wait for the next thread to finish processing. Furthermore, since the threads are inactive when their input queue is empty, computer resources are freed up.

Figure 3.13 illustrates a flowchart of the core functionality of the primary GUI. A key feature to note is that not only can the *WEBS* master detect connected slaves on power-up, but also on request from the GUI. Following the appropriate command byte from the GUI, the master performs a slave discovery and responds with a list of connected slave addresses. The GUI configuration drop-down boxes (that select the reference electrode in normal mode and the source and reference electrodes in signal-source mode) are then populated with this list.

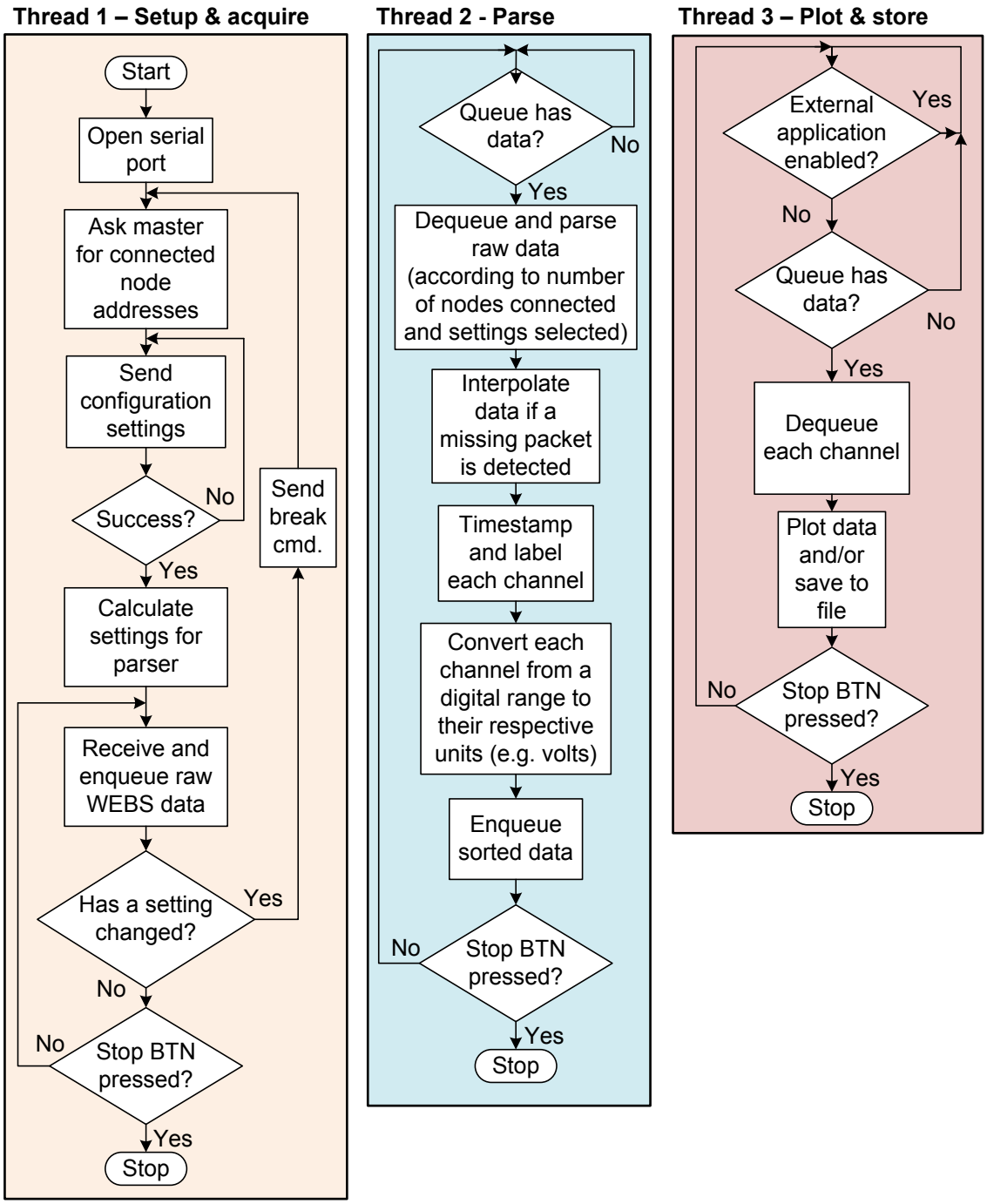

Figure 3.13: A flowchart of the primary GUI created in LabVIEW. The three multi-threaded operations are highlighted here. If no response is received from master at any stage in thread 1, the program terminates each thread and ends.

Another key feature is that the primary GUI can self-configure itself depending on the number of slaves connected and configuration options. Each time a configuration option is altered, such as individual sensor activation or deactivation, the number of bytes to receive is re-calculated and the sensor data is parsed into the appropriate active

channels. The main graph also responds by maintaining the vertical axis separation for each sensor type. Different sensor configurations also have a bearing on the maximum achievable sampling frequency of the *WEBS* (see Appendix C). Therefore, the primary GUI can dynamically alter the time base that is assigned to the received data channels.

Figure 3.14 shows a screenshot of the primary GUI, highlighting the *WEBS* configuration options, system feedback textbox and GUI controls. In this case the on-screen graph contains biopotential activity from a three-electrode ECG recording as well as the associated electrode movement activity (x-axis, y-axis and z-axis) from each of the recording electrodes (right arm, left arm and left leg). The left vertical axis represents the *WEBS* slave's ADC measurement in volts. The inner right hand side vertical axis represents the accelerometer movement in g (where 1 g = 9.81 m/s^2). The far right hand side vertical axis represents the package counter value. The primary GUI provides the user with many configuration options including individual accelerometer axis activation and ADC settings.

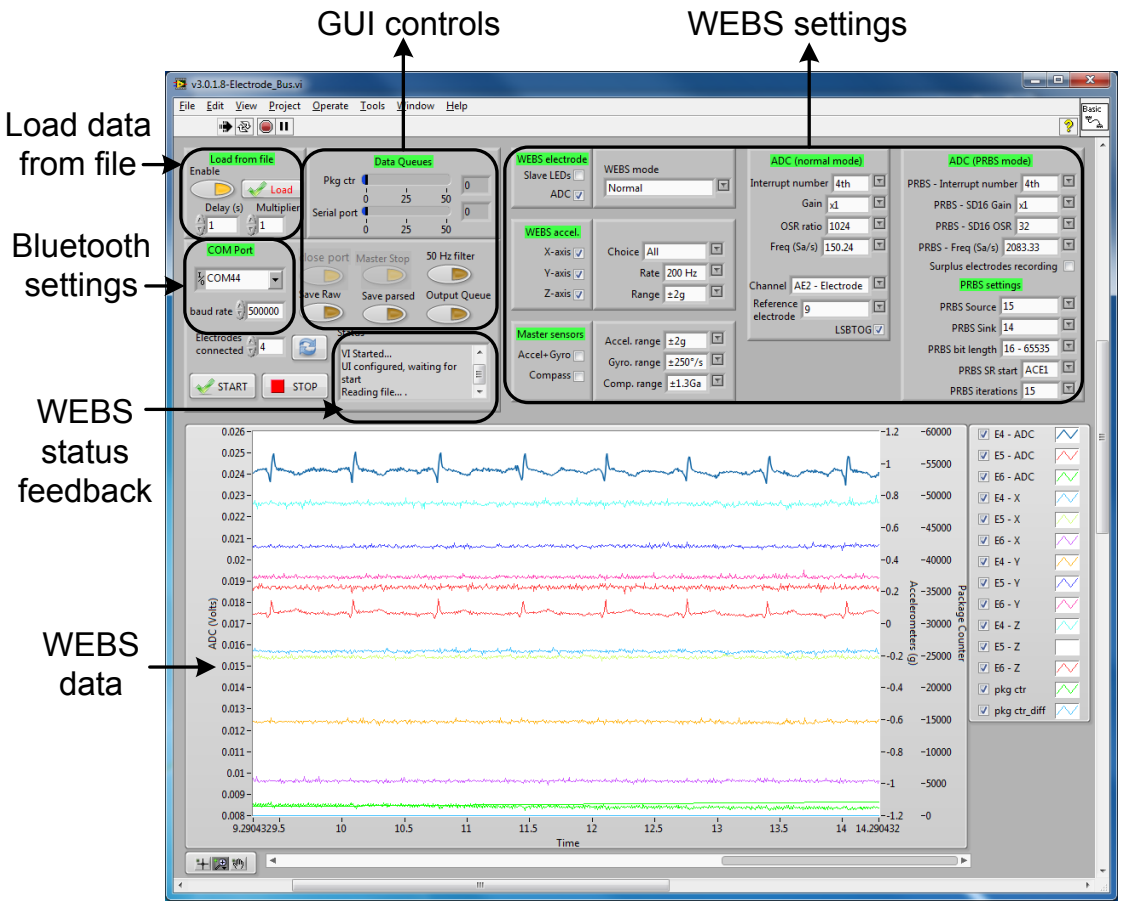

Figure 3.14: A screenshot of the primary GUI that was designed in LabVIEW for communicating with the *WEBS* sensor network. Various GUI properties are highlighted and an example recording is plotted from a 3-lead ECG with associated accelerometer measurements from each electrode. E4, E5 and E6 are the right arm, left arm and left leg electrodes respectively.

As alluded to in Figure 3.12, an optional LabVIEW GUI handles any additional processing or graphical representation that might be required for specific applications. For example, an EOG-based HMI requires algorithms and classifiers that are unique to that biopotential system. These secondary GUIs can be easily custom built to suit each application. At the press of an on-screen button, thread 3 in the primary GUI is disengaged and the output data queue from thread 2 is taken over by the secondary GUI. An example secondary GUI, specific to 6-lead ECG, is illustrated in Figure 3.15. This particular GUI receives the parsed data from the primary GUI (*i.e.*, the three electrode ECG signals from Figure 3.14) and performs the necessary calculations to obtain the bipolar lead (Lead I, Lead II and Lead III) and augmented lead (aVR, aVL and aVL)

signals (more on this in Section 5.4). Various secondary GUIs will be discussed later in the thesis in their respective application sections.

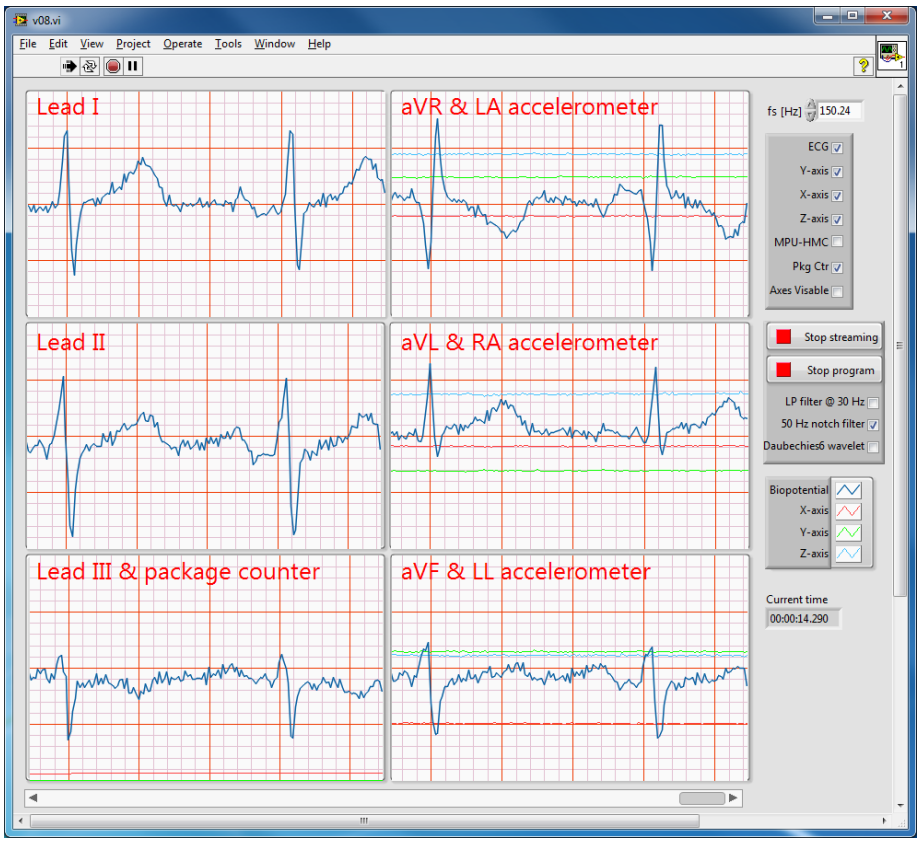

Figure 3.15: A screenshot of a secondary GUI that was designed in LabVIEW. This particular GUI was created to calculate, filter, and graphically present each of the lead measurements (Lead I, Lead II, Lead III, aVR, aVL and aVL) from a 6-lead ECG recording. In this GUI, the graph scaling was set to be the same as conventional ECG graph paper (vertical axis at 0.1 mV per minor division and horizontal axis at 40 ms per minor division). The accelerometer scaling ranges over ± 2g. The data plotted in this GUI corresponds to the final second of data plotted previously in Figure 3.14.

Although a PC-based application is described here, any Bluetooth enabled device can connect to the *WEBS*. For example, several free applications are available on Android-based mobile phones and tablets (*e.g.*, "Bluetooth SSP" and "GetBlue") that provide a serial port connection to the *WEBS* whereby transmitted data can be stored locally to a file in the systems memory.

3.4 *Method of use*

a. Prepare skin and attach electrodes.

The skin surface should be prepared before attachment of the electrodes to create a lower impedance connection with the *WEBS*. To exfoliate the skin (thereby reducing the skin's impedance), 20 unidirectional strokes with electrode preparation pads (*i.e.*, pads typically containing Isopropyl Alcohol and pumice) should be applied to the skin (Webster 1984). As stated previously, each *WEBS* slave is soldered directly on top of button clip electrode connector. As such, the *WEBS* slave can utilise many commercially available disposable button clip electrodes, such as those illustrated in Figure 3.16.

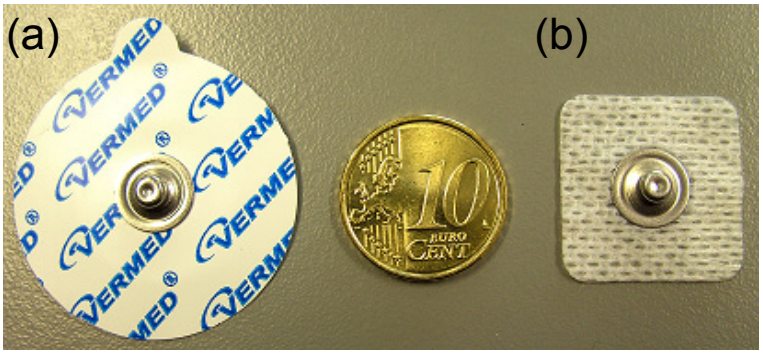

Figure 3.16: Examples of two disposable button clip electrodes that are suitable for use with the *WEBS* system. (a) has an electrode in contact with a sponge soaked in electrolyte gel with an adhesive plastic backing. (b) has an electrode in contact with a conductive and highly adhesive-gel with a cloth backing which is useful for comfortable long-term monitoring.

If required by the electrode type (*e.g.*, electrode (a) in Figure 3.17), a pea-sized drop of Ag/AgCl electrolyte gel should be applied to each electrode prior to attachment to the skin. For optimum results, 20 minutes should be allowed while the electrolyte gel soaks into the skin (Webster 1977).

b. Connect *WEBS* electrodes.

The *WEBS* master and slave electrodes are connected together via light 4-core wires with JST-SH connectors (JST Manufacturing Company Ltd. 1997) at each end. Up to four wires can be connected together using pre-fabricated bus junctions, as illustrated in Figure 3.17.

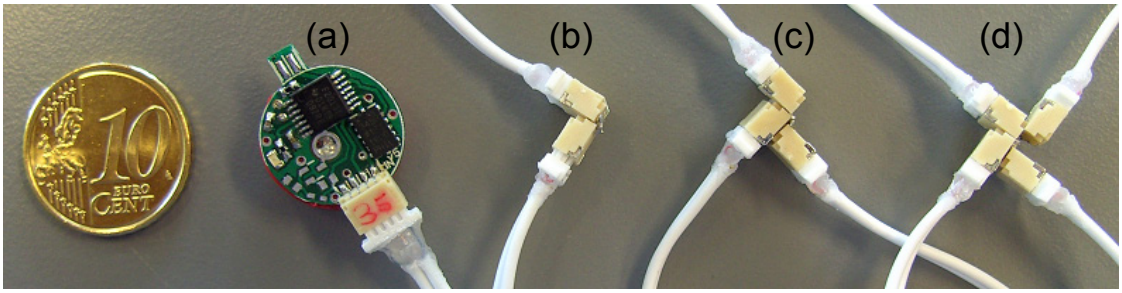

Figure 3.17: An illustration of: (a) slave electrode with a surface-mount female JST-SH connector and attached male connector with wire; (b) 2-way, (c) 3-way and (d) 4-way straight-through bus junctions fabricated by soldering multiple female JST-SH connectors together at a 90° angles.

Utilising combinations of multiple lengths of wire and multiple bus junctions, a huge variety of configurations of the *WEBS* system is possible. This removes the need for a custom-made fixed wiring network for individual applications. A user can alter a measurement configuration at will by simply plugging and unplugging pre-fabricated parts. Figure 3.18 shows an example of how the *WEBS* system can be connected together - in this case, for bicep electromyogram measurement.

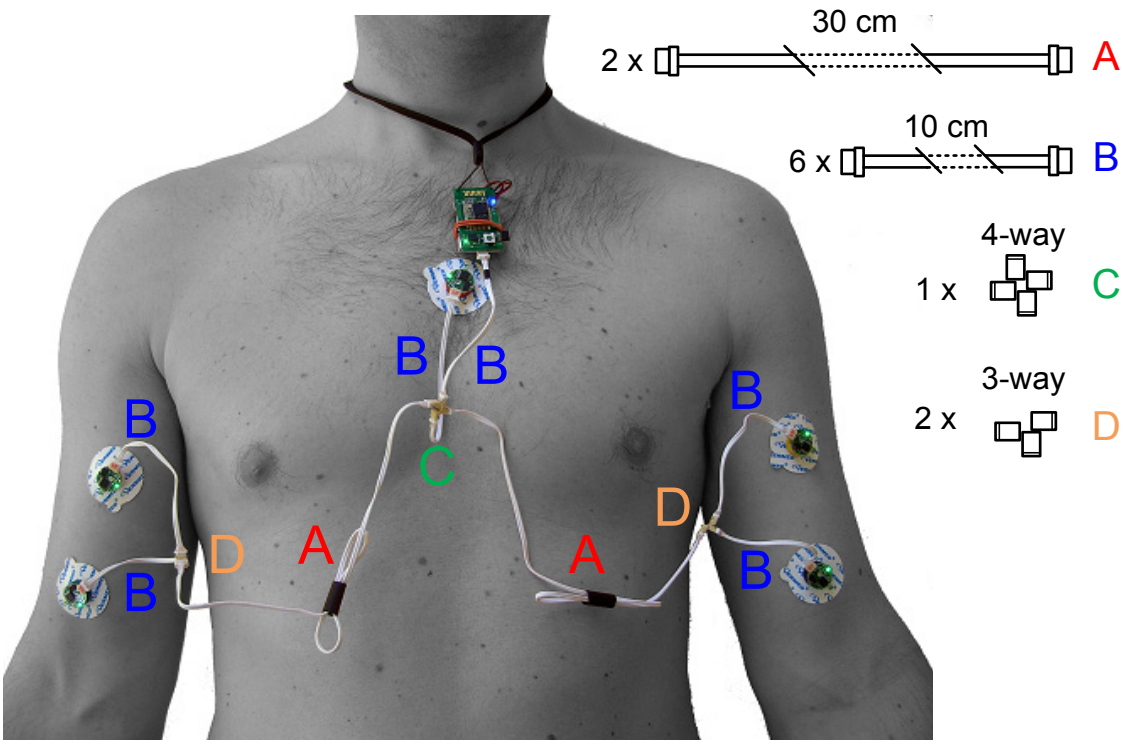

Figure 3.18: An illustration of an example *WEBS* wiring configuration for bicep EMG measurement. Five *WEBS* slaves are connected together via 4-way wire with JST-SH connector ends. Multiple wires are connected together by pre-fabricated multi-way junctions.

c. Initiate *WEBS* master.

A switch on the side of the *WEBS* master connects turns on the system. Once switched, a circuit is completed between the on-board Lithium-ion polymer battery and a voltage regulator circuit that provides power for the entire *WEBS* system. On power-up, the Bluetooth transceiver in the *WEBS* is activated. Using a base computer, the user can now pair and connect with the *WEBS* system which will appear as a virtual serial port.

d. Start primary GUI.

The *WEBS* is now ready to be configured and recorded from via the primary LabVIEW GUI. A sequence of steps is required before measurement can commence and these are highlighted on the configuration panel in Figure 3.19 and subsequently described below.

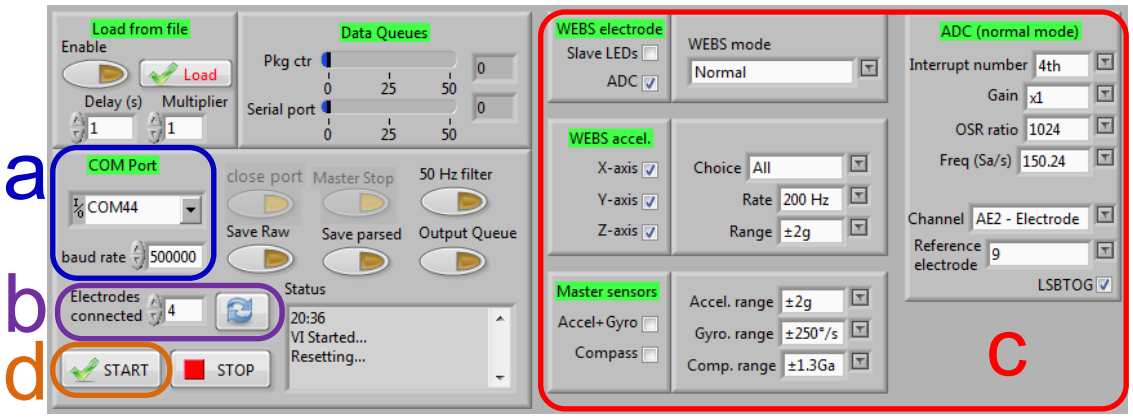

Figure 3.19: A view of the primary *WEBS* GUI's control panel. To initiate the *WEBS*, a user must: a) configure the appropriate COM port; b) request from the master a list of connected *WEBS* nodes; c) select desirable *WEBS* configuration settings; and d) press the start button.

i. **Select the appropriate serial (COM) port.** A drop-down box is populated with a list of the available COM ports in the local computer on start-up. The virtual COM port created by the *WEBS* Bluetooth link will be listed here.

ii. **Request a list of connected electrodes from master.** Pressing the highlighted refresh button sends a request to the *WEBS* master to perform a slave discovery and respond back to the GUI with a list of connected slaves. The drop-down box for reference electrode selection is then populated with this list. The highlighted numerical control is used to perform a crosscheck with the master to confirm the number of slaves connected. If there is a mismatch between the two numbers, the GUI will respond with an error on initialisation.

iii. **Choose the desired *WEBS* settings.** The user can now configure the *WEBS* with their desired settings to suit their application. The multiple options available allow configuration of the general *WEBS* operation, the *WEBS* ΣΔ ADC, the slave accelerometers, and the *WEBS* master's sensors.

iv. **Start.** The *WEBS* is now ready to be inialised. Once the start button is pressed, the text window gives the user feedback regarding the *WEBS* system's status.

3.5 Summary

This chapter provided a detailed design description of both the hardware and software aspects of the developed multimodal sensor system, the *WEBS*. The *WEBS* system is a body sensor network that employs multiple sensing modalities in a novel bioelectrical and biomechanical signal measurement configuration. Particular attention was paid to describing the *WEBS* system's features, how it operates and the considerations that need to be taken into account for use in a biosignal measurement context. Although the described internal operation of the *WEBS* system is complex in nature, careful consideration has been placed on the design of the *WEBS* GUI and the method of attachment to the body in order to facilitate a usable and intuitive means for a wearer to easily interact with the *WEBS* system.

This chapter also showed that since the *WEBS* nodes are multifunctional digital electrodes, they are not limited to just biopotential signal measurement. When operating in signal source mode, any electrode can be digitally selected to act as a low-impedance connection to the human body or as a signal source for use, for example, in system identification of the electrode-skin junction impedance. The method of operation for signal source mode was discussed in this chapter.

As described in this chapter, the *WEBS* system is a scalable, dynamic and wearable sensor network, which opens new avenues for HMI and biosignal measurement. However, before the developed system can be fully utilised, it is important to gauge the performance of the system and the competency of the device in both biopotential and biomechanical signal measurement - which is the topic of the next chapter.

Chapter 4 Performance Testing of the WEBS System

To gauge the performance of the *WEBS* electrode under various conditions and in different modes of operation, a series of experiments was carried out. Given the multitude of configuration combinations and broad range of possible applications for the *WEBS*, it is not possible to document detailed specifications covering all eventualities in this chapter. However, the experiments described here cover a diverse range of operating conditions. This chapter begins by investigating the input characteristics of the *WEBS*, namely its frequency response and noise characteristics at various user-configurable settings. This chapter goes on to describe the performance of the *WEBS* in measuring biopotential signals using ECG, EOG and VEP as examples. Comparisons are included between the *WEBS* and a commercial device, the BioSemi ActiveTwo, which is widely used by researchers worldwide. Finally, the measurement of biomechanical activity is described, using an example based on an efferent hotspot, the throat (via laryngeal vibrations).

4.1 Experiment 1: Input characteristics of the WEBS electrode

As is typical with any data acquisition system, the performance of the *WEBS* electrode is dependent on numerous electrical and software properties. Two such properties of the system are the frequency response and the noise level. The frequency response gives an indication of the range of electrical frequencies that can be detected by the *WEBS*, which has a bearing on what types of biopotential signals it can measure. The frequency response of the *WEBS* is governed not only by the speed of the analog-to-digital conversion process, but also by the speed at which the conversion data can be retrieved from each sensor such that no data backlog exists. The noise performance indicates how much background noise is detected by the *WEBS*, which can result in a negative impact on the measurement of tiny biopotential signals. Both of these properties vary with various *WEBS* configuration settings. Therefore, in this section, each one is investigated for different configuration combinations.

4.1.1 Frequency response of the *WEBS* system

As highlighted in Section 3.2.2, the *WEBS* system is assumed to be a linear time-invariant system which, at the signal amplitudes and frequencies of interest, is a reasonable assumption. A frequency sweep analysis was chosen as the simplest method in order to obtain the system response (magnitude and phase) of the *WEBS*. The experimental set-up, as illustrated in Figure 4.1, was used to obtain the characteristics (gain and phase shift) of the *WEBS* system at different frequencies. In LabVIEW, two analog voltage signals were generated with a sampling rate of 8 kHz. The first signal was a simulated digital signal that, while high, signalled the *WEBS* master to record data

from a slave and transmit it back to a base computer. The second signal was a sine wave at amplitude 0.3 V that was active when the first signal was high (*i.e.*, when the *WEBS* was recording). The sine wave had a particular frequency ranging from 0.1 Hz up to the Nyquist-Shannon frequency of the *WEBS* which was, in this case, limited by the oversampling ratio (OSR) setting (*e.g.*, at OSR = 32, f_{NYQ} = 1020 Hz). Two digital-to-analog converter (DAC) channels from a National Instruments multifunction data acquisition module (the NI-USB 6215) provided the means to output the generated signals from LabVIEW. Each channel was connected to an input pin of the master and slave devices as shown.

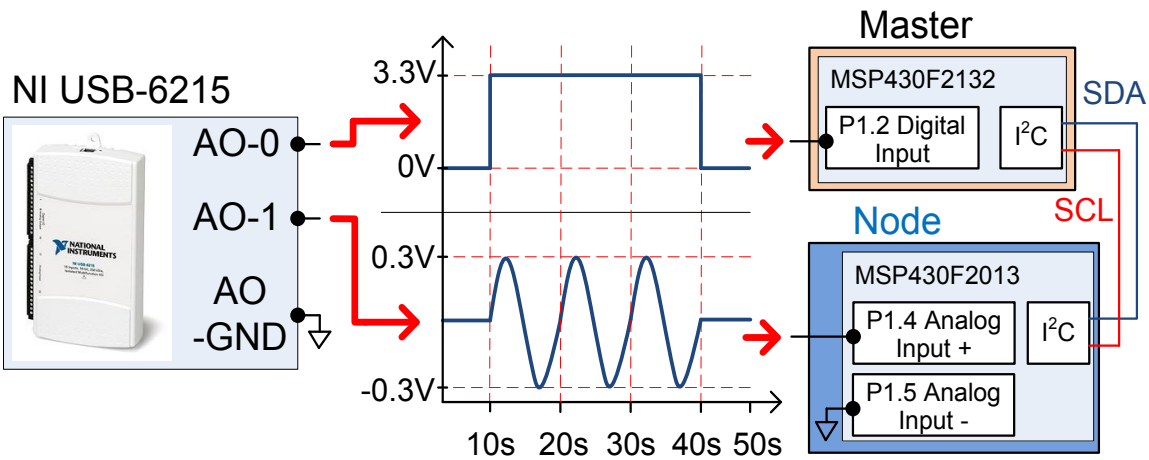

Figure 4.1: A block diagram of the experimental set-up for testing the properties of each *WEBS* electrode. Two output voltage signals from a National Instruments multifunction data acquisition module (the NI-USB 6215) were used. The first as a test initialisation trigger to the *WEBS* master and the second as the test signal to the input of the *WEBS* slave. The experiment was repeated for each electrode over a broad range of test signal frequencies up to the Nyquist-Shannon frequency of the *WEBS*.

At the start of each test, both channels were set at 0 V for 10 s. This allowed any transients to settle in the slave ADC between separate tests. Following this, the simulated digital signal to the master went to a logic high state whilst, simultaneously, the sine wave was sent into the ADC of the slave. The digital signal remained high for the duration of the sine wave until the 30 s had elapsed, at which point both signals

returned to 0 V for a further 10 s. The experiment was automated in LabVIEW and, for each value of OSR, it repeatedly cycled for a specific number of frequencies in order to provide a sufficient number of magnitude plot data points up to the Nyquist-Shannon frequency. Table 4.1 provides a list of the test frequencies used at each OSR setting.

Table 4.1: This table lists the various test frequencies used at each OSR setting for analysing the analog input characteristics of the *WEBS* slave. The test frequencies were chosen so that a sufficient number of data points could be obtained for the magnitude plot up to the Nyquist-Shannon frequency.

OSR	Maximum sampling rate	Test frequencies	Total number of test frequencies
32	2041 Sa/s	0.1 Hz	38
		10 Hz to 100 Hz: every 5 Hz	
		100 Hz to 1000 Hz: every 50 Hz	
64	1465 Sa/s	0.1 Hz	33
		10 Hz to 100 Hz: every 5 Hz	
		100 Hz to 700 Hz: every 50 Hz	
		730 Hz	
128	1045 Sa/s	0.1 Hz	36
		10 Hz to 100 Hz: every 5 Hz	
		100 Hz to 500 Hz: every 25 Hz	
256	663 Sa/s	0.1 Hz	31
		10 Hz to 100 Hz: every 5 Hz	
		100 Hz to 320 Hz: every 20 Hz	
512	375 Sa/s	0.1 Hz	43
		1 Hz to 100 Hz: every 3 Hz	
		100 Hz to 180 Hz: every 10 Hz	
1024	205 Sa/s	0.1 Hz	35
		1 Hz to 100 Hz: every 3 Hz	

Post-testing, the recorded data was processed in MATLAB whereby it was audited for missing data packets and the time base was corrected and/or set. Interpolation was used to reconstruct missing data packets; although this was only necessary for approximately 1 in 9259 data packets. Of the 30 s of recorded test signal data, the first 20 s was taken to be the settling time of the system and therefore calculations were only performed on the remaining 10 s. To calculate the magnitude and phase, the discrete Fourier transform was computed in MATLAB on the measured output signal at each test frequency using the following analysis equations (Smith 1997). Firstly, theoretical sine and cosine signals were created with the same frequency and sampling time as the test signal being sent out by the NI-DAQ. At each sample instant, the sine and cosine signals were multiplied (sample by sample) by the measured sample:

$$X_{\mathrm{Re}}[k] = \sum_{n=0}^{N-1} y[n] \cdot \cos\left(\frac{2\pi kn}{N}\right) \tag{4.1}$$

$$X_{\mathrm{Im}}[k] = \sum_{n=0}^{N-1} y[n] \cdot \sin\left(\frac{2\pi kn}{N}\right) \tag{4.2}$$

where $X_{\mathrm{Re}}[k]$ and $X_{\mathrm{Im}}[k]$ are the real and imaginary parts of the DFT, n is the sample number, N is the number of samples, y is the measured output amplitude, k is the test signal frequency.

$$|y[k]| = \sqrt{X_{\mathrm{Re}}[k]^2 + X_{\mathrm{Im}}[k]^2} \tag{4.3}$$

$$\Theta[k] = \mathrm{atan2}(X_{\mathrm{Im}}[k], X_{\mathrm{Re}}[k]) \tag{4.4}$$

where *atan2* is the computer language implementation of a four-quadrant inverse tangent (*arctangent*) using two input arguments, A_{input} is the amplitude of the test signal, $|y|$ is the magnitude and Θ is the phase.

Figure 4.2 shows a graph of the calculated Bode plot for twelve different electrodes at a sampling rate of 2041 Sa/s. Electrodes numbered one to eleven are configured as described in Chapter 3, whereby the circuit is soldered on top of a button-clip electrode connector. A crocodile clip on a short wire was used to connect the output of the NI-DAQ DAC to the button-clip electrode connection. For an ideal-case comparison, electrodes numbered thirteen and fourteen were modified such that a wire was directly soldered onto the electrode circuitry, bypassing the button-clip connection in order to minimise stray impedances or other non-ideal characteristics. The opposite end of the wire was connected to the NI-DAQ DAC output. As described in Section 3.2.2, the sigma-delta ADC converter within each slave utilises a $SINC^3$ comb decimation filter with a selectable OSR. The output response of this internal digital filter, for an OSR setting of 32, is represented in Figure 4.2 as a dashed blue line.

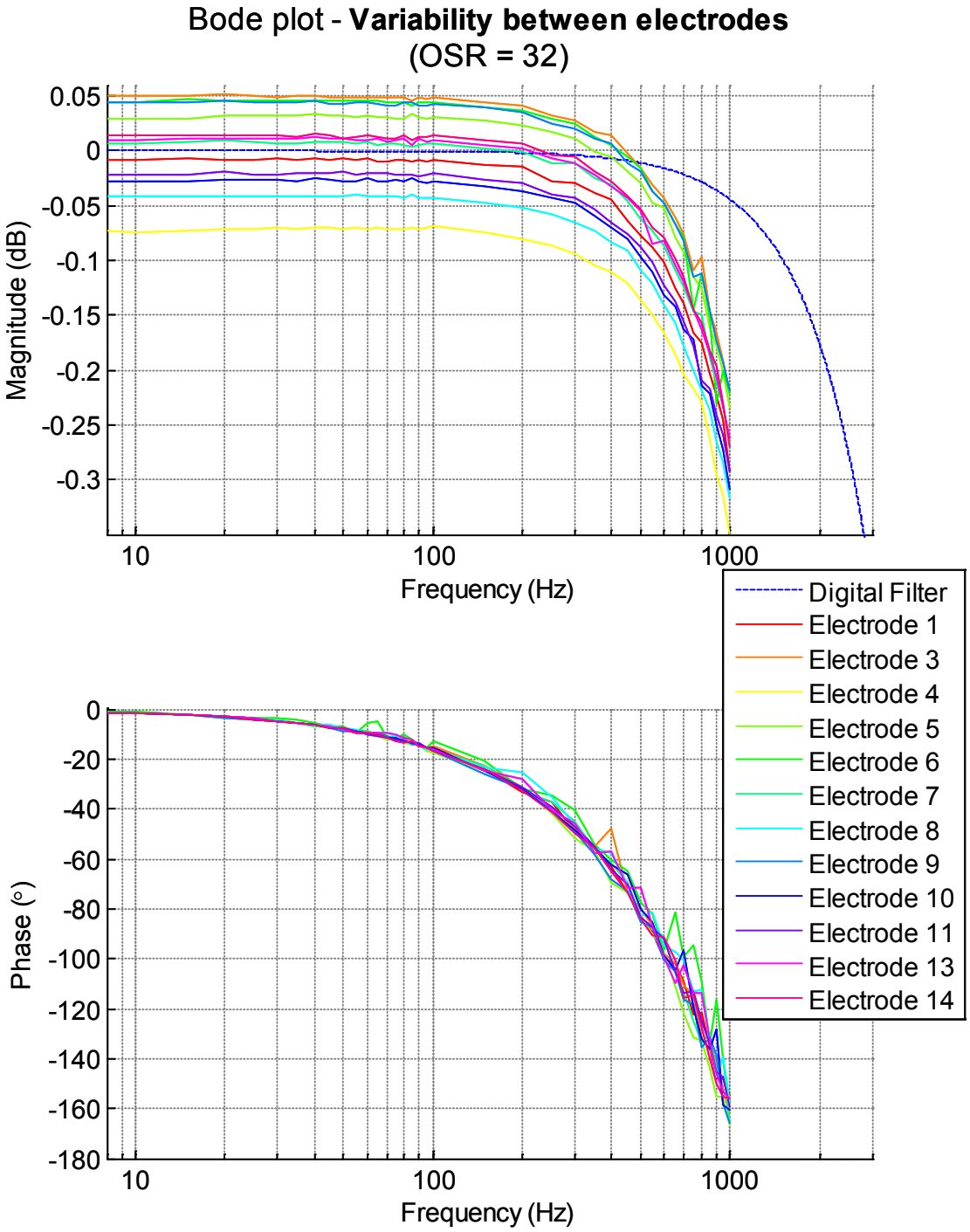

Figure 4.2: A Bode plot illustrating the variability of input characteristics for twelve *WEBS* electrodes configured identically. For each electrode, the OSR is set at 32 and the sampling rate at 2041 Sa/s. Negligible variation in magnitude and phase occurred at test frequencies below 8 Hz.

The discrepancy between the magnitude of the digital filter output and the recorded data is due to the communication speed limitations of the *WEBS* digital network. If the data throughput was unlimited, the sampling frequency would increase up to the maximum sampling frequency of the ADC, in which case, a shift in the magnitude plot would be expected up to a maximum of the decimation filter output.

The slight disparity between each electrode's output magnitude at frequencies less than 100 Hz indicates the presence of offset and/or gain errors within the different electrodes. These errors can be attributed to hardware inconsistencies in the individual ADCs, the pre-digitisation gain stages, or the PCB construction. The offset and gain errors are small and should be constant for each *WEBS* configuration setting. Therefore, once pre-calibrated (by measuring the offsets), compensation can be added in software for each electrode. The SD16_A within the MSP430F2013 provides the ability to measure its own internal gain error. Through the *WEBS* user interface, the gain offsets for all *WEBS* slaves can be measured by simply changing the recording channel via the drop-down box provided.

Figure 4.2 suggests that the input phase response to the *WEBS* has a steep decline from 0º at 8 Hz to -160º at the Nyquist-Shannon frequency. It is worth noting that the input to the ADC is a fourth order system consisting of a first order RC filter followed by a third order $SINC^3$ comb decimation filter. A small variability in the input phase responses is evident on some of the lines in Figure 4.2. This feature will become more evident later in this section (see Figure 4.4). Relative phase shifts are not a significant issue with regard to conventional multichannel biopotential measurement as a single ADC with multiple channels is normally used. However, in the case of the *WEBS* system, input impedance variations between different *WEBS* ADCs could result in an incorrect phase alignment when calculating bipolar lead voltages. For the phase

variations noted here however, it is hypothesised that they are due to a calibration issue between the various experimental devices (such as a NI-DAQ output latency between each of the analog output channels) rather than something that could affect everyday biopotential measurement with the *WEBS* system. One source of evidence for this is that the number of packets in the recorded data file for each frequency was slightly inconsistent (varying by fewer than 5 packets). At low frequencies, this number of lost packets (out of a total number of 61,230 at an OSR of 32) is not significant but at higher frequencies, this can result in increasingly inaccurate phase calculations. To investigate this phenomenon further, a different system identification method, such as that described in Section 5.5, could be utilised.

To demonstrate the input response continuity, the same test was repeated thirteen times on a single electrode. Figure 4.3 illustrates the results from this series of tests along with the decimation filter as described previously. Test numbers one to nine were performed in series, one set after the other. In order to disregard chance as being a factor in the results, before tests ten to thirteen, the connection to the electrode was disconnected, then reconnected and the entire system reset.

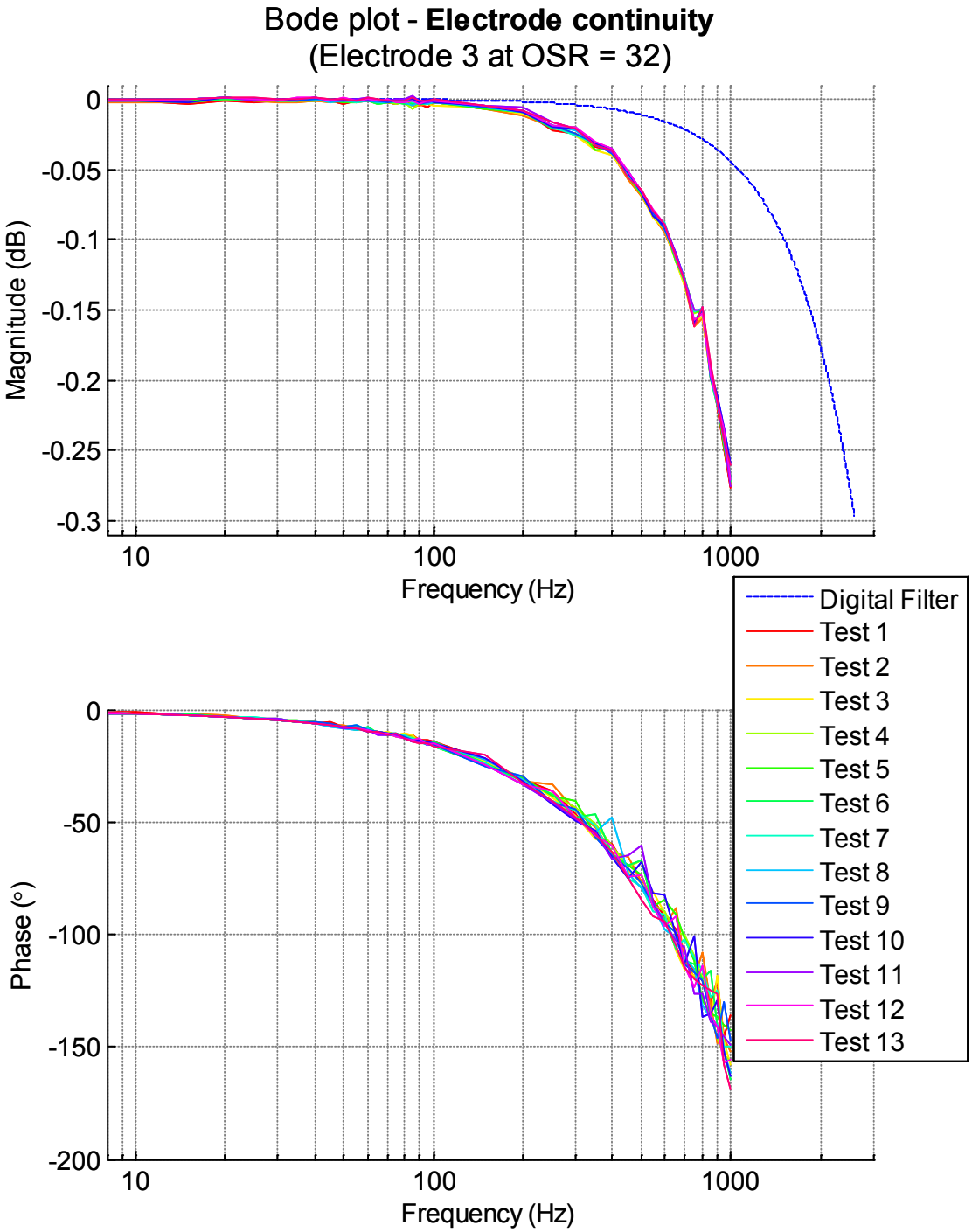

Figure 4.3: A Bode plot for a single *WEBS* electrode with an OSR rate of 32. The experiment was repeated thirteen times to illustrate the continuity of the electrode response. On each occasion, the testing apparatus was reassembled from scratch to increase the validity of the results. The sampling rate for each test was set at 2041 Sa/s. For illustration purposes, the consistent offset error in electrode 3 of +0.0504 dB has been subtracted from the magnitude plot of each test. Negligible variation in magnitude and phase occurred at test frequencies below 8 Hz.

It is evident from Figure 4.3 that there is a high correlation between tests. A distinct feature of the magnitude plot, which becomes more apparent in Figure 4.3, is a series of notches on the magnitude graph. The output sample rate of the NI-USB 6215 was set at 8 kSa/s and it is hypothesised that aliasing of this sampled signal is manifested as consistent disturbances on the input response of the electrodes (*i.e.*, at 800 Hz, 400 Hz, 200 Hz, *etc.*).

Figure 4.4 illustrates a similar test to that of Figure 4.3, carried out on a single electrode but at different OSR settings. Five tests were performed at each OSR setting of 32, 64, 128, 256, 512 and 1024. A dashed blue line that accompanies each set of tests represents the frequency response of the internal filter at each OSR setting. As the OSR value increases towards 1024, the respective magnitude responses begin to converge. This confirms the description given for Figure 4.2 whereby, at lower OSR values, the internal over-sampling filter increasingly governs the frequency response due to communication speed limits on the *WEBS* digital network. The phase response in Figure 4.4 further illustrates the problem described previously whereby an inconsistency in the total number of recorded data packets for each test has led to a variability in phase measurement, especially evident for the test where OSR was equal to 128.

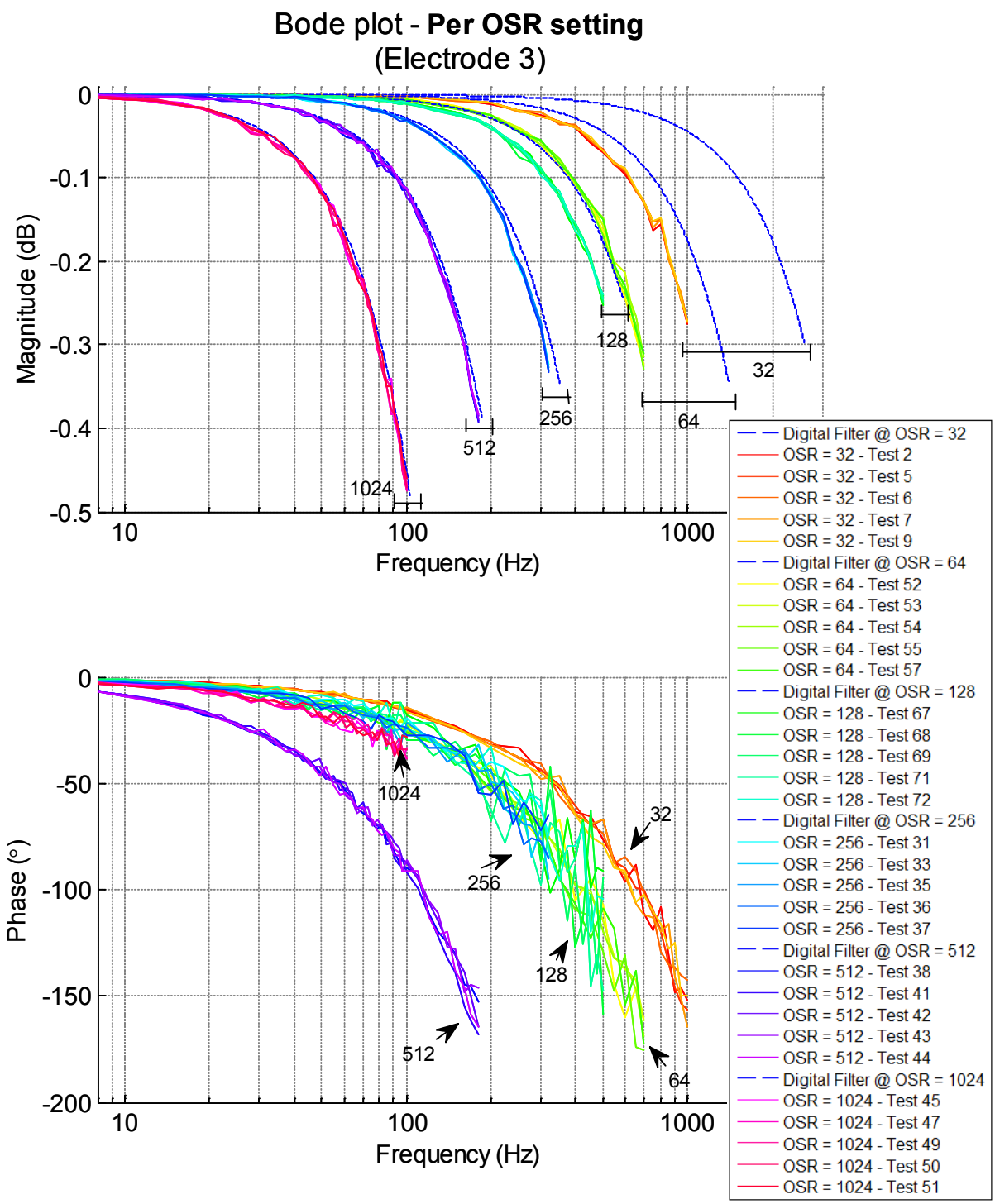

Figure 4.4: A Bode plot illustrating the *WEBS* input characteristics for various OSR settings. A representative electrode (electrode 3) was chosen at random and tests were performed on it at OSR settings of 32, 64, 128, 256, 512 and 1024 with respective maximum sampling rates of 2041 Sa/s, 1465 Sa/s, 1045 Sa/s, 663 Sa/s, 375 Sa/s and 205 Sa/s. The results from five tests for each OSR setting are illustrated. For illustration purposes, the consistent offset error in electrode 3 of +0.0504 dB has been subtracted from the magnitude plot of each test. Negligible variation in magnitude and phase occurred at test frequencies below 8 Hz.

4.1.2 Noise performance

The noise level in a signal recorded by an ADC is a measure of the non-signal noise power that can originate from noise sources and unwanted signals. This noise can comprise random (*e.g.*, thermal noise, quantisation noise and ADC clock jitter) or non-random (*e.g.*, containing harmonic, spurious or DC components) components (Slepicka 2007). Detailed derivations for calculating various noise levels in an ADC are given by (Terlep 2002, Kester 2008, Kester *et al.* 2005). For the purpose of this discussion, the measured average noise of the *WEBS* ADC input will be compared against the calculated thermal noise and ideal noise given by the following equations.

The equation for the ideal noise of an ADC, as stated in the IEEE standard 1241-2000 (The IEEE Standards Association 2001), is given in dB over the full scale range (dBFS) by:

$$NF_{ideal}(dBFS) = 6.02N + 1.76 + 10\log_{10}\left(\frac{M}{2}\right) \tag{4.5}$$

where N is the number of ADC output bits, M is the window length in samples. The above equation assumes that a rectangular window is used. The equation for thermal noise is derived from the Johnson-Nyquist noise equation (Nyquist 1928) and, by taking into account processing gain and conversion to decibels over the full-scale range (Slepicka 2007), can be represented as:

$$NF_{thermal}(dBFS) = -10\log_{10}\left(\frac{MV_{FS(rms)}{}^{2}}{RkTfs}\right) \tag{4.6}$$

where k is Boltzmann's constant ($k = 1.381\times10^{-23} m^2\ kg\ s^{-2}\ K^{-1}$), T is the absolute temperature represented in Kelvins, fs is the sampling frequency and R is

the sum of the source and sampling resistances. As with equation (4.5), equation (4.6) assumes the use of a rectangular window.

4.1.2.1 Programmable-gain amplifier noise level

As described in Section 3.2.2, the programmable-gain amplifier (PGA) is a user programmable gain stage, built into the TI MSP430F2013's ΣΔ ADC. The PGA is located between the differential channel inputs and the ΣΔ modulator. The *WEBS* normally utilises the two differential inputs from channel A2 that are connected internally to external pins. A feature of the TI MSP430F2013 is that one of the available channels, A7, is an internally short-circuited channel as illustrated in Figure 4.5. This feature provides the ability to measure not only the offset errors in the PGA, but also to monitor the background noise in the ADC. As the PGA is the last item before a signal enters the ΣΔ modulator, the noise at the PGA will define the minimum level of noise in the system.

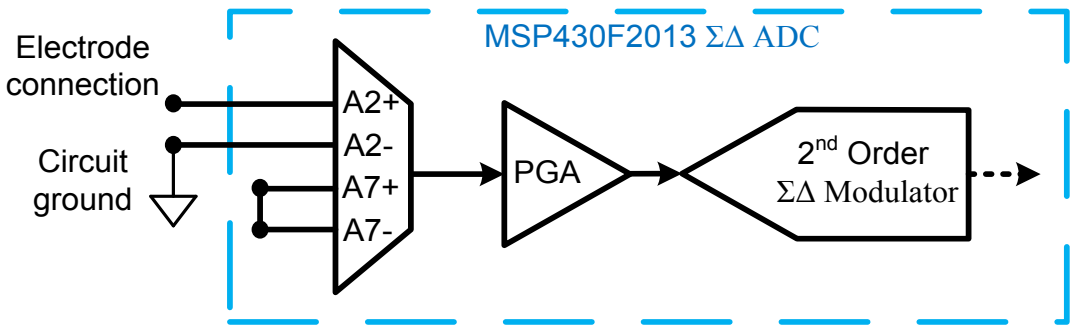

Figure 4.5: A simplified block diagram of the MSP430F2013's ΣΔ ADC as used in the *WEBS* slave. The electrode contact of the *WEBS* slave is connected into A2+ whilst A2- is connected to the circuit ground. Channel A7 is internally connected short-circuit that facilitates measurement of the PGA offset voltage and noise level.

To analyse the noise performance at the PGA, nine *WEBS* electrodes were placed at a distance of 1 m from the nearest source of mains interference and a 360 s recording was taken from channel A7 of each electrode. The Fast Fourier Transform

was calculated on the resulting recordings, the graph of which resembled a flat spectrum with no dominant frequency. The average magnitude for each FFT was calculated and Figure 4.6 illustrates a plot of the average magnitude of the nine electrodes at each OSR setting. To provide a direct comparison between each OSR setting, the sampling frequency was fixed at 142.05 Sa/s for every test – the fastest achievable sampling rate for a nine electrode system at the highest resolution setting.

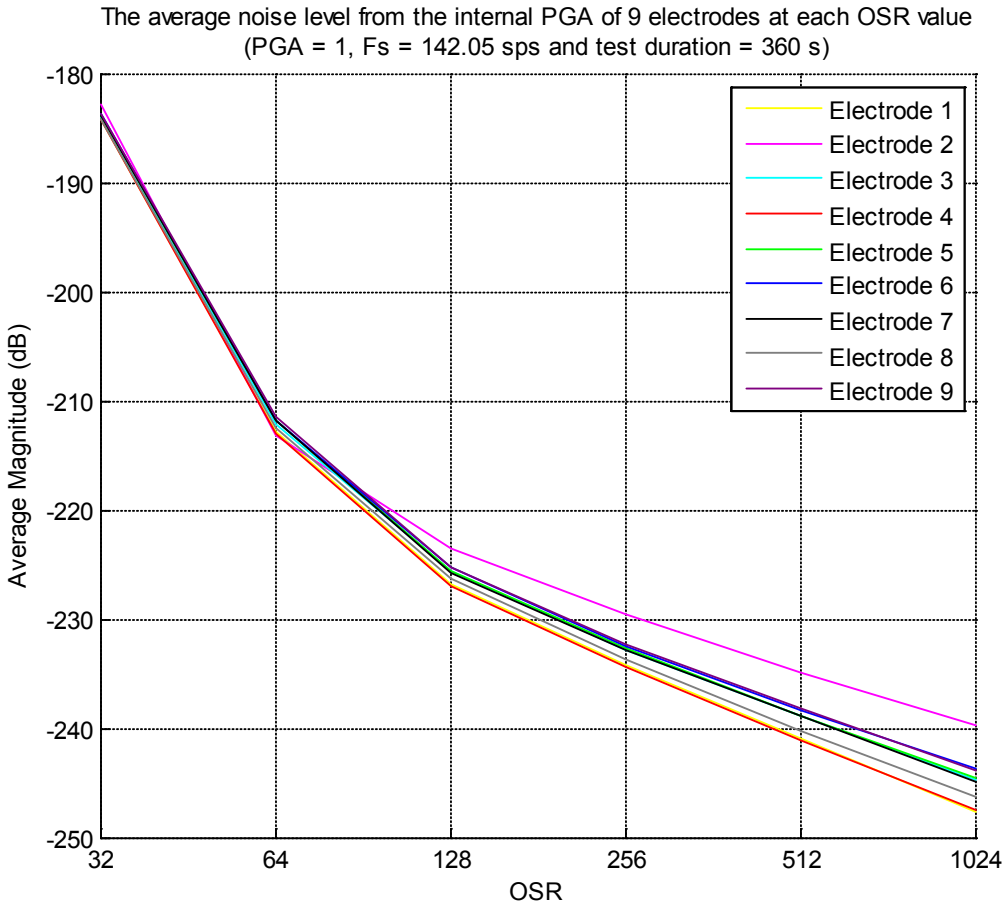

Figure 4.6: A plot of the average noise level from the PGA of nine electrodes. The average noise level decreases and becomes increasingly variable as the value of OSR increases. For each OSR test, the sampling frequency was set as 142.05 Sa/s for a duration of 360 s. The first FFT frequency bin (*i.e.*, DC) has been omitted when calculating the average magnitude at each test.

As expected, the level of noise decreases as the value of OSR (and therefore ADC resolution) increases. Another feature of Figure 4.6 is that the average noise level becomes increasingly variable for higher OSR values, which, although 5 dB or less in

the difference, could indicate performance inequalities between various *WEBS* electrodes.

4.1.2.2 Noise level due to sampling impedances

The ADC sampling stage is essentially a low-pass RC filter in which the resistance comprises the source and sampling resistances (*i.e.*, predominately the impedance at the electrode-skin junction) and the capacitance is dependent on the PGA setting. A change in either one of these factors alters the input characteristics of the ADC. The experiments described in this section are divided into two parts whereby a change in either the source impedance or the sampling capacitance is examined to see the effect on noise level. In each test, comparisons are also given for various values of OSR.

As described in Section 2.2.1, it has been shown that the impedance at the electrode-skin junction on pre-gelled skin can vary from approximately 400 kΩ upon first application to approximately 1.5 kΩ, over the course of a number of days (Grimnes 1983). The first experiment described in this section was performed using these two source impedance (R_S) values (400 kΩ to represent a mediocre electrode-skin connection and 1.5 kΩ to represent a very good one) whilst maintaining the same PGA (and therefore sampling capacitance) value. Conversely, in the second experiment, the source impedance was fixed at 1.5 kΩ and the PGA setting was varied. For each test, the inputs of nine *WEBS* electrodes were connected to ground via individual resistor networks. In order to minimise source resistance variability between electrodes, the test resistances were fine-tuned using a combination of fixed-value resistors along with low-value variable resistors. A 360 s recording was taken simultaneously from all electrodes at a fixed sampling rate of 142.05 Sa/s for all tests independent of OSR setting. A

distance of 20 cm between the *WEBS* slaves and the nearest source of mains interference was maintained throughout testing.

Figure 4.7 and Figure 4.8 show the results from the first experiment illustrating the DFT of the recordings taken at an OSR of 32 and 1024 for both a 400 kΩ and 1.5 kΩ source impedance. For illustrative purposes, the results from a single *WEBS* slave (chosen at random) are shown here. However, Figure 4.7 and Figure 4.8 give a representative view of the similar characteristics of each *WEBS* slave.

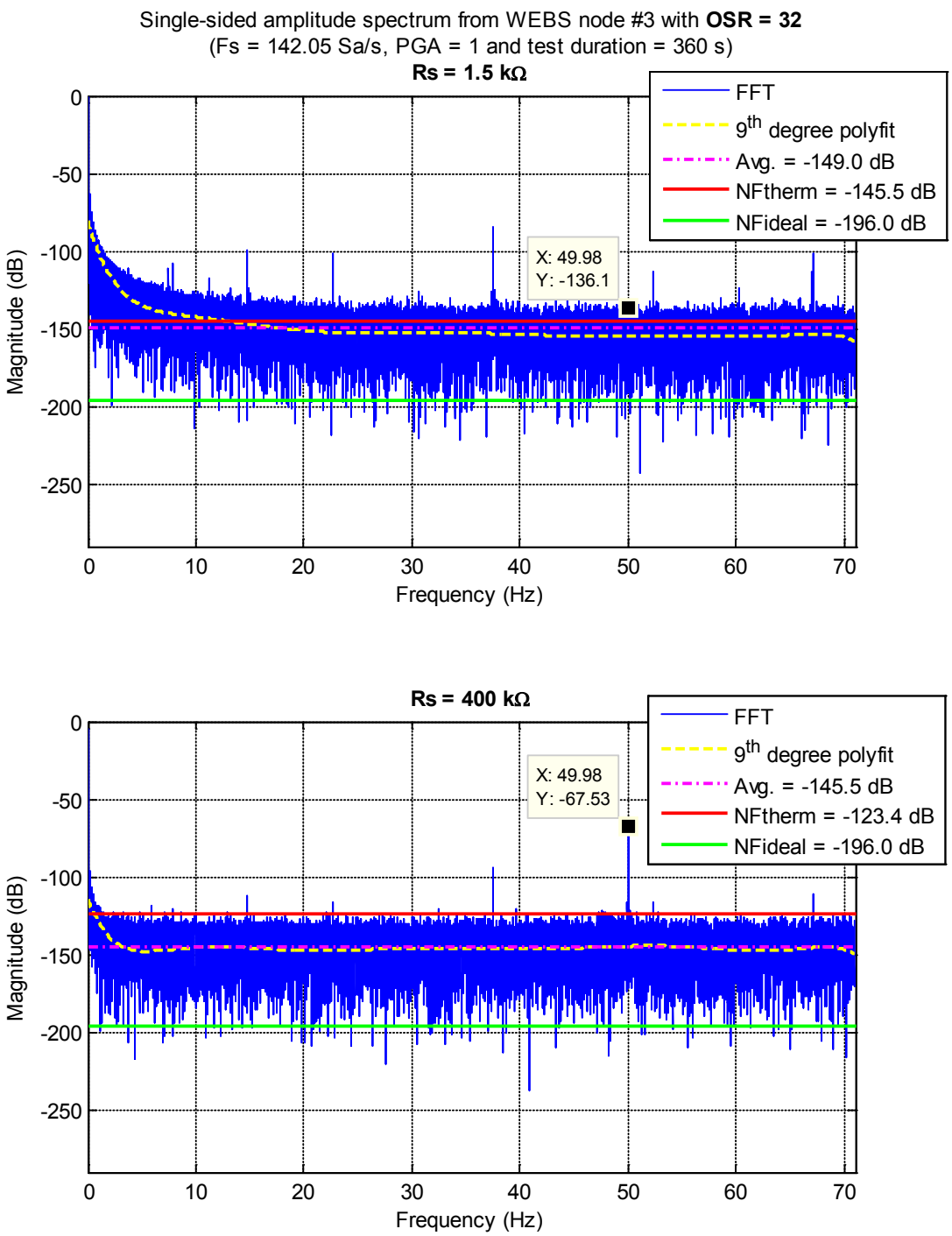

Figure 4.7: The single-sided amplitude spectrum from a sample electrode with OSR of 32 (corresponding to an ADC resolution of 15-bits) over 360 s. The DFT is plotted for two connected source resistances of 1.5 kΩ and 400 kΩ. The magnitude at 50 Hz is highlighted and the values of thermal and ideal noise floors are also illustrated. The first FFT frequency bin (*i.e.*, DC) has been omitted when calculating the average magnitude at each test.

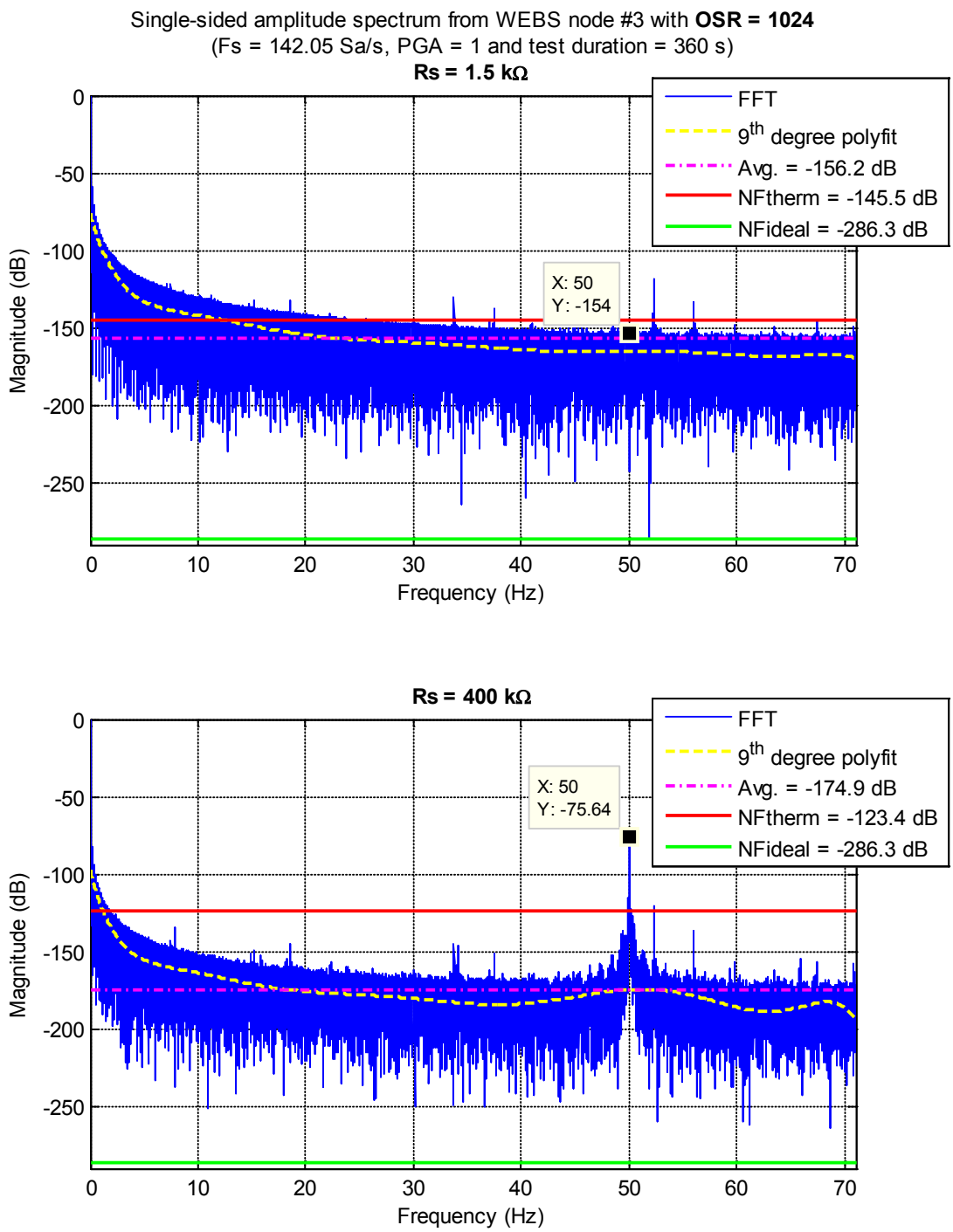

Figure 4.8: The single-sided amplitude spectrum from a sample electrode with OSR of 1024 (corresponding to an ADC resolution of 30-bits) over 360 s. The DFT is plotted for two connected source resistances of 1.5 kΩ and 400 kΩ. The magnitude at 50 Hz is highlighted and the values of thermal and ideal noise floors are also illustrated. The first FFT frequency bin (*i.e.*, DC) has been omitted when calculating the average magnitude at each test.

At the higher value of source impedance, 400 kΩ in Figure 4.7 and Figure 4.8, mains interference at 50 Hz is easily identifiable on the *WEBS* recording. The difference in the level of interference visible at each source impedance value in Figure 4.7 and Figure 4.8 underlines the importance of a stable and low-valued source impedance, specifically with regard to biopotential measurement with the *WEBS*. This can be achieved through proper skin preparation and ensuring minimal motion artefacts during recording. Even using the low source impedance, the thermal noise floor is substantially above the ideal noise floor, indicating that limitations in the existing noise performance lie here rather than in the sample resolution. One point of interest is that the unique ability of the *WEBS* to act not only as a recording electrode, but also as a signal source provides a novel means of characterising the electrode-skin junction impedance. This idea is explored in Section 5.5.

The results of the second experiment are illustrated in Figure 4.9. Each plot line represents the average noise level from each of nine electrodes at each PGA value (up to 16). The source impedance was fixed at 1.5 kΩ and a test was performed at each OSR setting - totalling 30 tests in total for each electrode (5 PGA values and 6 OSR values per electrode).

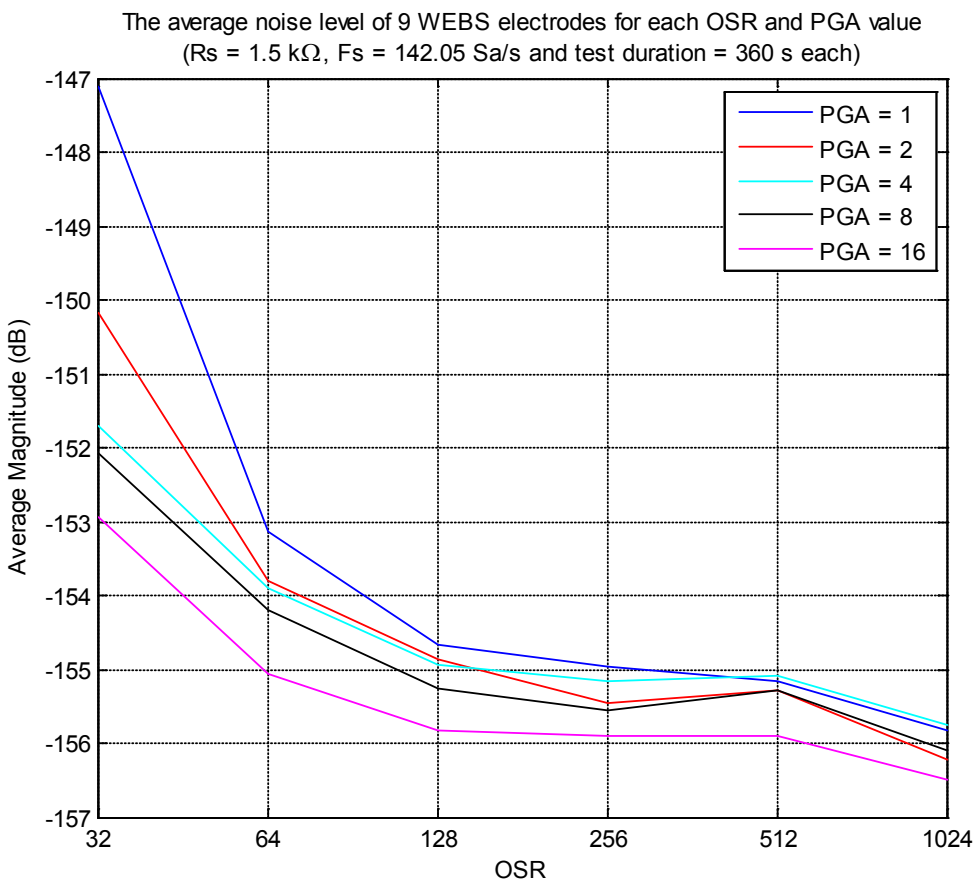

Figure 4.9: A graph of the average noise level of nine *WEBS* electrodes – each with a source impedance of 1.5 kΩ – at each OSR and PGA setting (up to PGA with gain of 16). For each combination of OSR and PGA, totalling 30 tests of duration 360 s each, the average noise level for all nine electrodes was computed from their respective DFTs. This graph indicates that not only does the noise level decrease as the OSR increases, but also as the value of PGA increases. The first FFT frequency bin (*i.e.*, DC) has been omitted when calculating the average magnitude at each test.

As expected, the average noise level decreases noticeably as the OSR increases. Another feature of the graph is that, although less evident, an increase in PGA also reduces the average noise level. It is important to note that it was not possible to obtain a recording with the combination of 1.5 kΩ source impedance and PGA set to a gain of 32 (corresponding to a sampling capacitance of 10 pF). It should be noted that, as these experiments were performed using simplified impedance values, this represents an ideal scenario and does not take into account various circuit dynamics, manufacturing variability of integrated circuits or a change in source impedance due to electrolyte soakage.

4.2 Experiment 2: Comparison between a 3-lead ECG recording of the WEBS system and a commercial biopotential recorder

To demonstrate the applicability of the *WEBS* network to ECG measurement, a series of tests were undertaken comparing its performance to that of a commercially available precision biopotential recording system, the BioSemi ActiveTwo. A 3-lead ECG measurement was performed on a subject using each system. The *WEBS* set-up consisted of four electrodes: three unipolar measuring electrodes (left arm, right arm and left leg) and one electrode connected to the right leg and configured as a low-impedance connection to the body, *i.e.*, circuit ground. The BioSemi ActiveTwo set-up was similar except that, as necessitated by the device, the low-impedance connection to the body was replaced by two electrodes in close proximity - a common-mode sense electrode and an active driven-right-leg electrode.

The individual systems were tested separately and the two sets of results were subsequently compared. Although this method of experimentation prohibits direct comparison of individual ECG complexes from the two systems, the separate (identical) experiments ensured that the systems would not interfere with each other's measurements. As the BioSemi ActiveTwo includes an active driven-right-leg electrode, this could significantly influence the normal *WEBS* measurement.

The difference between each test discussed in this section is in the distance between the subject and the mains supply. In the first test, the subject was positioned 1 m away from nearest source of mains interference (a mains supply socket that was powering equipment used in the experiment). The second test aimed to highlight the deficiencies of both systems in a non-ideal scenario. For this reason, the measurement

equipment (*WEBS* master and BioSemi AD-box) were placed in the immediate vicinity of an AC mains current carrying wire and a noise comparison of the recorded signals is described in this section. Ethical approval was granted for this experiment (DIT reference number: 18/08) and the test subject gave informed consent.

The test subject, a healthy male (age, 29; height, 180 cm; weight, 85 kg), was placed in a relaxed seated position so that there would be minimal movement during testing. The skin-surface test locations were prepared as described previously in Section 3.4. The *WEBS* system utilised standard button clip electrodes whilst the BioSemi ActiveTwo required its own active electrodes. The arm electrodes were placed on the skin surface avoiding thick muscle underneath. The leg and reference electrodes were placed on each calf muscle. On each limb, the locations used for the two systems' electrodes were 2.5 cm apart. This was done to prevent longer exposure of the skin to electrolyte gel from biasing the electrode skin junction impedance experienced by the second system's electrode (*N.B.*, the electrodes were not attached at the same time). In each test (normal and in the presence of noise), recordings of duration 360 s were taken for each system. Figure 4.10 illustrates the wiring configuration used for the *WEBS*.

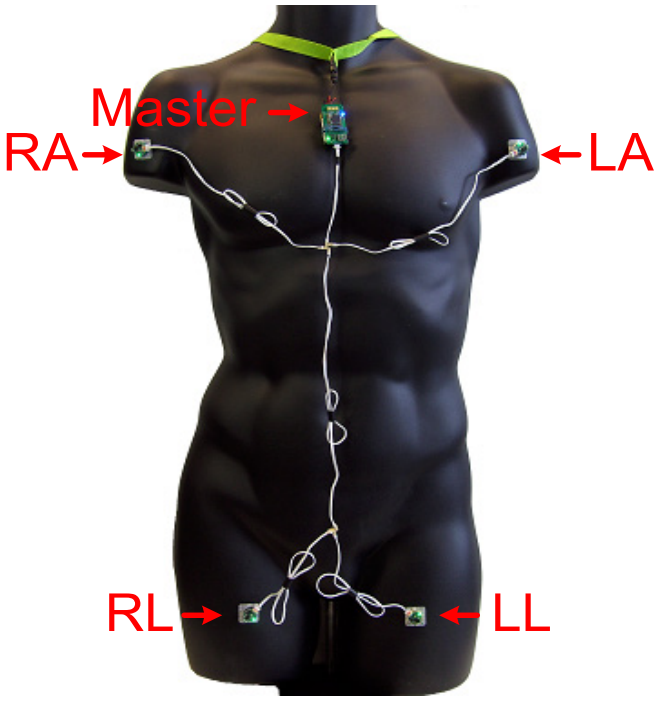

Figure 4.10: The *WEBS* wiring configuration used during the 3-lead ECG measurement. The actual location of each of the leg electrodes, RL and LL, was on the calf muscle. The arm electrodes, RA and LA, were positioned on the skin-surface, avoiding thick muscle. A single digital-bus wire connected each of the slave electrodes. The BioSemi ActiveTwo electrodes were placed in similar positions on the respective limbs, 2.5 cm away from the *WEBS* measurement locations.

The sampling rate of the *WEBS* system was set at 190.55 Sa/s in the highest resolution setting of 30-bits with an OSR of 1024 and gain setting of 1 over an input voltage range of ± 600 mV. The sampling rate of the BioSemi ActiveTwo was 2048 Sa/s with an inherent 24-bit resolution over an input voltage range of ± 262.144 mV. During analysis, the following equations were used to calculate the bipolar limb leads that form Einthoven's triangle.

$$Lead\ I = Left\ Arm - Right\ Arm \tag{4.7}$$

$$Lead\ II = Left\ Leg - Right\ Arm \tag{4.8}$$

$$Lead\ III = Left\ Leg - Left\ Arm \tag{4.9}$$

4.2.1 Test 1: 3-lead ECG under normal conditions

As stated previously, throughout test 1, the subject and all measurement equipment (connected electrodes, the *WEBS* master and the BioSemi AD-box), were situated 1 m away from nearest mains supply source. The 360 s recording from each system was plotted in MATLAB on the same time axis and Figure 4.11 illustrates an excerpt from this in which three sequential ECG complexes are shown. Throughout the 360 s test duration, each set of data contained both varying DC offset (*e.g.*, 0.3 mV – 7.1 mV for Lead I) and heartbeat rate (54 bpm – 66 bpm). To facilitate visual comparison, the windows of data shown in Figure 4.11 have been chosen such that the sequences of ECG complexes are similar. A constant DC offset was added to each of the BioSemi limb lead signals for simplified graphical representation. A second-order IIR notch filter, with a quality factor of 35 at 50 Hz, has been applied to the *WEBS* data whilst the BioSemi data is the raw, unfiltered output from the BioSemi ActiView acquisition program.

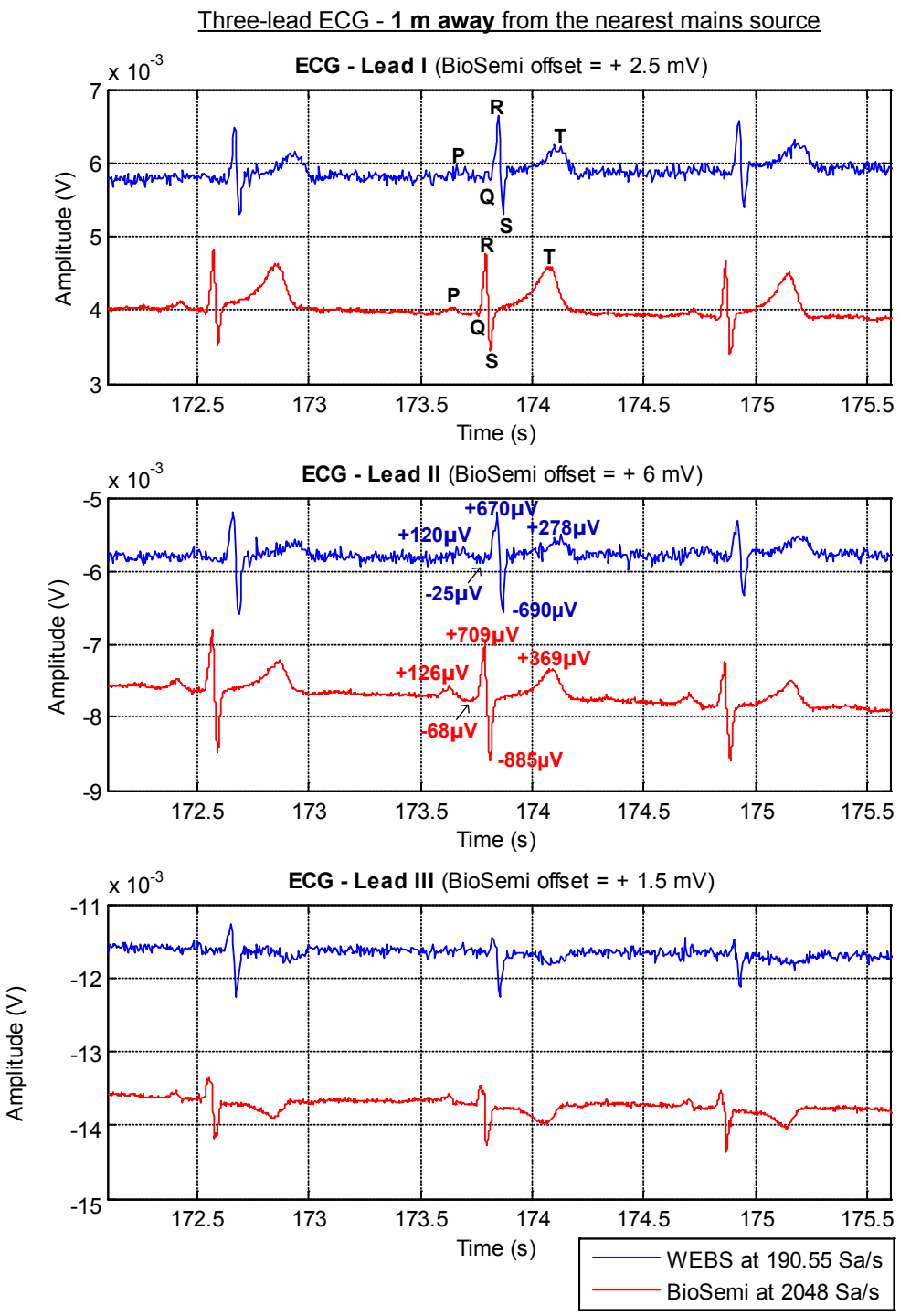

Figure 4.11: A time-domain comparison of three sequential cardiac cycles from a 3-lead ECG recording by the *WEBS* and BioSemi ActiveTwo devices. In this test, the subject and both systems were situated 1 m away from the nearest mains power source. A second-order IIR notch filter, with a quality factor of 35 at 50 Hz, has been applied to the *WEBS* data whilst the BioSemi signals are unfiltered. Example deviations from the DC offset for one ECG complex are indicated. Note that to eliminate the chance of each system interfering with the other, the test on each system was performed at separate times and therefore the signals are not expected to be identical. The purpose of this plot is to facilitate a general comparison between the two systems. For illustrative purposes, a constant DC offset voltage has been added to each of the BioSemi signals.

As can be seen, the low-cost *WEBS* system performs well against the high precision BioSemi ActiveTwo. Although the BioSemi signals are cleaner, the ECG complex features, PQRST, are all clearly identifiable in the *WEBS* signals. The amplitudes of each limb lead signal closely match each other. In this example, the Q deflections of the BioSemi's ECG are distinctly more noticeable at 2.72 times the size of the corresponding *WEBS* recorded deflection. This is compared with the S deflection at 1.28 and the T deflection at 1.33 times the size. The P and R deflections are closest in range, both are 1.05 times bigger for the BioSemi. Any discrepancies can be attributed to variation in different heartbeats or by variations in the individual *WEBS* slave's PGA that have not been accounted for in this experiment.

To investigate the noise contained in the recordings and see if further digital filtering might improve the quality of the *WEBS* data, the power spectral density (PSD) was calculated using the short-time Fourier transform on the signal from an example electrode in each test system. This calculation was performed using the MATLAB '*spectrogram*' command, which calculates the short-time Fourier transform over a rolling Hamming window. Figure 4.12 shows the resulting spectrogram from the calculated PSD for each window. In this figure, the full-range spectrograms of the (a) BioSemi and (c) *WEBS* are shown. For comparison, (b) shows a magnified view of the BioSemi spectrogram. For (a) and (c), a Hamming window of 256 data points was chosen with a window overlap of 240 and an FFT length of 256. It was found that these specifications produced a satisfactorily high output resolution in both time and frequency with minimal noise introduced from the Hamming window. To increase the resolution for (b), each of the windowing properties was multiplied by a factor of 10 (*i.e.*, corresponding to the approximate increase in sampling frequency between the *WEBS* and BioSemi recordings).

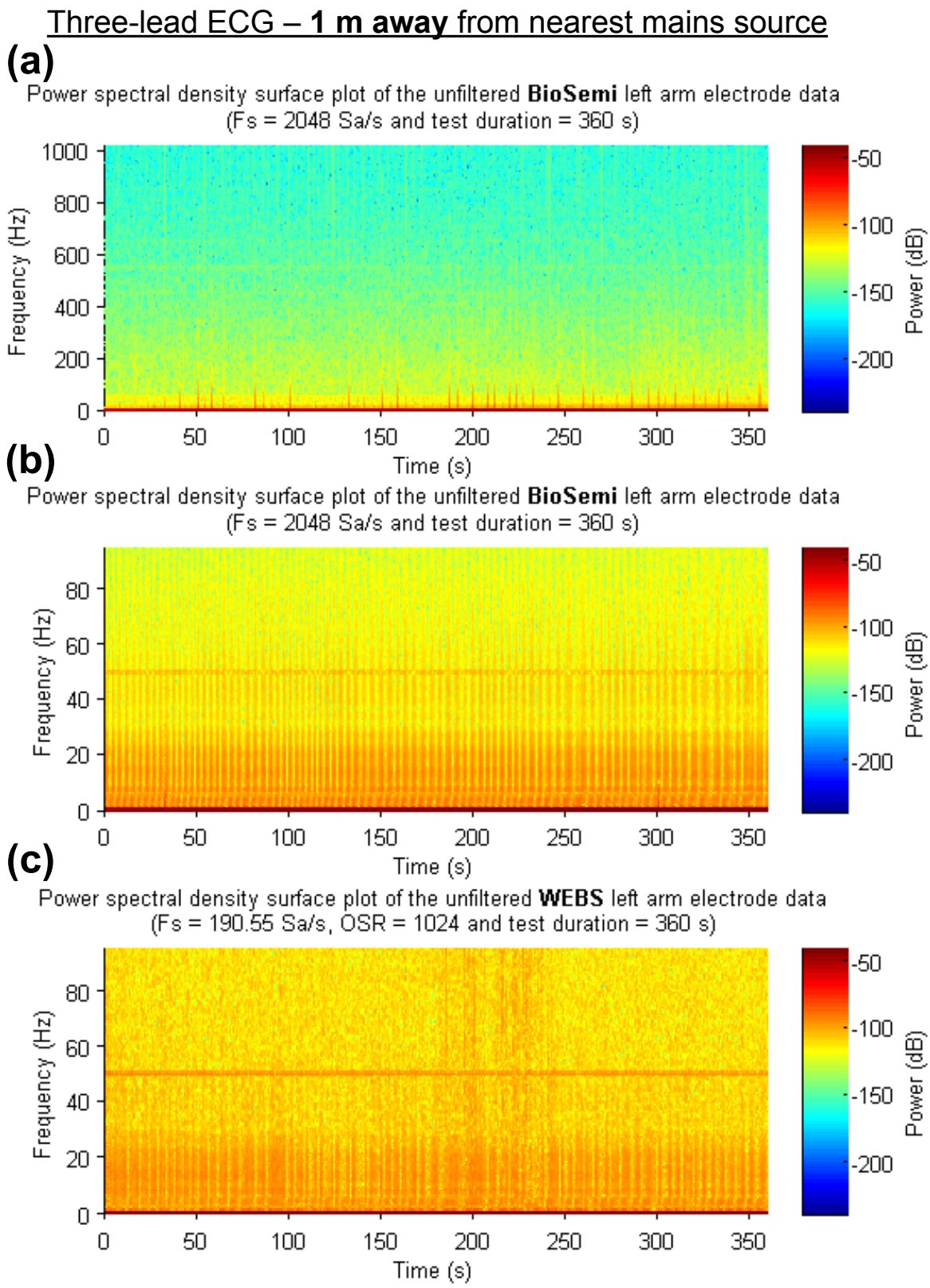

Figure 4.12: Spectrograms of the power spectral density for the unfiltered left arm electrode data from the *WEBS* and BioSemi ActiveTwo systems. In this test, the subject and both test systems were situated <u>1 m away from the nearest mains power source</u>. For (a) and (c), the power spectral density was calculated using the short-time Fourier transform over a Hamming window of 256 with an overlap of 240 and an FFT length of 256. To obtain a higher resolution in (b), each windowing property was multiplied by 10.

At first glance, the *WEBS* recording appears to contain a significantly higher noise component then that of the BioSemi. However, it is important to compare the *WEBS* recording over the corresponding frequency range in the BioSemi data. Upon doing so, it is evident that, although the *WEBS* recording is somewhat noisier (≤ 20 dB in the difference), the BioSemi recording also contains significant activity below 100 Hz. Mains interference is visible on both spectra at 50 Hz and mains harmonics are also visible in the BioSemi signal at 450 Hz, 550 Hz and 650 Hz. Intervals of increased noise between 0 Hz and 30 Hz can also be seen in the *WEBS* spectrum. A closer inspection of the BioSemi data indicates a similar phenomenon in the sub 30 Hz range. A possible explanation for this feature is due to QRS complexes falling in or out of the Hamming window. Motion artefacts are possibly the cause of the increase in noise activity in the *WEBS* data set between 175 s and 250 s. As the design of the *WEBS* slave electrode does not include a high-impedance input stage, the sensor is sensitive to changes in source impedance, which is predominately attributed to electrode movement. However, the spectrum for the BioSemi also contains sporadic 'spikes' of noise, particularly below 200 Hz. Further investigation by using the *WEBS's* on-board accelerometers could in the future be used to investigate this hypothesis. Sources of electrical interference from the surrounding environment that could be manifested in the ECG recordings include air conditioning systems, lab equipment, computer fans, fluorescent lighting, *etc.* (Webster 1977).

The discrete Fourier transform (DFT) was calculated in MATLAB using the fast Fourier transform (FFT) algorithm on the unfiltered left arm electrode data in each system and Figure 4.13 illustrates the single-sided amplitude spectrum of the output results.

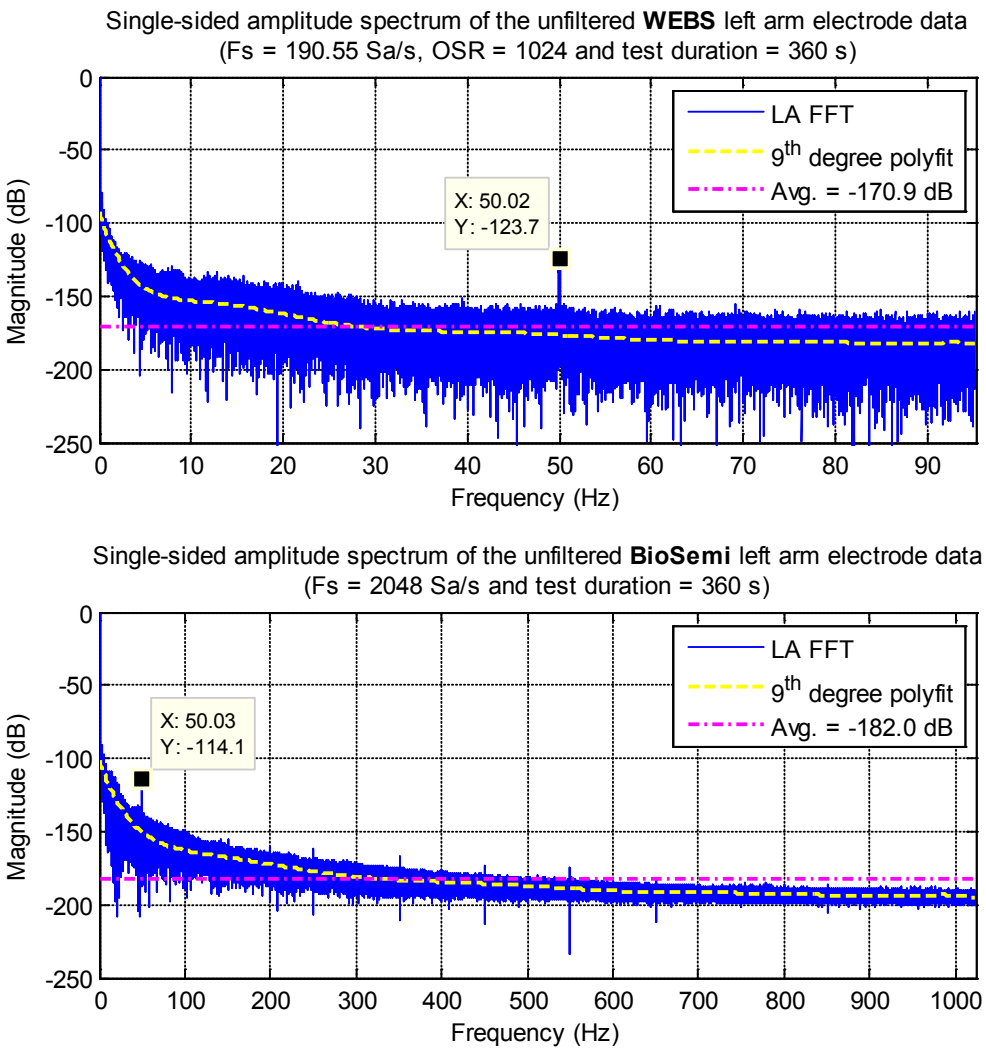

Figure 4.13: The single-sided amplitude spectra of the unfiltered left arm electrode data for the *WEBS* and BioSemi ActiveTwo systems. In this test, the subject and both systems were situated 1 m away from the nearest mains power source. The DFT was calculated in MATLAB using the FFT algorithm. The average magnitude level and a 9th order polynomial fitted line are also shown. Pointers mark the magnitude of 50 Hz mains interference recorded by each system. The first FFT frequency bin (*i.e.*, DC) has been omitted when calculating the average magnitude at each test.

A comparison of both graphs, up to the 95 Hz Nyquist sampling frequency of the *WEBS*, gives further evidence that the *WEBS* data contains more noise than that of the BioSemi. For example, at 90 Hz the *WEBS* data varies by up to 64.1 dB and whilst the BioSemi varies by 13.2 dB. Past the maximum sampling frequency of the *WEBS*,

the BioSemi has a narrow spectrum varying by 7.3 dB at 900 Hz with low magnitude mains harmonics visible up to 850 Hz.

In this example, the magnitude difference at 50 Hz between each test system seems to indicate that the *WEBS* rejects more mains interference then the BioSemi. This is possibly due to the elimination of analog voltage carrying wires from the system. The difference in the average magnitude level of 11.1 dB between the two graphs indicates that the BioSemi is, overall, better at rejecting interference. However, this averaging calculation was performed over different frequency ranges – as limited by the Nyquist sampling frequency for each system – and should be taken into account.

4.2.2 Test 2: 3-lead ECG in the presence of a high level of mains power supply interference

As described previously, the second test aimed to highlight deficiencies in the *WEBS* under a worst-case scenario of operation in an environment with a high-level of electrical interference. In this test, the *WEBS* master and BioSemi AD-box were positioned on top of an AC mains current carrying wire supplying approximately 140 W to a powered-on LCD monitor, the NEC LCD3215. All other experimental procedures and subsequent data analysis steps, as carried out previously in test 1, were maintained. Figure 4.14 illustrates a time-domain comparison of three ECG complexes as recorded by the *WEBS* and the BioSemi ActiveTwo.

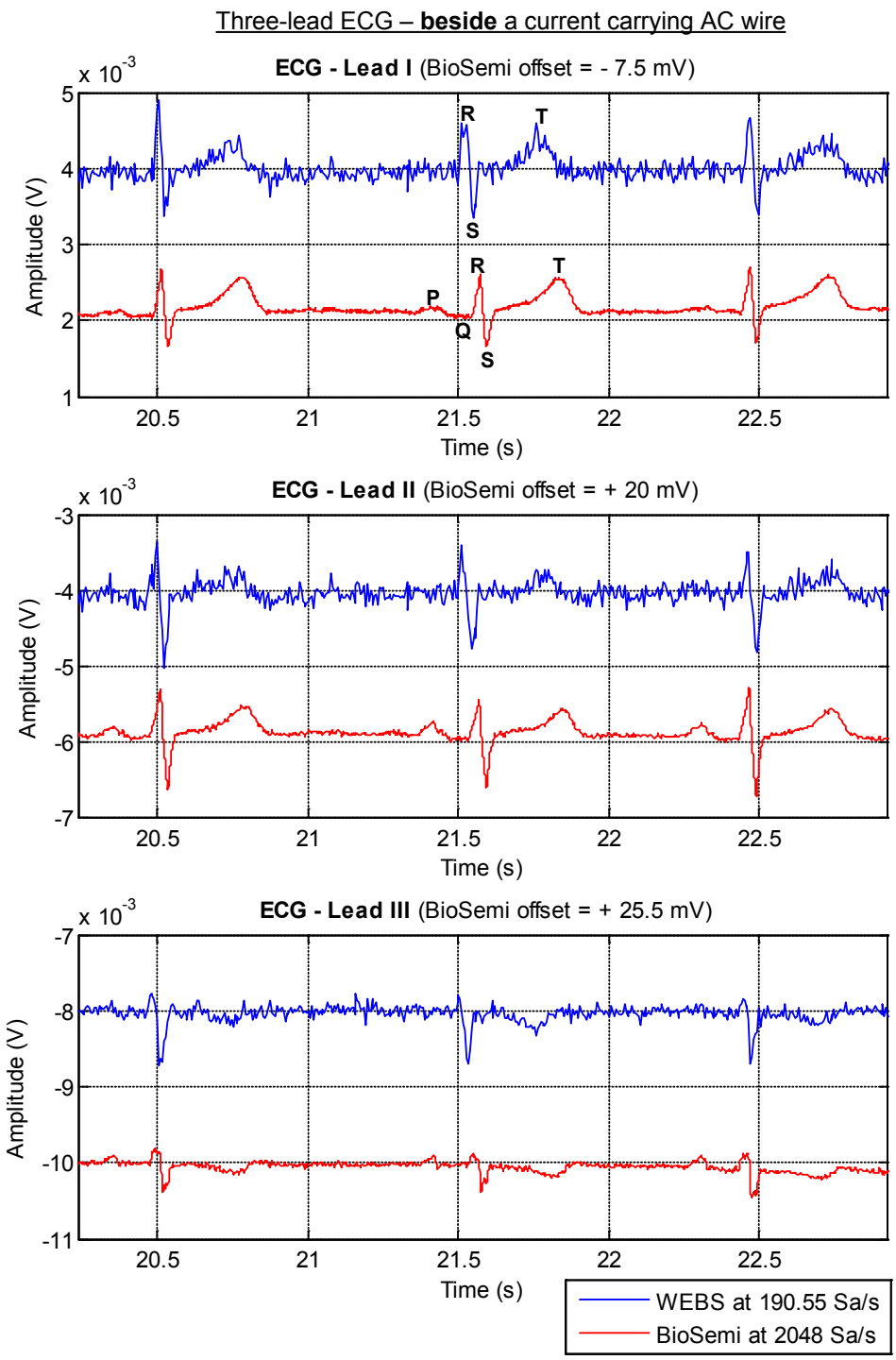

Figure 4.14: A time-domain comparison of three sequential cardiac cycles from a 3-lead ECG recording by the *WEBS* and BioSemi ActiveTwo devices. In this test, the *WEBS* master and BioSemi AD-box were positioned <u>on top of an AC mains current carrying wire</u> in order to intentionally expose the system to interference. A second-order IIR notch filter - with a quality factor of 35 at 50 Hz - has been applied to the *WEBS* data whilst the BioSemi signals are unfiltered. Mains interference is visible on both recordings but in particular from the *WEBS* system. Note that to eliminate the chance of each system interfering with the other, the test on each system was performed at separate times and therefore the signals are not expected to be identical. The purpose of this plot is to facilitate a general comparison between the two systems. For illustrative purposes, a constant DC offset voltage has been added to each of the BioSemi signals.

As shown in Figure 4.14, even after a 50 Hz notch filter has been applied to the *WEBS* ECG recording, noise is clearly visible in the *WEBS* recording whilst the BioSemi signal is significantly less affected. The PQRST waves of the ECG complex are still clearly distinguishable from BioSemi signal whereas although the QRS complex and T wave remain visible in the *WEBS* recording, the P wave is no longer identifiable. Further analysis, by means of the PSD surface plot, as shown in Figure 4.15, yields additional information on the spectral components of each signal.

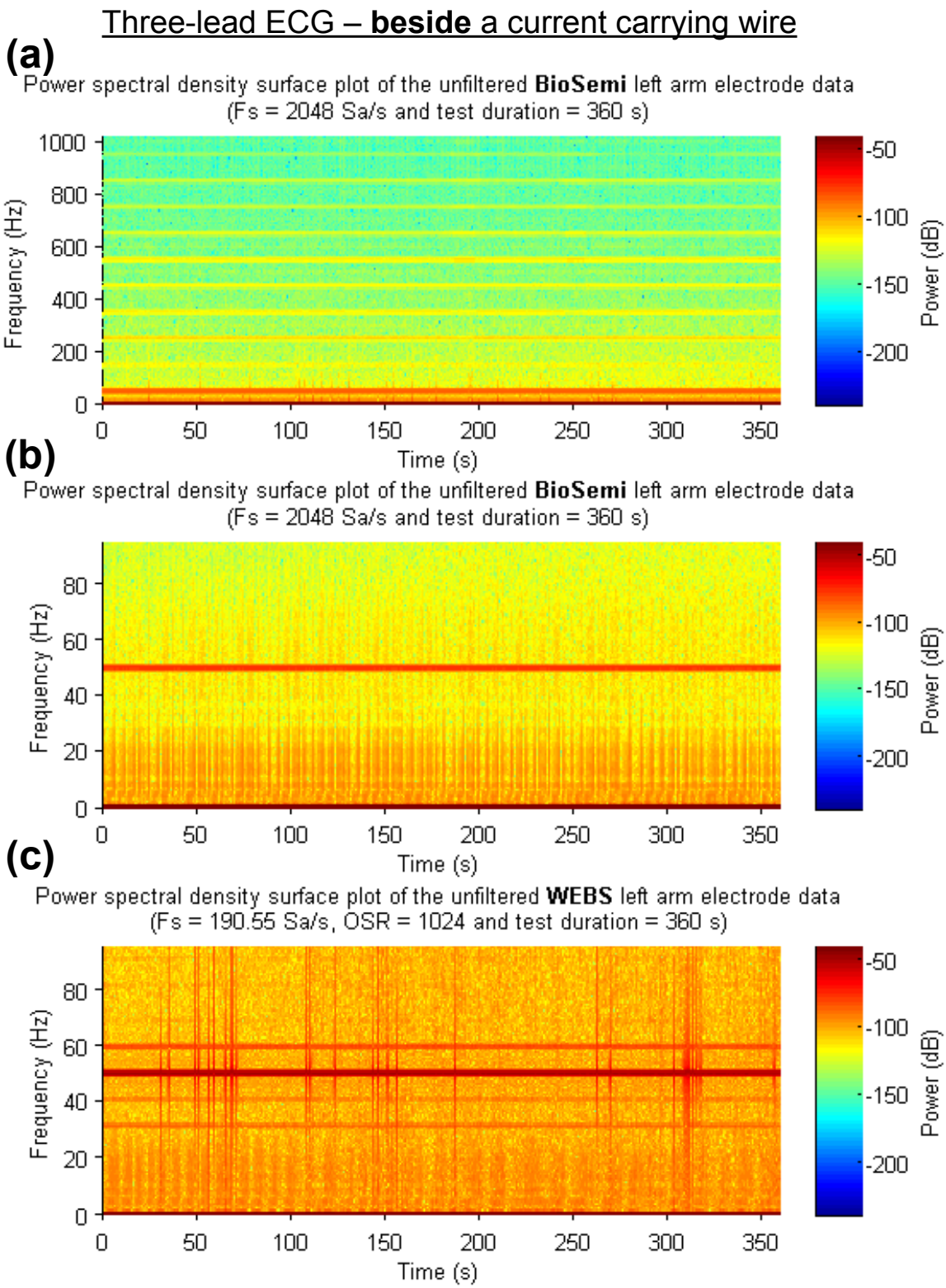

Figure 4.15: Spectrograms of the power spectral density for the unfiltered left arm electrode data from the *WEBS* and BioSemi ActiveTwo systems. In this test, the *WEBS* master and BioSemi AD-box were positioned <u>on top of an AC mains current carrying wire</u>. The mains wire supplied power to a monitor with a refresh rate of 60 Hz and this interference, along with the mains, is observable here. For (a) and (c), the power spectral density was calculated using the short-time Fourier transform over a Hamming window of 256 with an overlap of 240 and an FFT length of 256. To obtain a higher resolution in (b), each windowing property was multiplied by 10.

Upon comparison of Figure 4.15 to Figure 4.12, an increase in the power spectral density of approximately 40 dB/Hz at 50 Hz can be noted between each *WEBS* recording. However, this comparison also shows that the BioSemi recording is also significantly affected by the presence of mains interference. Mains frequency harmonics are present at every 50 Hz increment up to 1 kHz. Concurrently, a general increase in the background noise magnitude intensity is visible up to approximately 600 Hz. It should be noted that as the monitor refresh rate is set at 60 Hz, this appears as an increase in the power spectral density at 60 Hz, which is particularly visible in the *WEBS* recording. The interference at 30 Hz, 40 Hz, 80 Hz and 90 Hz could be caused by other sources of interference such as monitor-related electronics, fluorescent room lighting or air conditioning fans.

The amplitude spectra illustrated in Figure 4.16 further highlight the susceptibility of the *WEBS* to mains interference. Whereas the right-leg driver within the BioSemi system actively drives down common-mode signal in the subject, the *WEBS* system currently has no such feature. In close proximity to a mains source, the BioSemi is almost twice as effective at rejecting 50 Hz noise compared to the *WEBS* system - from approximately -26.89 dB to -57.29 dB taking into account different frequency bins.

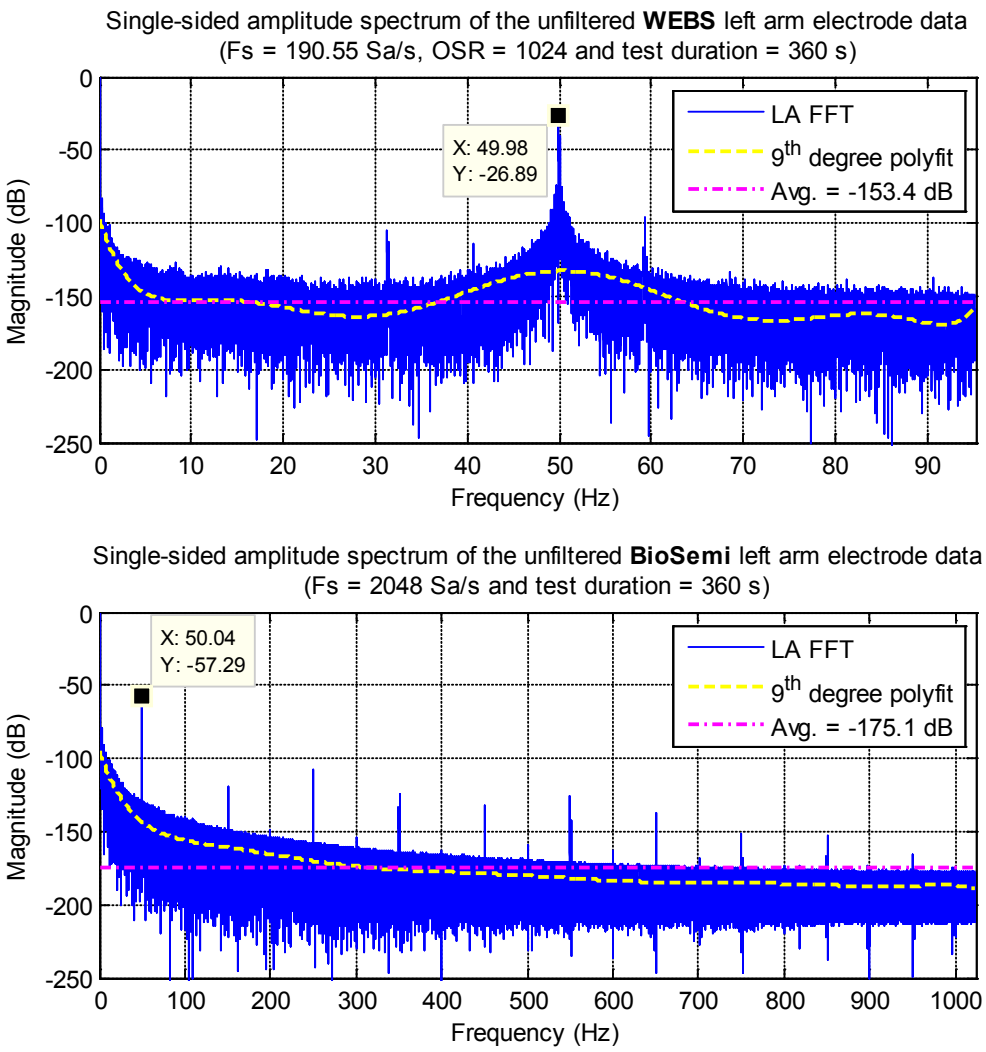

Figure 4.16: The single-sided amplitude spectra of the unfiltered left arm electrode data for the *WEBS* and BioSemi ActiveTwo systems. In this test, the *WEBS* master and BioSemi AD-box were positioned <u>on top of an AC mains current carrying wire</u>. The DFT was calculated in MATLAB using the FFT algorithm. The average magnitude level and a 9th order polynomial fitted line are also represented. Pointers mark the magnitude of 50 Hz mains interference recorded by each system. Significant mains interference is visible in both test device recordings. The first FFT frequency bin (*i.e.*, DC) has been omitted when calculating the average magnitude at each test.

4.3 Experiment 3: Comparison between EOG recordings from the WEBS system and a commercial biopotential recorder

As described in Section 2.2.1, the electrooculogram (EOG) is an easily detectable biopotential signal that exhibits a high degree of voluntary conscious control and facilitates a high-bandwidth communication channel between the human brain and the outside world. As such, it has numerous potential applications in HMI and assistive technology. Therefore, EOG constitutes an interesting target for testing the capabilities of the *WEBS*. With this in mind, an experiment was devised to compare gaze position measurement from the *WEBS* to a commercially available BioSemi ActiveTwo biopotential acquisition device. Using an approach similar to that described in Section 4.2, the EOG experiment was performed separately on each test system to avoid one biasing the other. The results from the two systems were subsequently analysed in MATLAB. The electrodes were positioned as illustrated in Figure 4.17. Vertical EOG activity was calculated from the difference between the unipolar electrodes labelled V+ and V-, horizontal activity from the unipolar electrodes H+ and H- and finally a low-impedance connection electrode (*i.e.*, circuit ground) positioned behind the ear on the mastoid process.

$$Vertical\ EOG = V_{+} - V_{-} \tag{4.10}$$

$$Horizontal\ EOG = H_{+} - H_{-} \tag{4.11}$$

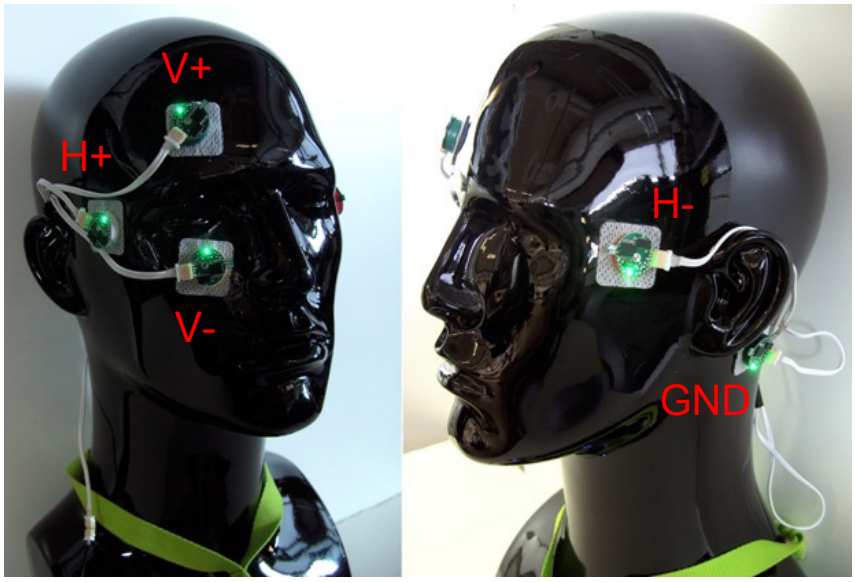

Figure 4.17: An illustration of the *WEBS* electrode placement for EOG measurement. Vertical EOG activity is the calculated difference between the unipolar electrodes V+ and V- whilst horizontal EOG activity is the calculated difference between the H+ and H- unipolar electrodes. A fifth electrode positioned behind an ear on the mastoid process acts as a low-impedance connection to the body. As illustrated, all *WEBS* electrodes share a single digital communication bus. In the case of the BioSemi ActiveTwo, the corresponding electrodes were placed in the same locations as those illustrated here.

As the available skin-surface area at the selected points on the head is limited, and the physical electrodes are relatively large, it was necessary to position the EOG electrodes on the same locations for each test system. Therefore, to ensure an unbiased experiment, a 24 hr interval between tests was observed to allow the epidermis to regenerate. The electrodes were applied in the same manner as described in Section 4.2: the electrode locations were prepared with 20 unidirectional strokes of an electrode preparation pad; a pea-sized drop of electrolyte gel applied to each electrode; and a 20 minute rest time was allowed for electrolyte gel soakage. Figure 4.18 illustrates the EOG experimentation configuration.

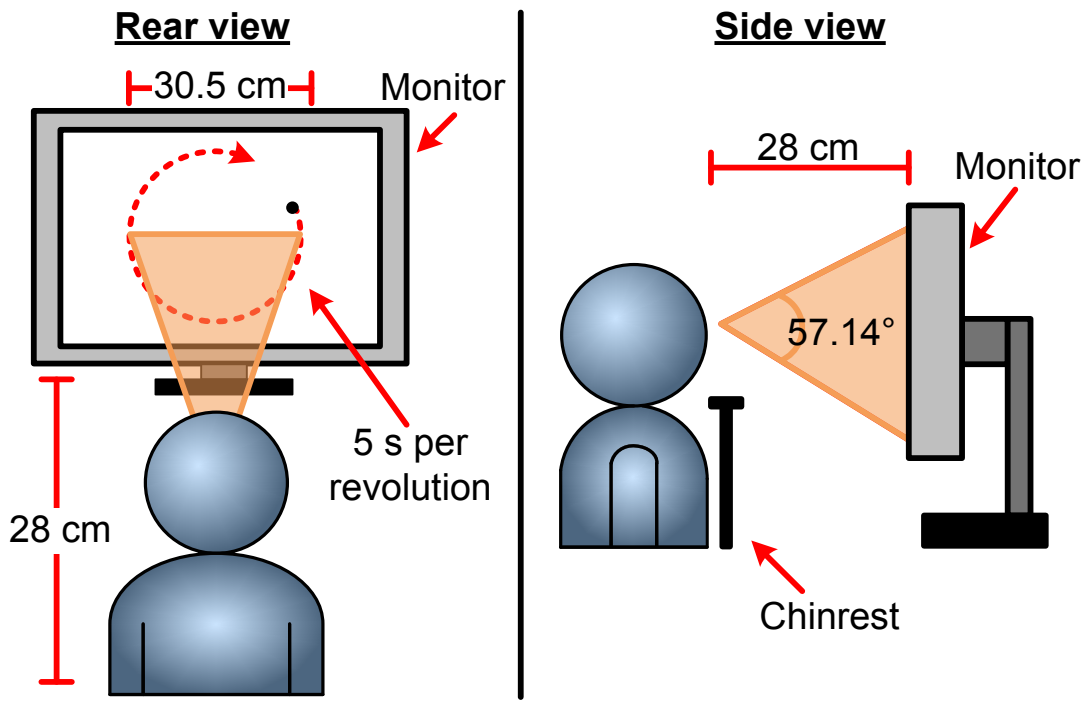

Figure 4.18: A diagram illustrating the EOG experimentation set-up. The subject's head rested on an adjustable chinrest that helped maintain a fixed position and distance between the subject's head and the centre of the monitor. A sequence of stimuli were shown to the subject on the monitor to elicit a response in the EOG. An example stimulus is shown here whereby a black dot rotated 360º around the monitor centre point resulting in both horizontal and vertical EOG activity. The full test was performed separately on the *WEBS* and BioSemi ActiveTwo systems.

The subject, a healthy male (age, 29; height, 180 cm; weight, 85 kg), was placed in a relaxed seated position with his head resting on an adjustable chinrest. The height of the chinrest was altered so that the subject's eye level was directly in line with the centre of the monitor. A distance of 28 cm was maintained between the subject's eyes and the monitor, which corresponded to a stimulus viewing angle of 57.14º. This angle was chosen as it adequately covered a sufficient field of view size for the subject whilst being within the approximately linear range of the EOG. The EOG is generally assumed to have a linear relationship to gaze position over a range of ± 30º (Simini *et al.* 2011). An additional consideration, which this angle accommodated, was to limit the strain imposed on the subject's eyes during testing. Ethical approval was granted for this

experiment (DIT reference number: 18/08) and the test subject gave informed consent. Figure 4.19 illustrates the EOG stimulus sequence.

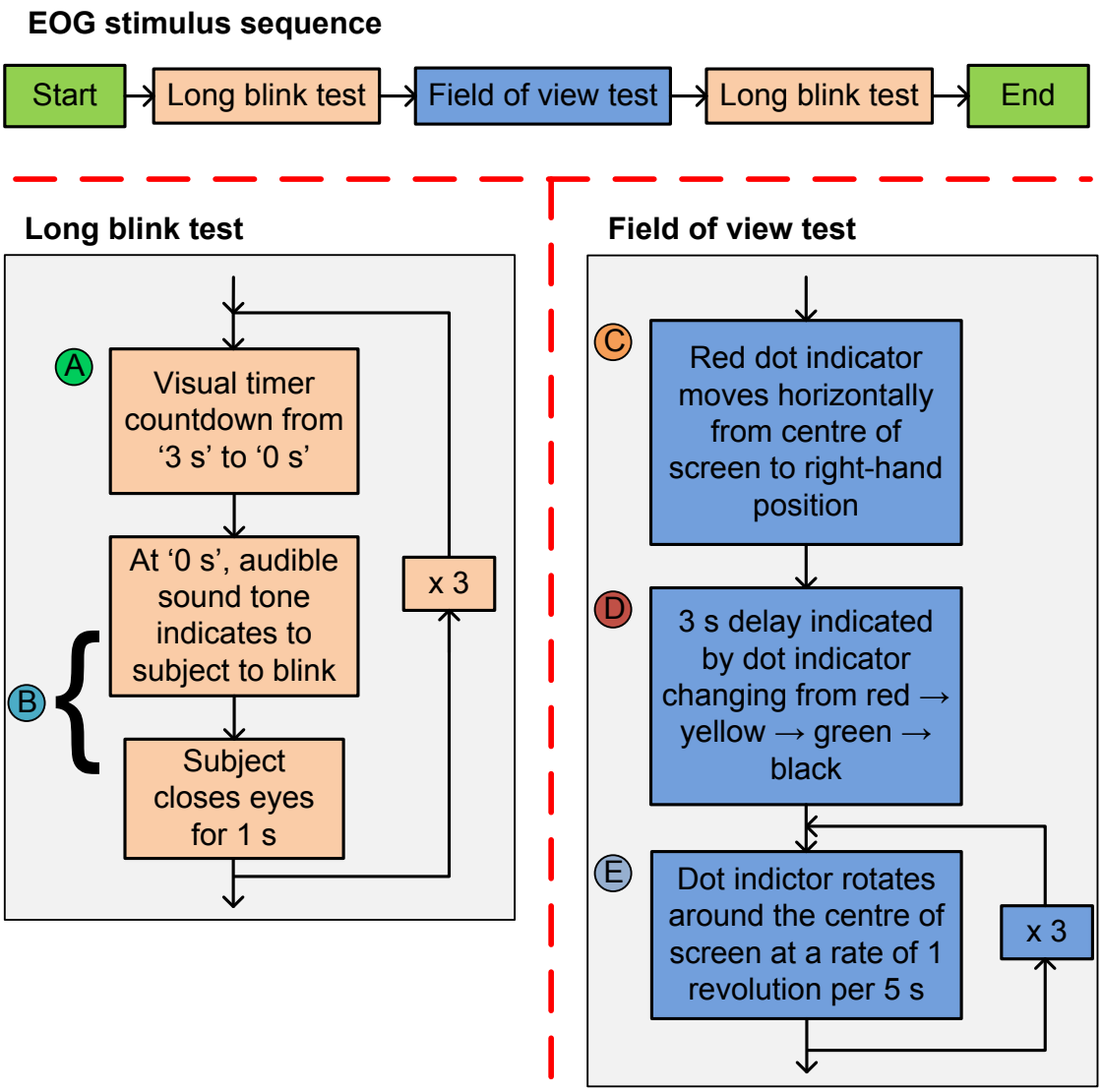

Figure 4.19: A flowchart of the EOG stimulus sequence. The sequence consisted of two unique stimuli titled the 'long blink test' and the 'field of view' test and a flowchart is illustrated for each one. The blink test was used as a marker to indicate the start and end of the testing sequence so that the results from the *WEBS* and the BioSemi could be subsequently aligned post-testing. Alphabetic markers indicate the various test stages.

The EOG stimulus design had two aims. The first aim was to measure the accuracy of the EOG as measured by the *WEBS* and the BioSemi ActiveTwo. This was achieved by, what has been titled in Figure 4.19, the 'field of view' test. A small dot rotated 360º around the centre point of the screen at a fixed viewing angle of 57.14º.

This was repeated successively for three full rotations at a rate of 5 s/rev. The second aim was to provide a means of direct comparison between the two systems during subsequent analysis. For this reason, before and after the 'field of view' test, the subject was prompted to perform a 'long blink' of 1 s duration, three times with a 3 s interval between blinks. A visual countdown timer counted down from 3 s to 0 s and, on the 0 s indicator, a 1 s long audible beep was played to the subject to indicate the duration for which the subject should close his eyes. These 'long blinks' produced a distinct change in vertical EOG activity and facilitated an almost exact alignment of the *WEBS* and BioSemi ActiveTwo datasets, as illustrated in Figure 4.20. A Butterworth low-pass filter at 40 Hz has been applied to *WEBS* data. For illustration purposes, the corresponding mean values have been subtracted from each of the *WEBS* and BioSemi's vertical and horizontal EOG signals and a 1.5 mV offset has been added to the BioSemi signals.

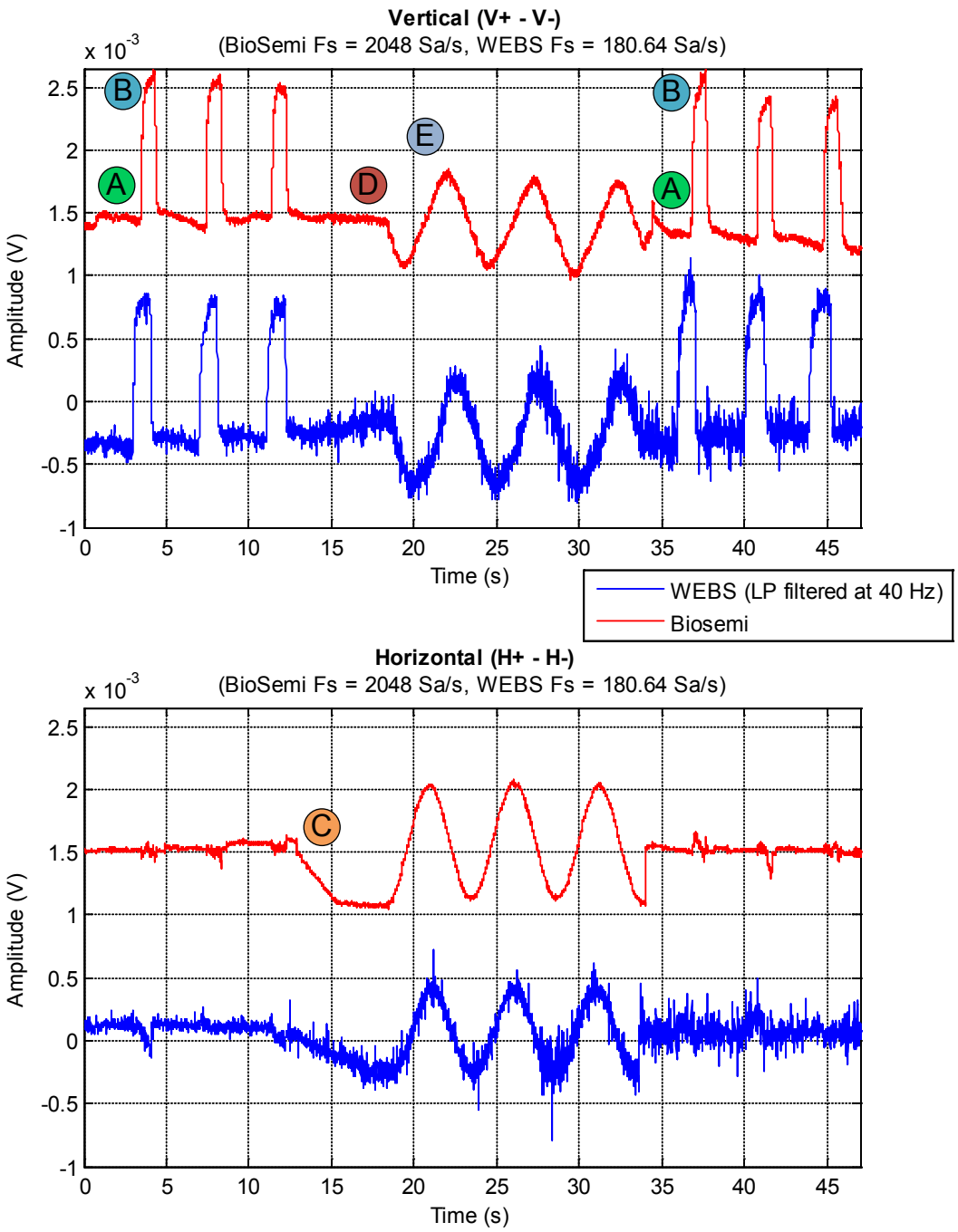

Figure 4.20: Graphs illustrating EOG recorded by the *WEBS* and BioSemi ActiveTwo devices. Two different visual stimuli were displayed to a subject on a monitor whilst EOG was recorded. The long-blink stimulus was used at the start and end of the test to facilitate synchronisation of datasets during analysis and consisted of a 3 s countdown timer at the end of which the subject was instructed to close his eyes for 1 s. The field-of-view stimulus consisted of a small black dot rotating in a circular fashion around the screen centre point at a rate of 5 s/rev. Alphabetic markers indicate the various test stages. A Butterworth low-pass filter at 40 Hz has been applied to the *WEBS* data. For illustration purposes, the mean voltage has been subtracted from both the *WEBS* and BioSemi signals and a constant 1.5 mV offset voltage has been added to each of the BioSemi signals.

As anticipated, the *WEBS* EOG signal contains a bigger noise component than that of the BioSemi. This can be attributed primarily to the lower common-mode rejection of the current *WEBS* system - unlike the BioSemi which has high impedance input buffers and a right-leg driver. Therefore, the potential benefits of software filtering are more significant in the *WEBS* in order to remove electrical interference induced in the subject and the measurement equipment.

The results from this experiment indicate that the *WEBS* system is very capable of measuring EOG. However, due to the level of noise present, the ability for saccade and blink detection is somewhat reduced in comparison with the BioSemi, a high-precision measurement system. In this test, the average resolution of the vertical and horizontal EOG activity for the BioSemi was 14.49 μV/º, resulting in a higher amplitude voltage signal for a given EOG stimulus compared to the *WEBS* at 12.83 μV/º. Further experimentation could involve the use of a video projector instead of the monitor so that the viewing angle of the stimulus can be maintained whilst increasing the distance between the subject and sources of electrical interference.

4.4 Experiment 4: Comparison between a visual evoked potential recording from the WEBS system and a commercial biopotential recorder

As described in Section 2.2.1, the EEG measures biopotentials originating in the brain. The EEG has a tiny signal amplitude (low microvolt range) when measured on the scalp surface and is therefore a challenging candidate for exploring the capabilities of any biopotential measurement system, including the *WEBS*. The visual evoked potential (VEP) is, as the name suggests, a potential change in occipital EEG that is evoked by a visual stimulus. The advantage of targeting the VEP in particular is that it is a repeatable and predictable response that is mainly dependent on the type of stimulus used. Different types of visual stimuli (*e.g.*, pattern or flash stimulation) elicit identifiable VEP responses. The conventional procedure for measuring VEP is that a stimulus is triggered for a set number of repetitions and the VEP is obtained by calculating the time averaged voltage signal between stimulus initiations, as measured by electrodes over the occipital lobe region.

In this section, a pattern-reversal VEP, as recorded by the *WEBS*, is compared against a BioSemi ActiveTwo recording and the pattern-reversal example VEP from the measurement standard as set by the International Society for Clinical Electrophysiology of Vision (ISCEV) (Odom *et al.* 2010). In this experiment, the electrode locations followed the standard 10-20 system defined by the American Electroencephalographic Society (Sharbrough *et al.* 1991), as illustrated in Figure 4.21. This internationally recognised set of guidelines divides the line joining the nasion and inion of the skull into several proportionally sized intervals. The electrodes of interest in this experiment, labelled Fz (reference electrode) and Oz (active electrode), were placed on the skin surface at the intersection of these regions along the midline of the skull. For the *WEBS*,

a third electrode, with low-impedance connection to the body (*i.e.*, circuit ground), was placed behind the ear on the mastoid process. For the BioSemi, this was also the location for the CMS/DRL combination electrodes. The final unprocessed VEP signal was calculated by subtracting the two unipolar lead electrodes (Oz – Fz).

$$VEP_{RAW} = O_Z - F_Z \tag{4.12}$$

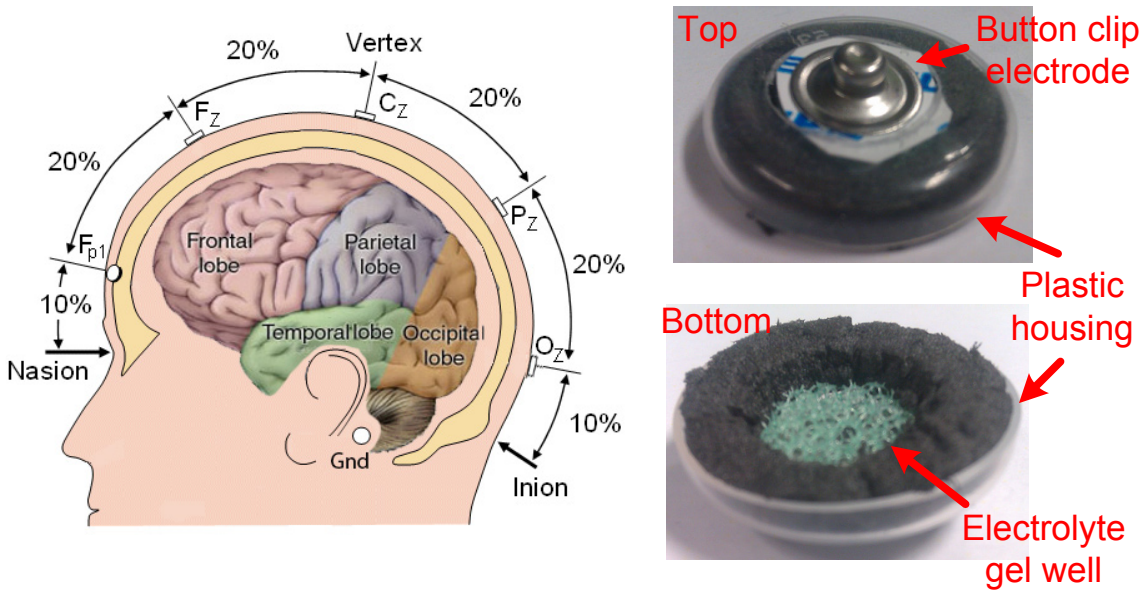

Figure 4.21: A diagram of a subset of the EEG electrode placement guidelines set out by the international 10-20 system. The electrodes of interest in this VEP experiment, labelled Fz (reference electrode) and Oz (active electrode), were placed, as indicated, on the skin surface along the midline of the skull. A third electrode, with low-impedance connection to the body (*i.e.*, circuit ground), was placed behind the ear. Also illustrated is an example of the fabricated electrode used to measure EEG with the *WEBS*. The flattened hemisphere design held additional electrolyte gel in place to improve electrode-skin contact and each electrode was secured in position by an adjustable strap around the head. Diagram modified from (Malmivuo and Plonsey 1995: 259) which, in turn, was redrawn from (Sharbrough *et al.* 1991). The brain image is modified from (Wikimedia 2008).

In previous experiments, the *WEBS* slave electrodes have been attached to the skin via standard button clip electrodes that have an incorporated adhesive pad. However, this method of adhesion is specifically designed for skin surface attachment and is not suitable for use on long cranial hair - as would be present on most people. Therefore, a unique electrode attachment solution was required, as illustrated in

Figure 4.21. A plastic housing was fabricated with a flattened hemispherical shape of outer diameter 23 mm and wall thickness of 0.5 mm. A 12.5 mm diameter hole was drilled into the top so that the *WEBS* slave could be clipped down on to a trimmed button clip electrode, which approaches from the underside. This design facilitates the use of additional electrolyte gel so that more gel can seep into the hair on the scalp - thereby improving the electrode-skin connection. A toroidal piece of foam is positioned inside the plastic housing to retain the electrolyte gel in the centre region. The *WEBS* electrodes were secured in position on the scalp by adjustable Velcro straps wrapped around the head. The BioSemi electrodes were held in position using an electrode cap. After the electrodes were attached to the skin, a 20 minute rest time was allowed for electrolyte gel soakage. Between testing on the individual systems, a 24 hr waiting period was observed to allow the epidermis to regenerate.

The experimental protocol was based on recommendations set out by (Odom *et al.* 2010) with further elaborations on stimuli configurations by (Yadav *et al.* 2012, Creel 1995). A pattern-reversal stimulus was chosen consisting of a grid of 24 x 18 black-and-white square checks, as illustrated in Figure 4.22. This checkerboard configuration obtained the recommended 4:3 aspect ratio. The monitor used was a 32" LCD monitor (NEC LCD3215) with the background colour set to a neutral shade of grey between black and white, as illustrated in Figure 4.22. An additional box, separate to the checkerboard, was used as a trigger indicator and was affixed to the upper left-hand corner of the screen. This trigger indicator alternated between black and white at the same rate as the checkerboard reversal and provided the stimulus to a phototransistor, as illustrated in Figure 4.22. The analog output voltage of the phototransistor's associated circuitry resembled a repeated charge and discharge cycle of a capacitor - corresponding to a white or black stimulus respectively - and was

connected into a fourth *WEBS* slave via a twisted pair cable. This configuration ensured that the analog-to-digital conversion process was synchronised along the same time axis for both the recorded VEP (from “Ref” and “Oz”) and the trigger indicator - thereby facilitating simple separation of the data windows between stimulus initialisations during subsequent analysis. Using the same principle in the case of the BioSemi, the phototransistor was connected into a voltage comparator circuit that supplied the trigger to a digital input on the BioSemi USB2 Receiver.

The ISCEV standard recommends a minimum ADC resolution of 12-bit and sampling rate of 500 Sa/s per channel. However, in order to obtain the most accurate measurement possible, the resolution of each *WEBS* slave was set to the highest resolution setting of 30-bits (OSR = 1024) - thus limiting the sampling rate to 190.55 Sa/s in this test. The BioSemi ActiveTwo has a 24-bit resolution (over a 524.288 mVpp range) and sampling frequency of 2048 Sa/s.

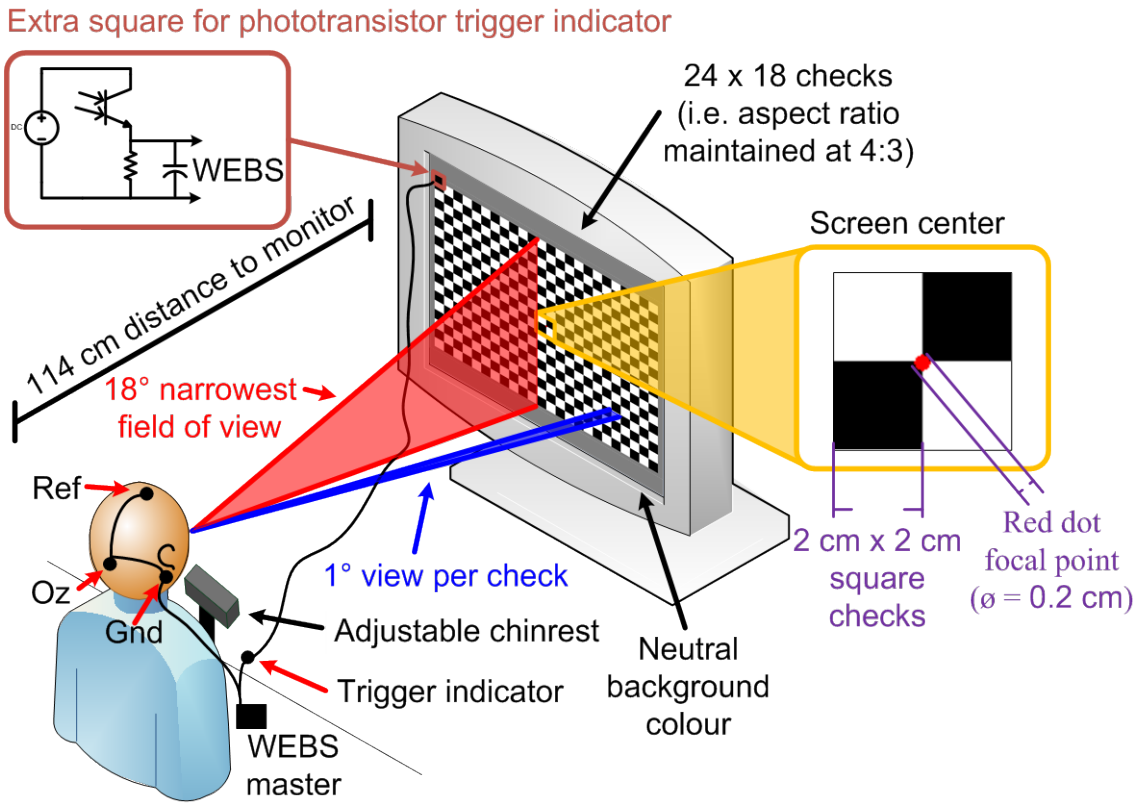

Figure 4.22: A diagram of the *WEBS* pattern-reversal VEP experimental set-up. A checkerboard of 24 x 18 square boxes was displayed on a monitor. The subject's eye level was adjusted to be in line with centre of the monitor and a distance was chosen that would maintain a fixed viewing angle of approximately 1° per check. A separate stimulus indicator box, located in the top corner of the monitor, provided the input to a phototransistor circuit that acted as a trigger indicator in the recorded data. The output of this circuit was connected into an additional *WEBS* slave to allow for synchronous data recording. The BioSemi experimental configuration was identical except that the electrodes were held in position using an electrode cap and the phototransistor fed into a digital input of the BioSemi USB2 Receiver via a comparator circuit.

During testing, a healthy male subject (age, 29; height, 180 cm; weight, 85 kg) was positioned in a relaxed seated position with his head resting on an adjustable chinrest. The subject was seated 1 m away from the nearest source of mains interference. The room was dark with no light source other than a monitor facing the subject. The distance between the subject and the monitor was adjusted in order to obtain a viewing angle of approximately 1° per check and greater than 15° in the narrowest field of view. The height of the chinrest was altered so that the subject's eyes lined up with a red dot, of viewing angle 0.1°, at the centre of the monitor. The stimulus

was presented binocularly to the subject who was asked to focus on this dot whilst the checks alternated colour every 0.5 s for a total of 1000 reversals. The test was repeated three times with a short break between tests. When the subject's eyes are closed, no VEP is generated. Moreover, blinking generates a big EOG disturbance, which can cause substantial EEG artefacts. The subject was therefore requested to try to minimise blinking for the duration of the test. Lubricating eye drops were provided when required to moisten the eyes and reduce the need to blink. Ethical approval was granted for this experiment (DIT reference number: 18/08) and the test subject gave informed consent.

Post-testing, all recorded data was analysed in MATLAB. The *WEBS* data was filtered at 50 Hz by a second-order IIR notch filter with a quality factor of 35, followed by Butterworth high-pass filter with a cutoff frequency of 1.5 Hz. It was subsequently separated into 1000 stimulus windows using the maximum and minimum points on the trigger indicator signal as starting points. The BioSemi data was filtered through a Butterworth band-pass filter between 1 Hz and 100 Hz, as per the ISCEV standard, and segmented using the digital trigger indicator. To allow for settling of both the VEP and the trigger indicator circuitry, a number of reversal windows were removed from the start of the data – forty for the *WEBS* and thirty-six for the BioSemi. The remaining windows were averaged together for both systems and the resulting VEP graph is illustrated in Figure 4.23. The BioSemi data is averaged over 64 reversals as defined as the minimum number by the ISCEV standard. In the case of the *WEBS*, a greater number of windows were required in order to achieve a satisfactory VEP. Therefore, all three tests, totalling 2880 reversals, were averaged. The normal pattern-reversal VEP for an adult of 18-60 years of age, as defined by the ISCEV standard, is also illustrated.

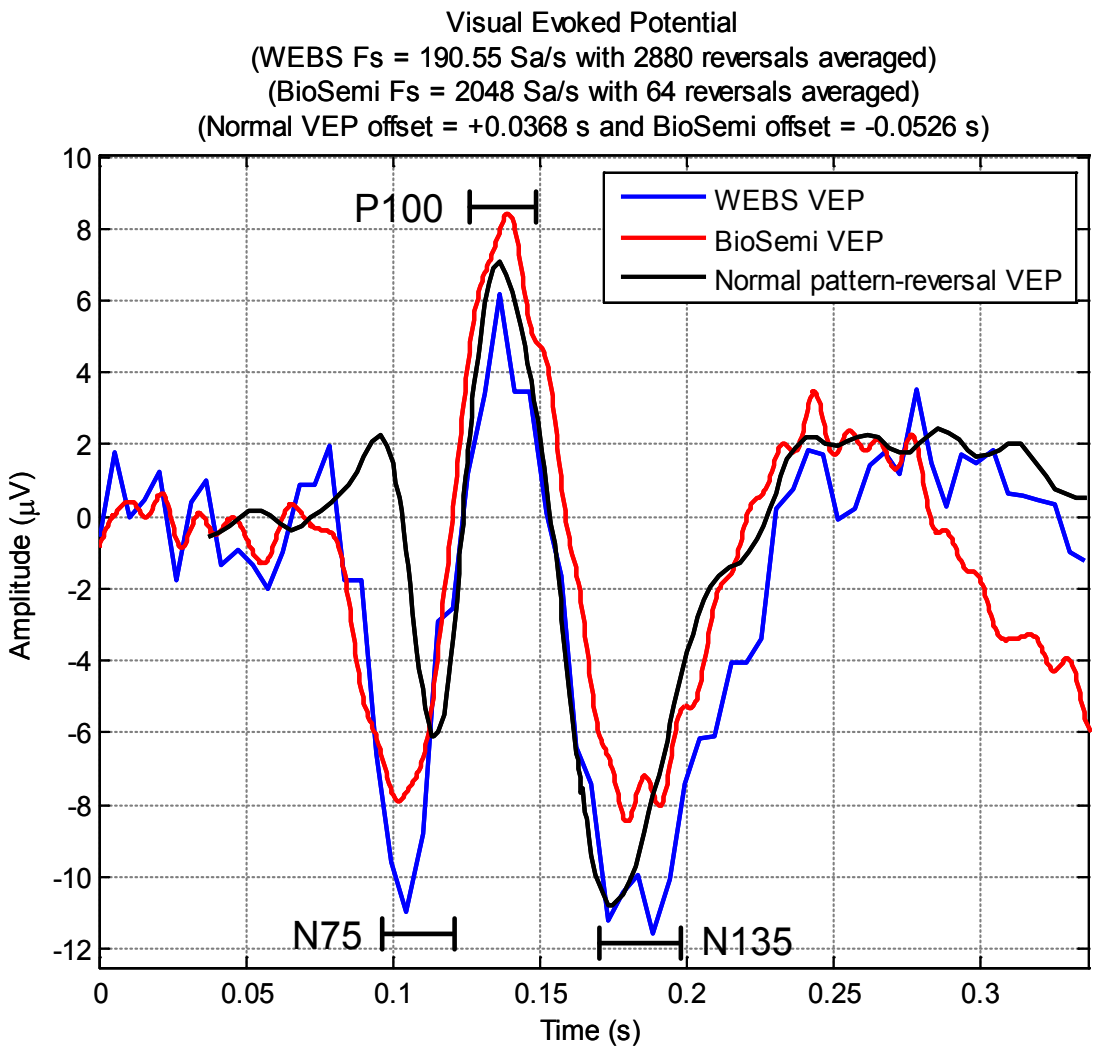

Figure 4.23: A graph comparing the pattern-reversal VEP recorded by the *WEBS* with that of BioSemi ActiveTwo recording and the normal pattern-reversal VEP, as depicted in the ISCEV standard (Odom *et al.* 2010). Markers indicate the N75, P100 and N135 peaks for each signal. For illustration purposes, an offset of 0.0368 s has been added to the normal pattern-reversal VEP and 0.0526 s subtracted from the BioSemi VEP.

As can be seen in Figure 4.23, there is a high correlation between the three VEP signals. The majority of the BioSemi VEP contours are mirrored in the *WEBS* VEP. An approximate latency of 136.8 ms exists in the *WEBS* VEP compared to the normal pattern-reversal VEP, which is out of the expected range for a healthy subject in their late twenties of between 95 ms to 105 ms (Emmerson-Hanover *et al.* 1994) but is within the peak latency as recorded by some groups of up to 146 ms (Di Russo *et al.* 2002). The BioSemi latency is probably increased due to an inherent latency in the trigger

comparator circuit switching between states. To obtain the mean latency for each experimental system with greater certainty would require further testing on multiple subjects. In clinical evoked potential measurement, the typical procedure is that each laboratory would perform the same experiment on at least 35 normal subjects to establish a mean latency (Chiappa 1997: 27). Most evoked potential parameters have a Gaussian distribution and the acceptable latency range is usually calculated to be within 2.5 (*i.e.*, 98.8 %) to 3 (*i.e.*, 99.7 %) standard deviations from the mean (Chiappa 1997: 27). However, for the purpose of this investigation, the similarity of the recorded VEPs provides sufficient evidence that the *WEBS* is capturing this tiny signal faithfully - albeit averaged over a greater number of reversal windows. On this front, the BioSemi has outperformed the *WEBS* by producing a VEP in forty-five times less reversal windows. However, the *WEBS* has a sampling rate ten times less than the BioSemi and nearly three times less that the ISCEV standard recommends – leading to misaligned averaging of samples. Additional testing has revealed a similar quality *WEBS* VEP over 925 reversal windows for a minimal increase in sampling rate of 10 Hz. Given the very different design focus of the *WEBS* (ultra-simple, low-cost and unobtrusive) as compared with a laboratory research system such as the BioSemi (high-precision, high-cost and high maintenance), the quality of the recorded *WEBS* VEP is quite compelling.

4.5 Experiment 5: Comparison of detected laryngeal vibrations versus microphone-recorded phonations

The throat can be regarded as an efferent hotspot that provides a high-bandwidth channel of communication from the human brain to the outside world through laryngeal vibrations produced during speech. This biomechanical signal can be measured from the skin surface using an accelerometer. This approach has several desirable characteristics compared with audio recordings acquired by traditional microphone-based techniques. For example, an accelerometer placed on the throat is less susceptible to background audio noise than a microphone. Laryngeal vibration measurement is discussed in greater detail in chapter 5 (together with applications). However, the experiment described in this section aims to emphasise the similarities between vocal recordings and laryngeal vibrations and the ability of the *WEBS* device to record such vibratory signals. With this in mind, the experiment illustrated in Figure 4.24 was devised in which vocal recordings (recorded by a microphone) are compared to laryngeal vibrations (recorded using a single *WEBS* slave attached to the throat). Similar studies have been carried out using standalone accelerometers on the suprasternal notch (Cheyne 2006) and the suprasternal notch and sternum bone (Lamarche and Ternström 2008). Ethical approval was granted for this experiment (DIT reference number: 18/08) and the test subject gave informed consent.

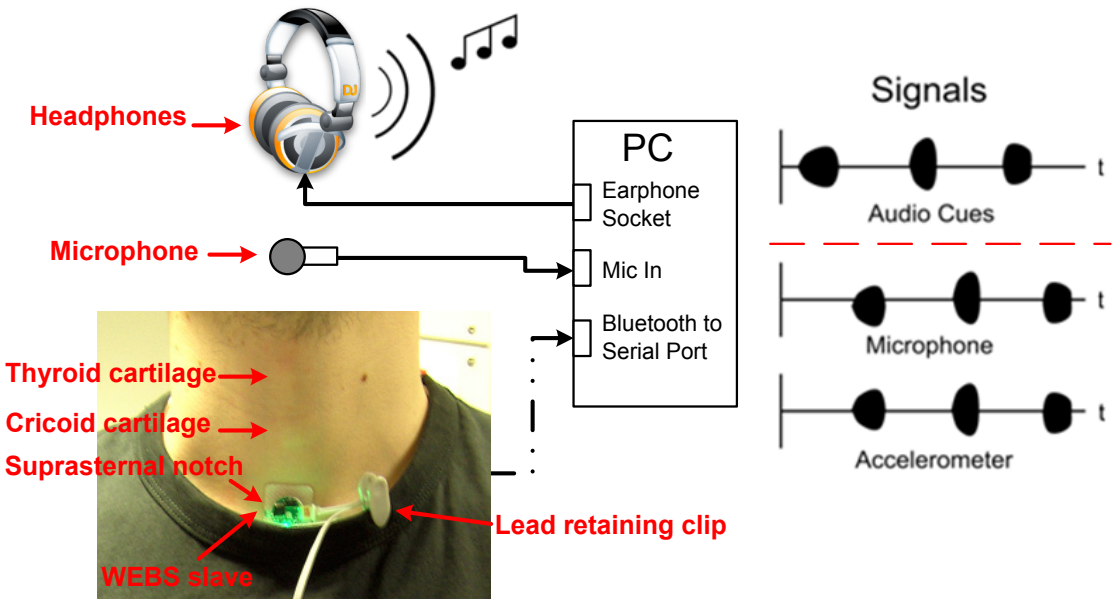

Figure 4.24: A diagram illustrating the laryngeal vibration test configuration. Piano note audio cues are played individually to the subject through headphones. The subject repeats each of the notes back using the vowel sound 'ee' and a 4 s recording is taken of the vocalisations as simultaneously recorded by a microphone, positioned 30 cm away, and a *WEBS* slave electrode positioned on the throat. A retaining clip attached to the subject's clothing helped minimise movement of the wire attached to the *WEBS* slave. The headphone image is modified from (Iconshock 2009).

A single *WEBS* slave was attached to the skin over the suprasternal notch of a healthy male subject (age, 29; height, 180 cm; weight, 85 kg). The subject was placed in a seated position with his head positioned on an adjustable chinrest. The chinrest helped to maintain a fixed position of the accelerometer relative to the anatomical features of the throat while also ensuring minimal movement of the subject during testing. In order to obtain a high sampling rate, the *WEBS* system was configured to record accelerations from a single axis in the accelerometer, *i.e.*, the z-axis (perpendicular to the skin). The accelerometer in the *WEBS* slave was configured to record from this axis at the most sensitive setting available of ± 2 g from which the *WEBS* master sampled at a rate of 2403.85 Sa/s. A microphone, connected to the sound card of a PC, was positioned directly in line with the subject's mouth at a distance of 30 cm. The Microsoft software

application, “Sound Recorder”, produced an audio file from the recorded microphone input at a sampling rate of 44.1 kHz.

A sequence of seven pre-recorded piano notes, C3 (130.81 Hz), G3 (196 Hz), C4 (261.63 Hz), G4 (392 Hz), C5 (523.25 Hz), E5 (659.25 Hz) and G5 (783.99 Hz), were played individually to the subject through headphones. The subject attempted to sing, using the vowel sound ‘ee’, at the corresponding audio cue frequencies. Once an approximate pitch match was achieved for each note, the subject was asked to sustain the note whilst a 4 s snapshot of both the laryngeal vibrations and the microphone input were recorded. The specific notes were chosen as they cover a broad frequency spectrum of human vocal range. The test was repeated for each note until the closest match to the original piano note was achieved. This experiment was not designed to demonstrate the ability of the subject to match the note, but rather the ability of the accelerometer recordings to accurately match the microphone recording. The repetition of the test for each note was performed purely for definitive note identification and separation in the results. The Fast Fourier Transforms (FFT) of the three signals (original piano notes, recorded microphone and accelerometer z-axis signals) were calculated in MATLAB and the resulting peak normalised plots are illustrated in Figure 4.25.

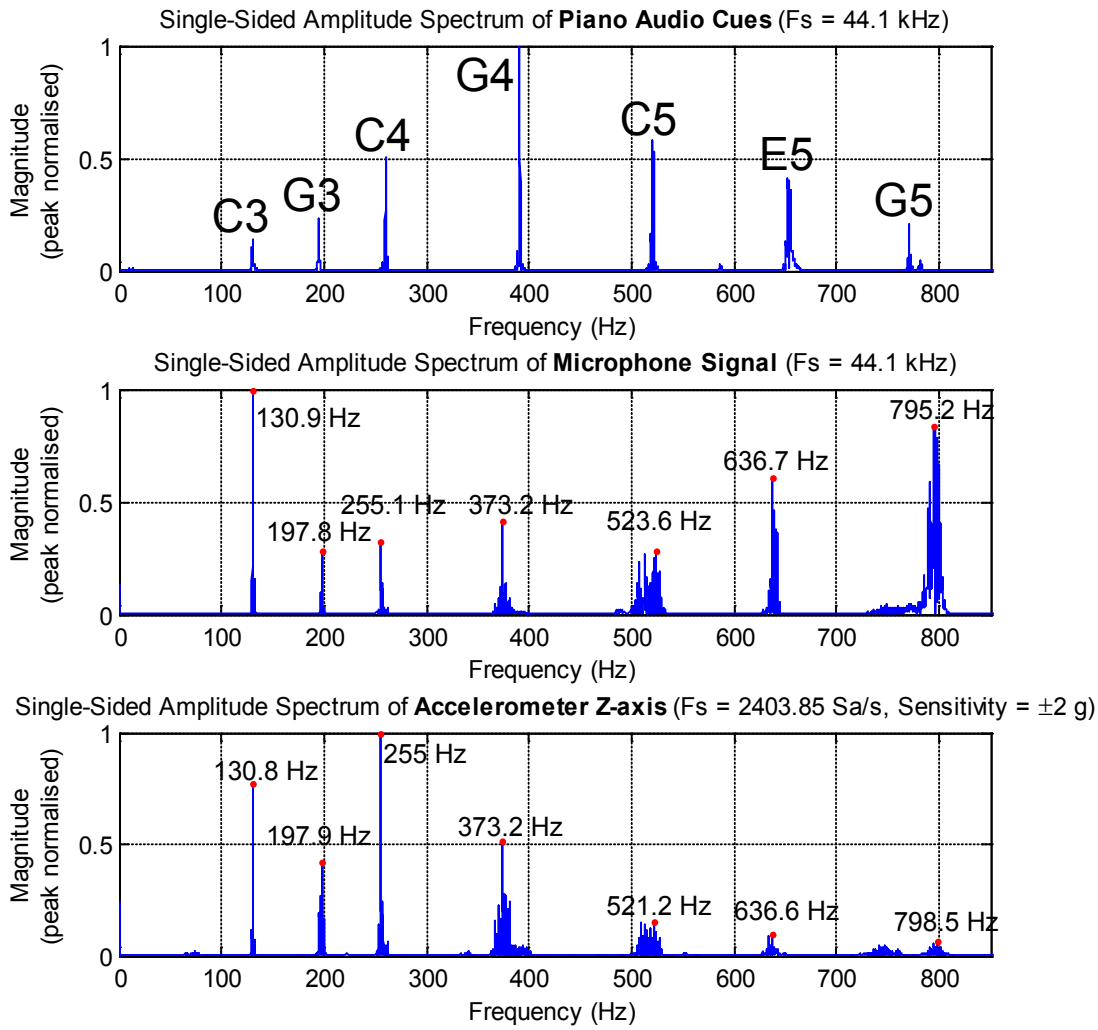

Figure 4.25: The peak-normalised FFT of the audio cues, microphone recording and accelerometer z-axis signals over a 28 s recording interval. A sequence of seven piano notes, C3 (130.81 Hz), G3 (196 Hz), C4 (261.63 Hz), G4 (392 Hz), C5 (523.25 Hz), E5 (659.25 Hz) and G5 (783.99 Hz), was played to a subject (one note at a time) through earphones. The subject attempted to sing each of the notes back using the vowel sound 'ee'. For each note, a 4 s snapshot of both the laryngeal vibrations (from a single *WEBS* on the throat) and a microphone input (from a microphone positioned at a distance of 30 cm) were recorded. The separate 4 s recordings were then concatenated to produce a single 28 s recording from which the FFT was calculated.

It is evident from the Figure 4.25 that there is good correlation between the microphone and accelerometer recordings, which validates the use of the *WEBS* slave's accelerometer for pitch detection. Even at notes G4 to G5, when the subject was unable to vocalise a precise note, the recorded accelerometer activity includes similar

frequency components to those recorded by the microphone. It should be noted that, as the piano cue frequency increased (particularly from C5 onwards), the subject had to increase the intensity of his vocalisation in order to effect the desired laryngeal vibrations. This phenomenon can be further investigated by analysing the summary of results listed in Table 4.2.

Table 4.2: A summary of the results obtained in the comparison of laryngeal vibrations versus microphone recordings. The original audio cue frequency for each note is listed and the peak normalised amplitude and associated frequency of the subject's phonation and corresponding laryngeal vibrations, as measured by a microphone and accelerometer respectively, are provided. Finally, the calculated frequency difference and amplitude ratio from the measured signals are also tabulated.

Piano		Microphone (at peak freq.)		Accelerometer (at peak freq.)		Δf (Hz) (Mic. – Accel.)	Amplitude ratio (Mic. ÷ Accel.)
Note	**Freq. (Hz)**	**Freq. (Hz)**	**Amplitude (pk. norm.)**	**Freq. (Hz)**	**Amplitude (pk. norm.)**		
C3	130.81	130.9	1	130.8	0.7712	- 0.1	1.3
G3	196	197.8	0.2734	197.9	0.4127	+ 0.9	0.7
C4	261.63	255.1	0.3209	255	1	- 0.1	0.3
G4	392	373.2	0.4192	373.2	0.5198	0	0.8
C5	523.25	523.6	0.2829	521.2	0.1497	- 2.4	1.9
E5	659.25	636.7	0.6057	636.6	0.09692	- 0.1	6.2
G5	783.99	795.2	0.821	798.5	0.06565	+ 3.3	12.5

The amplitude ratio tabulated in Table 4.2 was calculated by dividing the peak normalised microphone magnitude by the peak normalised accelerometer magnitude. This calculation indicates an almost parabolic relationship between the microphone and the accelerometer with the trough, *i.e.*, the closest match, at C4. Starting at C5, the ratio increases until G5 where the microphone amplitude is 12.5 times that of the accelerometer. With regard to pitch detection, the calculated frequency difference confirms that the accelerometer recordings accurately reflect those of the microphone

recordings. The maximum difference, relative to the peak microphone recorded frequency, is 0.46 % whilst the minimum is close to 0 %. The results shown here suggest that, the positioning of the *WEBS* slave on the suprasternal notch during laryngeal vibration measurement is sufficient for pitch detection but is subject to damping at higher frequencies. In order to obtain consistent results across a broader frequency spectrum, a more suitable location for *WEBS* slave placement is explored in Section 5.1.1.

4.6 Summary

This chapter described the thorough testing that has been performed on the *WEBS* system. The initial emphasis was placed on a methodical investigation into the input electrical characteristics of several sample *WEBS* nodes. The results showed that, although the maximum sampling frequency of the *WEBS* sensor network is lower than high-end biopotential measurement systems, the recorded signal quality (*i.e.*, signal *vs.* noise) is sufficient for detecting the majority of biopotential signals. Some variability between the input characteristics of individual *WEBS* sensors was noted which could be reduced in the future by improved sensor assembly methods.

In this chapter, tests were also described in which multiple types of biopotential signals were recorded by the *WEBS* system and compared with those from a high-end biopotential measurement system. Notably, an EEG measurement experiment was performed wherein a pattern-reversal VEP was successfully detected from a *WEBS* recording; albeit over a larger number of reversals than was required by the high-end system.

Finally, an experiment was described which tested the biomechanical signal measurement abilities of the *WEBS* system on a subtle body movement signal, *i.e.*, skin-surface vibrations emanating from laryngeal vibrations. In this experiment, a comparison with audio - which was recorded simultaneously from a microphone - showed that the *WEBS* sensor is capable of detecting the pitch of vocalisation over a wide range of human vocal frequencies.

The design of the *WEBS*, as discussed in the previous chapter, was successfully validated here. The next stage, as explored in the following chapter, is to demonstrate the use of the *WEBS* system in several novel HMIs that capitalise on the unique features of the *WEBS* sensor network.

Chapter 5 Applications

This chapter describes several practical applications that are made possible by the unique characteristics of *WEBS* system. Unlike many traditional assistive technology user interface solutions, the *WEBS* facilitates the design of software-defined user interfaces which represents a real universal design (UD) approach (North Carolina State University 1997). Note that, aside from the specific assistive technology applications described in this chapter, the UD approach to the design of the *WEBS* makes it readily amenable to adaptation for additional assistive technology applications such as wheelchair navigation, mouse pointer control or other computer input.

The first three sections of this chapter describe applications that facilitate communication and control, play, and creative expression through biopotential signals, subtle and/or gross body movements, or a combination of the two, as measured by the *WEBS* system. The first section describes work carried out using early prototypes of the *WEBS* system in the measurement and mapping of laryngeal vibrations. Three-dimensional acceleration trajectories are observed at points on the surface of the neck, emanating from laryngeal vibrations, which illustrate the rich information channel that exists there. Specific applications in communication, control and creative expression are described where laryngeal vibrations and head movement are used together to facilitate control of a radio-controlled car and a musical synthesizer by children with physical disabilities. The second section describes an initial investigation into turning an area of the skin surface into a human-to-machine interface by measuring vibrations from finger taps emanating across the skin surface. This application capitalises on the *WEBS* system as a movement sensing body-area network to locate the

point of impact of each finger tap. The third section describes an application that demonstrates how a combination of a consciously controllable biopotential (*e.g.*, bicep EMG) along with gross body movement (*e.g.*, arm orientation), are harnessed as input to a video game.

The final two sections of this chapter demonstrate benefits of the *WEBS* system that extend beyond assistive technology. The first of these sections shows how biomechanical information, as measured within each electrode, can be utilised to augment biopotential recording in clinical applications – providing information such as body activity level and electrode movement activity. In this example, a real-time 12-lead ECG user interface has been developed which displays biomechanical information alongside the recorded biopotential signals.

The work described in this chapter's final section further capitalises on the *WEBS* as a digitally controllable body-area network to perform pseudo-random binary sequence (PRBS) system identification between a pair of *WEBS* electrodes – as described previously in Section 3.2.6. In this mode, the *WEBS* can be applied to investigate the quality of the electrode-skin connection at each measurement point. This section starts by demonstrating the feasibility of the *WEBS* to perform system identification on various test circuits. Finally, preliminary results are shown from system identification experiments that were performed between pairs of electrodes connected to the body. A comparison is shown between two types of electrodes on prepared and unprepared skin.

Some of the work in this chapter is described in (Nolan *et al.* 2009a, Nolan *et al.* 2009b).

5.1 Control utilising laryngeal vibrations

The use of an accelerometer to facilitate control using laryngeal vibrations has several advantages compared to vocal recordings from a microphone. One is that the control of an instrument or device is more tightly bound to the user and less prone to interference from external sources. Extraneous audio (*i.e.*, noise from the surrounding environment) can be assumed to have a negligible impact on the accelerometer measurement and therefore does not interfere with a user controlling an instrument or device. Another advantage is that the user wears a very lightweight device in a discreet location as opposed to a microphone, which ordinarily needs to be positioned in the vicinity of the mouth.

Having identified laryngeal vibrations as a candidate for facilitating control, it was necessary to determine an appropriate location for an accelerometer to measure the vibration activity. An experiment was performed to obtain a detailed map of skin-surface vibrations during vocalisation and the results are presented in this section. Furthermore, detailed analysis of the time-varying acceleration function at various measurement positions reveals a rich and complex source of information. Previously unseen visualisations of these signals are presented. Equipped with the results from this study, an early prototype of the *WEBS* system was designed to tap into this information-rich channel of communication to assist children with physical disabilities to engage with toys and music-making activities to which they would otherwise have limited access to.

5.1.1 Neck surface vibration mapping

5.1.1.1 Introduction

Accelerometer recordings of neck skin vibrations, have been found to be closely related to vocalisations as recorded using a microphone (Svec *et al.* 2005). Previous studies have used accelerometers to measure the intensity of vibration emanating from the throat (Hamlet *et al.* 1992) and to give a general mapping of the skin surface vibrations of the neck and thorax region during sleep (Rendon *et al.* 2007). This section provides a detailed study of the vibrations on the surface of the neck during a vocalisation of a predefined fundamental frequency and intensity.

The terms fundamental frequency and pitch often refer to subtly different quantities (actual and perceived fundamental frequency respectively). Here however, the term pitch refers to fundamental frequency of phonation. The range of vocal pitch during speech varies substantially from one person to another. However, the average fundamental frequency of speech (as measured during spontaneous speech and reading out loud) usually lies between 100 Hz and 146.3 Hz for adult males and 192.4 Hz and 224.3 Hz for adult females (Baken and Orlikoff 2000: 175-179).

An initial aim of this study was to identify one or more suitable locations for the positioning of a hands-free electro-larynx (Madden *et al.* 2010, Madden *et al.* 2011). Since removal of the larynx has an enormous physical structural impact on the anatomy of the throat, investigation of vibration patterns in able-bodied subjects can provide only limited insight into what may occur in the case of a laryngectomee. This aim was therefore a speculative/exploratory one. Once the initial experiments revealed the rich source of information that lay in the measured vibrations, it became clear that it could be harnessed as a useful channel of control in a much broader range of applications.

Therefore, the original aim receded into being of secondary importance after the more fundamental aim of exploring how neck surface vibration can be used as a channel of communication and control.

5.1.1.2 Materials and methods

To perform a study on skin vibrations using an accelerometer, it is desirable that the device used be as small and light as possible in order to minimise the potential for the sensor itself to affect the recordings. For this reason, in this early prototype of the *WEBS*, the accelerometer selected was the STMicroelectronics LIS3L02AL, which is a 3-axis, ± 2 g, analog accelerometer, capable of measuring accelerations over a bandwidth of 1.5 kHz for all axes. It has external dimensions of 5 mm x 5 mm x 1.6 mm, a mass of 80 mg, and requires just five wires connected to it to measure acceleration in all three axes. Single strands of 100 µm diameter wire were used to ensure that the inertia of the measuring device was minimised so that the vibration of the skin was not significantly affected. This also helped to reduce erroneous results that could arise from movement of the subject. A block diagram of the recording system is shown in Figure 5.1.

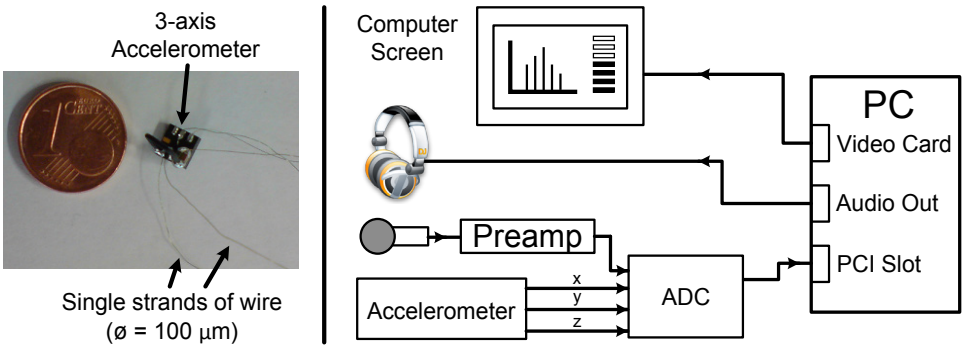

Figure 5.1: A block diagram of the experimental apparatus and an image of the accelerometer used in the experiment. Audio cues were played to the subject through earphones whilst their laryngeal vibrations (as recorded by an accelerometer on the neck skin surface) and vocalised audio signals (as recorded by a microphone) were recorded. A computer screen provided user-feedback during testing to indicate when a vocalisation was within range of the desired frequency and intensity. The headphone image is modified from (Iconshock 2009).

A combined microphone and preamplifier (Maplin KJ44X) was used to record the vocalised audio signals. To ensure synchronised sampling of all signals, the microphone and accelerometer were both connected to a National Instruments 6023E 12-bit analog-to-digital converter (ADC). The ADC was set to a sampling frequency of 22.05 kHz on all channels. Prior to testing, the pre-amplified microphone was calibrated using a Brüel & Kjær 2231 Sound Level Meter, at a distance of 15 cm from a constant audio signal source. The audio intensity was adjusted and the output voltage from the microphone preamplifier was compared with the corresponding recorded sound pressure level (SPL). A virtual instrument (VI) was created in LabVIEW to stream data from the microphone and the three-axis accelerometer via the ADC. The incoming data stream was segmented into 200 ms windows. The sound intensity and fundamental frequency of each window was estimated. The VI gave a visual display of these calculated values and this user feedback was updated with each analysis.

After testing, the data from the individual channels was combined in MATLAB. Utilising equations (5.1), (5.2) and (5.3), the average magnitude of acceleration was calculated for each 200 ms window at each measurement point. This result does not preserve the three-dimensional characteristics of the vibrations on the surface of the neck; however, for the purpose of positioning a communication sensor, this scalar value is adequate.

$$\vec{a}_{pn} = x_{pn}\,\vec{i} + y_{pn}\,\vec{j} + z_{pn}\,\vec{k} \tag{5.1}$$

$$\left|\vec{a}_{pn}\right| = \sqrt{x_{pn}^2 + y_{pn}^2 + z_{pn}^2} \tag{5.2}$$

$$\left|\vec{a}_{p}\right| = \frac{\sum_{n=0}^{N-1}\left|\vec{a}_{pn}\right|}{N} \tag{5.3}$$

where p is a point on the neck, N is the number of samples per window and n is the sample number. This study was performed on two able-bodied male subjects

(subject 1: age, 26; height, 180 cm; weight, 85 kg and subject 2: age, 28; height, 183 cm; weight, 70 kg). Ethical approval was granted for this experiment (DIT reference number: 18/08) and both test subjects gave informed consent. The experimental procedure was as follows:

1) The subject's neck dimensions were measured and a personalised grid of the neck was calculated based on that shown in Figure 5.2. The reference points of this grid (marked in blue) are the chin, each angle of the mandible, the hyoid bone, the thyroid cartilage, the cricoid cartilage, the sternal head and the points where the sternocleidomastoideus meets the clavicle. The points illustrated by green markers were calculated by dividing the distance between the reference points using the percentage ratios as shown. Utilising both of these sets of points, the remaining area was divided up (red markers) so that the result was a grid consisting of forty-five vibration measurement locations.

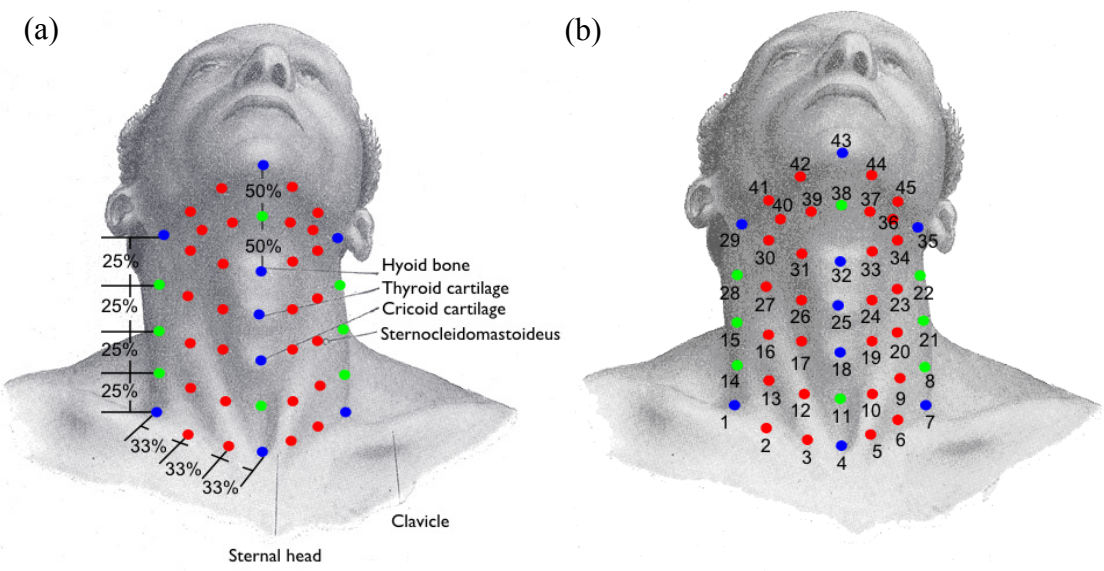

Figure 5.2: Two diagrams illustrating: (a) the calculation of accelerometer measuring points, (b) the resulting numbered measuring points. The blue markers indicate the grid reference points, including the chin, each angle of the mandible, the hyoid bone, the thyroid cartilage, the cricoid cartilage, the sternal head and the points where the sternocleidomastoideus meets the clavicle. The green and red markers are derived from the reference points using the proportions as shown. Background image modified from Fig. 1195 (Gray 1918).

2) To keep each subject's posture constant during testing, his forehead was supported in a headrest, as shown in Figure 5.3. The angle of the head was set by locating the anterior triangle (Gray 1918: 562) of the neck and maintaining a constant angle of 100° between the mandible and the line that travels along the sternocleidomastoideus. The height of the subject's seat was adjusted until this angle was achieved. The microphone was then positioned 15 cm away from the subject's mouth, as shown in Figure 5.3.

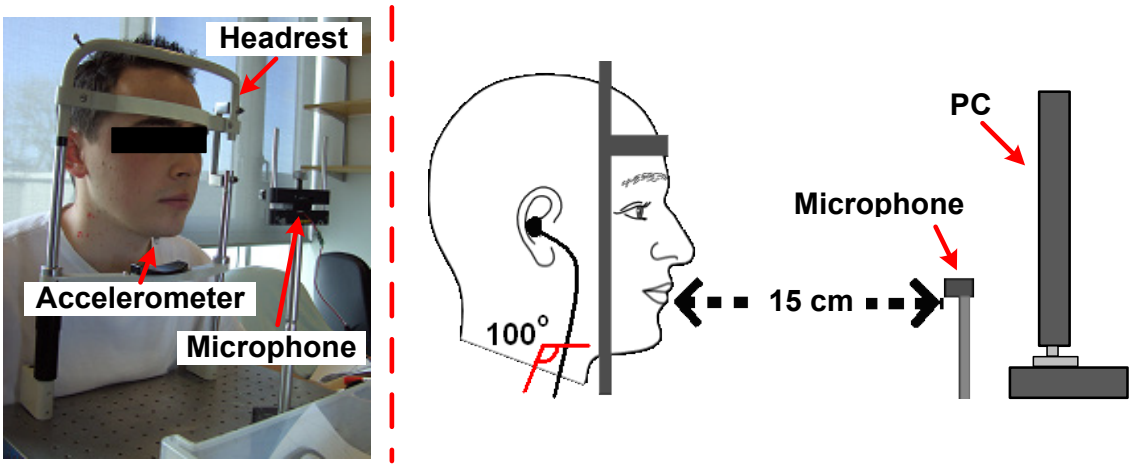

Figure 5.3: A picture and diagram of the experimental configuration. A headrest was utilised during testing to maintain a fixed angle of 100° between the head and neck whilst also maintaining a constant distance of 15 cm to a recording microphone. The audio cues were played to the subject through the earphones and a computer interface provided feedback about the fundamental frequency and intensity level of the subject's vocalisation. Once the subject was within a 5 % tolerance of the desired frequency and intensity values, a 200 ms recording was taken of the audio and laryngeal vibrations. The test was repeated at 150 Hz, 200 Hz and 250 Hz for each of the 45 points on the pre-defined grid of measurement points.

3) The accelerometer node was then positioned on the first point in the grid, Figure 5.2, and the subject was asked to make the vowel sound /i/ (long e) at three different fundamental frequencies, 150 Hz, 200 Hz and 250 Hz, and at a SPL of 70.8 dB (at the microphone).

4) Utilising the live visual display of fundamental frequency and sound intensity, the subject was able to adjust his phonation. When his voice reached the desired values, within a 5 % tolerance, the LabVIEW VI automatically saved a 200 ms window of data from the audio and the vibrations at that point on the neck.

5) The accelerometer was repositioned to the next point in the grid and the procedure repeated from step 3.

5.1.1.3 Results

The vibration magnitude values (measured as average magnitude of acceleration over 200 ms) for all measurement points on subject A are listed for each frequency in Table E.1, Table E.2 and Table E.3 in Appendix E. The same values are represented graphically in Figure 5.4. Both the size and colour of each dot represents the average magnitude of acceleration at that point. However, the dot colour mapping is normalised for each graph, while the dot size scale is constant across all graphs. Since the results from both subjects are very similar, only those from Subject A are shown graphically below. Subject B's measurement values and the corresponding graphical representations can be found in Appendix E.

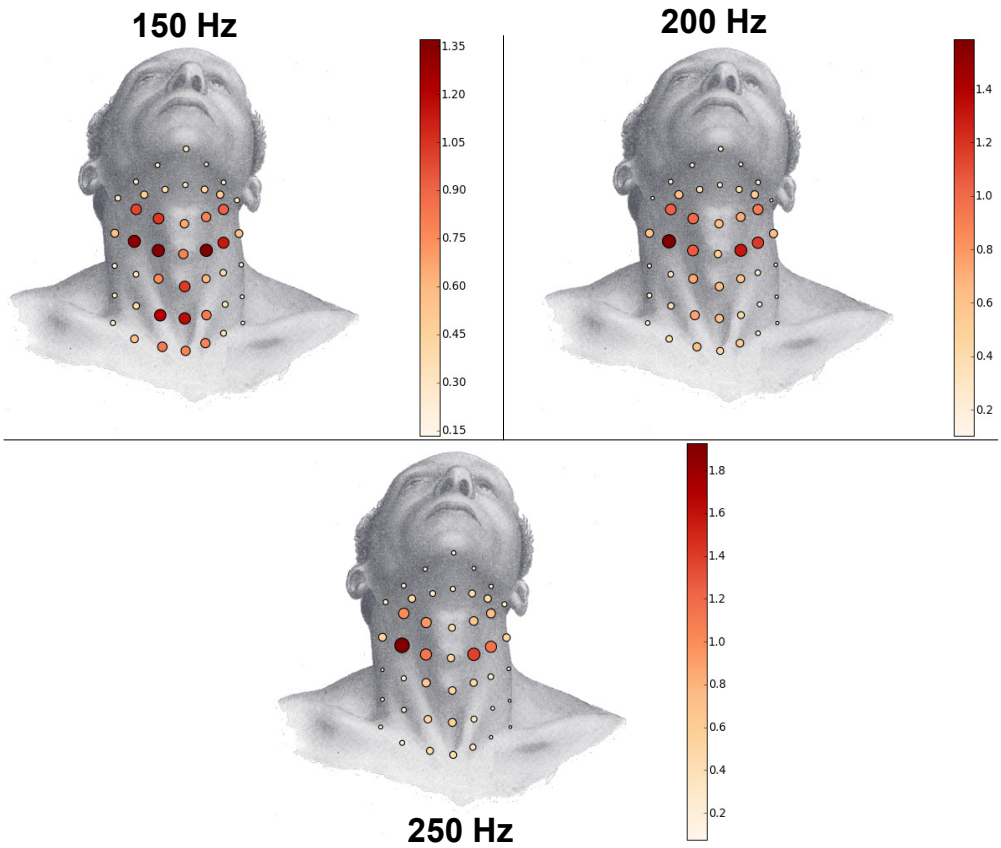

Figure 5.4: A plot of Subject A's results showing the variation in average magnitude of acceleration (measured in m/s^2) over the measurement grid at phonation frequencies 150 Hz, 200 Hz and 250 Hz. Both the size and colour of each dot represent the average magnitude of acceleration at that point. The dot colour mapping is normalised for each graph, while the dot size scale is constant across all graphs. The head image is modified from Fig. 1195 (Gray 1918).

The previous diagram shows that the region in which neck skin-surface vibrations are most intense varies with phonation frequency. At lower frequencies, vibratory activity is spread along the throat with distinct activity either side of the thyroid cartilage and around the suprasternal notch. As the frequency increases, the concentration of vibratory activity shifts upwards until the majority of activity occurs solely around the thyroid cartilage. This phenomenon corresponds to the physical movement of the cricoid cartilage vertically with increasing phonation frequency. This alters the dynamics of the throat and shifts the concentration of skin-surface vibrations upwards.

In addition to the expected vibration magnitude results as shown in the previous diagrams, what emerged from the three-dimensional skin-surface acceleration recording was an interesting pattern of three-dimensional oscillatory motion which is distinctly different at each of the measurement points. Sample acceleration trajectories for two points are illustrated in Figure 5.5 and Figure 5.6. The low amplitude of the measured vibrations resulted in the visible quantisation of data points in both of these figures (particularly visible on the left-hand graph in Figure 5.6).

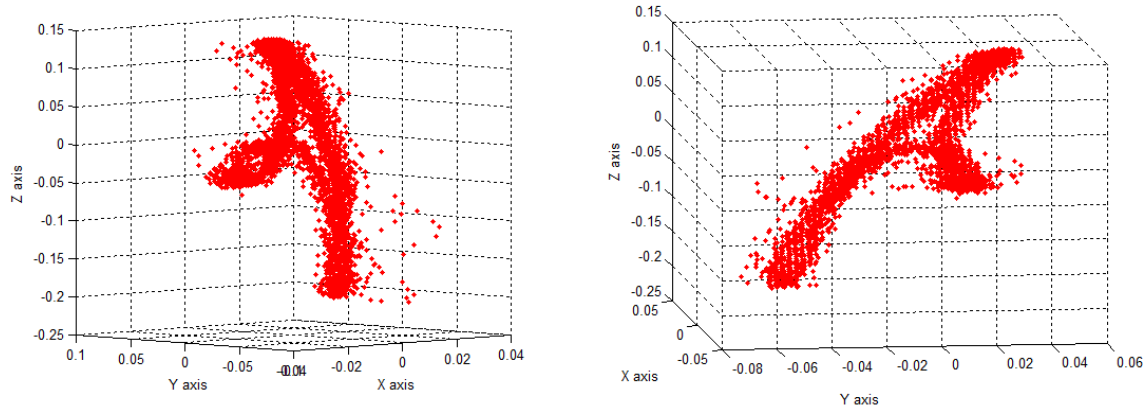

Figure 5.5: Three-dimensional diagrams showing the acceleration trajectory at a phonation frequency of 150 Hz for measurement <u>point 11</u> on Subject A. In this figure, the same data points are displayed from two different viewing orientations. Units are measured in m/s^2.

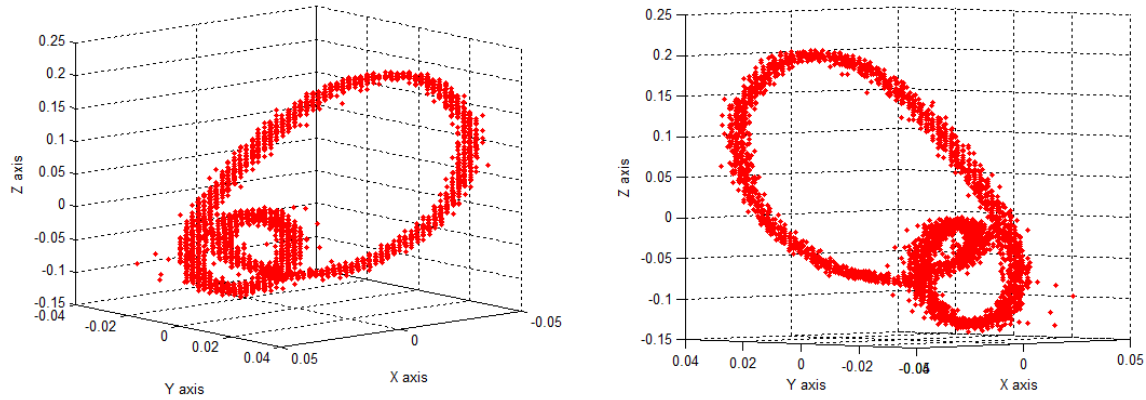

Figure 5.6: Three-dimensional diagrams showing the acceleration trajectory at a phonation frequency of 150 Hz for measurement <u>point 27</u> on Subject A. In this figure, the same data points are displayed from two different viewing orientations. Units are measured in m/s^2.

Figure 5.7 illustrates the difference between the normal and tangential acceleration trajectories. It is evident from these figures that, whilst certain points on the neck typically consist of vibration that is normal to the surface of the skin, there are other points that have significant tangential components.

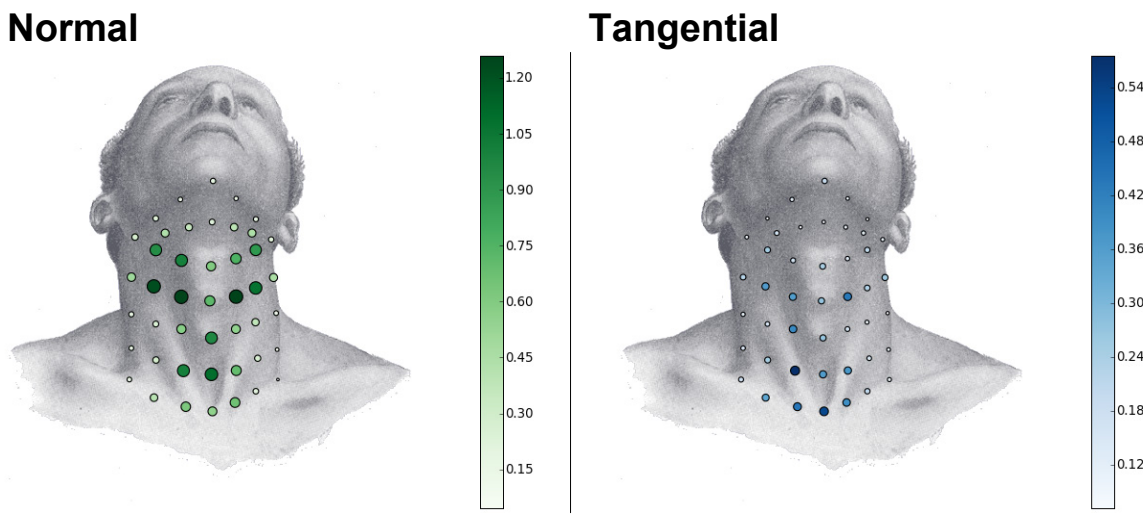

Figure 5.7: A plot showing the average magnitude of acceleration (measured in m/s^2) <u>normal and tangential</u> to the skin surface at a phonation frequency of 150 Hz on Subject A. The size and colour of each dot represents the average magnitude of acceleration at that point. The dot colour mapping is normalised for each graph, while the dot size scale is constant across both graphs. The background image is modified from Fig. 1195 (Gray 1918).

5.1.1.4 Conclusions

The variation in vibration amplitude over the region of investigation is largely consistent with expectations. The average magnitude of acceleration tends to be greatest on and in the immediate vicinity of the larynx. It decreases as distance from the larynx increases, but the rate of decrease is dependent upon the direction. It can be seen that at 150 Hz, there are significantly more intense vibrations at the base of the neck compared to those at 250 Hz (Figure 5.4). The two areas either side of the cricoid cartilage (approximately points 27 and 23 in Figure 5.2) appear to show signs of measureable laryngeal vibrations at each test frequency. These could be suitable regions for the

future positioning of *WEBS* devices for human-to-machine communication applications. However, the surface area of skin on the suprasternal notch (point 11 in Figure 5.2) would be more suitable when taking into account practical considerations such as: user comfort; the desirability of an unobtrusive sensor location; and reducing the sensitivity to head movement.

Although the initial objective of this experiment was to investigate the suitability of different locations for a hands-free electrolarynx, vibrations on the mandible (*i.e.*, the typical location where an electrolarynx is applied) are minimal for all frequencies. This suggests that these vibration maps, while useful and interesting for other purposes, do not reveal much information about what occurs when an electrolyarnx is applied under pressure to a single point on the neck.

The three-dimensional acceleration plots reveal a complex pattern of oscillatory motion at the skin-surface due to vocalisation, which may have several interesting applications. However, further investigation is required to confirm that these trajectories can be observed consistently, and to gauge how sensitive their specific form is to the measurement apparatus and method used.

5.1.2 Communication, play and creative expression

The previous section identified and investigated a high-bandwidth channel of information flow from the brain to the outside world (*i.e.*, from laryngeal vibrations as measured on the neck skin surface). This section describes two applications that demonstrate the use of this signal source in assistive technology solutions, with an emphasis on communication, play and creative expression for children with physical disabilities.

Play is an important component of a child's development, during which they develop their creativity, imagination and dexterity whilst building their physical, cognitive and emotional strength (Ginsburg 2007). Modern smart toys provide extra dimensions for a child's play and interaction with a toy through the use of motion, pressure and auditory sensors. Children with physical disabilities, who cannot interact with these toys, are at a distinct disadvantage. It has even been found that limitations on a child's ability to interact with toys, as can occur due to a disability, can lead to regression (Barker *et al.* 1941, reviewed in Child and Waterhouse 1952). Similarly, creative expression, through the medium of music benefits the development of children in areas such as language, reasoning and spatial intelligence (Phillips 2006). Musical instruments that requires a player to perform multiple operations and to have sufficient dexterity and coordination are inaccessible to the majority of children with moderate to severe physical disabilities. To remove this barrier, it is desirable to take a UD approach (North Carolina State University 1997) and to create toys and musical instruments which are accessible to children with a very broad range of abilities.

As stated in Section 2.4.1, the principles of UD encourage the creation of products that are easily usable by the greatest range of people, regardless of their age or ability. With these principles in mind, an early prototype *WEBS* system was deployed in a number of novel communication, play and creative expression applications to allow a child with a physical disability to have the same level of control that any other user would have over a toy. If they were to compete against a peer, they could do so on a level playing field without being stigmatised or segregated.

Two communication, play and creative expression applications are demonstrated in this section: a musical synthesizer interface and a remote-controlled vehicle interface. Both applications were originally developed using an early prototype of the *WEBS*

device (Nolan *et al.* 2009a). However, the musical synthesizer has since been updated to work with the current *WEBS* device. Whether using the early *WEBS* prototype or the current model, the sensor topology and positioning is as illustrated in Figure 5.8. In both cases, a master device is clipped behind the ear, which measures gross head movement. A supplemental device is attached to the skin on the suprasternal notch (*i.e.*, over the trachea and below the cricoid cartilage), which measures subtle laryngeal vibrations.

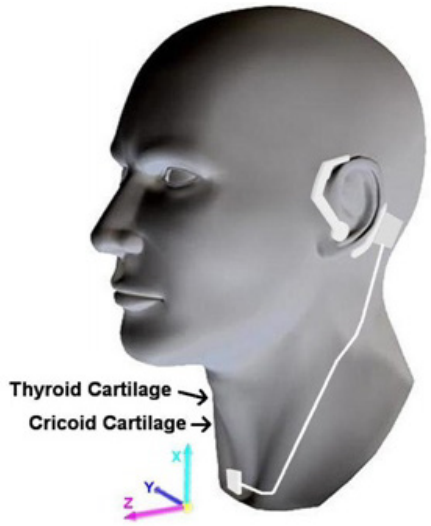

Figure 5.8: Positioning of accelerometer sensors for measuring subtle laryngeal vibrations and head movement. An accelerometer is located in the main device that is placed behind the ear. A supplemental accelerometer is attached to the skin on the suprasternal notch (*i.e.*, over the trachea and below the cricoid cartilage). The head image is modified from (Sanchez 2008).

5.1.2.1 The Play My Melody program

The *Play My Melody* program translates the proper acceleration (*i.e.*, acceleration independent of gravity) of body movement into control of a musical synthesizer in real time. A previous example of an interface based on a similar concept is the *OSCulator* by *Wildora* (2009). This Apple Mac software interface utilises commercial motion sensing devices, such as the Wiimote or Apple iPhone, as MIDI controllers. Actions, such as changes in pitch, roll and yaw, can be defined by the user as events that control the properties of a MIDI synthesizer. Utilising the *WEBS* system

as a hardware platform, the *Play My Melody* program was designed to provide two adaptable channels of user input, subtle body movement, in the form of laryngeal vibrations, and gross body movement, in the form of head orientation.

The *Play My Melody* user interface was created in LabVIEW (Figure 5.9) as a secondary layer GUI - in addition to the primary *WEBS* GUI described in Section 3.3. It consists of a waveform graph, multiple text box indicators and a simple on-screen musical keyboard. A MIDI synthesizer is also initiated in the *Play My Melody* program using the sound card in the computer. The *Play My Melody* program reads the accelerometer data from the output data queue of the primary GUI and calculates the frequency of phonation and head orientation information based on this data stream. The frequency of phonation controls musical pitch while left-right head movement controls timbre. Forwards and backwards head movement can turn the keyboard on/off. A second forwards movement, whilst the keyboard is turned on, initiates a sound recorder to allow the user to record their musical melody.

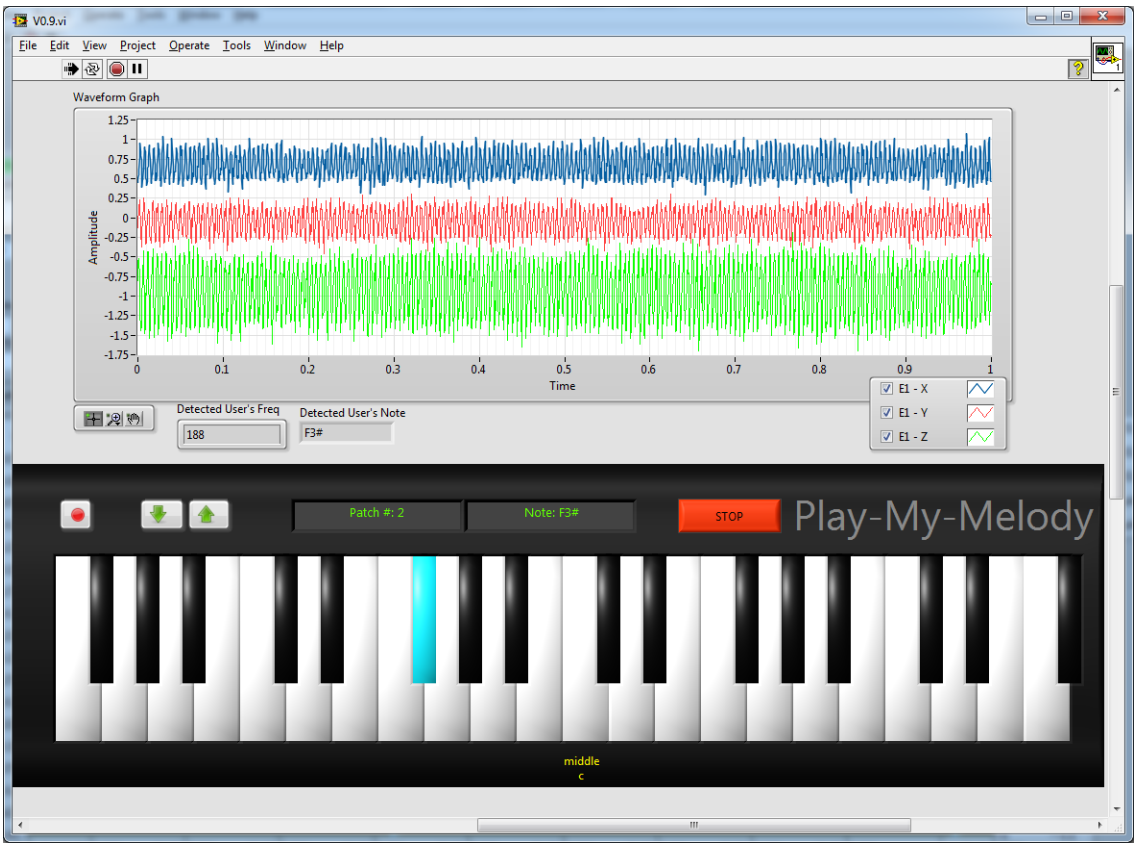

Figure 5.9: The *Play My Melody* program. Using laryngeal vibrations and gross head movement, the musical note and choice of intrument for the displayed keyboard can be selected respectively. The graph at the top of the user interface shows the current window of recorded data that is under analysis and the text box below shows the estimated fundamental frequency of laryngeal vibrations for the current window of data. The keyboard graphic used in the *Play My Melody* program is modified from (Heimbach 2008).

The waveform graph illustrated in Figure 5.9 plots a rolling window of laryngeal accelerometer data along the x, y and z axes. The *WEBS* sampling rate is set at 1157.41 Sa/s – just under the maximum for a two-electrode system reading from all three accelerometer axes. The limits of the human vocal frequency range lie at approximately 78 Hz and 698 Hz for males and 139 Hz and 1108 Hz for females (Hollien *et al.* 1971). This sampling rate is only adequate up to the Nyquist-Shannon frequency of 578.71 Hz. Future iterations of the *WEBS* could increase this sampling frequency limit by redesigning the *WEBS* transmission protocol. However, based on user trials, it can be assumed that the majority of users' vocal characteristics fall below this limit.

The magnitude of acceleration is calculated from the laryngeal accelerometer's axes over a window of 289 samples (*i.e.*, approximately every 0.25 s) and analysis is performed on the result to find the tone with the highest amplitude (using the built-in 'Extract Single Tone Information' express VI in LabVIEW). The computed tone is then displayed in an on-screen text box and used to control the musical note being played on the keyboard. The currently selected piano key lights up and the musical note associated with the key is played through the computer's speakers.

Once initialised, the LabVIEW VI performs a small set-up procedure to find the user-specific limits of head movement and vocal range. The user is requested to angle their head to their maximum left, right, forward and backward positions and then to sing their lowest note followed by their highest note. Based on these measurements, threshold values are set for instrument switching and for on/off/record control.

5.1.2.2 Augmented control of a motorised vehicle

To demonstrate the feasibility of controlling a wheelchair/vehicle, an early prototype of the *WEBS* device was adapted to allow guidance of a radio-controlled toy car. This initial prototype for the *WEBS* consisted of two modules. The main body of the device, which was less than 20 cm^3 in volume and weighed less than 50 g, contained a microcontroller, wireless transceiver, battery, and one accelerometer. A supplementary module, which contained a second accelerometer, was connected to the main device by thin wires. This module is very light-weight and can therefore be directly attached to the skin to measure not only laryngeal vibration - as envisaged in this application - but also signals like the mechanomyogram or cardiac muscle movement. Like most powered wheelchairs and many other vehicles, conventional radio-controlled cars have four controls; forward, backward, left and right. Direction, in this case, was controlled by

tilting the head, as measured by the accelerometer in the main device. The speed of the car was dependent on the frequency of phonation, as measured by the supplementary accelerometer. Block diagrams for the early prototype system and associated images of the devices are illustrated in Figure 5.10.

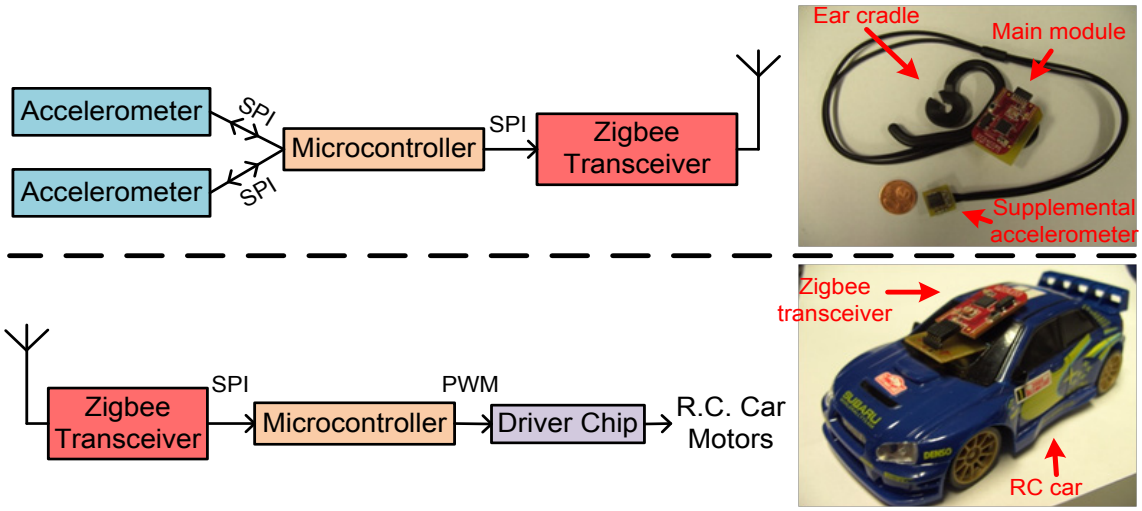

Figure 5.10: Block diagrams and accompanying illustrations of an early *WEBS* prototype deployed as a control interface for a remote-controlled car. The wearable device consists of a main module containing a microcontroller, accelerometer, battery power supply and ZigBee transceiver. A supplemental accelerometer attaches to the main module via a short and lightweight wire. The main module was designed to be worn around the ear with the supplemental module attached to the skin over the larynx (refer to Figure 5.8). The main module communicates wirelessly to a modified RC car containing a ZigBee transceiver, microcontroller and motor driver chip. In this application, head tilt controlled the car's direction whilst frequency of phonation controlled the speed.

The device communicates wirelessly with the radio-controlled car using the ZigBee (2009) wireless protocol (which is based on the IEEE 802.15.4 standard for wireless personal area networks). The advantages of ZigBee include low cost, low power and secure networking. The microcontroller in the main module communicates with both accelerometers and the ZigBee transceiver via Serial Peripheral Interface (SPI). It polls the accelerometers (STMicroelectronics LIS3LV02DL) for the three 16-bit values, each of which represents the acceleration on one of the three axes. The axes were sampled at a rate of 1280 Sa/s over a sensitivity range of ± 2 g.

The ZigBee network processor in the wearable device was configured as an *end device*. Once it is wirelessly connected to a ZigBee network, the data is transmitted to the *coordinator* (*i.e.*, the car) where it can be processed. This ZigBee network used the Texas Instruments (2007a) CC2480 ZigBee network processor, which has a 10 m indoor range and operates in the unlicensed 2.4 GHz range. It provides an over-the-air raw data transmission rate of 250 kb/s. However, after taking into consideration packet acknowledgment time and various transmission overheads, the maximum usable data throughput is 115.5 kb/s (Burchfield *et al.* 2007). This transmission rate provides insufficient bandwidth to cope with the quantity of data from the two accelerometers. Therefore, the frequency of phonation was calculated by the microcontroller in the main module using a software zero-crossing pitch detector on the laryngeal vibration data stream. The result of this calculation, along with the data associated with head orientation, was transmitted to the *coordinator* in the car. Inside the car, a driver chip (the L293D) powered both the directional and driving motors. A change in head orientation triggered the car's *coordinator* microcontroller to toggle a digital output, which altered the state of the directional motor. The speed of the car was controlled by a pulse-width modulated signal where, based on a pre-defined look-up table stored in the memory of the *coordinator* microcontroller, the received frequency of phonation corresponded to a motor speed setting that altered the duty-cycle of the pulse-width modulated signal.

Multiple user trials concluded that this system had a relatively short learning curve for users to adapt to using the accelerometer device. Feedback from these trials indicated that the system is intuitive and, with more practice, a user could easily compete with a peer using a conventional controller. This experiment is described in greater detail in (Nolan *et al.* 2009a).

5.2 An investigation into the spatial localisation of tapping vibrations on the skin-surface for a human-computer interface

5.2.1 Introduction

Traditional human-computer interfaces suffer from the need to have a physical controller, which allows the user to control some functionality of a computer device. Mice, keyboards and touch screens form the basis of conventional interaction between able-bodied people and computer technology. These input devices consume space and require fine motor control and dexterity. Touch screens are becoming increasingly usable and reliable. However, the communication medium is limited by the size of the screen, they have a limited durable lifetime, and dirt or other foreign objects on the surface area can affect their use. Modern input device concepts, such as facial expression recognition software or projection keyboards, go some way towards minimising the number of physical components in the communication channel between the user and a computer. This section describes an investigation into another minimal technology approach that could be taken in which the surface area of skin on the human body, such as a forearm, could be transformed into an accessible human-to-machine communication platform.

Several recent studies into the adaption of surfaces in a user's environment as human-computer interfaces can be found in the literature. Harrison and Hudson (2008) have developed a scratch input recognition device. Their acoustic sensor, when attached to a textured material such as wood or plaster, has the ability to recognise several predefined scratch gestures. Waterloo Labs (2009) have demonstrated a method for impact detection and approximate position localisation on a wall's surface utilising a

grid of four accelerometers. Their system projects a graphics display onto a wall where a user can hit the wall's surface and the spatial location of the impact is estimated. This impact position then triggers a mouse click at the corresponding screen coordinates. Harrison *et al.* (2010) have also demonstrated that it is possible to localise the source of an acoustic wave travelling through the human body for the purpose of appropriating the body as an input surface. Their system, titled *Skinput*, utilises two arrays of five cantilevered piezo films; each sensitive to different frequency ranges. The sensor arrays are attached on a band around the upper arm and, utilising the variable acoustic amplitude (depending on the distance of a tap), can detect taps on ten locations spread across a 2-D surface on the forearm with an accuracy of 81.5 %. Various systems exist in which an accelerometer or gyroscope is directly used for position and orientation detection without the use of a medium. Examples such as gyro-mice and computer game controllers are commercially available. However, they suffer from the same disadvantages as conventional keyboard and mice as discussed previously.

The *WEBS*-based tap detector provides an adaptable user input facility that allows a user to exploit his or her skin-surface as a computer interface using a simple, low-cost and intuitive device that can be installed or removed in a matter of seconds by any user regardless of their technical ability. In this section, an experiment is described that demonstrates the feasibility of using two *WEBS* slaves as vibration sensors for a 1-D skin-surface keypad. An initial classifier is described which uses the magnitude of acceleration and phase difference, as measured by the two *WEBS* slaves, to differentiate between three tap positions.

5.2.2 Materials and methods

When the surface of the skin is impacted, waves of sound propagate through the air whilst vibration waves propagate through the tissue itself. The measurement approach taken here involves monitoring the vibration waves that travel transversely through the skin-surface medium after a tap has occurred. Figure 5.11 illustrates a simplified model of a forearm with two *WEBS* slave sensors, node A and node B, positioned at either end.

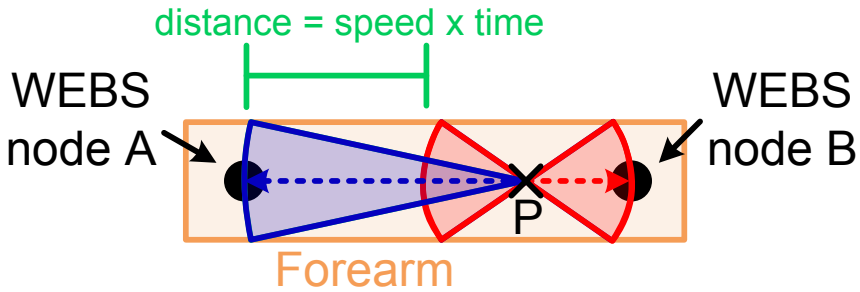

Figure 5.11: A simplified diagram of a forearm illustrating a tap occurring at point P between *WEBS* nodes A and B. The vibration wave (red and blue shaded arcs) propagates transversely out from the point-of-contact and arrives at *WEBS* node A shortly after it arrives at *WEBS* node B.

When a tap occurs at point P, a vibration wave travels outwards from the point of contact; first reaching node B and then shortly afterwards at node A. The further the wave travels through the tissue, the more the amplitude of the wave decreases. The position of the tap can be estimated by analysing the difference in the recorded magnitude of acceleration and the time delay, as measured at the two locations.

An experiment was devised to examine the feasibility of the analytical approach for taps with varying applied force. Figure 5.12 illustrates a forearm with two *WEBS* slaves (attached to the skin via button electrodes) and three tap locations (consisting of strips of conductive adhesive tape) situated between them. The conductive adhesive tape was used as a tap position indicator. On the opposing hand, a forth strip of conductive

adhesive tape was attached to the underside of the index finger which completed a circuit when in contact with a tap location. An accelerometer was also attached to nail surface of the index finger on the opposing hand (via double-sided tape), which recorded the force of each tap. The position of the *WEBS* slaves and tap locations were determined by measuring the length of the forearm between the two prominent anatomical features (*i.e.*, the medial epicondyle and the pisiform) of an outstretched arm and dividing the distance using the ratios shown in Figure 5.12. In this experiment, the overall length was measured to be 29 cm on this subject.

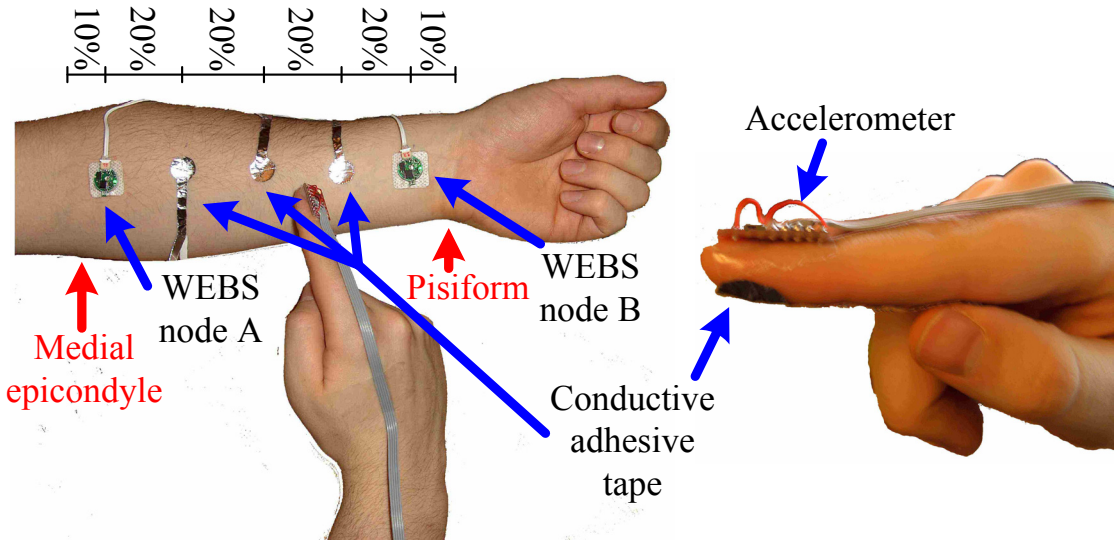

Figure 5.12: A diagram illustrating the experimental set-up for investigating skin tapping as a human-to-machine communication modality. The *WEBS* nodes and tapping locations were positioned in the area between medial epicondyle and the pisiform using the ratios shown. The subject tapped on each of the tapping locations using thirty light, medium and hard taps (totalling 270 taps). Each of the *WEBS* slaves recorded accelerometer activity in the z-axis (normal to the skin) whilst a data acquisition device (the NI-USB 6215) recorded the actual position and force of the tap. The tap position was recorded by measuring the output voltage from different voltage divider networks that were formed with the connection of conductive adhesive tape on the forearm and index finger. The tap force was recorded from an accelerometer located on the index finger of the opposing hand.

The tap position indicator, which was only used during the experiment and would not form part of the interface in normal use, worked using a voltage divider

circuit where the junction between the resistances consisted of the conductive adhesive tape attached to the forearm and index finger. Conductive adhesive tape was used as it is thin and lightweight and therefore has a minimal damping effect on the tap vibration wave. Each strip of conductive tape on the forearm was connected to the circuit ground via a different resistance value (33 kΩ, 1.8 kΩ and 1 kΩ). The conductive tape on the index figure was connected to the 3.3 V supply via a separate resistance (3.2 kΩ). A data acquisition device, the NI-USB 6215, measured the voltage on the index finger conductive tape. When the index finger came into contact with each tap location, the voltage divider circuit was completed and a different voltage was measured by the NI-USB for each tap location. The NI-USB also recorded the force of the tap by measuring the output of the tri-axial analog accelerometer situated on the index finger. The NI-USB sampled the tap position indicator and x, y and z axes at a rate of 2 kSa/s.

The *WEBS* slaves' accelerometers were set to their most sensitive setting of ± 2 g. Only the z-axis was sampled in order to achieve a high sampling rate of 1358.70 Sa/s – the maximum for single accelerometer axis measurement from a two-slave system. During testing, a healthy male subject (age, 29; height, 180 cm; weight, 85 kg) was requested to place their elbow on a flat surface with the forearm at a fixed elevation of 20°. The subject was asked to perform thirty light, medium and hard taps on each of the three tap positions (totalling 270 taps) with a short delay between taps (approximately 1 s). A virtual instrument (VI) was created in LabVIEW to receive and store the two data streams (from both the *WEBS* and the NI-USB) to an output data file. The data was subsequently processed and analysed in MATLAB. Ethical approval was granted for this experiment (DIT reference number: 18/08) and the test subject gave informed consent.

5.2.3 Results

Figure 5.13 shows a window of the recorded data file illustrating one tap on each tap location, as highlighted by the voltage change in the tap position indicator. In order to prevent the orientation of individual *WEBS* nodes from influencing the experiment, the mean acceleration was subtracted from both *WEBS* z-axes respectively followed by rectification. As long as the arm remained stationary during testing, the exact orientation of both the arm and each individual *WEBS* node was inconsequential. As there were two different data streams with separate time bases from the NI-USB and *WEBS* devices, it is possible that the time delay from the moment of contact to the detection of the vibration wave by the *WEBS* nodes, as illustrated in Figure 5.13, is very slightly inaccurate. However, for the purposes of this experiment, an exact delay time is not necessary.

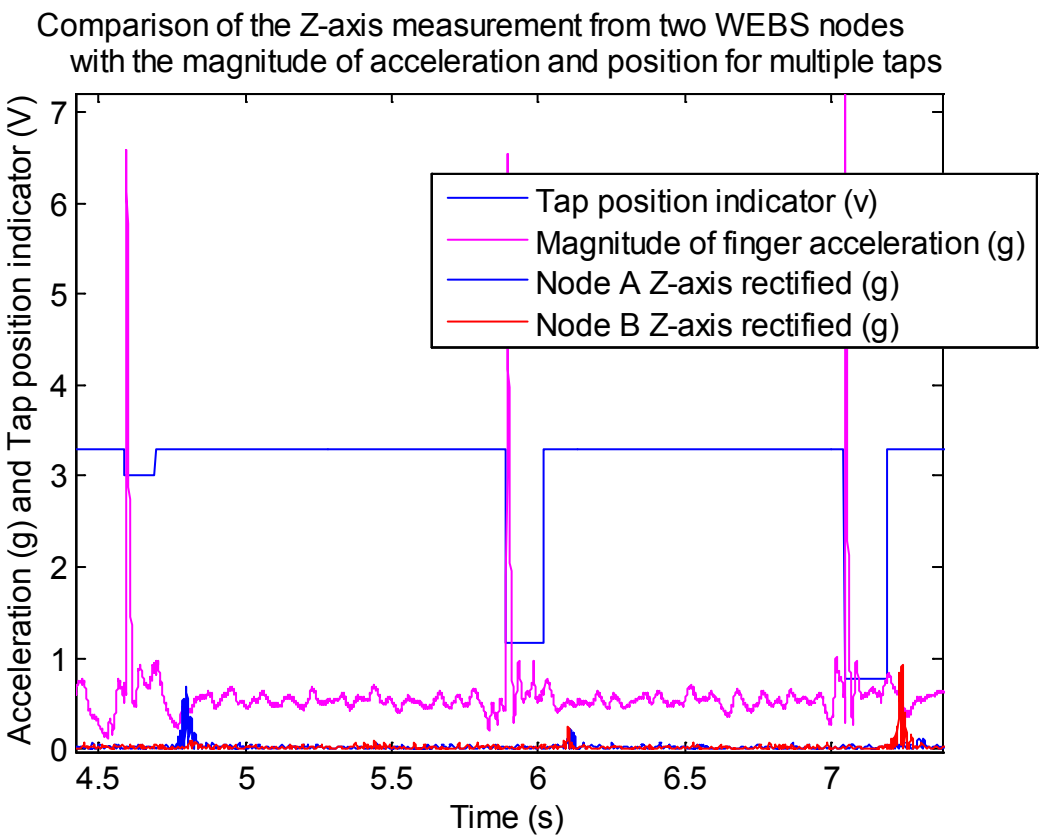

Figure 5.13: A time-series plot illustrating the results from three taps at different forearm positions. The position of each tap is indicated by the blue line. The magnitude of acceleration, as measured by an accelerometer attached to the finger, is represented by the pink line with the very prominent peaks. The z-axis measurement from two *WEBS* nodes, positioned at each end of the forearm, are illustrated by blue and red lines near the bottom of the graph. The time shift in the *WEBS* data is a result of measurement from two unsynchronised recording systems.

It is evident from Figure 5.13 that each *WEBS* node responds differently to taps at each location. In the middle location, both nodes have roughly the same amplitude of acceleration occurring at approximately the same time. At the outer locations, the *WEBS* node that is closest to the point-of-contact recorded a higher amplitude of acceleration, occurring slightly before the other *WEBS* node. A script was written in MATLAB to identify the peak amplitude of the rectified z-axis signal at each *WEBS* node for each tap and calculate the time difference and amplitude difference between the peaks. Figure 5.14 illustrates all 270 taps in terms of these two factors. Using the NI-USB data,

a different symbol is used to highlight each tap position and a varying colour scale represents the peak magnitude of acceleration of the tapping finger.

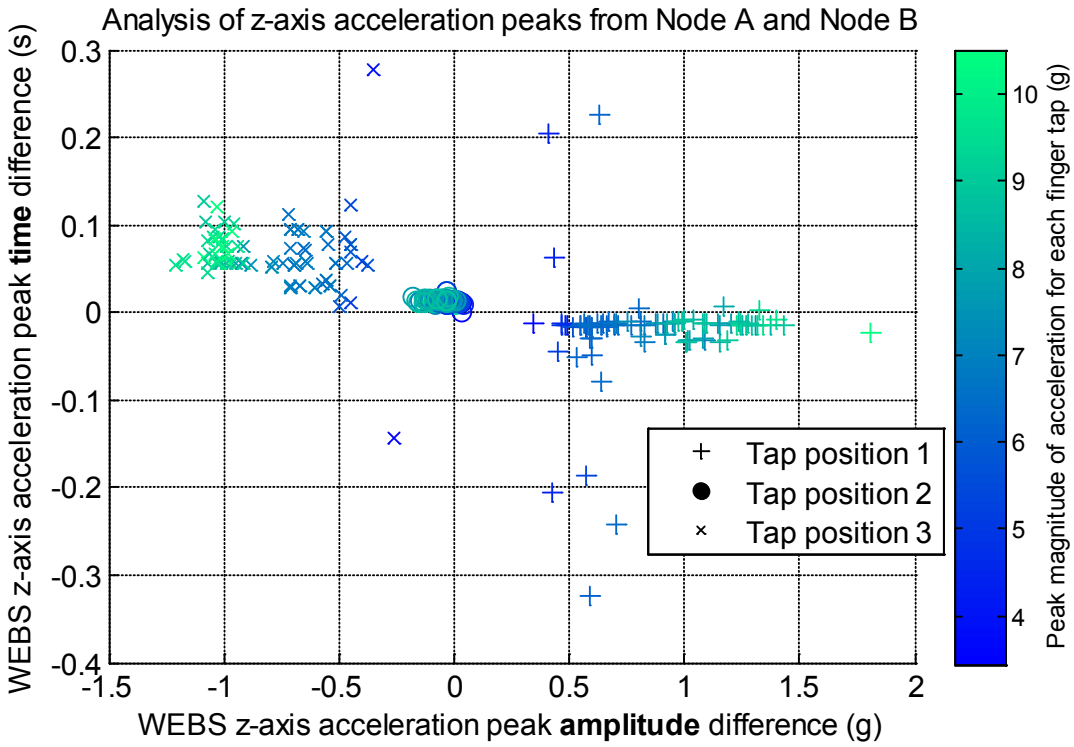

Figure 5.14: A scatter plot for the analysis of 270 taps on three pre-defined forearm tap locations comparing time difference and magnitude difference of z-axis acceleration peaks at each of the two *WEBS* nodes. Two *WEBS* sensors recorded z-axis acceleration trajectories from two positions on the arm. The actual tap position is indicated by different marker symbols. The actual magnitude of acceleration of each tap (measured using a separate finger-mounted sensor) is shown on the colour scale.

As shown in Figure 5.14, all tap positions can be reliably classified from the *WEBS* z-axes acceleration data; albeit with different levels of confidence depending on which feature is given more weight. The time difference between detection at each node is predominately in the ± 0.05 s region (taking into account the offset described in the next paragraph) with taps at each location lying mainly in specific regions. As the test region length was 29 cm and the maximum distance that the vibration wave needs to travel to the furthest node after it has arrived at the nearest node is 40 % of this length (refer to Figure 5.11 and Figure 5.12), a time difference of 0.05 s indicates that the

velocity of the surface waves is approximately ≥ 2.32 m/s. This is in line with values found in the literature (Sofia and Jones 2013). Some errors are observed outside of this range but only when tap intensity is low. More robust classification is achieved by analysing the peak acceleration amplitude difference between each node. In this case, the tap positions visibly fall into distinct regions.

One would expect that the vibration wave from the middle tap position would arrive at both nodes at the same time; however, the time difference illustrates a small offset. This could be a result of the middle tap position not being located precisely equidistant between the two nodes during the experiment and/or that the velocity of the vibration wave is affected by different tissue properties throughout the arm (*i.e.*, softer/harder body tissue results in slower/faster wave propagation respectively) (Sofia and Jones 2013). Similarly, various types of tissue will also affect the amplitude of the vibration wave, as initially determined by the intensity of tap applied. Figure 5.15 further illustrates the relationship between the force of impact and the vibration wave amplitude, as measured at each node. In this figure, the vertical axis represents the intensity of the tap. As shown, the peak amplitude difference reduces as the intensity of the tap decreases. The different responses shown between tap positions 1 and 3 as the tap intensity increases highlights the expected uneven wave propagation throughout the arm.

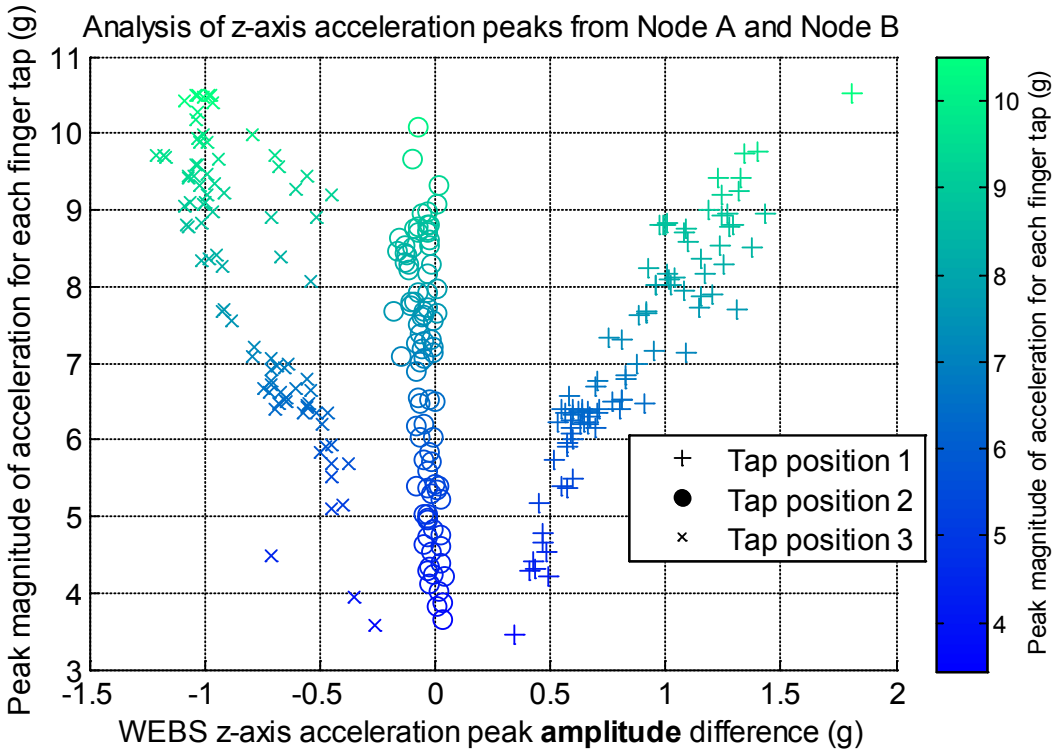

Figure 5.15: A scatter plot for the analysis of 270 taps on three pre-defined forearm tap locations comparing the magnitude of acceleration for each tap (as shown on the vertical axis and colour scale) with the magnitude difference of z-axis acceleration peaks at each of the two *WEBS* nodes. Two *WEBS* sensors recorded z-axis accelerations trajectories from two positions on the arm. The actual tap position is indicated by different marker symbols.

5.2.4 Conclusions

This section demonstrated the use of two *WEBS* slaves to measure skin-surface vibrations resulting from finger taps on the skin surface. Two features extracted from the *WEBS* slaves' z-axis accelerometer data, the time and amplitude difference of the peak accelerations, could be used to train a classifier to distinguish between various tap locations. When the magnitude of acceleration on either z-axis exceeds a threshold, analysis performed on both the time and amplitude difference of the peaks could reveal the tap position with a high-degree of certainty.

Since the frequency range of the vibration wave is low, a future experiment might sacrifice the high sampling rate used in this experiment in order to obtain the x, y

and z axes from each *WEBS* node; thus providing both tangential and longitudinal skin-surface vibration sensing. This would provide a greater number of features for a classifier, which might be needed when scaling up the number of tap locations.

Although the application described in this section was deployed on the human body, the same system could also be deployed on a wide array of other surface material types. In this way, a user could potentially turn surfaces in their surroundings into interactive touch pads.

5.3 *A computer game interface based on bioelectrical and biomechanical signal inputs*

The goal of this section is to demonstrate that the combination of bioelectrical and biomechanical activity, as recorded by the *WEBS* system, can be utilised as a control signal in a human-to-machine interface. The *WEBS* facilitates the translation of voluntarily controlled physiological signals into generic control signals. The electromyogram (EMG) (*i.e.*, electrical activity originating in working muscles) is an obvious candidate to target for a voluntarily controllable biopotential. An initial application was therefore devised to utilise bicep EMG and gross arm movement as control input for keystrokes in a PC interface. The *WEBS* system was configured as shown in Figure 5.16. Two *WEBS* slave electrodes were positioned across each bicep muscle and the EMG was calculated in software from the voltage difference between the measuring electrodes on each arm.

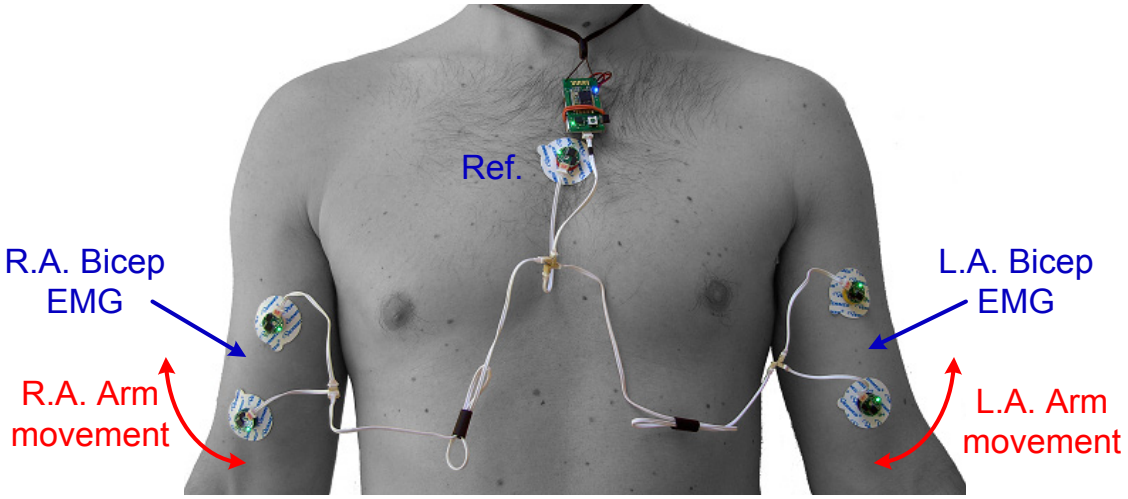

Figure 5.16: An image of the *WEBS* electrode locations for measuring bicep EMG and supplementary arm movement activity. Each voluntarily controllable biosignal can be harnessed as a channel of communication and control in a human-to-machine interface.

A VI was created in LabVIEW (shown in Figure 5.17) to process the information coming from the primary *WEBS* GUI (Section 3.3) and to provide an

interface that allows a user to link physiological signal events to specific keyboard buttons. The user can specify threshold bands (as shown by yellow bars in the on-screen gauges) for each signal and their corresponding keyboard buttons can be selected from adjacent drop-down boxes. A rolling average is calculated in real time on the rectified EMG signal and on the arm orientation data stream from each arm. Depending on the measured level of each signal, the chosen keyboard button is programmatically simulated.

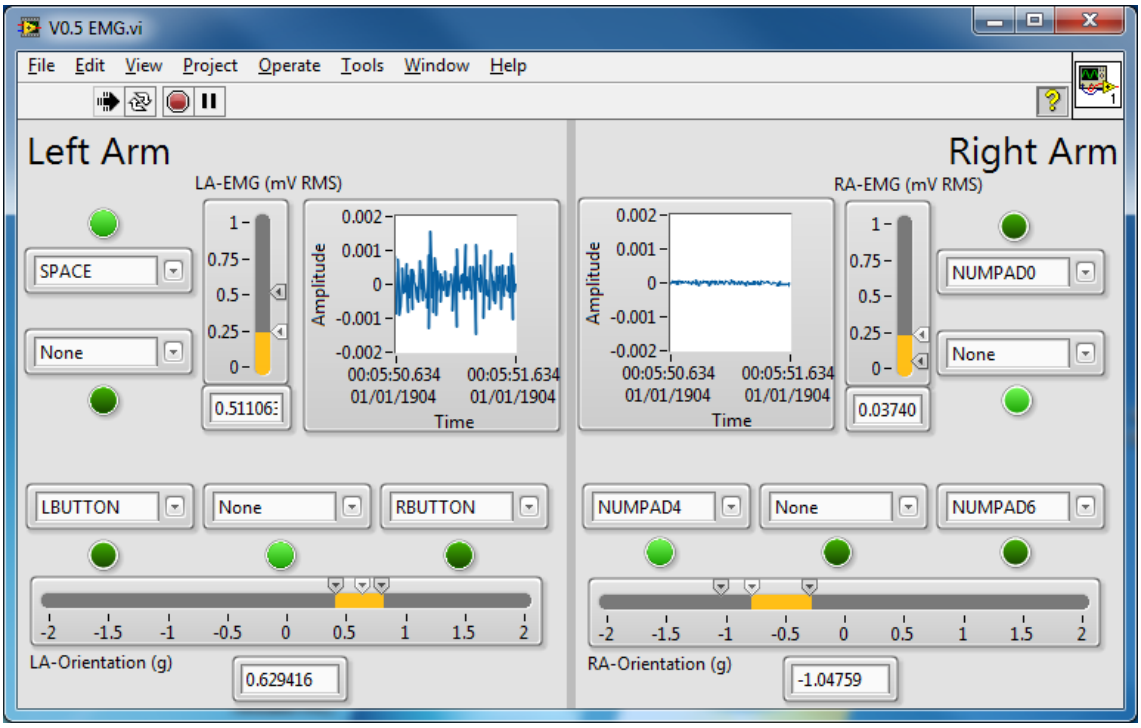

Figure 5.17: A screen shot of the VI that was created in LabVIEW to take the parsed biopotential and biomechanical signals from the primary GUI (described previously in Section 3.3) and translate them into a real-time computer interface. In this case, various user actions can be used to trigger user-definable simulated keystrokes. The screen is divided into two windows, one for the left arm and one for the right. The upper half of each window shows bicep EMG information and the lower half shows arm accelerometer information. In this example, by tensing the users' left bicep, they have triggered the 'SPACE' key and by altering the orientation of their right arm they have triggered the 'NUMPAD4' key (as highlighted by the on-screen LED indicators).

A simple computer game, titled *Bicep-Bullseye*, was also created to demonstrate the use of the *WEBS* as a human-to-machine control interface and this is illustrated in

Figure 5.18. In this game, the screen is divided into two windows, one for each arm input. A penguin appears at random locations along a horizontal axis in each window for a set interval. During this time, the user has to target the penguin by adjusting their arm orientation - which moves each crosshair horizontally. A short contraction of either bicep muscle causes the corresponding crosshair to turn red and, if the crosshair is pointing at the penguin, the user scores a point.

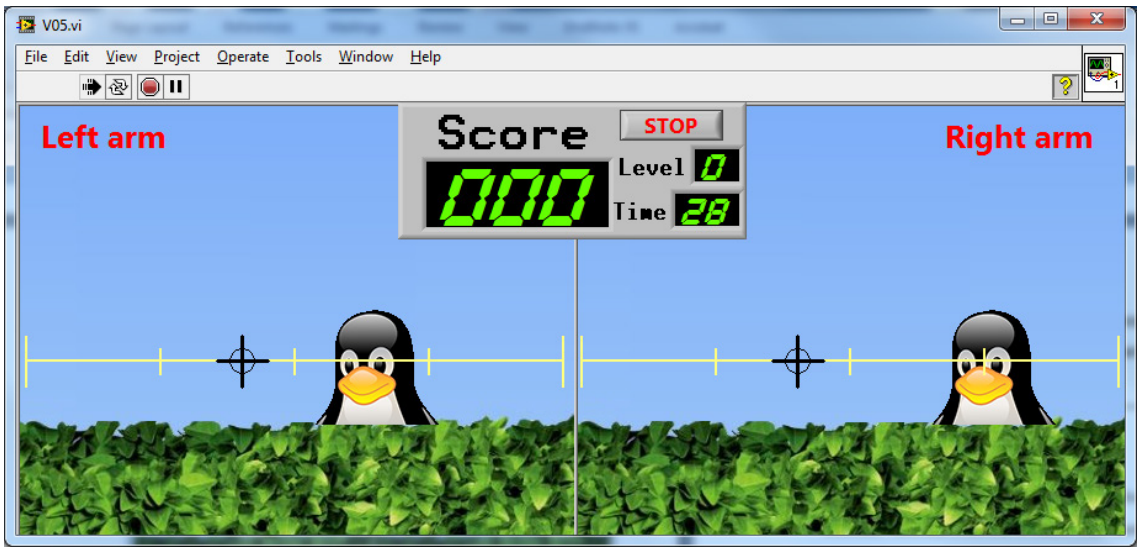

Figure 5.18: A screen shot of the *Bicep-Bullseye* game that was designed to demonstrate the ability of the *WEBS* to be utilised as a human-to-machine interface. The angular moment of each the arm controls the linear movement of the crosshair and a contraction of a bicep muscle causes a shot to be fired.

5.4 A digital 12-lead ECG strip chart with augmented biomechanical information

In clinical observation of the heart, the 12-lead ECG strip chart is ubiquitous. This strip chart is a standardised and informative method of presenting cardiac activity to a clinician for diagnosis of conditions such as arrhythmias (*e.g.*, atrial or ventricular fibrillation) or heart abnormalities (*e.g.*, enlarged heart). The 12-lead ECG strip chart is a plot representing the electrical potential variation originating within the heart from multiple view points on the surface of the human body. The name given to the 12-lead ECG does not arise from the number of electrodes placed on the body (only ten electrodes are used to obtain a 12-lead ECG), but rather from the combined number of directly measured and derived electrical signals that it presents. As illustrated in Figure 5.19, the 12-lead ECG consists of three bipolar limb leads (I, II and III), three augmented limb leads (aVR, aVL and aVF) and six unipolar chest leads (V1 to V6) (Malmivuo and Plonsey 1995: 286-289). The 12-lead ECG strip chart is conventionally divided into a 4 x 3 array containing each electrical signal (*i.e.*, 12-leads) plotted on the same graph.

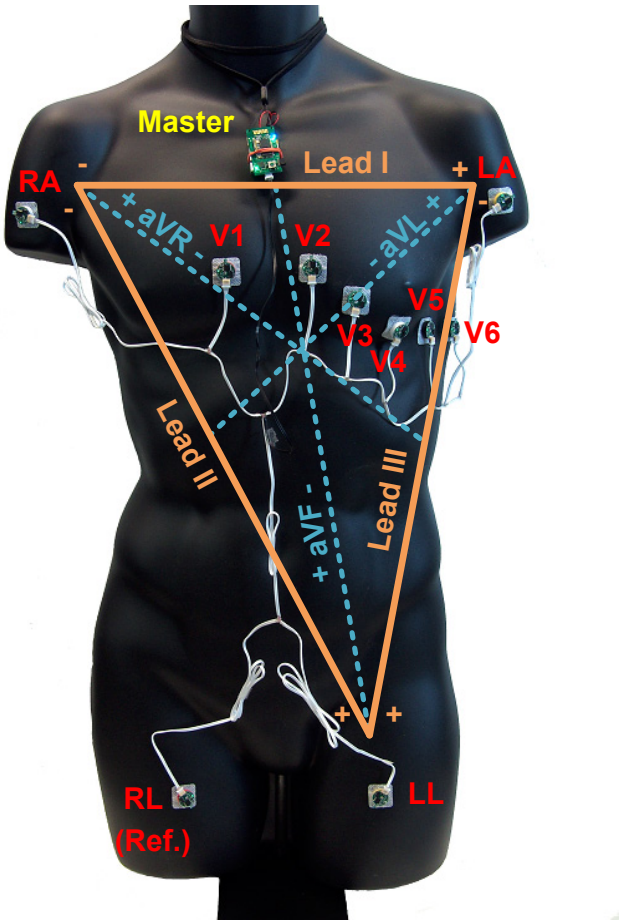

Figure 5.19: An image showing the *WEBS* electrode configuration for 12-lead ECG measurement. The three bipolar limb leads (I, II and III), the three augmented limb leads (aVR, aVL and aVF) and six unipolar chest leads (V1 to V6) are highlighted.

Various commercially available biopotential measurement systems exist that provide an integrated solution for measuring biopotential activity, storing the acquired information digitally and subsequently analysing it though a computer interface. Systems such as *CardioSoft* by *GE Healthcare* (2013) or *CardioCard* by *Nasiff Associates* (2013) combine a complete 12-lead ECG bioinstrumentation front end with custom-built software interfaces. The software interface design described in this section advances the state of the art by capitalising on the features of the *WEBS* to augment the bioelectrical record with a fully integrated biomechanical record - as recorded by an accelerometer incorporated into each *WEBS* electrode. The accelerometers provide rich information concerning subtle and gross movement activity from multiple points on the

body. This information can indicate possible instances of motion artefact or provide an indication of levels of user activity during ECG measurement.

A virtual instrument (VI) was designed in LabVIEW (Figure 5.20) to mimic the traditional 12-lead ECG strip chart, but with the additional improvements that are provided by the *WEBS* system. In this configuration, the designed application is capable of displaying 48 channels of biopotential and biomechanical information from the *WEBS* system (including the three bipolar limb leads and three augmented limb leads mentioned previously). The actual number of data channels that are transmitted from the *WEBS* system is 45. As can be seen in Figure 5.20, each window of biopotential activity (9 data channels) is augmented with 3-axis biomechanical information from either: the accelerometer built into each of the nine *WEBS* slave electrodes (27 data channels); or the accelerometer, gyroscope and magnetometer built into the *WEBS* master (9 data channels).

A traditional 12-lead ECG strip chart provides a single snapshot of ECG activity for a clinician to analyse. In this application, the information can be streamed in real time or loaded from a pre-recorded data file. A scrollbar facilitates synchronised scrolling between all of the graphs so that a clinician can scroll through a recording with the augmented biomechanical information providing additional relevant context to changes in the cardiac cycle of the heart.

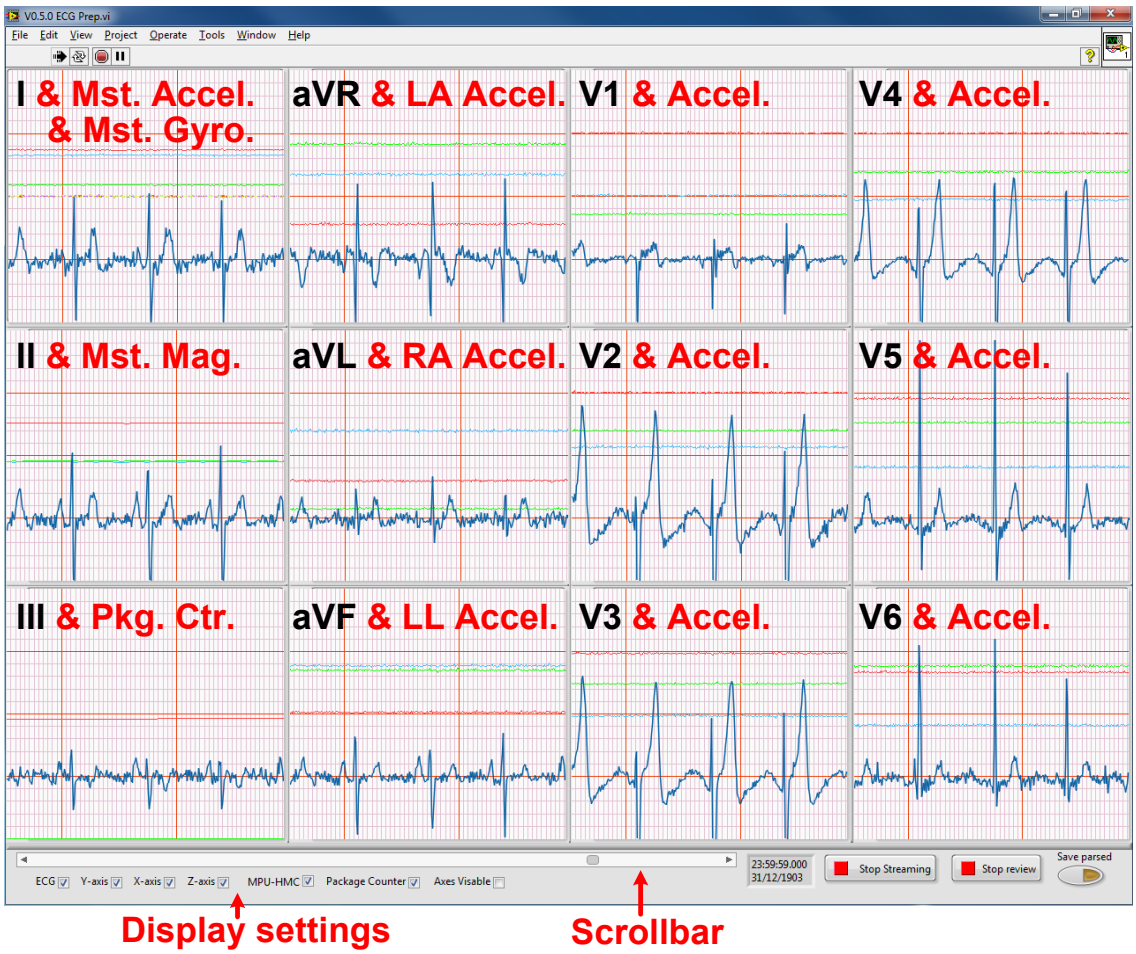

Figure 5.20: The novel accelerometer-enhanced 12-lead ECG strip viewer application. Electrical activity (dark blue lines) is augmented by the 3-axis accelerometer record of activity from each *WEBS* electrode (red, green and light blue lines). Additionally, the plots for leads I, II and III include the 3-axis accelerometer, gyroscope and magnetometer activity from the *WEBS* master. For illustrative purposes, each graph is shown over a window of 4.8 s. The vertical axis range for each signal is: – 5 mV to + 15 mV for electrical activity, ± 2 g for the accelerometers, ± 250 °/s for the gyroscope and ± 1883 mG for the magnetometer.

The results shown in Figure 5.20 were taken from a healthy male subject (age, 29; height, 180 cm; weight, 85 kg) who was placed in a relaxed seated position. The *WEBS* electrodes were attached by Ag/AgCl wet-gel electrodes using the method described in Section 3.4. The *WEBS* ADCs were configured to have an over-sampling ratio of 1024 (*i.e.*, the highest resolution setting) and a gain of 1. All 45 data channels were sampled at a rate of 122.55 Sa/s - just below the highest rate possible for this electrode configuration. The recorded biopotential signals were passed through a digital

50 Hz notch filter to remove AC mains interference followed by a digital high-pass filter with a cut-off frequency of 0.5 Hz to remove DC drift. Note that during normal operation, the VI graph scaling is set to be the same as 12-lead ECG strip chart paper – each minor division represents 0.1 mV in the vertical direction and 40 ms in the horizontal direction. However, for illustrative purposes each graph is displayed over a 4.8 s window in Figure 5.20. Ethical approval was granted for this experiment (DIT reference number: 18/08) and the test subject gave informed consent.

To demonstrate the effectiveness of the system, the subject was asked to stand upright and perform several jumps, each at various intervals. This sudden mechanical movement was sufficient to elicit a response in each of the *WEBS* mechanical sensors. Figure 5.21 shows a snapshot of the recordings in which the mechanical activity associated with the jump clearly causes an electrical disturbance in the biopotential signal. A short settling time in the biopotential signal is also visible after mechanical movement has ceased.

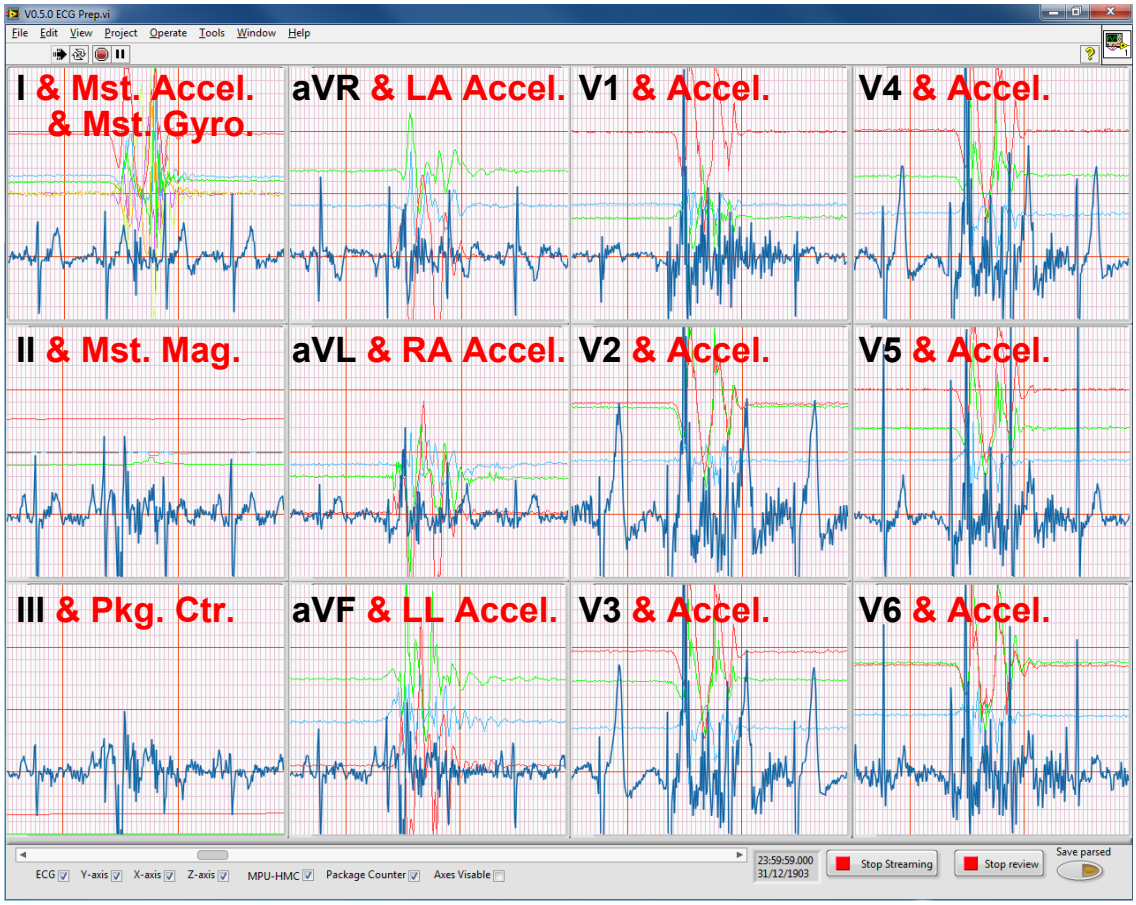

Figure 5.21: The novel accelerometer-enhanced 12-lead ECG strip viewer application illustrating the benefit of augmenting bioelectrical activity with mechanical movement information. In this example a subject was instructed to perform a jump whilst their 12-lead ECG with augmented biomechanical activity was recorded.

A point of interest that became apparent during the course this experiment is that there are subtle differences in the performance of each *WEBS* slave's ADC. Some electrodes (*e.g.*, at V1 and V6) produced a slightly noisier output than others. While this can partly be explained by variation between different electrode-skin junctions, another possible reason is inconsistency in the hand assembly of each electrode (*e.g.*, overheating of components during soldering or inadequate solder at junctions). This issue will be discussed further in the Section 6.3.

5.5 *Skin impedance investigation using pseudo-random binary sequence analysis*

In Chapter 2, various issues associated with a poor quality connection at the electrode-skin junction during biopotential measurement were discussed - such as an increased susceptibility to external electrical interference or an increased risk of motion artefacts. Also described was the impedance meter that is conventionally used to test the connection quality, specifically at two frequencies of interest - 10 Hz for EEG and 30 Hz for ECG. In Section 3.2.6, a circuit and software design for easily incorporating PRBS system identification into the *WEBS* architecture was discussed. In this section, the implementation of that design is described. The results from various tests are also presented in which the frequency response was obtained for each of the systems in the following list of experiments:

Experiment 1 – Band-pass filter

Experiment 2 – High-pass filter with electrode-skin model

Experiment 3 – Low-pass filter with electrode-skin model

Experiment 4 – High-pass filter with human body

To investigate the capabilities of PRBS system identification with the *WEBS* system, experiments 1 through 3 were devised to obtain the frequency response of multiple breadboard-based passive filter circuits. To test the design in a real-world application, experiment 4 was also performed in which the impedance between two points on the body was examined. In experiment 4, the subject was a healthy male (age, 29; height, 180 cm; weight, 85 kg). Ethical approval was granted for this experiment (DIT reference number: 18/08) and the test subject gave informed consent.

After experimentation was complete, analysis of the recorded signals was carried out in MATLAB; Table D.3 (in Appendix D) provides a simplified version of the MATLAB script written for this purpose. Figure 5.22 shows a block diagram of the MATLAB calculation steps. For each of the breadboard-based tests carried out in this section, the obtained frequency response is compared against simulated frequency responses. The MATLAB '*bode*' command was used to obtain the expected frequency response of the system from the calculated transfer function while the '*lsim*' command was used to simulate the time response of the system model to a PRBS signal input. For accurate comparison with the physical test results, both calculated frequency responses used a discrete-time system model of the calculated transfer function. This was achieved using the MATLAB '*c2d*' command, which uses a zero-order hold that is sampled at a fixed sampling frequency to convert from continuous model to a discrete model.

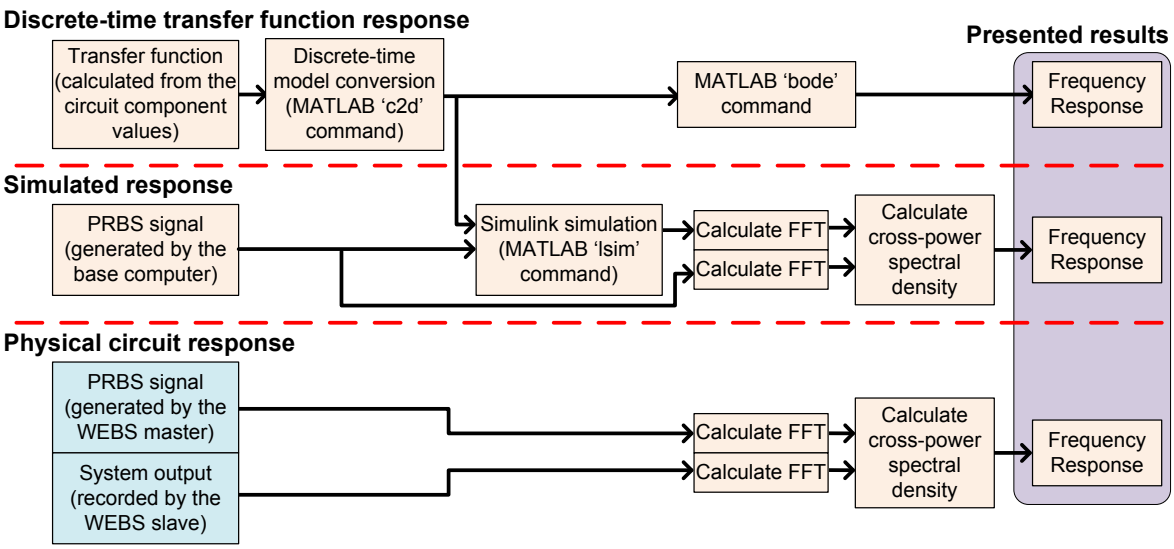

Figure 5.22: A block diagram showing the sequence of computation that were performed in the PRBS system identification experiments. The three sets of results (*i.e.*, the discrete-time transfer function response, the simulated response and the physical circuit response) were obtained for the breadboard-based series of experiments where the systems under investigation had known component values. For the experiment performed on a human body, only the physical circuit response was calculated. Blue shading signifies results that were obtained from *WEBS* system, orange shading signifies processing performed in MATLAB and purple shading signifies the results presented in this section.

As described in Section 3.2.6, by calculating the cross-power spectral density (using the direct calculation method shown in Appendix D) of the input PRBS signal and the measured and simulated output signals, the frequency response of the system can be obtained. Figure 5.23 illustrates a time-domain extract from one of the experiments performed which shows the input PRBS signal and the measured and simulated output signals on which the cross-power spectral density is calculated. The impulse response of the system in each experiment presented here was also calculated analytically (using the method shown in Appendix D) and they can be found in Appendix F.

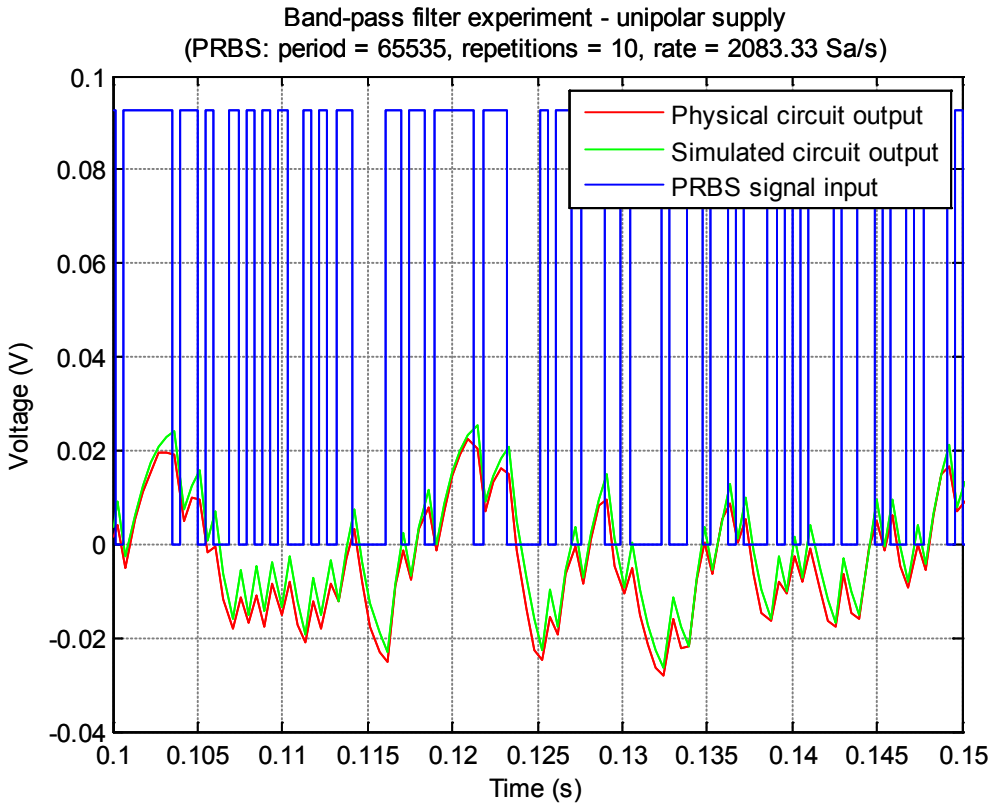

Figure 5.23: An extract of the time-domain response for PRBS system identification on a known system. The original PRBS signal is plotted alongside the measured and simulated output signals. The PRBS bit rate and the sampling rate are synchronised. However, there is a small ADC sampling delay of 133.81 µs between the PRBS bit change and the point when the ADC produces a sample, which has been taken into account in this figure.

Although the choice of PRBS bit rate, shift register length and number of iterations can be configured using the *WEBS* user interface (Section 3.3), for

consistency between the experiments carried out in this section, each of these values was held constant. The PRBS bit rate was fixed at 2083.33 Sa/s - the current maximum achievable sampling rate for a single *WEBS* slave system (see Appendix C). The PRBS sequence length was set at the maximum achievable with 16-bit shift register (*i.e.*, 65535 bits per iteration) and the number of PRBS sequence iterations was set to 10 (*i.e.*, 655350 bits in total). Since the frequency resolution of the resulting cross-power spectral density is Fs/N (*i.e.*, $2083.33 / (2^{16} - 1) = 0.032$ Hz) (Horowitz and Hill 1989: 659), the number of frequency response data points with these PRBS settings exceeds that which is required to uniquely determine the parameters of the low-order systems investigated in this section. However, this redundancy reduces the sensitivity of each parameter estimation to errors in measured response at each frequency.

For each experiment, the *WEBS* ADC was set to use a low over-sampling ratio (OSR) of 32 (in order to achieve a higher sampling rate). At this OSR rate, as stated previously in Section 3.2.4, there is a delay of approximately 133.81 µs between initialisation of *WEBS* slave ADC sampling (and therefore PRBS bit change in the *WEBS* PRBS implementation) and the point at which an ADC sample is produced - this small delay has been taken into account in Figure 5.23.

5.5.1 Experiment 1 – Band-pass filter

The first experiment was devised to prove the feasibility of PRBS system identification with the *WEBS* by analysing a simple passive band-pass filter. In this experiment, the PRBS circuitry described in Section 3.2.6 was reduced to the minimum number of required components - as illustrated in Figure 5.24. The PRBS signal was applied at the input to the filter and its output was measured.

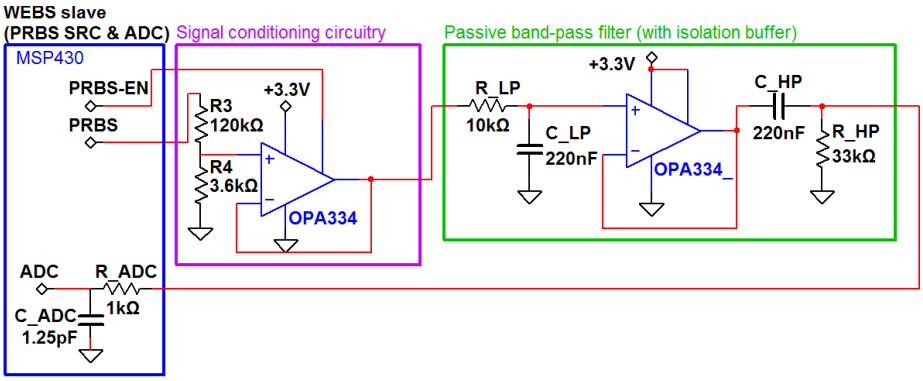

Figure 5.24: A schematic showing the circuit configuration for an initial test of the *WEBS* PRBS system identification capabilities. In this test, a PRBS signal is sent from a *WEBS* slave, via signal conditioning circuitry, into one end of a passive band-pass filter circuit. The output is then measured by an ADC in the same *WEBS* slave. The signal conditioning circuitry scales down the digital line output voltage from the MSP430 into a suitable voltage range for the ADC. An op-amp is placed between the two stages of the passive band-pass filter for isolation purposes.

A unity-gain operational amplifier (op-amp) circuit was used to isolate each stage of the passive band pass filter as shown. The transfer function of this filter is given below. Although the input impedance to the analog-to-digital converter (R_{ADC} and C_{ADC}) has a loading effect on the second stage of the filter, the impedance values are considered low enough to have minimal impact in this example. The input and output voltages of the filter are related as follows.

$$\frac{V_{OUT}}{V_{IN}} = \left(\frac{1}{1 + \frac{R_{LP}}{Z_{C_{LP}}}} \right) \times \left(\frac{\frac{R_{HP}}{Z_{C_{HP}}}}{1 + \frac{R_{HP}}{Z_{C_{HP}}}} \right) \tag{5.4}$$

The resulting frequency response obtained from the described experimental, simulated and theoretical methods is shown in Figure 5.25. This figure shows a high-degree of consistency in both the magnitude and phase of each response. As highlighted in Figure 5.25, the cutoff frequencies approximately match for each response. The roll-off is approximately 20 dB/decade for each response - as expected for each first-order system in the band-pass filter. The low level of variance in the physical circuit response is expected due to averaging over the 10 PRBS iterations.

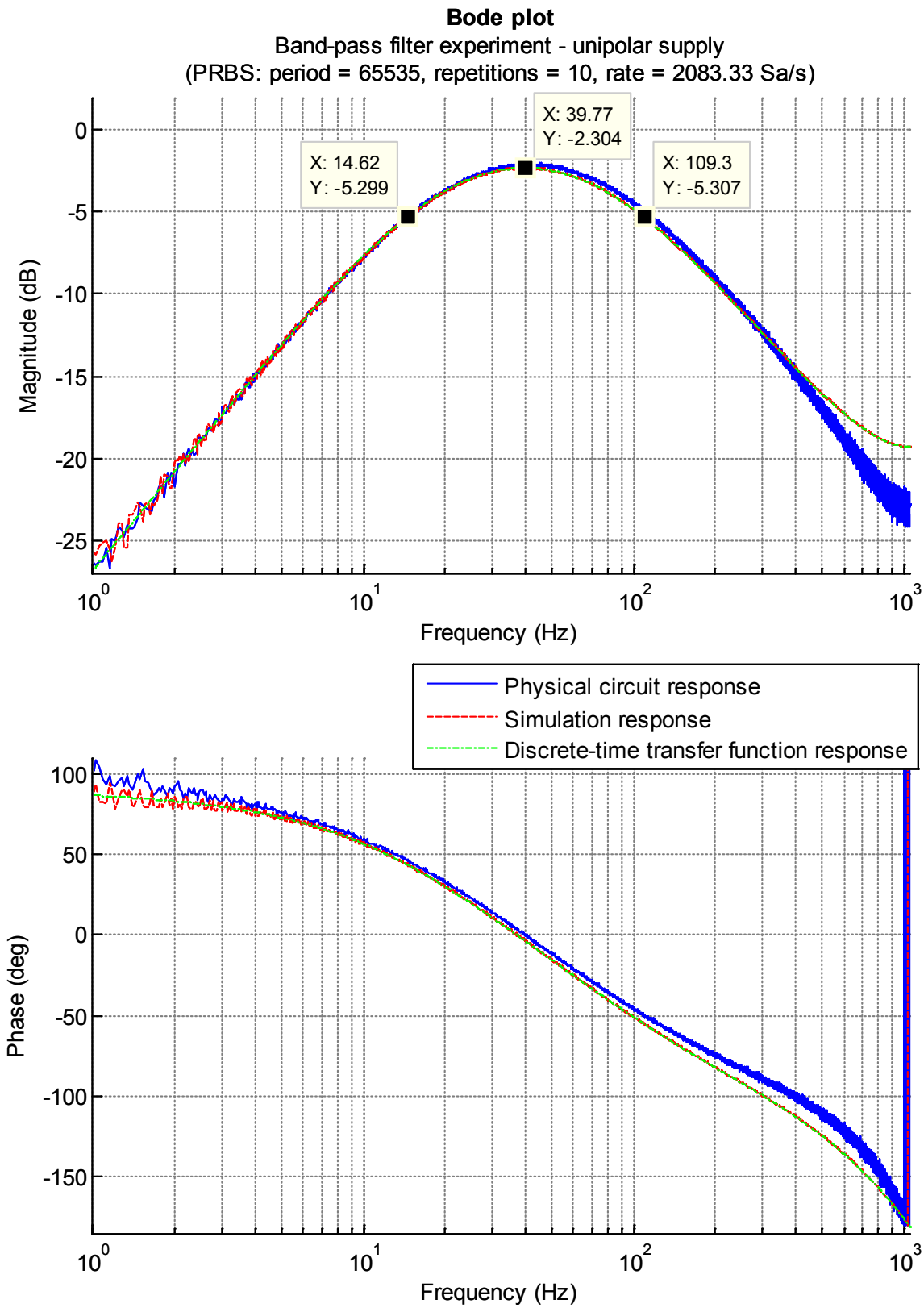

Figure 5.25: A Bode plot from the band-pass filter experiment. A comparison is shown of the frequency response from PRBS system identification using the physical circuit test, PRBS system identification using the simulated system model and the expected frequency response based on the discrete-time transfer function.

5.5.2 Experiment 2 – High-pass filter with electrode-skin model

The aim of the second experiment was to investigate how the *WEBS* PRBS circuit design might perform when deployed on the human body. The full circuit design described in Section 3.2.6 (*i.e.*, including the current limiting resistor, R_o and the high-pass filter capacitor C_{HP}) was applied to an equivalent circuit model of the impedance between two electrodes connected to the body (*i.e.*, from one electrode-skin interface to another). The circuit diagram for this experiment is illustrated in Figure 5.26. Note that in this configuration, the capacitor C_{HP} along with the impedance of the body form a high-pass filter, blocking DC current.

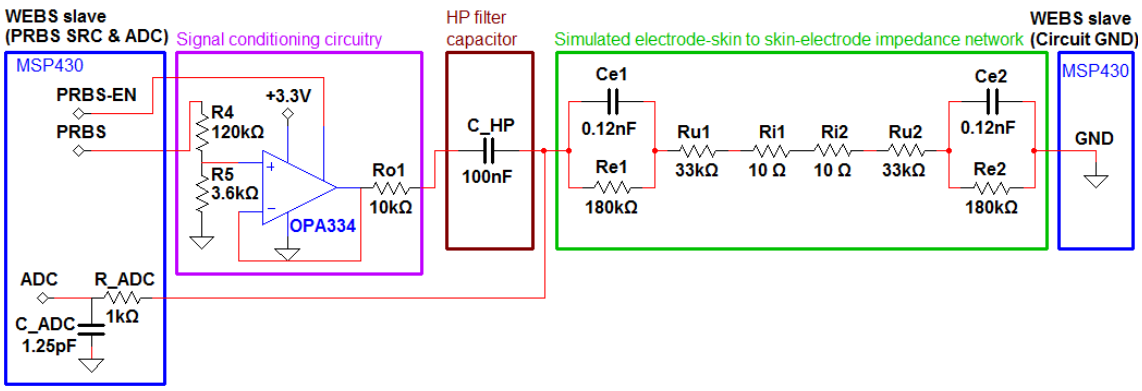

Figure 5.26: A schematic showing *WEBS* PRBS system identification on a known impedance network that forms part of a passive high-pass filter. This impedance network is a simplified model of what is present between two electrodes on the body (*i.e.*, from one electrode-skin junction to another). In this test, a PRBS signal is sent from a source *WEBS* slave, via signal conditioning circuitry, into a passive <u>high-pass filter</u> consisting of a fixed value capacitor (C_{HP}) and the described impedance network. The output of the high-pass filter is measured by an ADC in the same *WEBS* slave. A second *WEBS* slave acts as a circuit ground by setting its output as a digital low value (*i.e.*, circuit ground). To highlight the effect of a change of impedance at one electrode-skin junction, the test is repeated for R_{e1} values of 10 kΩ, 180 kΩ, 400 kΩ.

The chosen equivalent circuit model of the electrode-skin junction is based on that previously discussed in Figure 2.6. The values of C_e, R_u and R_i were chosen as standard component values that approximate the impedances that might be present in a real subject. The test was repeated for three values of R_{e1} to investigate whether a

change in impedance at one of the electrode-skin junctions would result in a detectable change in the frequency response. The three values of R_{e1} (10 kΩ, 180 kΩ and 400 kΩ) were chosen based on the range of impedances observed by Grimnes (1983) (also discussed in Section 2.2.1).

The transfer function of this system is given below. As with the previous experiment, R_{ADC} and C_{ADC} will have a loading effect on the test circuitry. For simplicity, since these impedance values are low, they have been omitted from the transfer function.

$$Z_{ELECTRODE-SKIN} = \frac{R_{e1}}{1+\frac{R_{e1}}{Z_{C_{e1}}}} + (2 \times R_u) + (2 \times R_i) + \frac{R_{e2}}{1+\frac{R_{e2}}{Z_{C_{e2}}}} \tag{5.5}$$

$$Z_{FIXED} = Ro + Z_{C_{LP}} \tag{5.6}$$

$$\frac{V_{OUT}}{V_{IN}} = \frac{1}{1+\left(\frac{Z_{FIXED}}{Z_{ELECTRODE-SKIN}}\right)} \tag{5.7}$$

Figure 5.27 shows the frequency response of the circuit at each value of R_{e1} based on results from the breadboard test, the MATLAB PRBS system identification simulation and the transfer function response. As can be seen, the simulation results and the transfer function response are approximately aligned; this is expected as both rely on the system model in MATLAB. There is a small frequency shift of approximately 1.4 Hz in the results obtained from PRBS system identification on the physical circuit. This shift could be due to the components used differing from their nominal values, which was not taken into account in the system model. The omission of the ADC's input impedance from the system model could also play a factor in this shift.

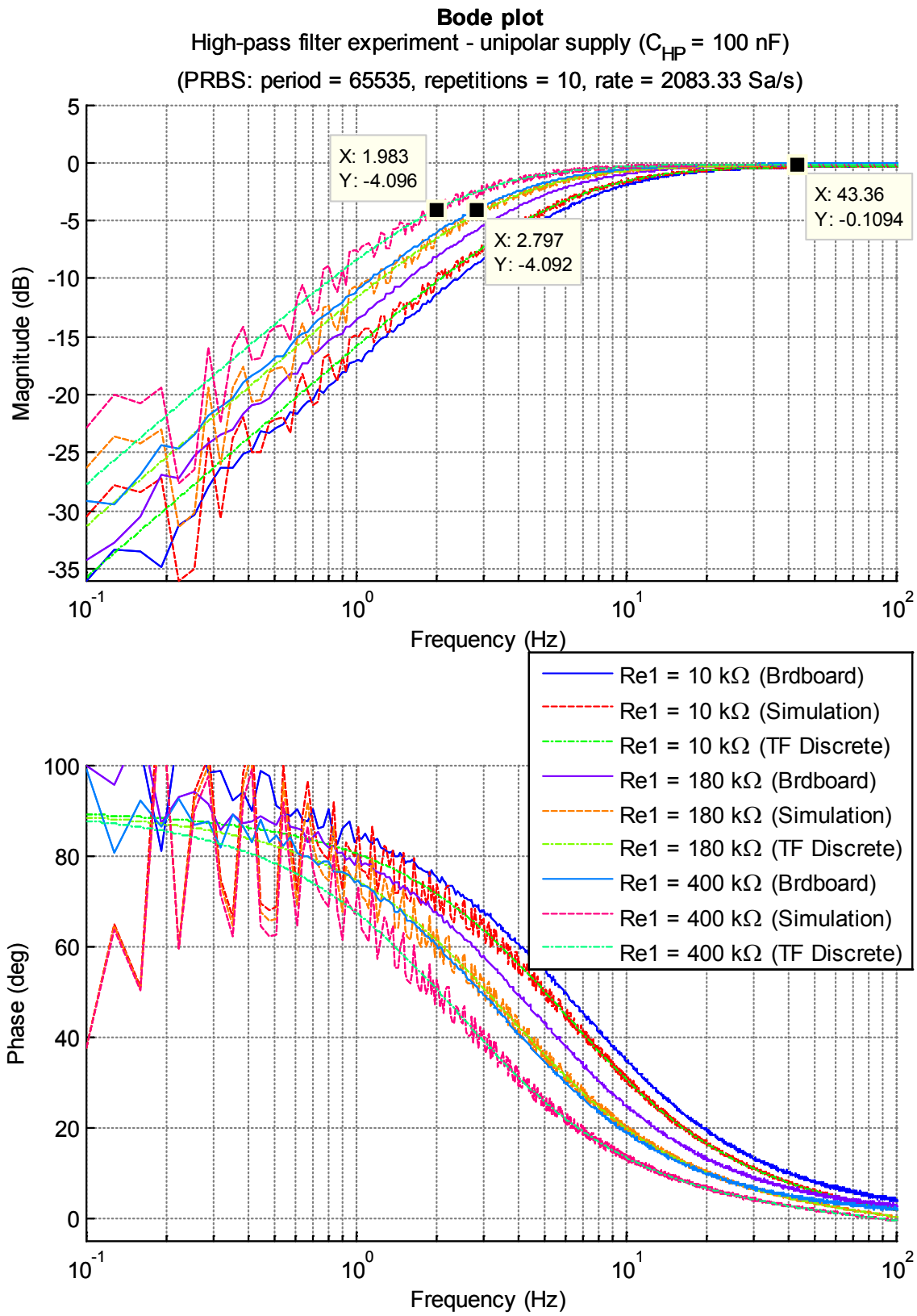

Figure 5.27: A Bode plot from the <u>high-pass filter</u> experiment. A comparison is shown of the frequency response from PRBS system identification using the physical circuit test, PRBS system identification using the simulated system model and the expected frequency response based on the discrete-time transfer function.

5.5.3 Experiment 3 – Low-pass filter with electrode-skin model

With the PRBS circuit design described up to this point, it is not feasible to place an isolation buffer between the system under examination and the ADC since, due to the single-sided supply op-amps used, the bipolar voltage at the output of the high-pass filter (*i.e.*, at the output of C_{HP}) would saturate the op-amp. An alternative topology would replace the high-pass filter configuration with a low-pass filter, as shown in Figure 5.28. In this configuration, one *WEBS* electrode would act as a PRBS source and a second would act as a measurement electrode.

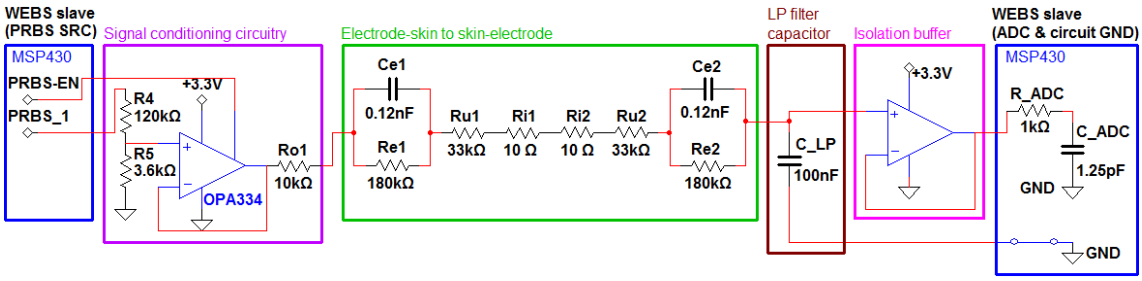

Figure 5.28: A schematic showing *WEBS* PRBS system identification on a known impedance network that forms part of a passive low-pass filter. This impedance network simulates what might be present between two electrodes on the body (*i.e.*, from one electrode-skin junction to another). In this test, a PRBS signal is sent from a source *WEBS* slave, via signal conditioning circuitry, into a passive low-pass filter consisting of the described impedance network and a fixed value capacitor (C_{LP}). The output of the low-pass filter is measured by an ADC in the same *WEBS* slave. To highlight the effect of a change of impedance at one electrode-skin junction, the test is repeated for R_{e1} values of 10 kΩ, 180 kΩ, 400 kΩ.

A disadvantage to this method is that the high input impedance of the isolation buffer op-amp creates a pathway for a tiny DC current to travel through the body. Although this DC current would be minuscule, due to health and safety concerns, this could make the described PRBS circuit topology unsuitable for long-term use on the body. However, it is worth investigating this topology in order to see the effect of isolating the ADC's input impedance from the test system as well as a providing a

general comparison with the high-pass filter method. The transfer function of this system is given below.

$$Z_{ELECTRODE-SKIN} = Ro + \frac{R_{e1}}{1+\frac{R_{e1}}{Z_{C_{e1}}}} + (2\times R_u) + (2\times R_i) + \frac{R_{e2}}{1+\frac{R_{e2}}{Z_{C_{e2}}}} \tag{5.8}$$

$$Z_{FIXED} = Z_{C_{HP}} \tag{5.9}$$

$$\frac{V_{OUT}}{V_{IN}} = \frac{1}{1+\left(\frac{Z_{ELECTRODE-SKIN}}{Z_{FIXED}}\right)} \tag{5.10}$$

As with the previous experiment, this test was repeated for R_{e1} values of 1 kΩ, 180 kΩ and 400 kΩ. Figure 5.29 shows each of the frequency responses for the system at each value of R_{e1}. The magnitude and phase responses indicate a high correlation in the results for each test. Unlike the previous experiment, both the physical and simulated PRBS generated responses are in line, which could suggest that the loading effect of the ADC in the high-pass PRBS circuitry topology might have a bigger impact than originally anticipated and may merit further investigation.

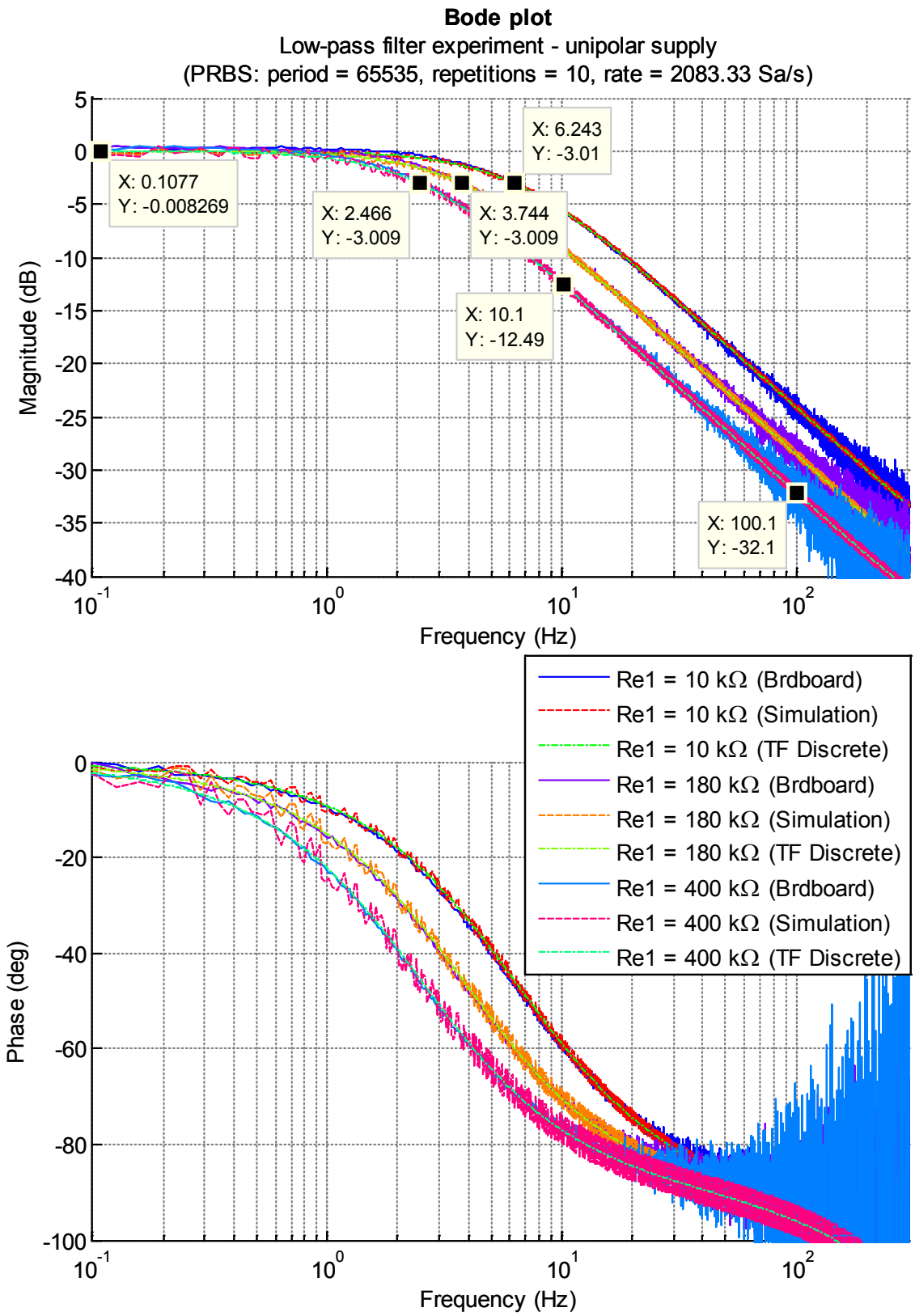

Figure 5.29: A Bode plot from the <u>low-pass filter</u> experiment. A comparison is shown of the frequency response from PRBS system identification using the physical circuit test, PRBS system identification using the simulated system model and the expected frequency response based on the discrete-time transfer function.

5.5.4 Experiment 4 – High-pass filter with human body

The final experiment involved taking the original high-pass PRBS circuit topology and applying it to the human body - as illustrated in Figure 5.30. In this case, a PRBS signal was sent from one of six locations on the left arm, through the body to a circuit ground electrode on the right arm.

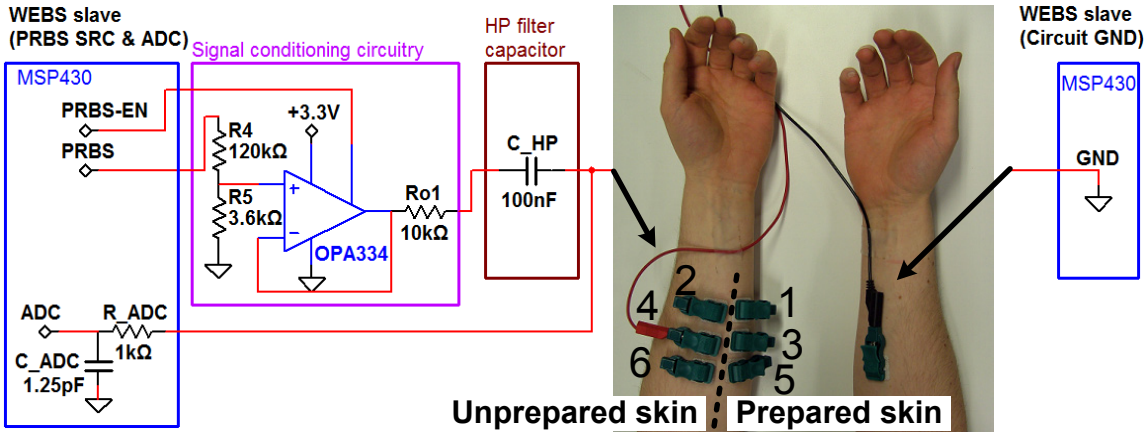

Figure 5.30: A schematic showing the configuration of the PRBS system identification experiment involving two *WEBS* slaves connected to the human body. A set of three sequential tests were performed between each of six different locations on the left forearm (half on prepared skin and half on unprepared skin) and a single location on the right forearm (on prepared skin). Each set of tests was performed on alternate skin-surface types in the numerical order shown.

Three of the test locations (points 1, 3, and 5) as well as the circuit ground connection where situated on skin that were prepared with an electrode preparation pad (70 % Isopropyl Alcohol and pumice). To explore the effect of different skin-electrode junction properties, the remaining test locations (points 2, 4 and 6) were situated on unprepared skin. Cloth electrodes with an adhesive electrolyte were used (similar to those labelled 'b' in Figure 3.16). To reduce possible biasing between test locations, each electrode was attached to the skin immediately prior to testing at that specific location and the test location order alternated between the skin-surface types. The same test was repeated three times for each electrode location. Figure 5.31 illustrates the frequency response obtained from PRBS system identification on each skin location.

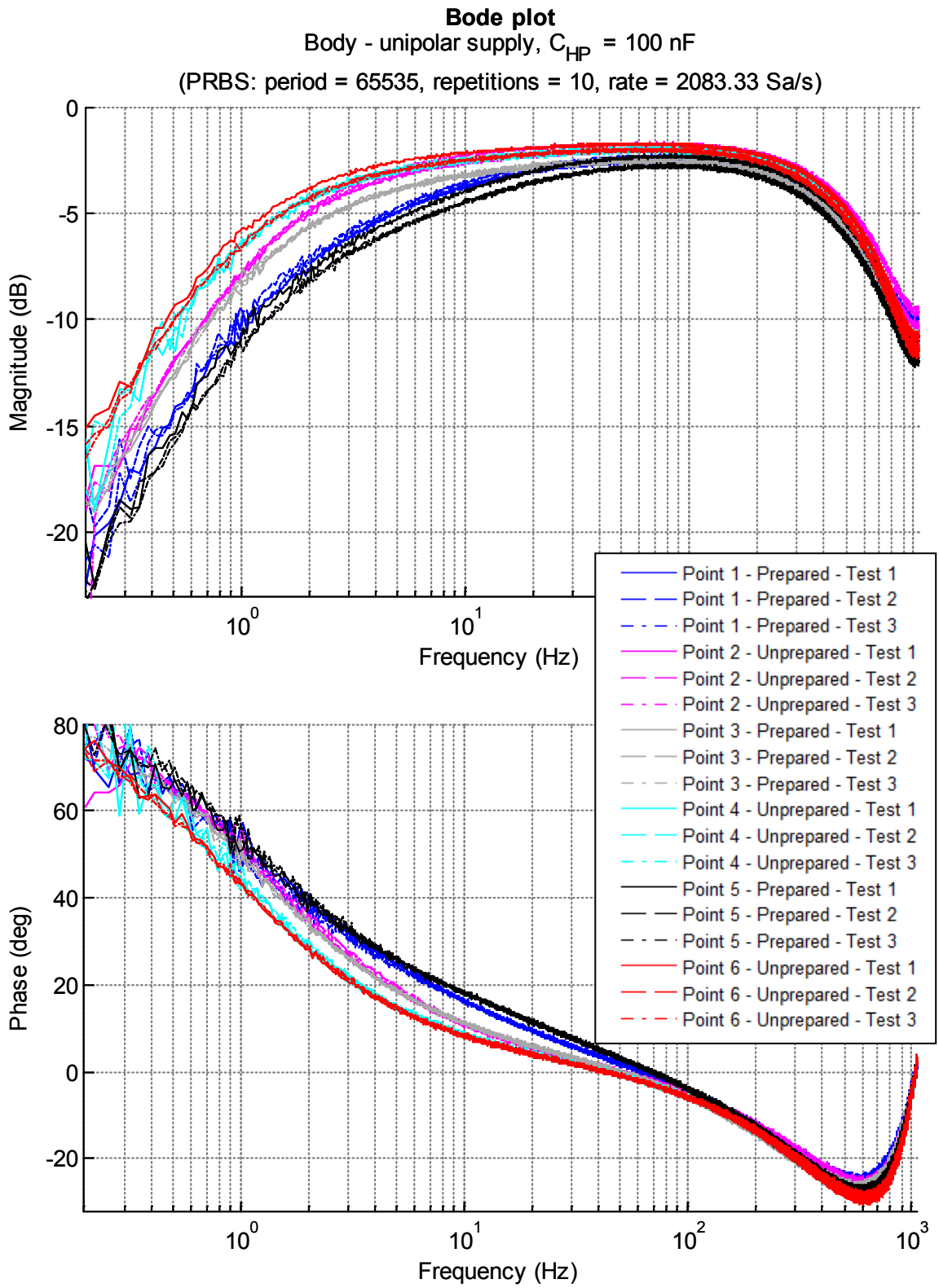

Figure 5.31: A Bode plot showing the frequency response obtained by PRBS system identification on the impedance of the <u>human body</u> from the left arm to the right arm <u>using adhesive cloth electrodes</u>. Separate lines highlight sets of three tests that were performed between each of six different locations on the left forearm (half on prepared skin and half on unprepared skin) and a single location on the right forearm (on prepared skin). The frequency responses from the three tests on each electrode have a similar shape whereas there is a clear difference between each electrode location, particularly noticeable between those on prepared and unprepared skin.

The results show intriguing frequency responses that have a similar shape yet are clearly distinguishable between each test location. From observation, it is clear that each of the magnitude responses between 0.2 Hz and 100 Hz do not exhibit an exponential behaviour – as one would expect with a single order resistor-capacitor system. The results indicate that the system (incorporating C_{HP}, each electrode-skin junction and the intermediary human body) is a higher order system.

A comparison of individual test iterations carried out at all of the measurement locations yields evidence of a change in the electrode-skin impedance during the course of testing. Figure 5.32 highlights this by showing a magnified version of the results from electrode points 5 and 6 from Figure 5.31.

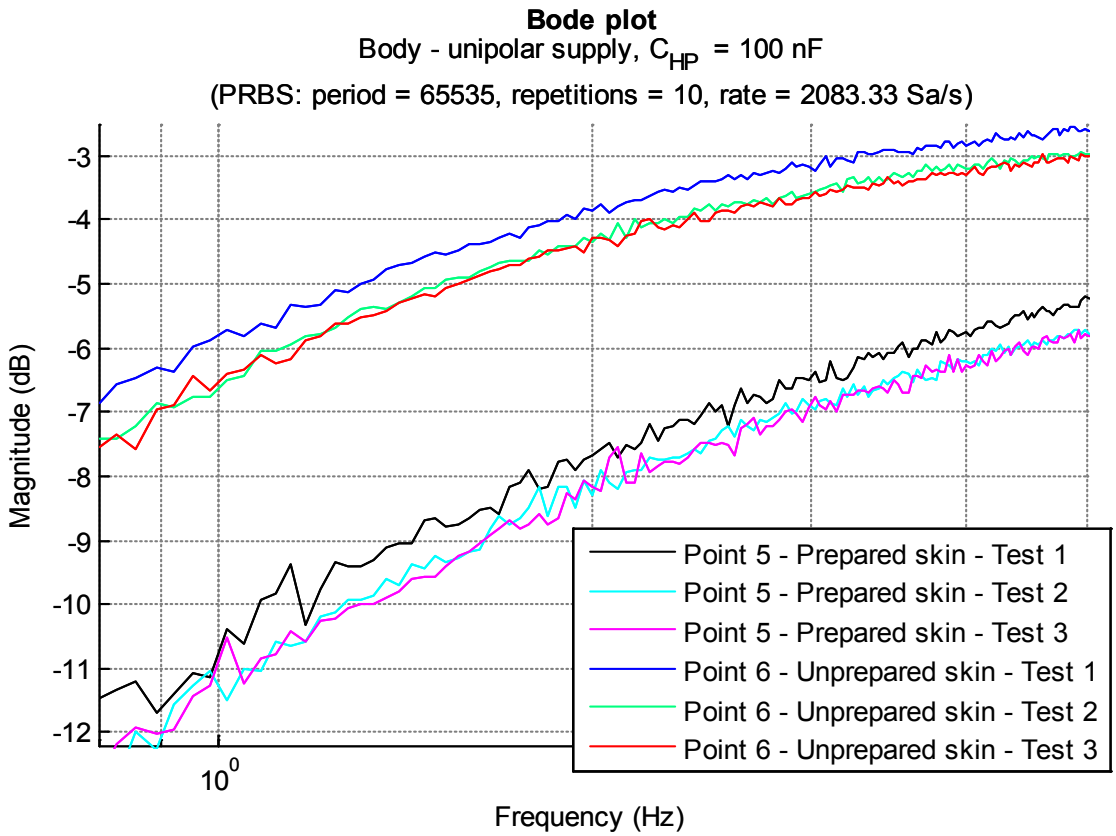

Figure 5.32: A magnified view of the Bode plot in Figure 5.31 showing the change in frequency response over the set of three tests at electrode locations 5 and 6. At each point, the cut-off frequency of the high-pass filter shifts slightly higher the longer the electrodes are attached (*i.e.*, from test 1 to test 3). This indicates a decrease in impedance at the electrode skin junction, possibly due to electrolyte soakage into the skin over time.

It is clear from the results that at each electrode location, there is a measurable decrease in the magnitude response between test 1 and test 3. As C_{HP} is a fixed value component, the visible increase in the lower cut-off frequency suggests a decrease in the overall impedance of the electrode-skin junction and/or body – possibly due to electrolyte soakage into the skin over time, altering the electrical characteristics of the electrode-skin junction.

As a supplemental experiment, the same test was repeated using three Ag/AgCl wet-gel electrodes (similar to those labelled 'a' in Figure 3.16) rather than the adhesive-gel cloth electrodes used previously. As described in the previous experiment, on the left forearm, one electrode was placed on prepared skin (point 7) and one on unprepared skin (point 8). A third electrode (circuit ground) was placed on prepared skin on the right forearm. The test was repeated three times for each left forearm electrode and the results are shown in Figure 5.33. For comparison, the maximum and minimum results from the cloth electrode experiment have also been included in this figure.

As can be seen, there is a noticeable difference between both types of electrodes on the corresponding skin types. The Ag/AgCl wet-gel electrodes achieve a detectable increase in the lower cut-off frequency, which suggests lower impedance at the electrode-skin junction. The results also show that the Ag/AgCl wet-gel electrode-skin connection has a significantly higher roll-off at the upper end of the frequency spectrum, which further indicates differences in the connection properties between the electrode types. As seen in the previous experiment, over the course of testing, the increase in lower cut-off frequency for each test location, which can be explained by a decrease in electrode-skin impedance due to electrolyte soaking into the skin over time.

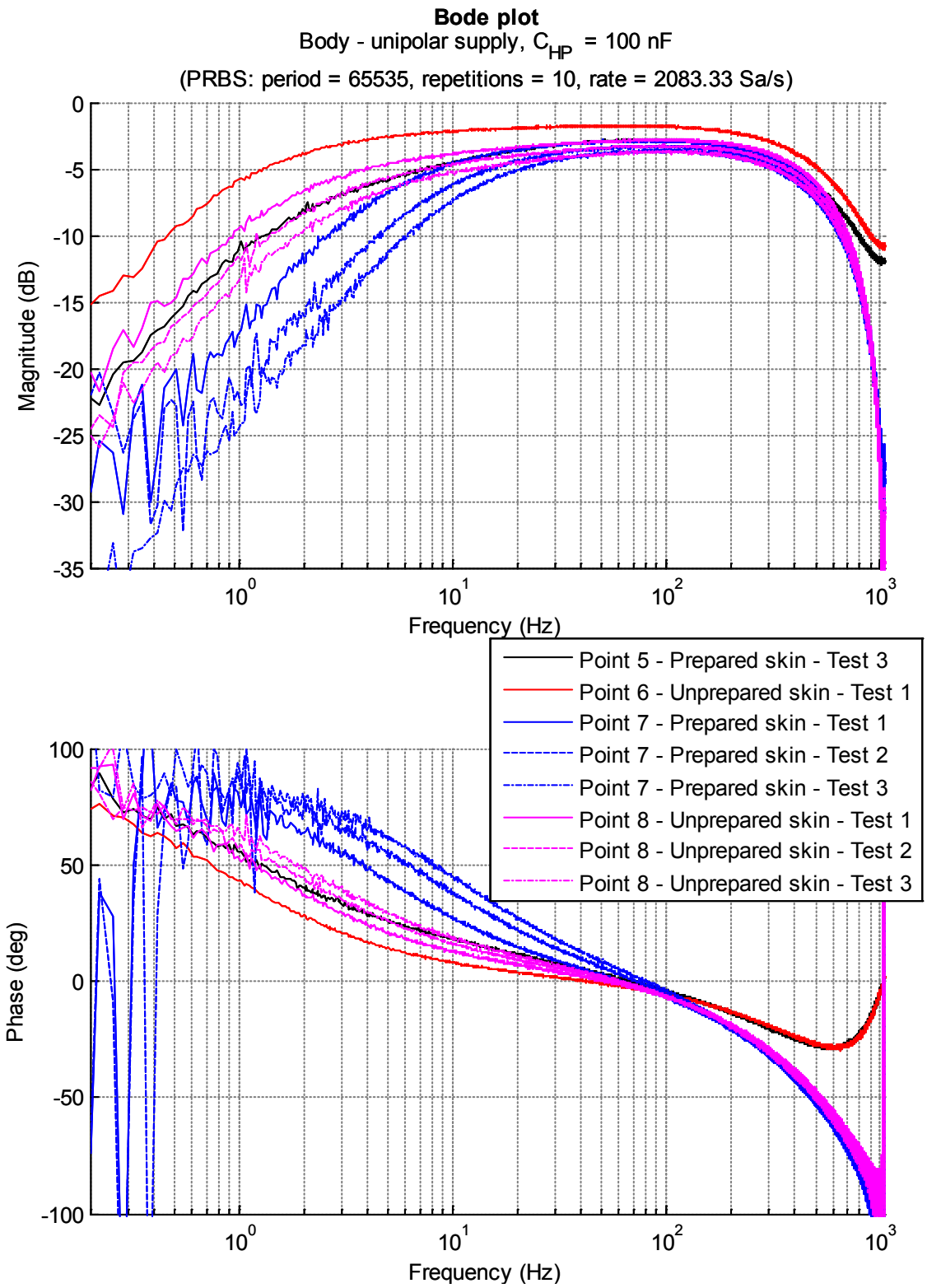

Figure 5.33: A Bode plot showing the frequency response obtained by PRBS system identification on the impedance of the <u>human body</u> from the left arm to the right arm <u>using Ag/AgCl gel electrodes</u>. The outermost test results from the previous cloth electrode experiment (*i.e*, from point 5 – test 3 and point 6 – test 1 in Figure 5.31) are included to facilitate comparison between electrode types. Elsewhere, separate lines highlight sets of three tests that were performed between each of two different locations on the left forearm (one on prepared skin and one on unprepared skin) and a single location on the right forearm (on prepared skin).

5.5.5 Discussion

This section has successfully demonstrated the feasibility of implementing PRBS system identification on the human body using the *WEBS*. In comparison to traditional electrode-skin impedance meters which tend to focus on investigating the impedance at a specific frequency relevant to the biopotential under investigation (*e.g.*, at 30 Hz for ECG and 10 Hz for EEG), PRBS system identification with the *WEBS* can provide impedance information across a range of frequencies.

Further developments could include tuning the PRBS parameters – such as bit rate, sequence length and number of sequence iterations – in order to produce a satisfactory frequency response resolution over a shorter test signal duration. Another enhancement might be to use a digital variable capacitor in place of C_{HP} so that the cut-off frequency of the overall high-pass filter could be dynamically adjusted to suit specific PRBS settings and/or variable tissue impedance properties.

It should be noted that, when implemented on a final *WEBS* based system, a short delay should be allowed when switching from stimulus mode (*i.e.*, during PRBS system identification) back to normal biopotential measurement mode. Mayer *et. al* (1992) state that, "*after a current pulse, there remains an electrode potential that decays quasi-exponentially*". A delay of up to several hundred milliseconds might be required before reliable biopotential measurements can be recorded.

With further development, it is envisioned that PRBS with the *WEBS* could be used in bioelectrical impedance analysis (the study of body composition to estimate water/fat content) (Kyle *et al.* 2004a, Kyle *et al.* 2004b) or in electrical impedance tomography (a medical imaging technique) (Cheney *et al.* 1999, Zou and Guo 2003).

5.6 Summary

The *WEBS* opens the door to new and exciting human-to-machine interfaces and clinical measurement applications. This chapter explored a number of avenues for harnessing rich channels of information from the human body for communication and control.

The initial focus of this chapter was on exploring the use of subtle and gross biomechanical signals emanating from the body (*e.g.*, the throat surface motion during speech) for novel assistive technology applications. The focus then expanded to investigate how a combination of biomechanical and bioelectrical signals measured at the same point on the body in each *WEBS* node - can be exploited in communication and control applications. It was also demonstrated how augmentation of a bioelectrical signal recording (*e.g.*, the ECG) with movement information can provide additional context that would be useful to a clinician (*e.g.*, user activity level or electrode movement giving rise to motion artefacts). Finally, an application was described that capitalises on the *WEBS* system as a digital sensor network to perform system identification between individual *WEBS* nodes. This can yield information regarding the impedance at the electrode-skin junction (*i.e.*, to indicate the quality of the connection to the body) or, with further development, the impedance of internal body tissue.

The applications discussed here give a glimpse into the future of human-to-machine communication utilising multiple channels of information from the human body. The next chapter will review what has been accomplished in this research and discuss future directions for additional research that could build upon it.

Chapter 6 Discussion, Suggestions for Further Research and Conclusions

This thesis has explored an extensive array of information regarding the author's work in the fields of biosignal measurement, augmented communication and control and human-machine interfaces. This chapter will draw this research to a conclusion by assessing the research aim and specific objectives that were set out at the beginning of Chapter 1. This will be followed by a detailed discussion of what the author perceives to be the original contributions to knowledge arising from this research. Suggestions for possible design and feature enhancements that could be explored in the future will also be discussed. Two suggested future applications are presented which help to set out the author's vision of how the technology that has been developed during the course of this research could be used in future, everyday human-machine interfaces. Finally, this chapter closes with some brief concluding remarks.

6.1 Assessment of research aim and objectives

As stated in Section 1.1, the aim of this research was **to facilitate the use of information-rich channels from the human body for augmented communication and control in novel human-machine interfaces**. To achieve this aim, three related research avenues were followed. Firstly, from a thorough review of the literature (Chapter 2), suitable locations on the human body for tapping into information-rich channels (*i.e.*, from bioelectrical and/or biomechanical signals) were identified. Signal

sources under some degree of voluntary control (*e.g.*, the hands, the throat and the face) as well as sources under unconscious control (*e.g.*, from the heart) were investigated and utilised in the course of this research (*e.g.*, Section 4.2, Section 5.1, Section 5.2 *etc.*).

The second research avenue (which is related to the principal project objective) was **to develop a novel sensor system (*i.e.*, the *WEBS*), incorporating both novel bioelectrical measurement and biomechanical signal measurement** (as discussed in Chapter 3). This system was designed to harness the identified information-rich channels for use as communication and/or control inputs to human-to-machine interfaces. The system underwent vigorous testing to determine its characteristics and biosignal measurement capabilities (Chapter 4).

Finally, the third research avenue (which is related to the second project objective) was **to demonstrate the operation of the *WEBS* prototype in one or more working augmented communication systems**. This objective was met by the development of several computer interfaces (as described in Chapter 5) which demonstrated the use of the *WEBS* system in novel communication and/or control applications.

6.2 Summary of key original contributions

In Chapter 1, the original contributions of this research were organised into three categories - those arising from: the physical *WEBS* device; the developed communication and control applications; and the subsequent physiological experiments that were made possible by the unique design of the *WEBS* device.

Physical *WEBS* device:

1. **The design, fabrication and testing of a multimodal biosignal sensor network.**

   a. The *WEBS* design has several advantages over existing measurement topologies including the reduction of wires and the facilitation of an increase in sensing modalities (Section 3.1), principally because it combines bioelectrical and biomechanical sensing in a single device.

   b. The *WEBS* system consists of a single *WEBS* master device with up to 25 *WEBS* slave devices – all connected via a shared digital bus connection (Section 3.2.1). The system can communicate wirelessly to base device using the standard Bluetooth protocol.

   c. The *WEBS* system has been designed so that the node recording topology is dynamically configurable by a wearer using pre-assembled plug-and-play connectors and wires. The *WEBS* electrodes connect to the body using standard off-the-shelf button clip electrodes (Section 3.4).

   d. Extensive care was taken in the design of the *WEBS* to ensure synchronised recording between all bus-connected electrodes (Section 3.2.4).

2. **The design of a novel bioinstrumentation configuration in which digitisation occurs at the point of measurement within the electrode.**

   2.a. The conducting path between the point of biopotential measurement on the body and the digitisation circuitry is reduced to a length of 3.5 mm – thus reducing the possibility for external electromagnetic interference to affect the tiny biopotential signals under investigation (Section 3.2.1).

2.b. As the *WEBS* electrodes are digitally controllable nodes, each can be configured to be either in normal measurement mode or in signal source mode. For example, any node can be selected as the low-impedance connection (*i.e.*, the reference or circuit ground) to the body (Section 3.2.2).

3. The augmentation of biopotential measurement with biomechanical movement sensing - as measured within each electrode.

3.a. Each *WEBS* slave features a tri-axial accelerometer that is capable of detecting subtle and/or gross body movement (Section 3.2.3). When multiple *WEBS* slaves are used, sensing over wide area of the human body is possible (Section 5.3). Detected movement of any electrode relative to the skin can also to be used to indicate the presence of motion artefacts (Section 5.4).

3.b. Each *WEBS* master features a tri-axial accelerometer, gyroscope and magnetometer to provide useful information such as body orientation, acceleration and general user activity level (Section 3.2.3).

<u>Communication and control applications:</u>

4. The design of multiple human-to-machine interfaces that transform software-definable user gestures into generic control input signals.

4.a. Laryngeal vibrations, as measured on the skin surface of the throat during vocalisation, were identified as an ideal candidate for use as a high-bandwidth channel of communication in human-to-machine interfaces. Two communication, play and creative expression applications were demonstrated which combined recorded macroscopic laryngeal vibrations with gross head

orientation information to facilitate control of a virtual musical instrument and a motorised vehicle (Section 5.1.2).

4.b. An application was explored to transform an area of the skin surface into a tap-based human-to-machine interface. It was demonstrated that a pair of *WEBS* slaves, spanning an area of skin, can localise taps within that area by analysing the vibration waves arriving at each node (Section 5.2).

4.c. The *WEBS* design facilitates communication with a true universal design based on software-definable user gesture inputs. By way of example, a software-based computer game controller was demonstrated which uses bioelectrical and biomechanical signals from selectable user gestures (Section 5.3).

5. The design of a computer interface that presents the biopotential and biomechanical signals recorded by the *WEBS* in a manner that is useful and accessible for clinical analysis.

5.a. The application of the *WEBS* system to recording a 12-lead electrocardiogram with augmented biomechanical information was demonstrated in Section 5.4. This software interface was designed to mimic the appearance of standard electrocardiogram graph paper used by clinicians in health monitoring, whist displaying 45 channels of biosignal information (*i.e.*, 9 bioelectrical channels and 36 biomechanical channels) from the *WEBS* system in real time.

<u>Additional experiments using the *WEBS* system:</u>

6. The discovery and investigation of the complex three-dimensional characteristics of neck skin surface vibrations during vocalisation at different phonation frequencies.

6.a. Multiple maps of skin-surface vibrations across the neck, emanating from laryngeal vibrations during vocalisation, were presented in Section 5.1. These results showed that, during vocalisation, the average magnitude of acceleration was greatest in the region of the larynx. Consequently, the concentration of vibrations over the surface of the neck varied due to the upward movement of the larynx at higher vocalisation frequencies.

6.b. A serendipitous outcome of the neck vibration mapping experiments was the discovery of the complex three-dimensional characteristics of neck surface vibrations. It was noted that the vibration measured at each point showed a unique oscillatory pattern that was dependent on measurement location and specific vocalisation frequency. Three-dimensional graphs from two sample points were presented (Section 5.1).

7. The development of a novel method of electrode-skin impedance analysis incorporating pseudo-random binary sequence system identification into the designed multimodal sensor network.

7.a. The software and circuitry needed for PRBS system identification between multiple electrodes in a *WEBS* network was discussed in Section 3.2.6. This flexible implementation allows a user to dynamically configure the PRBS characteristics (*e.g.*, bit-rate, sequence length, number of iterations *etc.*) and the role of each electrode connected to the *WEBS* network.

7.b. Experimentation on various passive circuit networks with known impedance values proved that the *WEBS*-based PRBS system identification method performed very well in comparison to both simulated and theoretical methods (discussed in Section 5.5.1, Section 5.5.2 and Section 5.5.3).

7.c. Further experimentation involved performing PRBS system identification across pairs of electrodes connected to the human body. The resulting frequency responses showed a discernible difference between electrodes that were attached to prepared and unprepared skin (*i.e.*, providing an indication of the quality of the electrode's connection to the skin). Similarly, a distinct difference was also noted when comparing wet-gel electrodes to adhesive-gel electrodes (discussed in Section 5.5.4).

6.3 Possible device design improvements

During the course of this research, a number of limitations in the current *WEBS* system came to light – some of which have been discussed in earlier sections (*e.g.*, Section 4.1, Section 4.2, *etc.*). This section reviews a mixture of intrinsic limitations arising from the current design of *WEBS* system. Suggested solutions are provided which should overcome - or in some cases circumvent - the issues causing these limitations in future iterations of the *WEBS* system.

Recorded biopotential signal quality

The *WEBS* system has been shown to perform well in comparison to a high-end commercial biopotential recording system (described in Section 4.2, Section 4.3 and Section 4.4). However, the author believes that further refinement of certain aspects of

the *WEBS* design could yield even better results. The areas that could have a high impact on the recorded biopotential signal quality are:

1. **Source impedance.** The *WEBS* electrode was specifically designed without a unity gain buffer at the input to the ADC for a number of reasons (*e.g.*, reducing the number of components and therefore size and cost). However, as the electrode connection in each *WEBS* slave is directly connected to the ADC input without a buffer stage, consistency between electrodes is highly dependent on the electrode-skin junction impedance (Section 5.5). Adequate skin preparation can reduce this impedance. However, variability can still exist between different electrode locations (Section 5.5.4). To mitigate the effect of the source impedance, a unity-gain buffer (using an operational amplifier with a low input-bias current) could be incorporated at the input stage to the ADC – thus isolating the user from the ADC. The benefit of this addition would need to be weighed against the increase in complexity of the *WEBS* slave.

2. **Sampling rate.** The current *WEBS* system employs single-shot ADC sampling (rather than continuous sampling) for two reasons: to help ensure synchronised sampling between *WEBS* slaves and to eliminate possible electromagnetic interference from digital data bus activity (Section 3.2.2). However, there is a significant sampling time overhead associated with this method (between 133.81 µs and 4.14 ms - Section 3.2.4). If the aforementioned issues could be overcome in a future iteration of the *WEBS* system, this would allow continuous sampling to be implemented, which would yield a considerable sampling rate increase.

3. **Variations between ADCs.** As noted in Section 3.2.2 and Section 4.1.1, each *WEBS* slave's ADC has inherent offset and gain errors that vary from one device

to another. The specific microcontroller used in the *WEBS* slave (MSP430F2013) provides the ability to measure these errors internally, yet the current *WEBS* system has not made use of this feature - leading to small errors in the recorded biopotentials. A future iteration of the *WEBS* system could quickly measure these errors on power-up, store them locally and deduct them from measured ADC samples before transmission to the *WEBS* master. Similarly, variations between the internal impedances in different ADCs affect the reliability of measurements. The inclusion of a unity-gain buffer (described in point 1 above) would reduce the effect of this issue.

4. **Cable and electrode shielding.** The *WEBS* data bus currently uses untwisted and unshielded 4-core wires. As the ADC in each *WEBS* slave references its measurement to one of the cores (*i.e.*, circuit ground), any electromagnetic interference induced on this cable could affect the recorded signal quality. This effect is assumed to be minimal as the signal-to-noise ratio on these wires is high. However, changing to shielded twisted-pair wiring could improve the signal-to-noise ratio. On the other hand, the current wiring is flexible, light and robust, so replacement wiring should ideally have these characteristics also. Similarly, the *WEBS* electrode circuit board could be enclosed in a shielding cage to further reduce electromagnetic interference.

5. **Uniform device assembly.** An issue that became apparent when attempting to obtain 12-lead ECG (Section 5.4) was that there were measureable variances in the quality of the recording from certain individual *WEBS* electrodes. As each *WEBS* electrode is identical in design, it was hypothesised that the problem lay in the assembly process. The components for each *WEBS* electrode (*i.e.*, the microcontroller, accelerometer and ancillaries) were originally soldered to the

printed circuit board prior to attachment to the electrode button clip connector. The button clip connector requires significant preheating before solder will adhere to it. When the *WEBS* electrode's PCB was brought into contact with the button clip connector, this heat was transferred into all of the pre-soldered components - possibly causing damage to them. After the microcontrollers in the affected *WEBS* electrodes were replaced, a reduction in the recorded level of noise was immediately noticed. One solution could be to firstly solder the PCB to the button clip connection at the required high temperature and then to solder the circuit board components on to the PCB at a lower temperature. This problem highlights the potential for more consistent recording characteristics to be achieved across different *WEBS* electrodes if a uniform manufacturing and assembly process is used.

Microcontroller oscillator frequency

The microcontrollers in the *WEBS* master and each slave are currently set to use their internal digitally controlled oscillators (DCOs) for timing purposes. In relation to the *WEBS* system's operation, the clock frequency of the oscillator is responsible for maintaining a fixed ADC sampling time and I^2C clock speed. Unfortunately, even though each DCO is pre-calibrated by the manufacturer, there remains some variance between the actual clock frequencies in different microcontrollers. In extreme conditions, this variance can be as high as ± 6 % (Texas Instruments 2005) and is a likely contributor to the *WEBS* sampling frequency drift and inaccuracies previously noted in Section 4.1.1 (although the expected variance in the *WEBS* network would be smaller as all electrodes share the same power supply and are likely to be at approximately the same operating temperature). One solution would be to incorporate a separate clock source on each *WEBS* device - such as a crystal or resonator – which

would provide greater accuracy and stability to the entire *WEBS* systems operation without overly compromising the size of the devices. Alternatively, each *WEBS* slave could calibrate its own clock relative to the *WEBS* master.

Data transmission error detection

It is the responsibility of the *WEBS* master to transfer the information from the *WEBS* slaves to a base computer in a timely manner whilst maintaining a constant sampling frequency. For this reason, it was decided that transmission errors (arising from either the I^2C bus or the Bluetooth link) would be handled at the base computer end – thus freeing resources in the *WEBS* system. The current system design facilitates a basic form of error detection by appending a 16-bit package counter to each data packet (see Section 3.2.4). When the *WEBS* user interface receives data, it checks the packet length and packet order (see Section 3.3) to detect if any packet data was dropped during transmission. However, the current system design does not provide the ability to detect if individual bits and/or bytes in each packet have been altered. A future design could utilise checksums to help verify the integrity of individual bytes through each stage of the *WEBS* communication sequence. A disadvantage to this approach would be a reduction in the maximum sampling rate due to an increase in packet length.

6.4 Possible feature enhancements for future device design iterations

In addition to the suggested design improvements described in the previous section, a number of possible feature enhancements have been conceived that would expand the *WEBS* system's functionality. Initial work has been conducted on a number of these proposed features and any results that have been obtained thus far are presented here.

6.4.1 Microphone recording

One item that might be considered for inclusion in a future iteration of the *WEBS* digital electrode is a microphone within each electrode. The possible applications include:

1. Recording body sounds (*e.g.*, MMG, digestive gurgling, *etc.*).

2. Multiple electrodes forming a microphone array to listen to sounds in the environment. This could be used to facilitate directional listening by an augmented hearing device. Using digital signal processing to combine the signals from an array of microphones in different ways, one could form a "beam" of sensitivity to sounds in a particular direction (*e.g.*, coming from a person who is talking in a noisy room).

3. Recording audio might provide useful context for electrophysiological or biomechanical recordings; for example, recording snoring and ECG simultaneously for diagnosis or monitoring of sleep apnoea. Other examples might include: motion artefacts caused by coughing; biosignal changes during spoken conversations; adding a speech interface to an HMI that already uses the digital electrodes as an input device.

4. Audio-enabled electrodes could be worn by children with neural developmental disorders (*e.g.*, profound autism) to monitor stress levels by analysing a combination of measured biosignals and recorded audio simultaneously.

A foreseeable obstacle that would need to be overcome is achieving a sufficiently high sampling rate with the *WEBS* system in order to record recognisable

audio. However, this limitation would be application-dependant as the current maximum sampling frequency of the *WEBS* system (*i.e.*, 3072.76 Sa/s from Appendix C) might be adequate in some circumstances.

6.4.2 Temperature sensing

Each *WEBS* device currently features a digital thermometer built into its on-board microcontroller. This thermometer can provide a general indication of the temperature at each electrode location but is principally governed by the internal temperature of the microcontroller itself. The addition of a separate integrated circuit thermometer, dedicated to monitoring the skin temperature at the point of contact on the wearer, would greatly increase the functionality of the *WEBS* system. An array of thermometer-enabled *WEBS* devices could facilitate the following applications:

1. They could be a useful tool in the diagnosis of cardiovascular disease (*e.g.* based on blood flow information as measured by the temperature of the skin at various locations).

2. They could link changes in the environment to measured physiological changes (*e.g.*, they could provide a timely warning of the body diverting blood away from the extremities to the body core during cold conditions).

3. They could provide an early detection of illness in a paralysed, locked-in or other at-risk person could facilitate timely intervention.

This feature could be accomplished by connecting a digital thermometer onto the existing I^2C data bus in each slave or by connecting an analog thermometer into an ADC channel of the *WEBS* slave's microcontroller.

6.4.3 Novel bioelectrical measurement using a digital biopotential monode

A more radical evolution of the *WEBS* system would involve the removal of any physical connection between individual electrodes connected to the human body. This section presents an initial investigation into a novel design of such a biopotential measurement circuit that could be incorporated into a future *WEBS* system. This design has only one physical point of contact with the body which, if implemented, would turn the *WEBS* into a *biopotential monode* (Nolan *et al.* 2011).

Monodal measurement of biopotentials poses very substantial circuit design challenges and has rarely been used in practice. Some examples of single-point biopotential measurement were described previously in Section 2.2.3 (Harland *et al.* 2002b, Song-Hee *et al.* 2004, Maruyama *et al.* 2007). In particular, the circuit used by Prance *et al.* (2000) utilises an ultra-low input bias current amplifiers in single-point bioelectrical measurements referenced to earth. Using the design proposed by Prance *et al.* as a starting point (see Figure 2.11), a novel amplifier design was developed, as illustrated in Figure 6.1. In this design, the non-inverting input of the instrumentation amplifier is connected to a wet electrode on the subject's skin whilst the inverting input is connected to a voltage divider that maintains a fixed voltage halfway between the supply rails. Before biopotential measurement commences, a switch is briefly closed which connects the voltage level at the electrode-skin junction to output of this voltage divider. This electrode-skin junction is the only point of contact with the body for each separate electrode. The circuit is battery powered so that there is no physical electrical connection between the circuit and earth or between the subject and earth. The electrical circuit is effectively completed by tiny capacitances that exist between the subject, the *monode* and earth.

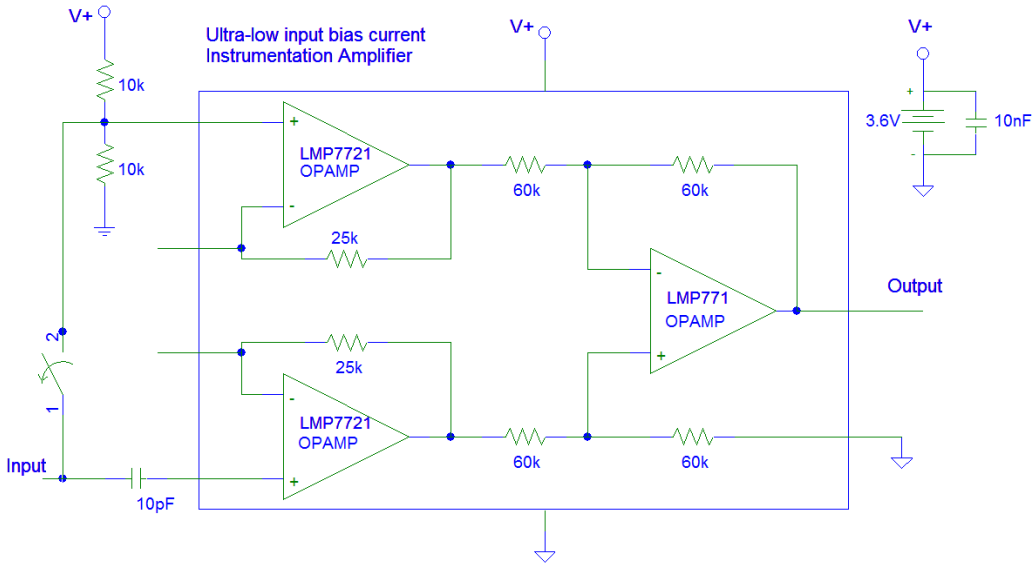

Figure 6.1: An experimental instrumentation design for a biopotential measurement system with a single point-of-contact on the human body, termed a *biopotential monode*. This design is based on work carried out by (Prance *et al.* 2000).

A *biopotential monode* may open the door to interesting new biopotential applications, but its development is at an early stage. Future iterations of this topology could focus on refining the hardware design to improve signal quality and to capitalise on the benefits of a physically unburdened biopotential electrode.

6.4.4 Arduino-based master

A suggested modification is the move towards an Arduino-based *WEBS* master by replacing the existing master MSP430F2132 microcontroller with an Atmel (2013) ATmega328P microcontroller. This would provide a number benefits over the existing system. Firstly, the current *WEBS* master's program code fills the existing 8 kB of flash memory space, which restricts inclusion of further features (*e.g.*, SD card storage implementation). The ATmega328P features a significantly larger flash memory space of 32 kB, which should be adequate for any future development of the *WEBS* system.

Secondly, one issue that was noted in Section 3.2.4 was that the *WEBS* I^2C clock rate varied depending on number of connected *WEBS* slaves and length of bus wire. The ATmega328P can supply a higher current on each output pin (up to 10 mA, in comparison to 1.5 mA for the MSP430) without overly compromising the voltage level. This allows for an increased stability in the I^2C clock rate with considerably less dependency on the *WEBS* network topology. Results from initial work that has been carried out into this conversion process have shown that an Arduino-based master can maintain a fixed clock frequency in all of the *WEBS* network configurations that have been demonstrated in this thesis (Appendix G).

Thirdly, the Arduino has a large online community providing developer support and extensive package libraries. An Arduino-based master would allow developers with a wide range of programming abilities to access and modify the *WEBS* operating code, which could spur on future applications for the *WEBS* system.

A disadvantage to an Arduino-based master is that the maximum sampling rate is noticeably less (*i.e.*, Appendix C *vs.* Appendix G). This is because the Arduino uses software libraries to implement UART and I^2C communication with no overlap between the execution of each operation. In the MSP430, the program code hands over responsibility for each operation to internal hardware such that the microcontroller is free to start sequential operations earlier; thus facilitating a higher overall sampling rate. The author believes that unless the MSP430-based master's output current can be increased (*e.g.*, using a constant current source or I^2C data bus repeater), the Arduino-based master's increased sampling rate stability is preferable to maintaining the higher sampling rate.

6.4.5 Other possible modifications

Several further modifications that could be utilised by future iterations of the *WEBS* system are listed in Table 6.1.

Table 6.1: This table lists several design modifications that could be incorporated into future iterations of the *WEBS* system.

	Modification	Description
1	microSD card slot	A built-in data storage device such as a microSD card could allow the *WEBS* to monitor biosignal activity over extended periods of time.
2	*WEBS* master sensors	Additional sensors (*e.g.*, barometric pressure sensor, electret microphone and a light dependent resistor) could be included into the design of the *WEBS* master to provide even more context to the biosignals under measurement. Figure H.2 and Figure H.3 in Appendix H show a proposed design for the next generation of *WEBS* master that includes the listed sensors.
3	I^2C-bus segmentation and isolation	An I^2C bus repeater, hub or extender could be utilised to isolate bus impedances in different sections of the *WEBS* network. This would allow a greater number of slave devices to be connected whilst maintaining the I^2C clock frequency. Figure H.1 in Appendix H shows a proposed design for PCA9517A based I^2C-bus repeater (NXP Semiconductors 2006).
4	24-bit sigma-delta ADC	Newer generations of ADCs offer increased resolution and sampling frequency. For example, the *WEBS* slave's microcontroller could be replaced with an MSP430AFE2xx microcontroller which features an integrated 24-bit sigma-delta ADC (Texas Instruments 2011).
5	I^2C High-speed mode	Recent revisions of the I^2C protocol list advances which could be incorporated into the system such as 16-bit addressing and a nine fold increase in the data throughput to 3.4 Mbits/s (NXP Semiconductors 2012).

6	Dedicated wireless spectrum for medical devices	The U.S. Federal Communications Commission (2012) recently assigned a specific range of the frequency spectrum (2.36 GHz to 2.4 GHz) for communication in medical body area networks. It is envisaged that this will reduce the number of cables connecting patients to equipment in hospitals. A future iteration of the *WEBS* could utilise new transceivers to capitalise on this dedicated frequency range.
7	Dallas 1-wire	The number of data bus wires could be decreased to two (data and ground) by implementing Dallas 1-wire (Maxim Integrated Products Inc 2013). Three compromises are that this protocol can only achieve a maximum data rate of approximately 125 kbps, it is more complex to implement in software and it is not supported by the current *WEBS* motion sensors.

6.5 Future applications

The *WEBS* design opens the door to new and exciting applications of biosignal measurement in human-machine communication, control and health monitoring. This section outlines the author's vision of how the next generation of the *WEBS* system might operate and presents a possible application that might be explored in the future.

6.5.1 The next generation of the *WEBS* device

This section outlines how the *WEBS* system could operate in the future with further development and with the inclusion of some of the suggested design additions discussed earlier in this chapter.

A future *WEBS* system application, which is a natural evolution to the work discussed in this thesis, is in facilitating large area biosignal sensing. This might take the form of a grid of electrodes with a digitally selectable reference point, as illustrated

in Figure 6.2 (a). A speculative application is that by increasing the number of electrodes on the skin over a particular muscle area, surface vibrations originating in the muscle as well as muscle electrical activity could be mapped to possibly yield information about the muscle's functioning - Figure 6.2 (b).

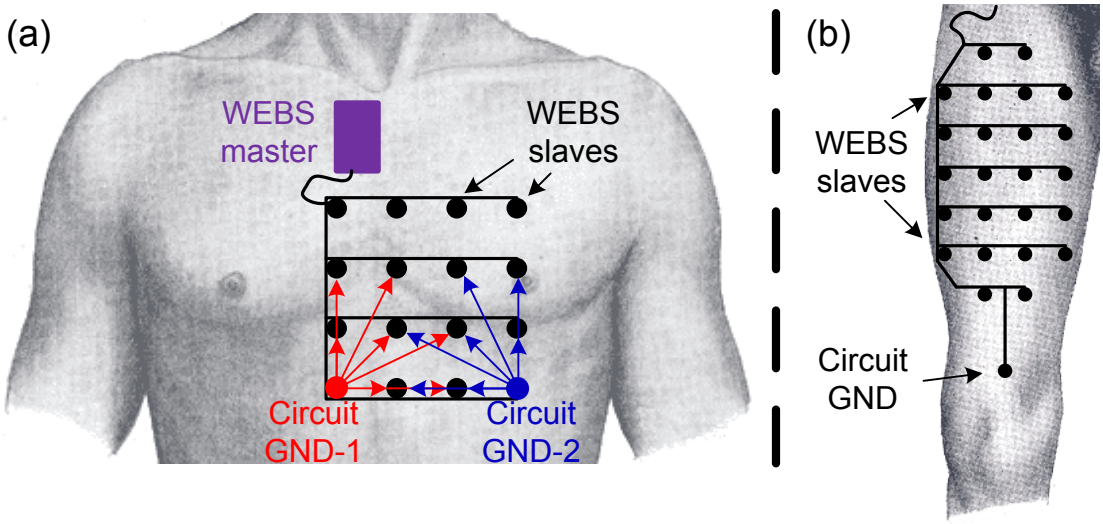

Figure 6.2: Diagrams showing how the *WEBS* might be configured to record biosignal activity over a large area of the body – in this case the (a) chest and (b) thigh. The example in (a) also highlights that the circuit ground electrode could be alternated during measurement to provide an additional viewpoint on the biopotential under investigation. These images are modified from (a) Fig. 1219 and (b) Fig. 1238 (Gray 1918).

The following sequence of steps shows how the next generation of *WEBS* system could operate:

1. On start-up, PRBS system identification could take place between all electrodes before measurement commences.

2. The system could notify the operator of any electrodes with potentially 'bad' connections to the body.

3. If configured in a grid topology (as illustrated in Figure 6.2), the system could identify the most suitable location to be configured as reference electrode (*i.e.*, the one with the lowest impedance connection to the body).

4. It could record biopotential and/or biomechanical signal under investigation.

5. It could periodically alternate the reference electrode, as illustrated in Figure 6.2, to provide multi-dimensional biopotential recording.

6. Live feedback of electrode and user movement including body orientation, macroscopic movement/acceleration and gross body deformation.

7. It could provide live information regarding the user's environment including ambient light level, atmospheric pressure reading, relative humidity and ambient temperature.

8. Optionally, all recorded data could be stored to an on-board microSD card with an accompanying timestamp for subsequent analysis.

6.5.2 An everyday foetal monitor

A suggested future application is the monitoring of the heart rate and activity level of a pregnant mother and her unborn child. A grid of *WEBS* slaves could be mounted on a pregnancy bump band, as illustrated in Figure 6.3. This novel application of the *WEBS* system could provide a wealth of information to clinicians or for feedback to a mother.

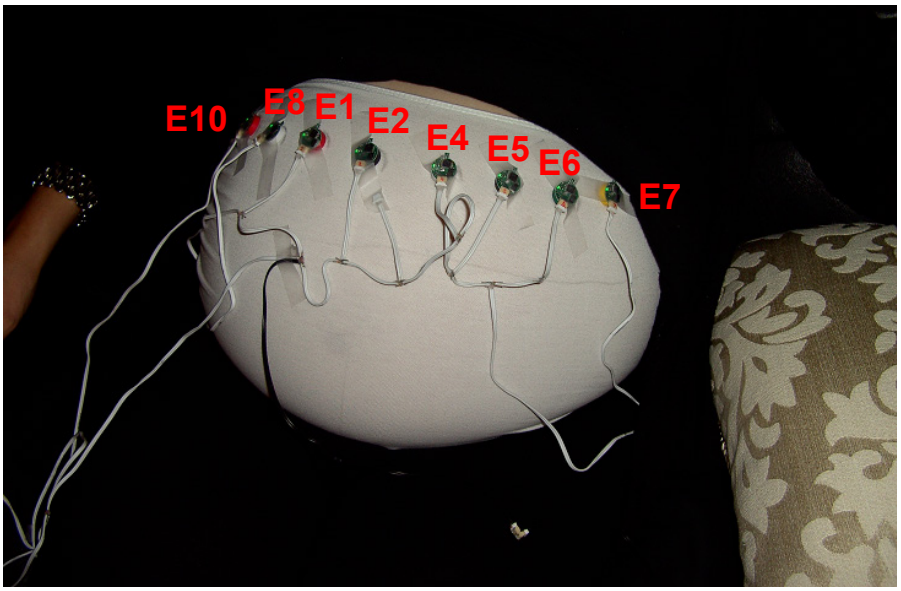

Figure 6.3: An image of a suggested future application in which several *WEBS* slaves mounted on a pregnancy bump band for monitoring the heart rate and activity level of a pregnant mother and her unborn child.

A *WEBS*-based everyday foetal monitor would provide several features such as:

1. It would be capable of monitoring maternal ECG and potentially even foetal ECG.

2. It could monitor the mother's gross body movement and subtle movement of the foetus (*e.g.*, kicking or rotation).

3. Feedback could be presented to the mother via a mobile phone interface (or any Bluetooth-enabled computer interface).

4. If the mother is physically active, this could manifest itself as detectable changes in foetus behaviour.

5. It could possibly give an early indication of a problem with the pregnancy (*e.g.*, from lack of foetus movement or from changes in the foetal ECG pattern).

6. From foetal movement it could help identify the three-dimensional orientation of the foetus - and therefore the heart orientation - which could facilitate better analysis of foetal ECG (Sameni and Clifford 2010).

6.6 Final conclusions

This research explored the design of a novel body-area sensor network, *i.e.*, the *WEBS* system, which incorporates several features that advance the state of the art in biosignal measurement. The system employs multiple sensing modalities that provide powerful new modes of interaction with technology for people with a broad range of physical abilities. This feature-rich system is capable of measuring biopotential signals, body orientation, macroscopic movement/acceleration and gross body deformation. The system is readily amenable to a large number of applications in HMI and, through its novel design, can facilitate new and exciting applications that are not possible with existing technology, a number of which have been demonstrated in this thesis. The author believes that the broad ranging capabilities of the *WEBS* system have only begun to be harnessed and that this system points towards the future of wearable biosignal measurement.

References

3M™. (2009) *Round Conductor Flat Cable* [Online]. Available: http://multimedia.3m.com/mws/mediawebserver?mwsId=66666UF6EVsSyXTt4XfVnxs6EVtQEVs6EVs6EVs6E666666--&fn=ts0452.pdf [Accessed 9 April 2013].

ABI RESEARCH. (2011) *Wearable Wireless Medical Devices to Top 100 Million Units Annually by 2016* [Online]. London. Available: http://www.abiresearch.com/press/wearable-wireless-medical-devices-to-top-100-milli [Accessed 26 September 2012].

ADER, C. (1897) Sur un nouvel appareil enregistreur pour cables sous-marins. *Comptes Rendus Hebdomadaires des Séances de l'Académie des Sciences,* 124: 1440-1442.

AKBARY, P. & RABBANI, H. (2010) Removing Power Line Interference and ECG signal from EMG signal using Matching Pursuit. 10th IEEE International Conference on Signal Processing (ICSP), 24-28 October. Beijing, China. 1741-1717.

ANALOG DEVICES. (2012) *iSensor MEMS Inertial Measurement Units* [Online]. Available: http://www.analog.com/en/mems-sensors/mems-inertial-sensors/products/index.html#iSensor_MEMS_Inertial_Measurement_Units [Accessed 19 September 2012].

ANALOG DEVICES. (2013) *ADXL345 Digital Accelerometer Data Sheet* [Online]. Available: http://www.analog.com/static/imported-files/data_sheets/ADXL345.pdf [Accessed 9 April 2013].

ANDREOLI, T.E., BENNETT, J.C., CARPENTER, C.C.J. & PLUM, F. (1997) *Cecil Essentials of Medicine* 4th ed. Philadelphia, Saunders.

ARISTOTLE. (ca. 350 BC) *De Anima: Book II* [Online]. Available: http://psychclassics.yorku.ca/Aristotle/De-anima/de-anima2.htm [Accessed 19 June 2013].

ATMEL. (2013) *ATmega48A/PA/88A/PA/168A/PA/328/P (Rev. F)* [Online]. Available: http://www.atmel.com/devices/atmega328p.aspx [Accessed 11 June 2013].

AUGUSTYNIAK, P., SMOLERI, M., BRONIEC, A. & CHODAK, J. (2010) Data Integration in Multimodal Home Care Surveillance and Communication System. *In:* PIETKA, E. & KAWA, J., eds. Information Technologies in Biomedicine. New York. Springer-Verlag Berlin Heidelberg, 391-402.

AZEVEDO, F.A., CARVALHO, L.R., GRINBERG, L.T., FARFEL, J.M., FERRETTI, R.E., LEITE, R.E., JACOB FILHO, W., LENT, R. & HERCULANO-HOUZEL, S. (2009) Equal numbers of neuronal and nonneuronal cells make the human

brain an isometrically scaled-up primate brain. *Journal of Comparative Neurology,* 513(5): 532-41.

BAEK, H.J., KIM, J.S., KIM, K.K. & PARK, K.S. (2008) System for unconstrained ECG measurement on a toilet seat using capacitive coupled electrodes : The efficacy and practicality. 30th Annual International Conference of the IEEE Engineering in Medicine and Biology Society (EMBC), 21-24 August. Vancouver, Canada. 2326-2328.

BAKEN, R.J. & ORLIKOFF, R.F. (2000) *Clinical Measurement of Speech and Voice*. Singular Thomson Learning.

BARKER, R.G., DEMBO, T. & LEWIN, K. (1941) Frustration and Regression: An Experiment with Young Children. *Studies in topological and vector psychology. Vol II.* Iowa City University of Iowa Press.

BEEBY, S., ENSELL, G., KRAFT, M. & WHITE, N. (2004) *MEMS Mechanical Sensors*. Boston, Artech House, Inc.

BIOSEMI. (2002). Amsterdam. Available: http://www.biosemi.com/products.htm [Accessed 15 March 2011].

BMEARNS. (2008) *Linear Feedback Shift Register* [Online]. Available: http://en.wikipedia.org/wiki/Linear_feedback_shift_register [Accessed 19 April 2013].

BOOSTANI, R. & MORADI, M.H. (2003) Evaluation of the forearm EMG signal features for the control of a prosthetic hand. *Physiological Measurement,* 24(2): 309-319.

BOSER, B.E. & WOOLEY, B.A. (1988) The design of sigma-delta modulation analog-to-digital converters. *IEEE Journal of Solid-State Circuits,* 23(6): 1298-1308.

BURCHFIELD, T.R., VENKATESAN, S. & WEINER, D. (2007) Maximizing Throughput in ZigBee Wireless Networks through Analysis, Simulations and Implementations. 1st International Workshop on Localized Algorithms and Protocols for Wireless Sensor Networks (LOCALGOS), 18-20 June. Santa Fe, New Mexico. CTI Press, Athens, 15-29.

CANDY, J.C. & TEMES, G.C. (1992) *Oversampling delta-sigma data converters: theory, design, and simulation*. New Jersey, Wiley-IEEE Press.

CHAMADIYA, B., HEUER, S., HOFMANN, U.G. & WAGNER, M. (2009) Towards a capacitively coupled electrocardiography system for car seat integration. 4th European Conference of the International Federation for Medical and Biological Engineering, 23-27 November. Antwerp, Belgium. Springer Berlin Heidelberg, 1217-1221.

CHENEY, M., ISAACSON, D. & NEWELL, J.C. (1999) Electrical impedance tomography. *Society for Industrial and Applied Mathematics review,* 41(1): 85-101.

CHEYNE, H.A. (2006) Estimating Glottal Voicing Source Characteristics by Measuring and Modeling the Acceleration of the Skin on the Neck. 3rd IEEE/EMBS International Summer School on Medical Devices and Biosensors, 4-6 September. Cambridge, Boston. 118-121.

CHIAPPA, K.H. (1997) *Evoked Potentials in Clinical Medicine*. 3rd ed. Philadelphia, Lippincott-Raven Publishers.

CHILD, I.L. & WATERHOUSE, I.K. (1952) Frustration and the quality of performance: I. A critique of the Barker, Dembo, and Lewin experiment. *Psychological Review,* 59(5): 351-362.

CLARK, J.W. (2009) The Origin of Biopotentials. *In:* WEBSTER, J. G. (ed.) *Medical Instrumentation: Application and Design.* 4th ed. New York: John Wiley & Sons, 126-188.

COLLINGER, J.L., WODLINGER, B., DOWNEY, J.E., WANG, W., TYLER-KABARA, E.C., WEBER, D.J., MCMORLAND, A.J.C., VELLISTE, M., BONINGER, M.L. & SCHWARTZ, A.B. (2013) High-performance neuroprosthetic control by an individual with tetraplegia. *The Lancet,* 381(9866): 557-564.

CONNECTBLUE. (2012) *Bluetooth Serial Port Module* [Online]. Available: http://www.connectblue.com/products/classic-bluetooth-products/classic-bluetooth-modules/bluetooth-serial-port-module-obs421/ [Accessed 26 March 2013].

CREEL, D.J. (1995) Visually Evoked Potentials. *In:* KOLB, H., FERNANDEZ, E. & NELSON, R. (eds.) *Webvision: The Organization of the Retina and Visual System.* Salt Lake City, Utah: University of Utah Health Sciences Center.

CROWLEY, K., SLINEY, A., PITT, I. & MURPHY, D. (2010) Evaluating a brain-computer interface to categorise human emotional response. 10th IEEE International Conference on Advanced Learning Technologies (ICALT), 5-7 July. Sousse, Tunisia. IEEE, 276-278.

DAKE. (2005) *Synapse diag4* [Online]. Available: http://commons.wikimedia.org/wiki/File:Synapse_diag4.png [Accessed 12 January 2010].

DAVIES, J.H. (2008) *MSP430 Microcontroller Basics*. Oxford, Elsevier Science.

DAVIES, W.D.T. (1970) *System identification for self-adaptive control*. New Jersey, John Wiley & Sons Ltd.

DEBANNE, D., CAMPANAC, E., BIALOWAS, A., CARLIER, E. & ALCARAZ, G. (2011) Axon physiology. *Physiological reviews,* 91(2): 555-602.

DELSYS. (2012) *Trigno* [Online]. Available: http://www.delsys.com/ [Accessed 19 December 2013].

DENISON, T., JINBO, K., SHAFRAN, J., JUDY, M. & LUNDBERG, K. (2006a) A Self-Resonant MEMS-based Electrostatic Field Sensor with 4V/m/Hz

Sensitivity. IEEE International Solid-State Circuits Conference (ISSCC), 6-9 February. San Francisco. 1121-1130.

DENISON, T., SANTA, W., MOLNAR, G. & MIESEL, K. (2007a) Micropower Sensors for Neuroprosthetics. IEEE Sensors Conference, 28-31 October. Atlanta, Georgia. IEEE, 1105-1108.

DENISON, T.A., SHAFRAN, J.S., JINBO, K. & LUNDBERG, K.H. (2007b) A Self-Resonant MEMS-Based Electrometer. IEEE International Instrumentation and Measurement Technology Conference (IMTC), 1-3 May. Warsaw, Poland. 1-5.

DENISON, T.A., SHAFRAN, J.S. & LUNDBERG, K.H. (2006b) Feedback loop design for an electrostatic voltmeter. American Control Conference (ACC), 14-16 June. Minneapolis, Minnesota. 1215-1220.

DENNY-BROWN, D. & PENNYBACKER, J.B. (1938) Fibrillation and Fasciculation in Voluntary Muscle. *Brain,* 61(3): 311-312.

DI RUSSO, F., MARTINEZ, A., SERENO, M.I., PITZALIS, S. & HILLYARD, S.A. (2002) Cortical sources of the early components of the visual evoked potential. *Humam Brain Mapping,* 15(2): 95-111.

DISHMAN, E. (2012) *The personal health technology revolution* [Online]. Ernst & Young. Available: http://www.ey.com/GL/en/Industries/Life-Sciences/The-personal-health-technology-revolution [Accessed 5 June 2013].

DUCKWORTH, H.E., BARBER, R.C. & VENKATASUBRAMANIAN, V.S. (1986) Detection of positive ions. *Mass spectroscopy.* 2nd ed. Cambridge, Boston: Cambridge University Press, 70-85.

ECONOMIC AND SOCIAL RESEARCH INSTITUTE. (2007) Hospital In-Patient Enquiry Scheme Report. Available: http://www.esri.ie/health_information/latest_hipe_nprs_reports/ [Accessed 8 September 2013].

EGGINS, B.R. (1997) The Analyte or Substrate. *Biosensors: An Introduction* New Jersey: John Wiley & Sons 1-12.

EINTHOVEN, W. (1895) Ueber die Form des menschlichen Electrocardiogramms. *Pflügers Archiv: European Journal of Physiology,* 60(3): 101-123.

EINTHOVEN, W. (1901) Un nouveau galvanomètre. *Archives néerlandaises des sciences exactes et naturelles, publiées par la Société* VI(2): 625-633.

EINTHOVEN, W. (1902) Galvanometrische registratie van het menschelijk electrocardiogram. *In:* ROSENSTEIN, P. S. (ed.) *Herinneringsbundel.* Leiden, Holland: Eduard Ijdo, 101-107.

EINTHOVEN, W. (1908) Weiteres über das Elektrokardiogramm. *Pflügers Archiv: European Journal of Physiology,* 122(12): 517-584.

ELEFTHERIADIS, S., GEORGOULIS, S., VRENAS, K., TZIONAS, D. & HADJILEONTIADIS, L.J. (2011) Epione 2: An Innovative Pain Management Solution. *Microsoft Imagine Cup 2011*

EMMERSON-HANOVER, R., SHEARER, D.E., CREEL, D.J. & DUSTMAN, R.E. (1994) Pattern reversal evoked potentials: gender differences and age-related changes in amplitude and latency. *Electroencephalography and Clinical Neurophysiology/Evoked Potentials Section,* 92(2): 93-101.

EMOTIV. (2012) *EPOC* [Online]. Available: http://emotiv.com/ [Accessed 28 August 2012].

ERNSTENE, A.C. & LEVINE, S.A. (1928) A comparison of records taken with the Einthoven string galvanomter and the amplifier-type electrocardiograph. *American Heart Journal,* (4): 725-731.

ESPOSITO, S. & SCHETTINO, E. (2012) Spreading scientific philosophies with instruments: the case of Atwood's machine. *History and Philosophy of Physics arXiv preprint arXiv:1204.2984*.

ESQUENAZI, A., TALATY, M., PACKEL, A. & SAULINO, M. (2012) The ReWalk powered exoskeleton to restore ambulatory function to individuals with thoracic-level motor-complete spinal cord injury. *American Journal of Physical Medicine and Rehabilitation,* 91(11): 911-921.

EYKHOFF, P. (1974) *System identification: parameter and state estimation*. London, Wiley-Interscience.

FADEM, K.C. & SCHNITZ, B.A. (2005) *Active, multiplexed digital electrodes for EEG, ECG and EMG applications*. 11/092,395.

FERNÁNDEZ, M. & PALLÁS-ARENY, R. (2000) Ag-AgCl electrode noise in high-resolution ECG measurements. *Biomedical Instrumentation & Technology,* 34(2): 125-130.

FOK, S., SCHWARTZ, R., WRONKIEWICZ, M., HOLMES, C., ZHANG, J., SOMERS, T., BUNDY, D. & LEUTHARDT, E. (2011) An EEG-based brain computer interface for rehabilitation and restoration of hand control following stroke using ipsilateral cortical physiology. 33rd Annual International Conference of the IEEE Engineering in Medicine and Biology Society (EMBC), 30 August - 3 September. Boston. 6277-6280.

FRICKE, H. & MORSE, S. (1925) The Electric Resistance and Capacity of Blood for Frequencies Between 800 and 4.5 Million Cycles. *Journal of General Physiology,* 9(2): 153-67.

FURMAN, J.M., O'LEARY, D.P. & WOLFE, J.W. (1979) Application of linear system analysis to the horizontal vestibulo-ocular reflex of the alert rhesus monkey using pseudorandom binary sequence and single frequency sinusoidal stimulation. *Biological Cybernetics,* 33(3): 159-165.

FURUSAWA, Y., UENO, A., HOSHINO, H., KATAOKA, S., MITANI, H. & ISHIYAMA, Y. (2003) Low invasive measurement of electrocardiogram for

newborns and infants. IEEE EMBS Asian-Pacific Conference on Biomedical Engineering, 20-22 October. Kyoto, Japan. 256-257.

GALJAN, W., NAYDENOVA, D., TOMASIK, J.M., SCHROEDER, D. & KRAUTSCHNEIDER, W.H. (2008) A portable SoC-based ECG-system for 24h x 7d operating time. IEEE Biomedical Circuits and Systems Conference (BioCAS), 20-22 November. Baltimore, Maryland. 85-88.

GANESH. (2011) *questions answering 3d character stock photo* [Online]. Erode, Tamilnadu, India. Available: http://cute-pictures.blogspot.ie/2011/08/75-free-stock-images-3d-human-character.html#more [Accessed 28 September 2012].

GARGIULO, G., BIFULCO, P., CALVO, R.A., CESARELLI, M., JIN, C. & VAN SCHAIK, A. (2008a) Mobile biomedical sensing with dry electrodes. International Conference on Intelligent Sensors, Sensor Networks and Information Processing (ISSNIP), 15-18 December. Sydney. 261-266.

GARGIULO, G., BIFULCO, P., CALVO, R.A., CESARELLI, M., JIN, C. & VAN SCHAIK, A. (2008b) A mobile EEG system with dry electrodes. IEEE Biomedical Circuits and Systems Conference (BioCAS), 20-22 November. Baltimore, Maryland. 273-276.

GE HEALTHCARE. (2013) *CardioSoft Diagnostic System* [Online]. Available: http://www3.gehealthcare.co.uk/en-GB/Products/Categories/Diagnostic_Cardiology/Stress_and_Exercise/CardioSoft [Accessed 24 May 2013].

GINSBURG, K.R. (2007) The importance of play in promoting healthy child development and maintaining strong parent-child bonds. *Pediatrics,* 119(1): 182-191.

GIPS, J. & OLIVIERI, P. (1996) EagleEyes: An Eye Control System for Persons with Disabilities. 11th International Conference on Technology and Persons with Disabilities Los Angeles.

GOLDSTEIN, E.A., HEATON, J.T., KOBLER, J.B., STANLEY, G.B. & HILLMAN, R.E. (2004) Design and implementation of a hands-free electrolarynx device controlled by neck strap muscle electromyographic activity. *IEEE Transactions on Biomedical Engineering,* 51(2): 325-332.

GONDRAN, C., SIEBERT, E., YACOUB, S. & NOVAKOV, E. (1996) Noise of surface bio-potential electrodes based on NASICON ceramic and Ag−AgCl. *Medical and Biological Engineering and Computing,* 34(6): 460-466.

GOODWIN, G.C. & PAYNE, R.L. (1977) *Dynamic system identification: experiment design and data analysis: experiment design and data analysis*. New York, Academic Press.

GORESKY, M. & KLAPPER, A.M. (2002) Fibonacci and Galois representations of feedback-with-carry shift registers. *IEEE Transactions on Information Theory,* 48(11): 2826-2836.

GRASS TECHNOLOGIES. (2013) *Electrode Impedance Meters* [Online]. Available: http://www.grasstechnologies.com/catalog/index.php?cPath=32_154&osCsid=cddee4d0a94c3b00acb2fc6c10bcf4fb [Accessed 4 April 2013].

GRAY, H. (1918) *Anatomy of the Human Body*. 20th Edition ed. Philadelphia, Lea & Febiger.

GREATBATCH, W., PIERSMA, B., SHANNON, F.D. & CALHOON, S.W. (1969) Polarization Phenomena Relating to Physiological Electrodes. *Annals of the New York Academy of Sciences,* 167(2): 722-744.

GRIMNES, S. (1982) Skin capacitance as a measure of effective electrode area. 1st World Congress on Medical Physics and Biomedical Engineering, 6-11 September. Hamburg.

GRIMNES, S. (1983) Impedance measurement of individual skin surface electrodes. *Medical and Biological Engineering and Computing,* 21(6): 750-755.

GUNN, R. (1932) Principles of a New Portable Electrometer. *Physical Review,* 40(2): 307-312.

HAAPALAINEN, E., KIM, S., FORLIZZI, J.F. & DEY, A.K. (2010) Psycho-physiological measures for assessing cognitive load. 12th ACM international conference on Ubiquitous computing, 26-29 September. Beijing, China. ACM, 301-310.

HAAS, J. (2012) *Neurons* [Online]. Available: http://en.wikipedia.org/wiki/File:Neurons_uni_bi_multi_pseudouni.svg [Accessed 20 June 2013].

HAMLET, S., PATTERSON, R., FLEMING, S. & JONES, L. (1992) Sounds of swallowing following total laryngectomy. *Dysphagia,* 7(3): 160-165.

HAMMOND, D.C. (2005) Neurofeedback with anxiety and affective disorders. *Child and Adolescent Psychiatric Clinics of North America,* 14(1): 105-123.

HARLAND, C.J., CLARK, T.D., PETERS, N.S., EVERITT, M.J. & STIFFELL, P.B. (2005) A compact electric potential sensor array for the acquisition and reconstruction of the 7-lead electrocardiogram without electrical charge contact with the skin. *Physiological Measurement,* 26(6): 939-950.

HARLAND, C.J., CLARK, T.D. & PRANCE, R.J. (2002a) Electric potential probes - new directions in the remote sensing of the human body. *Measurement Science and Technology,* 13(2): 163-169.

HARLAND, C.J., CLARK, T.D. & PRANCE, R.J. (2002b) Remote detection of human electroencephalograms using ultrahigh input impedance electric potential sensors. *Applied Physics Letters,* 81(17): 3284-3286.

HARLAND, C.J., CLARK, T.D. & PRANCE, R.J. (2003) High resolution ambulatory electrocardiographic monitoring using wrist-mounted electric potential sensors. *Measurement Science and Technology,* 14(7): 923-928.

HARRISON, C. & HUDSON, S.E. (2008) Scratch input: creating large, inexpensive, unpowered and mobile finger input surfaces. 21st annual ACM symposium on User interface software and technology, 19-22 October. Monterey, California, USA. ACM, 205-208.

HARRISON, C., TAN, D. & MORRIS, D. (2010) Skinput: appropriating the body as an input surface. 28th ACM Conference on Human Factors in Computing Systems (CHI), 10-15 April. Atlanta, Georgia, USA. 1753394: ACM, 453-462.

HARRISON, R.R., WATKINS, P.T., KIER, R.J., LOVEJOY, R.O., BLACK, D.J., GREGER, B. & SOLZBACHER, F. (2007) A Low-Power Integrated Circuit for a Wireless 100-Electrode Neural Recording System. *IEEE Journal of Solid-State Circuits,* 42(1): 123-133.

HAUSER, S.L. & BEAL, M.F. (2008) Biology of Neurologic Diseases. *In:* LONGO, D. L., FAUCI, A. S., KASPER, D. L., HAUSER, S. L., JAMESON, J. L. & LOSCALZO, J. (eds.) *Harrison's Principles of Internal Medicine.* 18th ed. New York: The McGraw-Hill Companies, Inc, 3224-3233.

HEATON, J.T., GOLDSTEIN, E.A., KOBLER, J.B., M., Z.S., W., R.G., J., W.M., E., G.J. & HILLMAN, R.E. (2004) Surface electromyographic activity in total laryngectomy patients following laryngeal nerve transfer to neck strap muscles. *The Annals of Otology, Rhinology, and Laryngology,* 113(9): 754-764.

HEIMBACH, G. (2008) *Piano made with LabVIEW* [Online]. Available: https://decibel.ni.com/content/docs/DOC-2112.

HENNEMAN, E. & OLSON, C.B. (1965) Relations between structure and function in the design of skeletal muscles. *Journal of Neurophysiology,* 28(3): 581-598.

HENNEMAN, E., SOMJEN, G. & CARPENTER, D.O. (1965a) Excitability and inhibitibility of motoneurons of different sizes. *Journal of Neurophysiology,* 28(3): 599-620.

HENNEMAN, E., SOMJEN, G. & CARPENTER, D.O. (1965b) Functional significance of cell size in spinal motoneurons. *Journal of Neurophysiology,* 28(3): 560-580.

HODGKIN, A.L. & HUXLEY, A.F. (1952) A quantitative description of membrane current and its application to conduction and excitation in nerve. *The Journal of Physiology,* 117(4): 500-544.

HOLLIEN, H., DEW, D. & PHILIPS, P. (1971) Phonational Frequency Ranges of Adults. *Journal of Speech and Hearing Research,* 14(4): 755-760.

HOLTER, N.J. (1961) New Method for Heart Studies: Continuous electrocardiography of active subjects over long periods is now practical. *Science,* 134(3486): 1214-1220.

HONEYWELL. (2011) *3-Axis Digital Compass IC HMC5883L* [Online]. Available: http://www51.honeywell.com/aero/common/documents/myaerospacecatalog-documents/Defense_Brochures-documents/HMC5883L_3-Axis_Digital_Compass_IC.pdf [Accessed 26 March 2013].

HOOGERWERF, A.C. & WISE, K.D. (1994) A three-dimensional microelectrode array for chronic neural recording. *IEEE Transactions on Biomedical Engineering,* 41(12): 1136-1146.

HOROWITZ, P. & HILL, W. (1989) *The Art of Electronics*. 2nd ed. New York Cambridge University Press.

HUHTA, J.C. & WEBSTER, J.G. (1973) 60-Hz Interference in Electrocardiography. *IEEE Transactions on Biomedical Engineering,* BME-20(2): 91-101.

HUIGEN, E., PEPER, A. & GRIMBERGEN, C. (2002) Investigation into the origin of the noise of surface electrodes. *Medical and Biological Engineering and Computing,* 40(3): 332-338.

HULL, A.W. (1932) Electronic Devices as Aids to Research. *Journal of Applied Physics,* 2(6): 409-431.

ICONSHOCK. (2009) *Headphones* [Online]. Wikimedia. Available: http://commons.wikimedia.org/wiki/File:Headphones_256.png [Accessed 10 January 2013].

IKEZU, T. & GENDELMAN, H.E. (2008) Neurobiology and Neural Systems. *In:* IKEZU, T. & GENDELMAN, H. E. (eds.) *Neuroimmune Pharmacology.* 1st ed. New Mexico: Springer, 171-182.

IMS RESEARCH. (2012) *Wearable Medical Technology Set To Take Off* [Online]. London. Available: http://imsresearch.com/press-release/Wearable_Technology_Market_to_Exceed_6_Billion_by_2016 [Accessed 26 September 2012].

INSTITUTE OF ELECTRICAL AND ELECTRONICS ENGINEERS. (2007) *IEEE 802.15 WPAN* [Online]. Available: http://www.ieee802.org/15/pub/TG6.html [Accessed 3 September 2012].

INTEL. (2011) *Personal Health & Health Information Technology* [Online]. Available: http://www.intel.ie/content/dam/www/public/us/en/documents/white-papers/personal-health-and-health-information-technology-paper.pdf [Accessed 5 June 2013].

INTERNATIONAL ELECTROTECHNICAL COMMISSION (2005) *Medical electrical equipment,* IEC 60601-1 General requirements for basic safety and essential performance, 65.

INVENSENSE. (2011) *MPU-6000/6050 Integrated 6-Axis (Gyro + Accelerometer) MotionProcessing solution* [Online]. Available: http://invensense.com/mems/gyro/mpu6000.html [Accessed 26 March 2013].

INVENSENSE. (2012) *Nine-Axis (Gyro + Accelerometer + Compass) MEMS MotionTracking™ Device* [Online]. Available: http://invensense.com/mems/gyro/mpu9150.html [Accessed 19 September 2012].

IRISH MOTOR NEURONE DISEASE ASSOCIATION. (2006) *Motor Neurone Disease Information Sheet* [Online]. Available: http://www.imnda.ie/index.cfm/loc/4-4.htm [Accessed 12 December 2009].

JACOBSON, J.D. (2009) *Symptoms of Multiple Sclerosis - Sensory Symptoms* [Online]. Available: http://www.my-ms.org/symptoms_sensory.htm [Accessed 19 June 2013].

JAWBONE. (2011) *UP* [Online]. Available: https://jawbone.com/up [Accessed 1 July 2013].

JIVET, I. (2009) Architecture of an on Electrode Integrated Electronics with an All Digital Interface for Electrical Impedance Tomography. *In:* VLAD, S., CIUPA, R. V. & NICU, A. I., eds. International Conference on Advancements of Medicine and Health Care through Technology, 23-26 September Cluj-Napoca, Romania. Springer Berlin Heidelberg, 205-208.

JIVET, I. & DRAGOI, B. (2008) On-electrode autonomous current generator for multi-frequency EIT. *Physiological Measurement,* 29(6): S193-S201.

JST MANUFACTURING COMPANY LTD. (1997) *JST-SH connector* [Online]. Available: http://www.jst-mfg.com/product/detail_e.php?series=231 [Accessed 27 March 2013].

KARNI, A., TANNE, D., RUBENSTEIN, B.S., ASKENASY, J.J. & SAGI, D. (1994) Dependence on REM sleep of overnight improvement of a perceptual skill. *Science,* 265(5172): 679-682.

KATO, T., UENO, A., KATAOKA, S., HOSHINO, H. & ISHIYAMA, Y. (2006) An Application of Capacitive Electrode for Detecting Electrocardiogram of Neonates and Infants. 28th Annual International Conference of the IEEE Engineering in Medicine and Biology Society (EMBC), 31 August - 3 September. New York. 916-919.

KE-MIN, L., RONGSHUN, C. & BRUCE, C.S.C. (2005) Design of a Thermal-Bubble-Based Micromachined Accelerometer. International Conference on MEMS, NANO and Smart Systems, 24-27 July. Banff, Alberta, Canada. IEEE Computer Society, 438-442.

KESTER, W. (2008) Understand SINAD, ENOB, SNR, THD, THD + N, and SFDR so You Don't Get Lost in the Noise Floor. *Tutorial MT-003.* Analog Devices.

KESTER, W.A. & BRYANT, J. (2005) Data Converter Architectures. *In:* KESTER, W. A. (ed.) *The Data Conversion Handbook.* 3rd ed. Oxford: Boston, 109-140.

KESTER, W.A., SHEINGOLD, D. & BRYANT, J. (2005) Fundamentals of Sampled Data Systems. *In:* KESTER, W. A. (ed.) *The Data Conversion Handbook.* 3rd ed. Oxford: Boston, 75-192.

KHAN, A. & GREATBATCH, W. (1974) Physiologic electrodes. *In:* RAY, C. D. (ed.) *Medical Engineering.* Chicago: Year Book Medical Publishers, 1073-1082.

KHERLOPIAN, A.R., GERREIN, J.P., YUE, M., KIM, K.E., KIM, J.W., SUKUMARAN, M. & SAJDA, P. (2006) Electrooculogram based system for computer control using a multiple feature classification model. 28th Annual International Conference of the IEEE Engineering in Medicine and Biology Society (EMBC), 31 August - 3 September. New York. 1295-1298.

KIN-FAI, W. & YUAN-TING, Z. (2008) Contactless and continuous monitoring of heart electric activities through clothes on a sleeping bed. 5th International Conference on Information Technology and Applications in Biomedicine (ITAB), 30-31 May Shenzhen, China. 282-285.

KO KEUN, K., YONG KYU, L. & KWANG SUK, P. (2005) Common Mode Noise Cancellation for Electrically Non-Contact ECG Measurement System on a Chair. 27th Annual International Conference of the IEEE Engineering in Medicine and Biology Society (EMBC), 1-4 September. Shanghai, China. 5881-5883.

KUBERT, H.L., STEPP, C.E., ZEITELS, S.M., GOOEY, J.E., WALSH, M.J., PRAKASH, S.R., HILLMAN, R.E. & HEATON, J.T. (2009) Electromyographic control of a hands-free electrolarynx using neck strap muscles. *Journal of Communication Disorders*: 211-225.

KYLE, U.G., BOSAEUS, I., DE LORENZO, A.D., DEURENBERG, P., ELIA, M., GÓMEZ, J.M., HEITMANN, B.L., KENT-SMITH, L., MELCHIOR, J.-C. & PIRLICH, M. (2004a) Bioelectrical impedance analysis-part I: review of principles and methods. *Clinical Nutrition,* 23(5): 1226-1243.

KYLE, U.G., BOSAEUS, I., DE LORENZO, A.D., DEURENBERG, P., ELIA, M., GÓMEZ, J.M., HEITMANN, B.L., KENT-SMITH, L., MELCHIOR, J.-C. & PIRLICH, M. (2004b) Bioelectrical impedance analysis-part II: utilization in clinical practice. *Clinical Nutrition* 23(6): 1430-1453.

LACKERMEIER, A., PIRKE, A., MCADAMS, E.T. & JOSSINET, J. (1996) Non-linearity of the skin's AC impedance. 18th Annual International Conference of the IEEE Engineering in Medicine and Biology Society (EMBC), 31 October - 3 November. Amsterdam. 1945-1946.

LAMARCHE, A. & TERNSTRÖM, S. (2008) An Exploration of Skin Acceleration Level as a Measure of Phonatory Function in Singing. *Journal of Voice,* 22(1): 10-22.

LIPPMANN, G. (1873) Beziehungen zwischen den capillaren und elektrischen Erscheinungen. *Annalen der Physik,* 225(8): 546-561.

LONGO, M. (2007) *What are we measuring in EEG and MEG?* [Online]. University College London. Available: http://www.fil.ion.ucl.ac.uk/~jchumb/powerpoint%20presentations/What%20are%20we%20measuring%20in%20EEG%20and%20MEG.ppt [Accessed 18 June 2013].

LUNDBERG, K.H., SHAFRAN, J.S., KUANG, J., JUDY, M. & DENISON, T.A. (2006) A self-resonant MEMS-based electrostatic field sensor. American

Control Conference (ACC), 14-16 June. Minneapolis, Minnesota, USA. 1221-1226.

MADDEN, B., NOLAN, M., BURKE, E., CONDRON, J. & COYLE, E. (2010) Intelligibility of Electrolarynx Speech using a Novel Actuator. IET Irish Signals and Systems Conference, 23-24 June. Cork, Ireland. 158-162.

MADDEN, B., NOLAN, M., BURKE, E., CONDRON, J. & COYLE, E. (2011) Intelligibility of Electrolarynx Speech using a Novel Hands-Free Actuator. 4th International Joint Conference on Biomedical Engineering Systems and Technologies, 26-29 January. Rome. 265-269.

MALMIVUO, J. & PLONSEY, R. (1995) *Bioelectromagnetism - Principles and Applications of Bioelectric and Biomagnetic Fields*. New York, Oxford University Press.

MAQUESTA. (2007) *Homunculus: diagram showing position of regions of the human cortex corresponding to the respective afferent/efferent nerve region of the body. Blue: sensor cortex. Red: motor cortex* [Online]. Available: http://commons.wikimedia.org/wiki/File:Homunculus.png [Accessed 12 November 2009].

MARIEB, E.N. & HOEHN, K. (2012) *Human Anatomy and Physiology*. 10th ed. San Francisco, Benjamin-Cummings Publishing Company.

MARTINI, F.H., NATH, J.L. & BARTHOLOMEW, E.F. (2011) *Fundamentals of Anatomy & Physiology* 9th ed. San Francisco, Pearson Benjamin Cummings.

MARUYAMA, T., MAKIKAWA, M., SHIOZAWA, N. & FUJIWARA, Y. (2007) ECG Measurement Using Capacitive Coupling Electrodes for Man-Machine Emotional Communication. IEEE/ICME International Conference on Complex Medical Engineering (CME), 23-27 May. Beijing, China. 378-383.

MAXIM INTEGRATED PRODUCTS INC. (2001) *Understanding SAR ADCs: Their Architecture and Comparison with Other ADCs* [Online]. Available: http://www.maximintegrated.com/app-notes/index.mvp/id/1080 [Accessed 28 September 2012].

MAXIM INTEGRATED PRODUCTS INC. (2013) *1-Wire Tutorial Presentation* [Online]. Available: http://www.maximintegrated.com/products/1-wire/flash/overview/ [Accessed 11 June 2013].

MAYER, S., GEDDES, L.A., BOURLAND, J.D. & OGBORN, L. (1992) Electrode recovery potential. *Annals of Biomedical Engineering,* 20(3): 385-394.

MELLINGER, J., SCHALK, G., BRAUN, C., PREISSL, H., ROSENSTIEL, W., BIRBAUMER, N. & KÜBLER, A. (2007) An MEG-based brain-computer interface (BCI). *Neuroimage,* 36(3): 581-593.

METTING VAN RIJN, A.C., PEPER, A. & GRIMBERGEN, C.A. (1991) High-quality recording of bioelectric events. Part 1. Interference reduction, theory and practice. *Medical and Biological Engineering and Computing,* 29(4): 433-440.

METTINGVANRIJN, A.C., KUIPER, A.P., DANKERS, T.E. & GRIMBERGEN, C.A. (1996) Low-cost active electrode improves the resolution in biopotential recordings. 18th Annual International Conference of the IEEE Engineering in Medicine and Biology Society (EMBC), 31 October - 3 November. Amsterdam. 101-102.

MINISTRY OF EDUCATION CULTURE SPORTS AND TECHNOLOGY - JAPAN. (2011) *Brodmann area 4 lateral* [Online]. Available: http://commons.wikimedia.org/wiki/File:Brodmann_area_4_lateral.jpg [Accessed 5 July 2012].

MOHSENI, P., NAJAFI, K., ELIADES, S.J. & XIAOQIN, W. (2005) Wireless multichannel biopotential recording using an integrated FM telemetry circuit. *IEEE Transactions on Neural Systems and Rehabilitation Engineering,* 13(3): 263-271.

MOODY, G.B., MARK, R.G., ZOCCOLA, A. & MANTERO, S. (1985) Derivation of Respiratory Signals from Multi-lead ECGs. *Computers in Cardiology* 113-116.

NAGEL, J.H. (1995) Biopotential Amplifiers. *In:* BRONZINO, J. D. (ed.) *The Biomedical Engineering Handbook* 1ed. Boca Raton, Florida: CRC Press Inc., 1185-1195.

NASIFF ASSOCIATES INC. (2013) *Nasiff CarioCard - PC Based Stress Testing System* [Online]. Available: http://www.nasiff.com/stress.html [Accessed 24 May 2013].

NATIONAL DISABILITY AUTHORITY. (2013) *Center for Excellence in Universal Design* [Online]. Available: http://www.universaldesign.ie/exploreampdiscover [Accessed 31 May 2013].

NEUMAN, M.R. (2009a) Biopotential Amplifiers. *In:* WEBSTER, J. G. (ed.) *Medical Instrumentation: Application and Design.* 4th ed. New York: John Wiley & Sons, 241-292.

NEUMAN, M.R. (2009b) Biopotential Electrodes. *In:* WEBSTER, J. G. (ed.) *Medical Instrumentation: Application and Design.* 4th ed. New York: John Wiley & Sons, 189-240.

NEUROSKY. (2012) *MindWave* [Online]. Available: http://www.neurosky.com/ [Accessed 20 September 2012].

NIKE INC. (2012) *Nike+ Fuelband* [Online]. Available: http://www.nike.com/us/en_us/c/nikeplus-fuelband [Accessed 1 July 2013].

NINTENDO. (2006) *Wii* [Online]. Available: http://www.nintendo.com/wii/what-is-wii [Accessed 1 July 2013].

NOLAN, M., BURKE, E. & COYLE, E. (2011) Novel Bioelectrical Measurement using a Digital Biopotential Monode. Bioengineering In Ireland, BINI, 28-29 January. Galway, Ireland. 100.

NOLAN, M., BURKE, E. & COYLE, E. (2012) A Wireless and Digital Electrode Bus Topology for Biopotential Measurement. 23rd Irish Signals and Systems Conference (ISSC), 28-29 June. Maynooth, Ireland. 70-73.

NOLAN, M., BURKE, E. & DUIGNAN, F. (2009a) Accelerometer based Measurement of Body Movement for Communication, Play, and Creative Expression. 4th European Conference of the International Federation for Medical and Biological Engineering, 23-27 November. Antwerp, Belgium. Springer Berlin Heidelberg, 1835-1838.

NOLAN, M., MADDEN, B. & BURKE, E. (2009b) Accelerometer based Measurement for the Mapping of Neck Surface Vibrations during Vocalized Speech. 31st Annual International Conference of the IEEE Engineering in Medicine and Biology Society (EMBC), 2-6 September. Minneapolis, Minnesota, USA. 4453-4456.

NOLAN, Y. & DEPAOR, A. (2004) The mechanomyogram as a channel of communication and control for the disabled. 26th Annual International Conference of the IEEE Engineering in Medicine and Biology Society (EMBC), 1-5 September. San Francisco, California. 4928-4931.

NORTH CAROLINA STATE UNIVERSITY. (1997) *The Center for Universal Design, The Principles of Universal Design* [Online]. North Carolina State University. Available: http://www.ncsu.edu/ncsu/design/cud/pubs_p/docs/poster.pdf [Accessed 4 September 2013].

NXP SEMICONDUCTORS. (2006) *PCA9517A - Level translating I²C-bus repeater* [Online]. Available: http://www.nxp.com/products/interface_and_connectivity/i2c/i2c_bus_repeaters_hubs_extenders/series/PCA9517A.html [Accessed 11 June 2013].

NXP SEMICONDUCTORS. (2012) I2C-bus specification and user manual Rev. 5. Available: http://www.nxp.com/documents/user_manual/UM10204.pdf [Accessed 25 October 2012].

NYQUIST, H. (1928) Thermal Agitation of Electric Charge in Conductors. *Physical Review,* 32(1): 110-113.

ODOM, J.V., BACH, M., BRIGELL, M., HOLDER, G., MCCULLOCH, D., TORMENE, A. & VAEGAN (2010) ISCEV standard for clinical visual evoked potentials (2009 update). *Documenta Ophthalmologica,* 120(1): 111-119.

OLSON, W.H. (2009) Basic Concepts of Medical Instrumentation. *In:* WEBSTER, J. G. (ed.) *Medical Instrumentation: Application and Design.* 4th ed. New York: John Wiley & Sons, 1-44.

PANTELOPOULOS, A. & BOURBAKIS, N.G. (2010) A Survey on Wearable Sensor-Based Systems for Health Monitoring and Prognosis. *IEEE Transactions on Systems, Man, and Cybernetics, Part C: Applications and Reviews,* 40(1): 1-12.

PENFIELD, W. & JASPER, H. (1954) *Epilepsy and the Functional Anatomy of the Human Brain*. 2nd ed. Boston, Litle, Brown and Company.

PETERSEN, M.K., STAHLHUT, C., STOPCZYNSKI, A., LARSEN, J.E. & HANSEN, L.K. (2011) Smartphones get emotional: mind reading images and reconstructing the neural sources. 4th international conference on Affective computing and intelligent interaction - Volume Part II, 9-12 October. Memphis, Tennessee. 2062929: Springer-Verlag, 578-587.

PHILLIPS, C. (2006) *Twelve Benefits of Music Education* [Online]. Available: http://www.childrensmusicworkshop.com/advocacy/12benefits.html.

POLAR ELECTRO. (2013) *Heart rate monitors* [Online]. Available: http://www.polar.com/en [Accessed 1 July 2013].

PRANCE, R.J., BEARDSMORE-RUST, S.T., WATSON, P., HARLAND, C.J. & PRANCE, H. (2008) Remote detection of human electrophysiological signals using electric potential sensors. *Applied Physics Letters,* 93(3): 033906-3.

PRANCE, R.J., DEBRAY, A., CLARK, T.D., PRANCE, H., NOCK, M. & HARLAND, C.J. (2000) An ultra-low-noise electrical-potential probe for human-body scanning. *Measurement Science and Technology,* 11(3): 291-297.

QUAN, D. & RINGEL, S.P. (2010) Neuromuscular Diseases. *In:* WEINER, W. J., GOETZ, C. G., SHIN, R. K. & LEWIS, S. L. (eds.) *Neurology for the Non-Neurologist.* 6th ed. Philadelphia: Wolters Kluwer Health/Lippincott Williams & Wilkins, 344.

RENDON, D.B., OJEDA, J.L.R., FOIX, L.F.C., MORILLO, D.S. & FERNANDEZ, M.A. (2007) Mapping the Human Body for Vibrations using an Accelerometer. 29th Annual International Conference of the IEEE Engineering in Medicine and Biology Society (EMBC), 23-26 August. Lyon, France. 1671-1674.

RIVERA-RUIZ, M., CAJAVILCA, C. & VARON, J. (2008) Einthoven's string galvanometer: the first electrocardiograph. *Texas Heart Institute Journal* 35(2): 174-8.

ROSELL, J., COLOMINAS, J., RIU, P., PALLAS-ARENY, R. & WEBSTER, J.G. (1988) Skin impedance from 1 Hz to 1 MHz. *IEEE Transactions on Biomedical Engineering,* 35(8): 649-651.

SALADIN, K.S. (2011) *Anatomy & Physiology: The Unity of Form and Function*. 6th ed. New York, McGraw-Hill Education.

SAMENI, R. & CLIFFORD, G.D. (2010) A Review of Fetal ECG Signal Processing; Issues and Promising Directions. *The Open Pacing Electrophysiology & Therapy Journal,* 3: 4-20.

SAMSUNG GROUP. (2013) *S Health Heart Rate Monitor* [Online]. Available: http://www.samsung.com/uk/consumer/mobile-devices/smartphones/smartphone-accessories/EI-HH10NNBEGWW [Accessed 1 July 2013].

SANCHEZ, D. (2008) *Male Head (Modified)* [Online]. Available: http://www.digitaldrone.com/-sanchez/HighPolyHead.jpg [Accessed 31 August 2012].

SCHNITZ, B.A., STEWART, J.A., ALLEN, R.V. & FADEM, K.C. (2004) Improving Signal Quality and Test Reliability in EEG Measurements Using Integrated High-Density Surface-Mount Electronics. SMTA Medical Electronics Symposium, 19-20 May. Minneapolis, Minnesota, USA.

SEONG-JUN, S., NAMJUN, C. & HOI-JUN, Y. (2007) A 0.2-mW 2-Mb/s Digital Transceiver Based on Wideband Signaling for Human Body Communications. *IEEE Journal of Solid-State Circuits,* 42(9): 2021-2033.

SHARBROUGH, F., CHATRIAN, G.-E., LESSER, R.P., LUDERS, H., NUWER, M. & PICTON, T.W. (1991) American Electroencephalographic Society Guidelines for Standard Electrode Position Nomenclature *Journal of Clinical Neurophysiology,* 8(2): 200-202.

SHIMA, K. & TSUJI, T. (2009) An MMG-based human-assisting manipulator using acceleration sensors. IEEE International Conference on Systems, Man and Cybernetics (SMC), 11-14 October. San Antonio, Texas, USA. 2433-2438.

SHIMMER RESEARCH. (2006) *Shimmer* [Online]. Available: http://shimmer-research.com/ [Accessed 9 February 2010].

SILVA, I.S.S., NAVINER, J.-F. & FREIRE, R.C.S. (2006) Compensation of Mismatch Electrodes Impedances in Biopotential Measurement. IEEE International Workshop on Medical Measurement and Applications (MeMea), 20-21 April. Benevento, Italy. 33-36.

SIMINI, F., TOUYA, A., SENATORE, A. & PEREIRA, J. (2011) Gaze tracker by electrooculography (EOG) on a head-band. 10th International Workshop on Biomedical Engineering, 5-7 October. Kos, Greece. 1-4.

SLEPICKA, D. (2007) Noise Floor in ADC Testing. 12th IMEKO International Workshop on ADC Modelling and Testing, 19-21 September. Iasi, Romania. 63-67.

SMITH, D.B., HOUSH, T.J., JOHNSON, G.O., EVETOVICH, T.K., EBERSOLE, K.T. & PERRY, S.R. (1998) Mechanomyographic and electromyographic responses to eccentric and concentric isokinetic muscle actions of the biceps brachii. *Muscle & Nerve,* 21(11): 1438-1444.

SMITH, S.W. (1997) *The Scientist and Engineer's Guide to Digital Signal Processing*. 1st ed. San Diego, California, California Technical Publishing.

SOFIA, K.O. & JONES, L.A. (2013) Mechanical and Psychophysical Studies of Surface Wave Propagation during Vibrotactile Stimulation. *IEEE Transactions on Haptics,* 99(PrePrints): 1-11.

SONG-HEE, P., AINA, A., DENISON, T. & LUNDBERG, K. (2004) Feedback control for a MEMS-based high-performance operational amplifier. American Control Conference (ACC), 30 June - 2 July. Boston. 380-385.

SONY COMPUTER ENTERTAINMENT. (2010) *PlayStation Move* [Online]. Available: http://us.playstation.com/ps3/playstation-move/ [Accessed 1 July 2013].

SPARKFUN. (2012) *SparkFun Eagle Libraries* [Online]. Available: https://github.com/sparkfun/SparkFun-Eagle-Libraries [Accessed 24 July 2013].

SREBRO, R. & WRIGHT, W.W. (1980) Visually evoked potentials to pseudorandom binary sequence stimulation: Preliminary clinical trials. *Archives of Ophthalmology,* 98(2): 296-298.

STILSON, T. (1996) *Electrode-Skin Interface* [Online]. Available: http://soundlab.cs.princeton.edu/learning/tutorials/sensors/img29.gif [Accessed 15 December 2009].

STOPCZYNSKI, A., LARSEN, J.E., STAHLHUT, C., PETERSEN, M.K. & HANSEN, L.K. (2011) A smartphone interface for a wireless EEG headset with real-time 3D reconstruction. 4th international conference on Affective computing and intelligent interaction - Volume Part II, 9-12 October. Memphis, Tennessee. Springer-Verlag 317-318.

STRAUSS, M., REYNOLDS, C., HUGHES, S., PARK, K., MCDARBY, G. & PICARD, R. (2005) The HandWave Bluetooth Skin Conductance Sensor. Affective Computing and Intelligent Interaction. New York. Springer Berlin Heidelberg, 699-706.

SVEC, J.G., TITZE, I.R. & POPOLO, P.S. (2005) Estimation of sound pressure levels of voiced speech from skin vibration of the neck. *The Journal of the Acoustical Society of America,* 117(3): 1386-1394.

SZOCIK, J., BARKER, S.J. & TREMPER, K.K. (2010) Fundamental Principles of Monitoring Instrumentation. *In:* MILLER, R. D. (ed.) *Miller's Anesthesia.* 7th ed. Philadelphia: Churchill Livingstone, 1197-1229.

TAE-HO, K., MERRITT, C.R., GRANT, E., POURDEYHIMI, B. & NAGLE, H.T. (2008) Nonwoven Fabric Active Electrodes for Biopotential Measurement During Normal Daily Activity. *IEEE Transactions on Biomedical Engineering,* 55(1): 188-195.

TAM, H.W. & WEBSTER, J.G. (1977) Minimizing Electrode Motion Artifact by Skin Abrasion. *IEEE Transactions on Biomedical Engineering,* BME-24(2): 134-139.

TERLEP, D. (2002) How Quantization and Thermal Noise Determine an ADC's Effective Noise Figure. *Tutorial 1197.* Maxim Integrated.

TEXAS INSTRUMENTS. (2003) *OPA334* [Online]. Available: http://www.ti.com/lit/ds/symlink/opa334.pdf [Accessed 1 May 2013].

TEXAS INSTRUMENTS. (2004) *MSP430x2xx Family User's Guide (Rev. I)* [Online]. Available: http://www.ti.com/product/msp430f2013 [Accessed 24 January 2013].

TEXAS INSTRUMENTS. (2005) *MSP430F20x1, MSP430F20x2, MSP430F20x3 Mixed Signal Microcontroller (Rev. H)* [Online]. Available: http://www.ti.com/lit/ds/symlink/msp430f2013.pdf [Accessed 9 April 2013].

TEXAS INSTRUMENTS. (2007a) *CC2480* [Online]. Available: http://www.ti.com/product/cc2480a1 [Accessed 5 July 2013].

TEXAS INSTRUMENTS. (2007b) *MSP430F21x2 Mixed Signal Microcontroller (Rev. J)* [Online]. Available: http://www.ti.com/lit/ds/symlink/msp430f2132.pdf [Accessed 9 April 2013].

TEXAS INSTRUMENTS. (2011) *MSP430AFE2xx* [Online]. Available: http://www.ti.com/product/msp430afe253 [Accessed 11 June 2013].

TEXAS INSTRUMENTS. (2012) *Medical Analog Front End* [Online]. Available: http://www.ti.com/lsds/ti/data-converters/medical-analog-front-end-products.page?paramCriteria=no [Accessed 12 September 2012].

THE IEEE STANDARDS ASSOCIATION (2001) *IEEE Standard for Terminology and Test Methods for Analog-To-Digital Converters,* IEEE Std 1241-2000.

TONG, S., BEZERIANOS, A., PAUL, J., ZHU, Y. & THAKOR, N. (2001) Removal of ECG interference from the EEG recordings in small animals using independent component analysis. *Journal of Neuroscience Methods,* 108(1): 11-17.

TORTORA, G.J. & DERRICKSON, B.H. (2011) *Principles of Anatomy and Physiology*. 13 edition ed. New Jersey, John Wiley & Sons, Inc.

TRANKLER, H.R. & KANOUN, O. (2001) Recent advances in sensor technology. 18th Annual International Conference of the IEEE Instrumentation and Measurement Technology Conference, 21-23 May. Budapest. 309-316.

TRAVAGLINI, A., LAMBERTI, C., DEBIE, J. & FERRI, M. (1998) Respiratory signal derived from eight-lead ECG. Computers in Cardiology, 13-16 September. Cleveland, Ohio, USA. 65-68.

U.S. FEDERAL COMMUNICATIONS COMMISSION. (2012) *FCC dedicates spectrum enabling medical body area networks to transform patient care, lower health care costs, and spur wireless medical innovation* [Online]. United States Federal Communications Commission. Available: http://www.fcc.gov/document/fcc-dedicates-spectrum-enabling-medical-body-area-networks [Accessed 24 July 2013].

UNITED NATIONS. (2006) UN Convention on the Rights of Persons with Disabilities. Available: http://www.un.org/disabilities/convention/conventionfull.shtml [Accessed 20 August 2012].

VALCHINOV, E.S. & PALLIKARAKIS, N.E. (2004) An active electrode for biopotential recording from small localized bio-sources. *Biomed Eng Online,* 3(1): 25.

VELLISTE, M., PEREL, S., SPALDING, M.C., WHITFORD, A.S. & SCHWARTZ, A.B. (2008) Cortical control of a prosthetic arm for self-feeding. *Nature,* 453(7198): 1098-1101.

WALLER, A.D. (1887) A Demonstration on Man of Electromotive Changes accompanying the Heart's Beat. *The Journal of Physiology,* 8(5): 229-234.

WATERLOO LABS. (2009) *Triangulate the position of an impact on a wall for the generation of a mouse click corresponding to that location* [Online]. Available: http://www.waterloolabs.com/ [Accessed 14th October 2010].

WEBSTER, J.G. (1977) Interference And Motion Artifact In Biopotentials. IEEE Region Six Conference Record, 25-27 May. Portland, Oregon. 53-64.

WEBSTER, J.G. (1984) Reducing Motion Artifacts and Interference in Biopotential Recording. *IEEE Transactions on Biomedical Engineering,* BME-31(12): 823-826.

WESTEYN, T., PRESTI, P. & STARNER, T. (2006) ActionGSR: A Combination Galvanic Skin Response-Accelerometer for Physiological Measurements in Active Environments. 10th IEEE International Symposium on Wearable Computers, 11-14 October. Montreux, Switzerland. 129-130.

WIKIMEDIA. (2008) *Brain_headBorder* [Online]. Available: http://commons.wikimedia.org/wiki/File:Brain_headBorder.jpg [Accessed 5 February 2013].

WILDORA. (2009) *OSCulator* [Online]. Available: http://www.osculator.net/ [Accessed 13 March 2013].

WINTER, B.B. & WEBSTER, J.G. (1983a) Driven-right-leg circuit design. *IEEE Transactions on Biomedical Engineering,* BME-30(1): 62-66.

WINTER, B.B. & WEBSTER, J.G. (1983b) Reduction of Interference Due to Common Mode Voltage in Biopotential Amplifiers. *IEEE Transactions on Biomedical Engineering,* BME-30(1): 58-62.

WOLPAW, J.R., MCFARLAND, D.J., VAUGHAN, T.M. & SCHALK, G. (2003) The Wadsworth Center brain-computer interface (BCI) research and development program. *IEEE Transactions on Neural Systems and Rehabilitation Engineering,* 11(2): 1-4.

WORLD HEALTH ORGANISATION. (2012) *Disabilities* [Online]. Available: http://www.who.int/topics/disabilities/en/ [Accessed 31 August 2012].

YADAV, N., LUDLAM, D. & CIUFFREDA, K. (2012) Effect of different stimulus configurations on the visual evoked potential (VEP). *Documenta Ophthalmologica,* 124(3): 177-196.

YAMAMOTO, T. & YAMAMOTO, Y. (1981) Non-linear electrical properties of skin in the low frequency range. *Medical and Biological Engineering and Computing,* 19(3): 302-310.

YEAGER, D.J., HOLLEMAN, J., PRASAD, R., SMITH, J.R. & OTIS, B.P. (2009) NeuralWISP: A Wirelessly Powered Neural Interface With 1-m Range. *IEEE Transactions on Biomedical Circuits and Systems,* 3(6): 379-387.

YOO, J., LONG, Y., EL-DAMAK, D., BIN ALTAF, M., SHOEB, A., HOI-JUN, Y. & CHANDRAKASAN, A. (2012) An 8-channel scalable EEG acquisition SoC with fully integrated patient-specific seizure classification and recording

processor. IEEE International Solid-State Circuits Conference Digest of Technical Papers (ISSCC), 19-23 February. San Francisco. 292-294.

ZHUANG, L., BINTAO, L., CHILAI, C. & DEYI, K. (2009) Design of MEMS electrometer for highly sensitive charge measurement. 9th International Conference on Electronic Measurement & Instruments (ICEMI), 16-19 August. Beijing, China. 1-590-1-593.

ZIGBEE ALLIANCE. (2009) *ZigBee Standards* [Online]. Available: http://zigbee.org/Standards/Overview.aspx [Accessed 7 July 2013].

ZOU, Y. & GUO, Z. (2003) A review of electrical impedance techniques for breast cancer detection. *Medical Engineering & Physics,* 25(2): 79-90.

Appendix A *Schematics and PCB Layouts for the WEBS Master and Slave Devices*

***WEBS* - Slave**

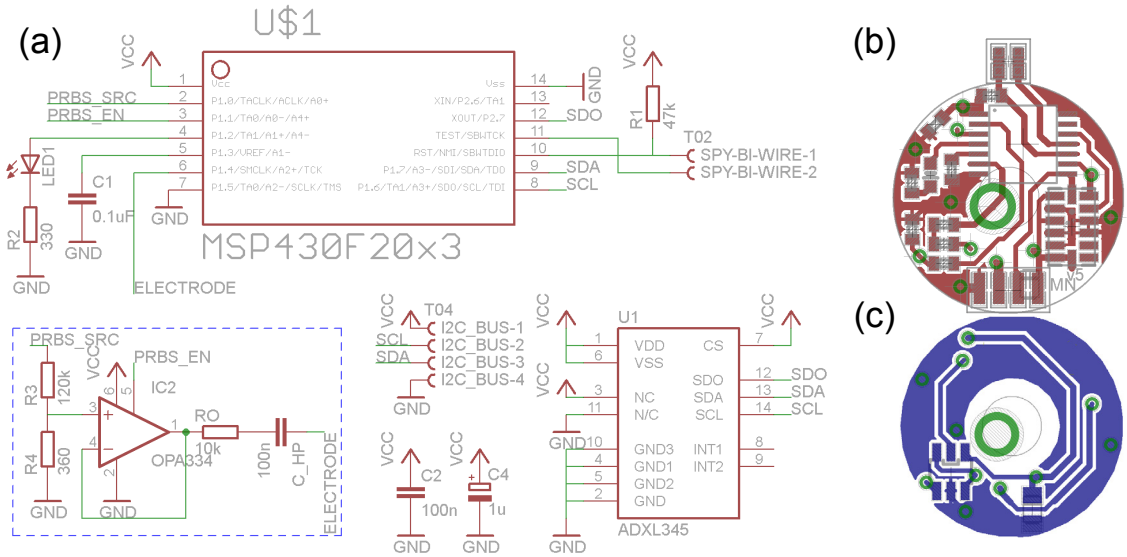

Figure A.1: The *WEBS* slave electrode's (a) schematic, (b) top PCB layout and (c) bottom PCB layout. Note that as the circuitry required for PRBS system identification is still under review, the associated components shown here have only been soldered onto a couple of test *WEBS* electrodes.

***WEBS* – Master**

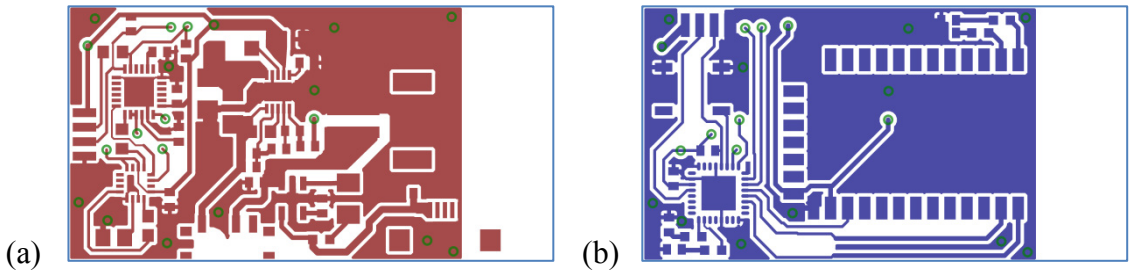

Figure A.2: The *WEBS* master (a) top and (c) bottom PCB layout.

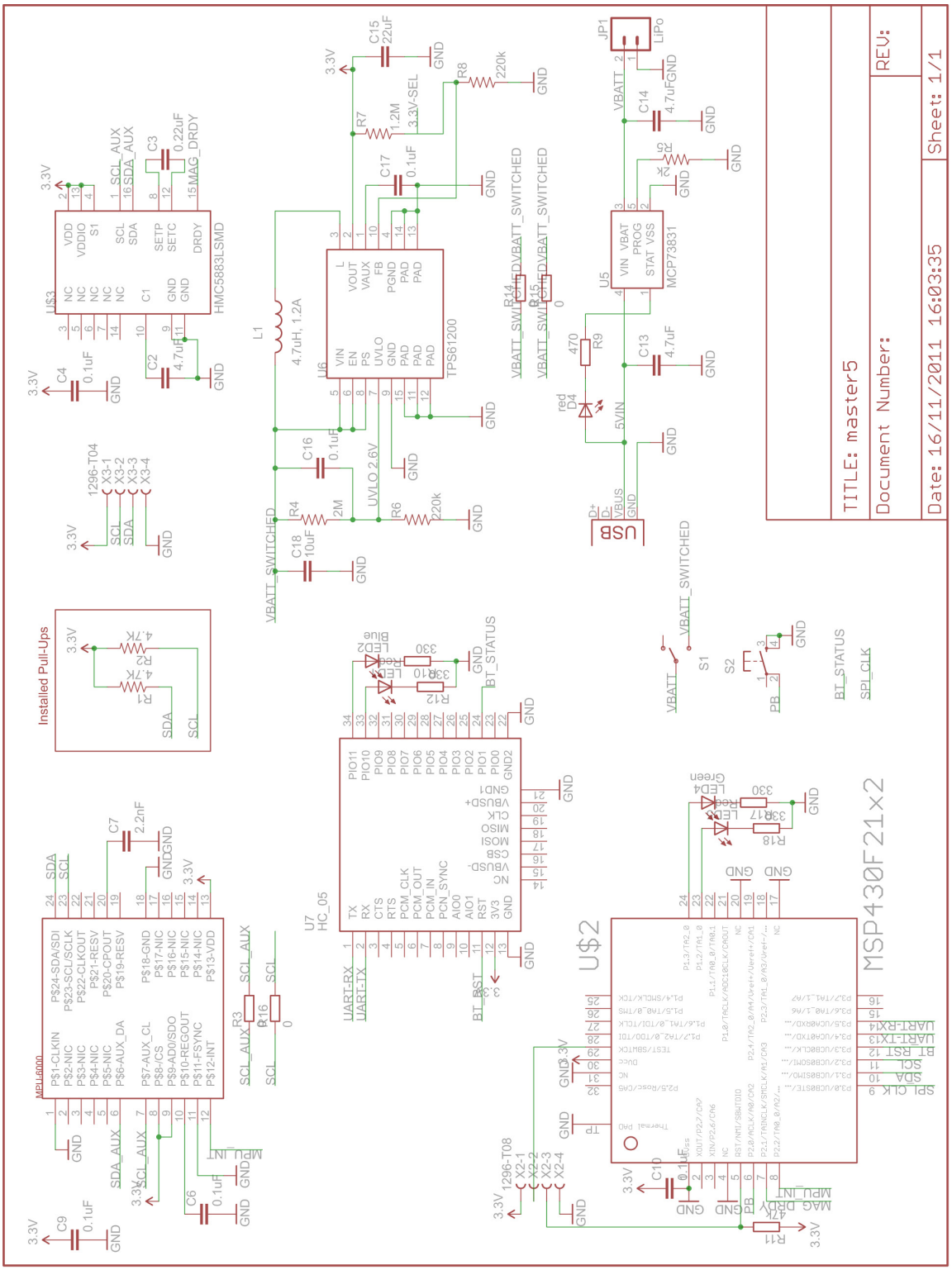

Figure A.3: The *WEBS* master schematic. This includes the circuit design for the microcontroller, accelerometer and gyroscope, Lithium-ion polymer battery charger, voltage boost convertor and regulator, Bluetooth module (HC_05) and multiple status LEDs. The schematic design of the sensors and power supply features are modified from (SparkFun 2012).

Appendix B Operational Information Relating to the WEBS

Table B.1: A table listing the *WEBS* I²C slave addresses. In this table, the *WEBS* user interface and the master program code, the I²C slave addresses are represented as a 7-bit address beginning in the least significant bit. In the *WEBS* slave program code, the I²C slave addresses are represented as a 7-bit address shifted left by one (*i.e.*, where bit 0 is the I²C read/write bit).

I²C address (7-bit in dec.)	I²C address (7-bit in hex.)	Device	Description
0	0x00	Electrodes (broadcast)	See Table B.2
1-28	0x01-0x1C	Electrodes (individual)	See Table B.2
29	0x1D	ADXL345	Accelerometer – sensor enabled
30	0x1E	HMC5883L	Magnetometer (no alternative address)
31-82	0x1F-0x52	Electrodes (individual)	See Table B.2
83	0x53	ADXL345	Accelerometer - sensor disabled (reserved)
84-104	0x54-0x68	Electrodes (individual)	See Table B.2
105	0x69	MPU-6000	Accelerometer & Gyroscope. Alternative of 0x68 is not used.
106-127	0x6A-0x7F	Electrodes (individual)	See Table B.2. Currently reserved for *WEBS* slaves with no accel. attached

Table B.2: A table listing the number of bytes in and out that are expected by each of the *WEBS* slave microcontrollers. The slave microcontrollers can be addressed using two I²C addresses, the broadcast address (decimal number 0) and an individual address as listed in Table B.1. The read/write bit is utilised to determine one of two conditions for each addresses - as shown in this table.

I²C address (8-bit in bin.)	Device	R/W	Description	Bytes in	Bytes out
00000000	Electrode Broadcast	W	Set ADC settings	2	0
00000001	Electrode Broadcast	R	Initiates ADC sampling	0	0
XXXXXXX0	Electrodes Individually	W	Set operational mode & PRBS settings	6	0
XXXXXXX1	Electrodes Individually	R	Transmit ADC value	0	2

Table B.3: A table listing the input capacitance for each component on the *WEBS* I^2C bus. In order to satisfy the I^2C specified limit of 400 pF bus capacitance, the maximum number of *WEBS* slaves on a 1 m long data bus is 25.

Device	Component	Qty.	Bus cap.	Reference	Total bus cap.
***WEBS* master**	MSP430F2132	1	5 pF	(Texas Instruments 2007b)	15 pF
	HMC5883L		* 5 pF	* estimate - not specified by the manufacturer	
	MPU-6000		≤ 5 pF	(InvenSense 2011)	
***WEBS* slave**	MSP430F2013	25	5 pF	(Texas Instruments 2005)	325 pF
	ADXL345		8 pF	(Analog Devices 2013)	
Wire	For example, using 3M ribbon cable (1 mm pitch, 28 AWG)	1	54.5 pF/m	(3M™ 2009)	54.5 pF
Total bus cap.				Based on a 1 m long data bus	394.5 pF
I^2C specified cap limit.				(NXP Semiconductors 2012)	400 pF

Table B.4: **A table listing the sampling time required by the *WEBS* slaves' ADC (the *SD16_A*) for all interrupt number and OSR setting combinations. The required number of slave cycles (at 1 MHz clock) and master cycles (at 16 MHz clock) are also shown. The time delay and master cycles were calculated using equations (B.1) and (B.2) respectively. To reduce the size of the *WEBS* masters' program code, the delay values were assigned a delay mode number wherein duplicate values could be eliminated.**

ΣΔ modulator frequency	ΣΔ interrupt number	OSR	Slave Cycles	Time Delay (s)	Master clock frequency	Master Cycles	Delay Mode
1 MHz	1	1024	1024	0.001024	16 MHz	16384	2
1 MHz	1	512	512	0.000512	16 MHz	8192	3
1 MHz	1	256	256	0.000256	16 MHz	4096	4
1 MHz	1	128	128	0.000128	16 MHz	2048	5
1 MHz	1	64	64	0.000064	16 MHz	1024	6
1 MHz	1	32	32	0.000032	16 MHz	512	7
1 MHz	2	1024	2048	0.002048	16 MHz	32768	1
1 MHz	2	512	1024	0.001024	16 MHz	16384	2
1 MHz	2	256	512	0.000512	16 MHz	8192	3
1 MHz	2	128	256	0.000256	16 MHz	4096	4
1 MHz	2	64	128	0.000128	16 MHz	2048	5
1 MHz	2	32	64	0.000064	16 MHz	1024	6
1 MHz	3	1024	3072	0.003072	16 MHz	49152	8
1 MHz	3	512	1536	0.001536	16 MHz	24576	9
1 MHz	3	256	768	0.000768	16 MHz	12288	10
1 MHz	3	128	384	0.000384	16 MHz	6144	11
1 MHz	3	64	192	0.000192	16 MHz	3072	12
1 MHz	3	32	96	0.000096	16 MHz	1536	13
1 MHz	4	1024	4096	0.004096	16 MHz	65536	0
1 MHz	4	512	2048	0.002048	16 MHz	32768	1
1 MHz	4	256	1024	0.001024	16 MHz	16384	2
1 MHz	4	128	512	0.000512	16 MHz	8192	3
1 MHz	4	64	256	0.000256	16 MHz	4096	4
1 MHz	4	32	128	0.000128	16 MHz	2048	5

$$\text{Time Delay} = \frac{\text{Slave cycles}}{1\,\text{MHz}} \tag{B.1}$$

$$\text{Master Cycles} = 16\,\text{MHz x}\left(\text{Time Delay}\right) \tag{B.2}$$

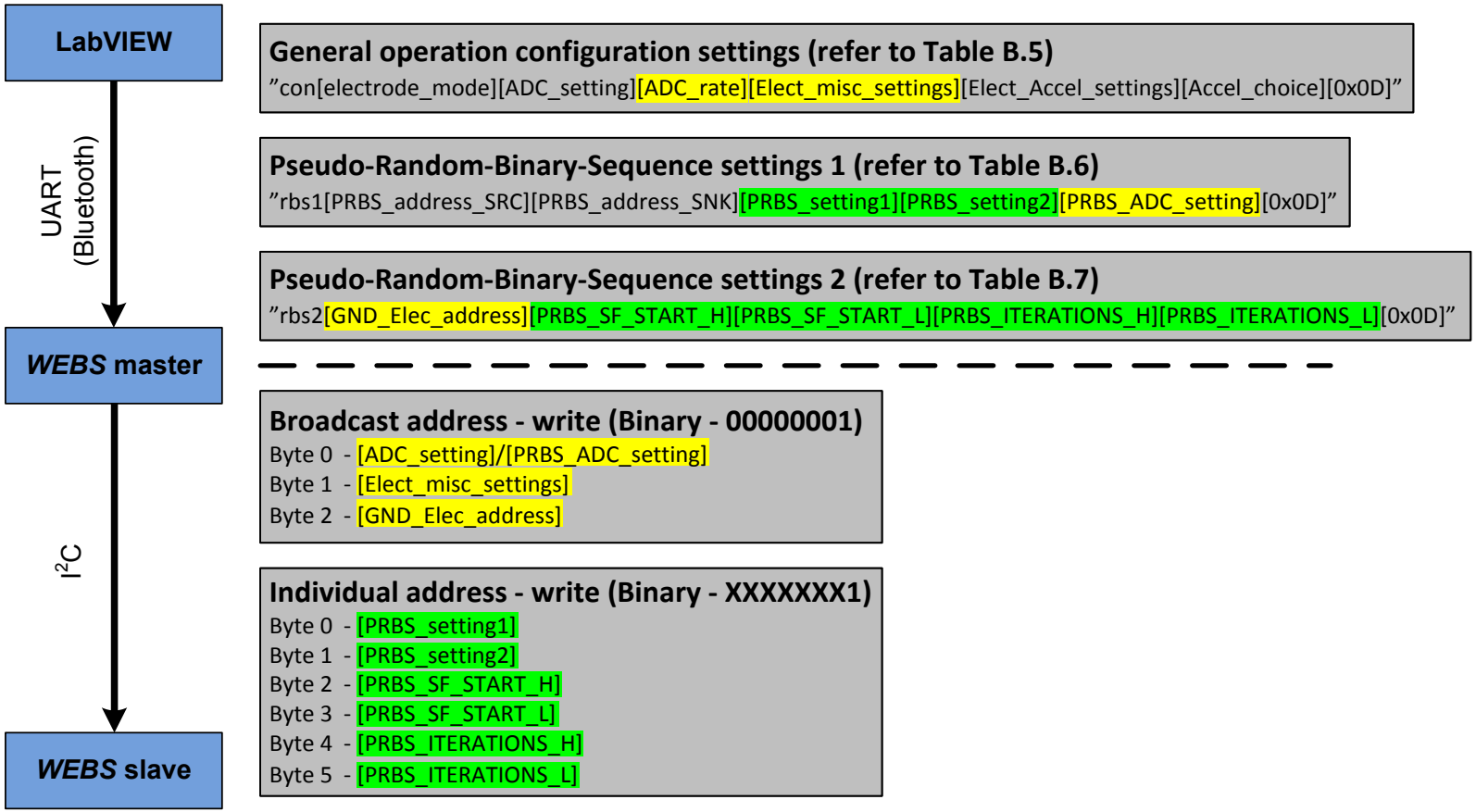

Figure B.1: A diagram illustrating the flow of configuration settings from the LabVIEW GUI to the *WEBS* master and, subsequently, on to the *WEBS* slave devices. Each data packet from the LabVIEW GUI begins with multiple ASCII characters (as shown), followed by a series of 8-bit configuration bytes (see tables B.5 to B.7) and, finally, an ASCII carriage return. The *WEBS* master sorts through the settings that belong to it and forwards on the *WEBS* slave settings to the appropriate slaves. UART ASCII commands that are not listed in this figure are “DISCO” (to which the master responds with a list of connected slaves), “START” (which initiates *WEBS* slave sampling) and “XXXXXXXXXX” (which terminates *WEBS* slave sampling).

Table B.5: A table listing the "general operation configuration settings" data packet that is transmitted from the LabVIEW GUI to the *WEBS* master. The configuration options that each bit in the data packet represents are listed in this table. The full UART command of this data packet is "con[electrode_mode][ADC_setting][ADC_rate][Elect_misc_settings][Elect_Accel_settings][Accel_choice][0x0D]".

Byte #	Description	Bit 7	Bit 6	Bit 5	Bit 4	Bit 3	Bit 2	Bit 1	Bit 0
Byte 0	**electrode_mode**	**Mst_MPU**	**Mst_MAG**	**Mode**			**Elect_X**	**Elect_Y**	**Elect_Z**
		Enables Master's Accelerometer/Gyroscope (MPU-6000)	Enables Master's Magnetometer	Used to set the system mode 000 Normal 001 PRBS 010 Electrode Test 011 Semi-augmented EOG			Enables Electrode Accelerometer X-axis	Enables Electrode Accelerometer Y-axis	Enables Electrode Accelerometer z-axis
Byte 1	**ADC_setting**	**SD16INTDLYx**		**SD16GAINx**			**SD16XOSR**	**SD16OSRx**	
		Interrupt delay generation after conversion start. These bits select the delay for the first interrupt. 00 4th sample causes interrupt 01 3rd sample causes interrupt 10 2nd sample causes interrupt 11 1st sample causes interrupt		*SD16_A* preamplifier gain 000 x1 001 x2 010 x4 011 x8 100 x16 101 x32 110 Reserved 111 Reserved			Extended oversampling ratio. This bit, along with the SD16OSRx bits, selects the oversampling ratio.	Oversampling ratio When SD16XOSR = 0 00 256 01 128 10 64 11 32 When SD16XOSR = 1 00 512 01 1024 10 Reserved 11 Reserved	
Byte 2	**ADC_rate**	**x**	**x**	**x**	**x**	**x**	**x**	**x**	**x**
		$ADC\_frequency = \frac{1MHz}{(ADC\_rate << 5)}$ (see Section 3.2.5)							
Byte 3	**Elect_misc_settings**	**LSBTOG**	**Elect_ADC**	**Elect_LED**	**IN_CHANNEL**		**Reserved**	**SD16_VREF**	**PRBS_SD16_VREF**
			Enables Electrode ADC	Enables Electrode LED	00 AE5 01 AE2 Elect		VREF as decided by the master based	0 Internal Reference	0 Internal Reference

					10 AE6 Temp 11 AE7 PGA	on whether the system is in PRBS mode or not. Bit2 is set by either Bit1 or bit0.	1 External Reference	1 External Reference
Byte 4	**Elect_Accel_settings**	**Reserved**	**-**	**Elect_Accel_range**		**Elect_Accel_rate**		
		Reserved for putting the ADXL345 into measurement mode or not. Decided at the master depending on GUI accel. axes tick boxes. Any tick boxes on — Measurement mode ON All tick boxes off — Measurement mode OFF	Unused	Range Setting. 00 ± 2 g 01 ± 4 g 10 ± 8 g 11 ± 16 g		Rate bits, corresponding output data rate and typical current consumption in normal power mode.		
Byte 5	**Accel_choice**	**All_accel_onoff**	**Single_accel_addr**					
		0 Single accel. used 1 All accel. engaged	If a single accelerometer is engaged, this is the address that it uses.					

Rate Code	Output Data Rate (Hz)	I_{DD}(µA)
1111	3200	140
1110	1600	90
1101	800	140
1100	400	140
1011	200	140
1010	100	140
1001	50	90
1000	25	60
0111	12.5	50
0110	6.25	45
0101	3.13	40
0100	1.56	34
0011	0.78	23
0010	0.39	23
0001	0.20	23
0000	0.10	23

Table B.6: A table listing the "Pseudo-Random-Binary-Sequence settings 1" data packet that is transmitted from the LabVIEW GUI to the *WEBS* master. The configuration options that each bit in the data packet represents are listed in this table. The full UART command of this data packet is "rbs1[PRBS_address_SRC][PRBS_address_SNK][PRBS_setting1][PRBS_setting2][PRBS_ADC_setting][0x0D]".

Byte #	Description	Bit 7	Bit 6	Bit 5	Bit 4	Bit 3	Bit 2	Bit 1	Bit 0
Byte 0	**PRBS_address_SRC**	**x**	**x**	**x**	**x**	**x**	**x**	**x**	**x**
		The I^2C slave address of the chosen PRBS source electrode							
Byte 1	**PRBS_address_SNK**	**x**	**x**	**x**	**x**	**x**	**x**	**x**	**x**
		The I^2C slave address of the chosen circuit ground electrode in PRBS mode							
Byte 2	**PRBS_setting1**	**PRBS_freq_setting [7:1]**							
		$PRBS\_frequency = \frac{1MHz}{(PRBS\_freq\_setting << 5)}$ (see Section 3.2.5)							
Byte 3	**PRBS_setting2**	**Reserved for PRBS_MODE**		**Surplus_elec_status**	**Reserved for PRBS_EN**	**PRBS_BIT_LENGTH**			
		Reserved for setting the state of each electrode during PRBS mode. Decided at the master. 00 Source 01 Circuit ground 10 Recording 11 Idle mode		Indicates the status of the surplus electrodes during PRBS 1 Recording 0 Idle	Reserved for setting PRBS enabled/disabled in the slaves. Decided at the master 1 Enabled 0 Disabled	PRBS shift register bit length (-1)			

Bits	SR bit Length	Loops
1111	16	65535
1110	15	32767
1101	14	16383
1100	13	8191
1011	12	4095
1010	11	2047
1001	10	1023
1000	9	511
0111	8	255
0110	7	127
0101	6	63
0100	5	31
0011	4	15
0010	3	7
0001	2	3

					0000	-	-
Byte 4	**PRBS_ADC_setting**	**SD16INTDLYx**	**SD16GAIN**		**SD16XOSR**	**SD16OSRx**	
		Interrupt delay generation after conversion start. These bits select the delay for the first interrupt. 00 — 4th sample causes interrupt 01 — 3rd sample causes interrupt 10 — 2nd sample causes interrupt 11 — 1st sample causes interrupt	*SD16_A* preamplifier gain 000 — x1 001 — x2 010 — x4 011 — x8 100 — x16 101 — x32 110 — Reserved 111 — Reserved		Extended oversampling ratio. This bit, along with the SD16OSRx bits, selects the oversampling ratio.	Oversampling ratio When SD16XOSR = 0 00 — 256 01 — 128 10 — 64 11 — 32 When SD16XOSR = 1 00 — 512 01 — 1024 10 — Reserved 11 — Reserved	

Table B.7: A table listing the "Pseudo-Random-Binary-Sequence settings 2" data packet that is transmitted from the LabVIEW GUI to the *WEBS* master. The configuration options that each bit in the data packet represents are listed in this table. The full UART command of this data packet is "rbs2[GND_Elec_address][PRBS_SF_START_H][PRBS_SF_START_L][PRBS_ITERATIONS_H][PRBS_ITERATIONS_L][0x0D]".

Byte #	Description	Bit 7	Bit 6	Bit 5	Bit 4	Bit 3	Bit 2	Bit 1	Bit 0
Byte 0	**GND_Elec_address**	**x**	**x**	**x**	**x**	**x**	**x**	**x**	**x**
		The I^2C slave address of the chosen reference (*i.e.*, circuit ground) electrode							
Byte 1	**PRBS_SF_START_H**	**x**	**x**	**x**	**x**	**x**	**x**	**x**	**x**
Byte 2	**PRBS_SF_START_L**	**x**	**x**	**x**	**x**	**x**	**x**	**x**	**x**
		PRBS shift register start data							
Byte 3	**PRBS_ITERATION_H**	**X**	**x**	**x**	**x**	**x**	**x**	**x**	**x**
Byte 4	**PRBS_ITERATION_L**	**X**	**x**	**x**	**x**	**x**	**x**	**x**	**x**
		Number of PRBS iterations							

Appendix C Table of WEBS Sampling Rates for Various Configurations (MSP430-based Master)

Table C.1: ***WEBS* maximum sampling rate for various slave configurations and settings using an *MSP430-based WEBS* master. Measured rates are based on a sample data packet recorded by a USBee SX logic analyser at a sampling rate of 16 Msps. Packet duration varies between packets, therefore this table represents the approximate upper limit of *WEBS* sampling rate for various configurations. Because of the variation, the chosen sampling rate should be set to be approximately 5 % less than the guides values listed here. Note that the I^2C bus capacitance is marginally increased by logic analyser equipment – thus affecting the I^2C clock rate. The yellow shaded boxes are estimated values based on the measured values shown and green shaded boxes represent values that are not applicable to their respective settings.**

Configuration	Properties	OSR	LSB TOG	ADC @ 4th sample	4th sample & X axis	4th sample & X + Y axes	4th sample & X + Y + Z axes
				Sa/s	Sa/s	Sa/s	Sa/s
ECG - 3-lead	3 electrodes recording (4 total)	1024	Y	207.04	187.97	178.57	170.36
			N	219.78	198.81	188.32	179.21
		512	Y	359.71	305.81	281.69	261.78
			N	401.61	336.70	307.69	284.09
	longest wire length = 118 cm	256	Y	625.00	478.47	421.94	378.79
			N	689.66	518.13	452.49	403.23
		128	Y	925.93	636.94	540.54	471.70
			N	1064.33	704.44	588.39	507.73
	I2C clock ≈ 347 kHz (0 V–3.19 V)	64	Y	1213.22	760.89	627.25	536.41
			N	1467.07	860.86	693.66	584.24
		32	NA	1807.70	961.54	763.36	628.93
		Just accelerometers			1476.82	1049.80	813.01
ECG - 12-lead	9 electrodes	1024	Y	163.13	131.06	117.92	107.30

	recording (10 total)		N	190.48	148.15	131.58	118.48
		512	Y	246.31	179.86	156.01	137.93
			N	314.47	213.68	180.83	156.99
	longest wire length = 118 cm	256	Y	387.60	245.10	202.84	173.31
			N	465.12	273.97	222.22	187.27
		128	Y	483.09	280.11	226.24	190.11
			N	613.50	319.49	251.26	207.47
	I2C clock ≈ 333 kHz (0 V–3.17 V)	64	Y	552.49	302.11	240.38	200.00
			N	729.93	348.43	268.82	219.30
		32	NA	806.45	404.86	278.55	225.23
		Just accelerometers			507.61	354.61	272.48
EOG	4 electrodes recording (5 total)	1024	Y	199.20	177.30	166.67	157.23
			N	215.52	190.11	177.94	167.22
		512	Y	337.84	279.33	253.81	232.56
			N	387.60	312.50	280.90	255.10
	longest wire length = 51 cm	256	Y	574.71	423.73	367.65	324.68
			N	645.16	460.83	395.26	346.02
		128	Y	819.67	543.48	454.55	390.63
			N	970.87	606.06	497.51	421.94
	I2C clock ≈ 364 kHz (0 V–3.19 V)	64	Y	1039.57	632.14	514.95	434.42
			N	1287.51	715.98	569.25	472.44
		32	NA	1545.74	793.65	617.28	505.05
		Just accelerometers			1173.97	826.45	636.94
Single Electrode Test (half breadboard)	1 electrodes recording (2 total)	1024	Y	226.24	218.82	214.59	210.53
			N	230.95	223.21	218.82	215.05
		512	Y	423.73	398.41	384.62	371.75
			N	442.48	414.94	400.00	386.10
	longest wire length = 20 cm	256	Y	781.25	699.30	657.89	621.12
			N	813.01	724.64	680.27	641.03
		128	Y	1315.46	1098.67	999.81	917.27
			N	1404.61	1160.17	1050.49	959.75
	I2C clock ≈ 381 kHz (0 V–3.21 V)	64	Y	1996.25	1536.24	1349.64	1203.46
			N	2202.35	1655.46	1440.80	1275.41
		32	NA	3072.76	2109.44	1775.00	1534.19
		Just accelerometer			3869.37	2913.33	2321.21
VEP	3 electrodes recording (2 biopotenital, 1 trigger) (4 total)	1024	Y	207.04	NA	NA	NA
			N	220.26	NA	NA	NA
		512	Y	361.01	NA	NA	NA
			N	403.23	NA	NA	NA
	longest wire	256	Y	628.93	NA	NA	NA

	length = 118 cm		N	689.66	NA	NA	NA
		128	Y	934.58	NA	NA	NA
	I2C clock ≈ 364 kHz (0 V–3.2 V)		N	1072.96	NA	NA	NA
		64	Y	1227.75	NA	NA	NA
			N	1482.58	NA	NA	NA
		32	NA	1836.95	NA	NA	NA
PRBS (breadboard)	1 electrodes recording (2 total with no accel.)	1024	Y	225.57	NA	NA	NA
			N	230.31	NA	NA	NA
		512	Y	422.30	NA	NA	NA
			N	439.54	NA	NA	NA
	longest wire length = 10 cm	256	Y	776.70	NA	NA	NA
			N	805.15	NA	NA	NA
		128	Y	1297.96	NA	NA	NA
	I2C clock ≈ 381 kHz (0 V–3.22 V)		N	1379.79	NA	NA	NA
		64	Y	1950.04	NA	NA	NA
			N	2144.17	NA	NA	NA
		32	NA	2959.63	NA	NA	NA

Appendix D PRBS Implementation

Table D.1: Various examples of polynomials for maximal-length LFSR. Table based on those given by (Davies 1970: 44-88). These masks ensure that every possible shift register value is realised (except the all zeros state).

Bits	Feedback polynomial	Bit mask	Period
n			$2^n - 1$
3	$x^3 + x^2 + 1$	0x0006	7
4	$x^4 + x^3 + 1$	0x000C	15
5	$x^5 + x^3 + 1$	0x0014	31
6	$x^6 + x^5 + 1$	0x0030	63
7	$x^7 + x^6 + 1$	0x0060	127
8	$x^8 + x^6 + x^5 + x^4 + 1$	0x00B8	255
9	$x^9 + x^5 + 1$	0x0110	511
10	$x^{10} + x^7 + 1$	0x0240	1023
11	$x^{11} + x^9 + 1$	0x0500	2047
12	$x^{12} + x^{11} + x^{10} + x^4 + 1$	0x0E08	4095
13	$x^{13} + x^{12} + x^{11} + x^8 + 1$	0x1C80	8191
14	$x^{14} + x^{13} + x^{12} + x^2 + 1$	0x3802	16383
15	$x^{15} + x^{14} + 1$	0x6000	32767
16	$x^{16} + x^{14} + x^{13} + x^{11} + 1$	0xB400	65535

Table D.2: The Galois LFSR implementation used in the *WEBS*. This extract of the *WEBS* microcontroller code (written in C) is modified from (Bmearns 2008).

```
lsb = lfsr & 0x01;          // Mask the least significant bit (lsb) of the linear
                            // feedback shift register (lfsr).
lfsr >>= 1;                 // Shift the lfsr right by 1 bit
if (lsb) {                  // If lsb is 1, apply toggle mask to the lfsr & set
                            // output pin high
       lfsr ^= lfsr_taps;   // Apply shift register mask (lfsr_taps) – as defined by
                            // user in the WEBS GUI. The mask has a bit value of 1
                            // at tap points & 0 elsewhere.
       ELECTRODE_DRIVER_HIGH();     // output lsb value
}
else {
       ELECTRODE_DRIVER_LOW();      // output lsb value
}
if(lfsr == lfsr_orig) {     // check if the current lfsr is equal to the initial
                            // value of the lfsr (i.e., after all possible lfsr
                            // values have occurred)
       iterations_cnt++;    // increment an iterations counter
       if(iterations_cnt = iterations_set) { // if completed iterations count equals
                            // count defined by user in WEBS GUI, disable PRBS mode
              PRBS_flag = 0; // disable PRBS flag
```

```
        } }
```

Table D.3: A sample MATLAB script which has been simplified from several scripts that were created to import, process and analyse the saved data from the *WEBS* PRBS experiments. The output of this script is a Bode plot that compares the frequency response obtained from the physical experiment, a simulation of the experiment (using '*lsim*' commands) and calculated from the transfer function of the system (using the '*bode*' command). The impulse response for the test system is also plotted. The example used in this script is based on the experiment shown in Figure 5.24.

```
close all
clear all

% variables
nr = 11;     % number of PRBS sequence repeats
N = 16;      % number of PRBS sequence bits
n1 = (2^N) - 1; % PRBS sequence length
fs = 2083.33;    % PRBS bit rate
T = 1/fs;
Nfft=(nr-1)*n1;
t=(0:n1-1)*T; % create time array,

% calculate transfer function of the system model
s = tf('s');
R_LP = 10e3;     % RLP = 10 k?
ZC_LP = 1/(s*220e-9);     % CLP = 220 nF
R_HP = 33e3;     % RHP = 33 k?
ZC_HP = 1/(s*220e-9);     % CHP = 220 nF
sys = (1/(1+(R_LP/ZC_LP))) * ((R_HP/ZC_HP)/(1+(R_HP/ZC_HP)));   %
Equation (5.4)

%%%%%%%%%%%%%%%%%%%%%%%%%%%%%%%%%%%%%%%%%%%%%%%%%%%%%%%%%%%%%%%%%%%%%%%%%%%%
% Set up the figure
figure(1)
set(gcf,'Position',[100 100 600 800])    % set figure size and position

subplot(2, 1, 1)
set(gca, 'XScale', 'log')
hold on
grid on
title({['{\bfBode plot}'], 'Band-pass filter experiment - unipolar
supply', ['(PRBS: period = ' num2str(n1) ', repetitions = '
num2str(nr-1) ', rate = 2083.33 Sa/s)']})
ylabel('Magnitude (dB)')
xlabel('Frequency (Hz)')

subplot(2, 1, 2)
set(gca, 'XScale', 'log')
hold on
grid on
ylabel('Phase (deg)')
xlabel('Frequency (Hz)')

figure(2)
hold on
grid on
title({['{\bfImpulse response}'], 'Band-pass filter experiment -
```

```
unipolar supply', ['(PRBS: period = ' num2str(n1) ', repetitions = '
num2str(nr-1) ', rate = 2083.33 Sa/s)']})
xlabel('Time (s)')

%%%%%%%%%%%%%%%%%%%%%%%%%%%%%%%%%%%%%%%%%%%%%%%%%%%%%%%%%%%%%%%%%%%%%%%%%%%%
% Breadboard test results
%%%%%%%%%%%%%%%%%%%%%%%%%%%%%%%%%%%%%%%%%%%%%%%%%%%%%%%%%%%%%%%%%%%%%%%%%%%%
% Import the file
newData1 = importdata('./WEBS_test_file.txt', '\t', 22);
% Create variables in the workspace for the imported fields.
vars = fieldnames(newData1);
for i = 1:length(vars)
    assignin('base', vars{i}, newData1.(vars{i}));
end

% assign variables PRBS input signal (Brdbdip) and measured signal
(Brdbdop), skip first iteration to allow for settling time
Brdbdip = data((n1+1):(n1*nr),3);
Brdbdop = data((n1+1):(n1*nr),2);

% scale input signal to +-1V and output by the same factor
subtraction_value = ((max(Brdbdip)-min(Brdbdip))/2) + min(Brdbdip);
mulitiplation_value = 1 / ((max(Brdbdip)-min(Brdbdip))/2);
Brdbdip(:) = (Brdbdip(:)-subtraction_value)* mulitiplation_value;
Brdbdop(:) = (Brdbdop(:)-subtraction_value)* mulitiplation_value;

% create a cell for the fft of each window
for j=1:(nr-1)
    Y1{j} = fft(Brdbdop((((j-1)*n1)+1):(j*n1)));
    X1{j} = fft(Brdbdip((((j-1)*n1)+1):(j*n1)));
end
% Cross power spectral density for each segment
for j=1:(nr-1)
    RYX{j} = Y1{j}.*conj(X1{j})/n1;
end
% calculate average Cross power spectral density over all cells
Ryx = zeros(n1,1);
for j=1:(nr-1)
    Ryx = Ryx + RYX{j}; % add up each of the cells
end
Ryx = Ryx / (nr-1); % divide by number of repeats

figure(1)
subplot(2,1,1)
fax=(0:n1-1)*fs/n1;
fax = fax';
semilogx(fax,20*log10(Ryx),'Color','b','LineStyle','-');
subplot(2,1,2)
semilogx(fax,atan2(imag(Ryx),real(Ryx))*(180/pi),'Color','b','LineStyl
e','-');

% plot the impulse response for the system
figure(2)
ryx=ifft(Ryx);  % inverse discrete Fourier transform (DFT) using fast
Fourier transform (FFT) algorithm
plot(t(1:length(ryx)),(ryx-mean(ryx)),'Color','b','LineStyle','-');

%%%%%%%%%%%%%%%%%%%%%%%%%%%%%%%%%%%%%%%%%%%%%%%%%%%%%%%%%%%%%%%%%%%%%%%%%%%%
% Simulink results
%%%%%%%%%%%%%%%%%%%%%%%%%%%%%%%%%%%%%%%%%%%%%%%%%%%%%%%%%%%%%%%%%%%%%%%%%%%%
%Galois linear feedback shift register - 16-bit and start sequence =
```

```
0xACE1
lfsr = hex2dec('ACE1');
high_value = 0.1; % digital high voltage (after voltage divider)
low_value = 0; % digital low voltage (after voltage divider)

index = 0;
condition = true;
while (condition == true)
  %/* taps: 16 14 13 11; characteristic polynomial: x^16 + x^14 + x^13
+ x^11 + 1 */
  lsb = bitand(lfsr,1);
  lfsr = bitshift(lfsr,-1);
  if (lsb == 1)
      lfsr = bitxor(lfsr,hex2dec('B400'));
  end
  prbs_sequence(index+1,1) = lsb;

  index = index + 1;

  if(lfsr == hex2dec('ACE1'))
      condition = false;
  end
end

for i=1:nr      % generate array for entire PRBS sequence based on nr
    if nr==1
        Simip(1:n1,1) = prbs_sequence;
    else
        Simip((n1*(i-1)+1):(n1*i),1) = prbs_sequence;
    end
end
%%%%%%%%%%%%%%%%%%%%%%%%%%%%%%%%%%%%%%%%%%%%%%%%%%%%%%%%%%%%%%%%%%%%%%%%%%%%
sys_discrete = c2d(sys, 1/fs);
Simop = lsim(sys_discrete,Simip,(0:(1/fs):((n1*(nr)*(1/fs)))-
(1/fs)),0,'zoh');

% assign variables PRBS input signal (Simip) and simulated output
signal (Simop), skip first iteration to allow for settling time
Simip = Simip((n1+1):(n1*nr),1);
Simop = Simop((n1+1):(n1*nr),1);

% scale input signal to +-1V and output by the same factor
subtraction_value = ((max(Simip)-min(Simip))/2) + min(Simip);
mulitiplation_value = 1 / ((max(Simip)-min(Simip))/2);
Simip = (Simip-subtraction_value)* mulitiplation_value;
Simop = (Simop-subtraction_value)* mulitiplation_value;

% create a cell for the fft of each window
for j=1:(nr-1)
    Y1{j} = fft(Simop((((j-1)*n1)+1):(j*n1)));
    X1{j} = fft(Simip((((j-1)*n1)+1):(j*n1)));
end
% Cross power spectral density for each segment
for j=1:(nr-1)
    RYX{j} = Y1{j}.*conj(X1{j})/n1;
end
% calculate average Cross power spectral density over all cells
Ryx = zeros(n1,1);
for j=1:(nr-1)
    Ryx = Ryx + RYX{j}; % add up each of the cells
end
```

```
Ryx = Ryx / (nr-1); % divide by number of repeats

figure(1)
subplot(2,1,1)
fax=(0:n1-1)*fs/n1;
fax = fax';
semilogx(fax,20*log10(Ryx),'Color','r','LineStyle','--');
subplot(2,1,2)
semilogx(fax,atan2(imag(Ryx),real(Ryx))*(180/pi),'Color','r','LineStyl
e','--');

% plot the impulse response for the system
figure(2)
ryx=ifft(Ryx);  % inverse discrete Fourier transform (DFT) using fast
Fourier transform (FFT) algorithm
plot(t(1:length(ryx)),(ryx-mean(ryx)),'Color','r','LineStyle','--');

%%%%%%%%%%%%%%%%%%%%%%%%%%%%%%%%%%%%%%%%%%%%%%%%%%%%%%%%%%%%%%%%%%%%%%%%%%%%
 % Transfer function calculations
%%%%%%%%%%%%%%%%%%%%%%%%%%%%%%%%%%%%%%%%%%%%%%%%%%%%%%%%%%%%%%%%%%%%%%%%%%%%
freqVec = logspace(-2, 4, 5000);    % Create test frequency array
sys_discrete = c2d(sys, 1/fs);  % convert continous sys to discrete
model
[mag, phs] = bode(sys_discrete, freqVec * (2*pi));
mag = squeeze(mag); % remove singleton array that is returned from
'bode'
mag = 20*log10(mag);
phs = phs(:); % remove singleton array that is returned from 'bode'

figure(1)
subplot(2, 1, 1)
semilogx(freqVec, mag,'Color','g','LineStyle','-.')
subplot(2, 1, 2)
semilogx(freqVec, phs,'Color','g','LineStyle','-.')

% plot the impulse response for the system
figure(2)
[h,t_imp]=impulse(sys_discrete);         % impulse response of a
dynamic system
plot(t_imp,h,'Color','g','LineStyle','-.');
xlim([0 t_imp(length(t_imp))])

%%%%%%%%%%%%%%%%%%%%%%%%%%%%%%%%%%%%%%%%%%%%%%%%%%%%%%%%%%%%%%%%%%%%%%%%%%%%
figure(1)
legend('Physical circuit response','Simulation response','Discrete-
time transfer function response');
legend('show');
```

Appendix E Laryngeal Vibration Mapping Results

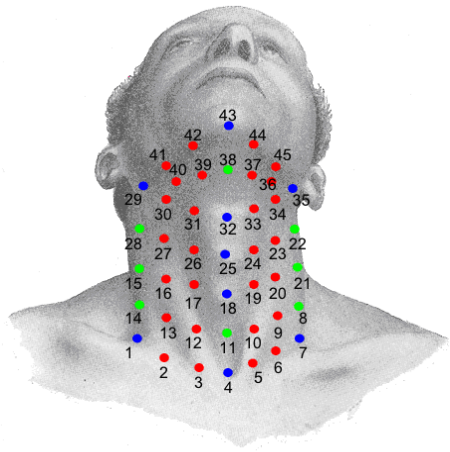

Figure E.1: The numbered measuring points copied from Figure 5.2 (b). The background image is modified from Fig. 1195 (Gray 1918).

Table E.1: The magnitude of acceleration for each measurement point on *Subject A* at a phonation frequency of 150 Hz.

Pos.[a]	MAG.[b]	Pos.[a]	MAG.[b]	Pos.[a]	MAG.[b]	Pos.[a]	MAG.[b]
1	0.249	***13***	0.400	***25***	0.790	***37***	0.424
2	0.549	***14***	0.223	***26***	1.350	***38***	0.262
3	0.823	***15***	0.239	***27***	1.320	***39***	0.377
4	0.778	***16***	0.302	***28***	0.576	***40***	0.488
5	0.781	***17***	0.754	***29***	0.314	***41***	0.249
6	0.318	***18***	1.024	***30***	1.000	***42***	0.214
7	0.132	***19***	0.605	***31***	1.036	***43***	0.310
8	0.144	***20***	0.405	***32***	0.658	***44***	0.169
9	0.321	***21***	0.190	***33***	0.794	***45***	0.206
10	0.819	***22***	0.557	***34***	0.914		
11	1.175	***23***	1.132	***35***	0.243		
12	1.208	***24***	1.372	***36***	0.486		

[a]Position of accelerometer

[b]Average magnitude of acceleration over 200 ms [measured in m/s^2]

Table E.2: The magnitude of acceleration for each measurement point on *Subject A* at a phonation frequency of 200 Hz.

Pos.[a]	MAG.[b]	Pos.[a]	MAG.[b]	Pos.[a]	MAG.[b]	Pos.[a]	MAG.[b]
1	0.199	***13***	0.372	***25***	0.503	***37***	0.361
2	0.396	***14***	0.232	***26***	1.064	***38***	0.231
3	0.615	***15***	0.161	***27***	1.587	***39***	0.376
4	0.451	***16***	0.299	***28***	0.605	***40***	0.595
5	0.539	***17***	0.735	***29***	0.108	***41***	0.205
6	0.196	***18***	0.642	***30***	1.045	***42***	0.199
7	0.102	***19***	0.581	***31***	1.002	***43***	0.224
8	0.107	***20***	0.293	***32***	0.635	***44***	0.157
9	0.214	***21***	0.122	***33***	0.713	***45***	0.209
10	0.442	***22***	0.627	***34***	0.928		
11	0.626	***23***	1.178	***35***	0.101		
12	0.749	***24***	1.307	***36***	0.530		

[a]Position of accelerometer

[b]Average magnitude of acceleration over 200 ms [measured in m/s^2]

Table E.3: The magnitude of acceleration for each measurement point on *Subject A* at a phonation frequency of 250 Hz.

Pos.[a]	MAG.[b]	Pos.[a]	MAG.[b]	Pos.[a]	MAG.[b]	Pos.[a]	MAG.[b]
1	0.149	***13***	0.230	***25***	0.507	***37***	0.434
2	0.227	***14***	0.139	***26***	1.137	***38***	0.246
3	0.451	***15***	0.102	***27***	1.927	***39***	0.308
4	0.443	***16***	0.244	***28***	0.556	***40***	0.485
5	0.352	***17***	0.632	***29***	0.235	***41***	0.212
6	0.105	***18***	0.524	***30***	1.002	***42***	0.165
7	0.074	***19***	0.469	***31***	0.942	***43***	0.182
8	0.077	***20***	0.303	***32***	0.437	***44***	0.136
9	0.130	***21***	0.125	***33***	0.674	***45***	0.171
10	0.337	***22***	0.522	***34***	0.724		
11	0.579	***23***	1.151	***35***	0.237		
12	0.513	***24***	1.378	***36***	0.488		

[a]Position of accelerometer

[b]Average magnitude of acceleration over 200 ms [measured in m/s^2]

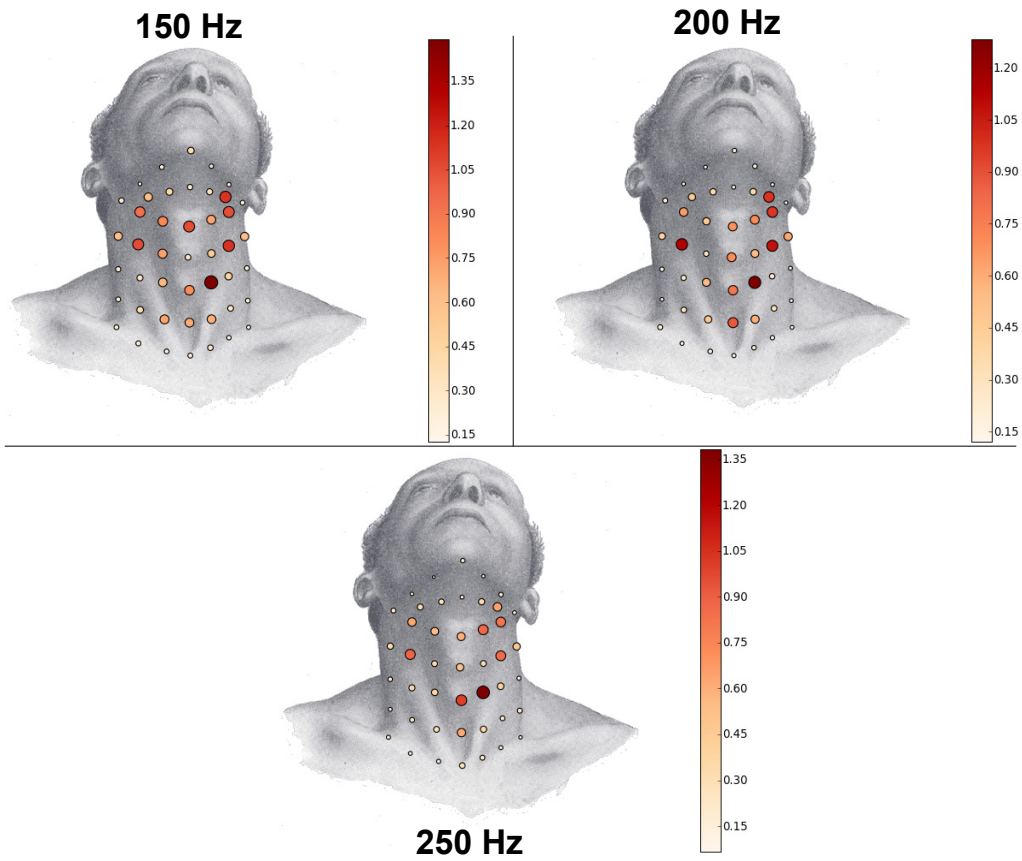

Figure E.2: A plot of Subject B's results showing the variation in average magnitude of acceleration (measured in m/s^2) over the measurement grid at phonation frequencies of 150 Hz, 200 Hz and 250 Hz. Both the size and colour of each dot represent the average magnitude of acceleration at that point. The dot colour mapping is normalised for each graph, while the dot size scale is constant across all graphs. The background image is modified from Fig. 1195 (Gray 1918).

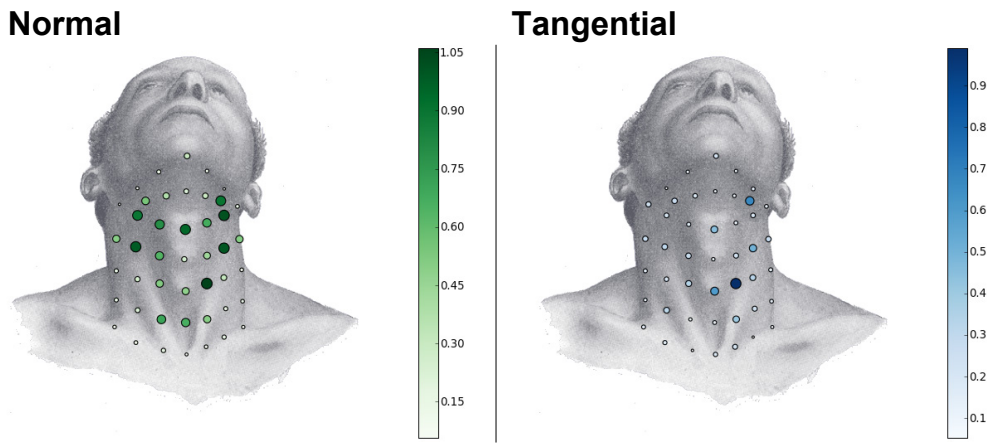

Figure E.3: A plot showing the average magnitude of acceleration (measured in m/s^2) normal and tangential to the skin surface at a phonation frequency of 150 Hz on Subject B. The size and colour of each dot represents the average magnitude of acceleration at that point. The dot colour mapping is normalised for each graph, while the dot size scale is constant across both graphs. The background image is modified from Fig. 1195 (Gray 1918).

Table E.4: The magnitude of acceleration for each measurement point on *Subject B* at a phonation frequency of 150 Hz.

Pos.[a]	MAG.[b]	Pos.[a]	MAG.[b]	Pos.[a]	MAG.[b]	Pos.[a]	MAG.[b]
1	0.211	***13***	0.396	***25***	0.295	***37***	0.325
2	0.229	***14***	0.211	***26***	0.735	***38***	0.260
3	0.200	***15***	0.244	***27***	1.056	***39***	0.430
4	0.217	***16***	0.326	***28***	0.606	***40***	0.616
5	0.270	***17***	0.653	***29***	0.266	***41***	0.126
6	0.183	***18***	0.807	***30***	0.927	***42***	0.204
7	0.152	***19***	1.493	***31***	0.827	***43***	0.387
8	0.203	***20***	0.469	***32***	1.057	***44***	0.175
9	0.302	***21***	0.217	***33***	0.708	***45***	0.155
10	0.678	***22***	0.612	***34***	1.048		
11	0.692	***23***	1.138	***35***	0.203		
12	0.719	***24***	0.514	***36***	1.130		

[a]Position of accelerometer

[b]Average magnitude of acceleration over 200 ms [measured in m/s^2]

Table E.5: The magnitude of acceleration for each measurement point on *Subject B* at a phonation frequency of 200 Hz.

Pos.[a]	MAG.[b]	Pos.[a]	MAG.[b]	Pos.[a]	MAG.[b]	Pos.[a]	MAG.[b]
1	0.228	***13***	0.280	***25***	0.700	***37***	0.378
2	0.148	***14***	0.130	***26***	0.259	***38***	0.147
3	0.193	***15***	0.177	***27***	1.139	***39***	0.363
4	0.156	***16***	0.249	***28***	0.408	***40***	0.463
5	0.181	***17***	0.553	***29***	0.217	***41***	0.127
6	0.170	***18***	0.778	***30***	0.643	***42***	0.125
7	0.130	***19***	1.283	***31***	0.467	***43***	0.183
8	0.130	***20***	0.265	***32***	0.683	***44***	0.191
9	0.290	***21***	0.139	***33***	0.704	***45***	0.126
10	0.597	***22***	0.613	***34***	0.970		
11	0.880	***23***	1.082	***35***	0.120		
12	0.467	***24***	0.547	***36***	0.982		

[a]Position of accelerometer

[b]Average magnitude of acceleration over 200 ms [measured in m/s^2]

Table E.6: The magnitude of acceleration for each measurement point on *Subject B* at a phonation frequency of 250 Hz.

Pos.[a]	MAG.[b]	Pos.[a]	MAG.[b]	Pos.[a]	MAG.[b]	Pos.[a]	MAG.[b]
1	0.151	***13***	0.213	***25***	0.499	***37***	0.342
2	0.133	***14***	0.138	***26***	0.301	***38***	0.136
3	0.155	***15***	0.185	***27***	0.890	***39***	0.276
4	0.286	***16***	0.328	***28***	0.341	***40***	0.323
5	0.215	***17***	0.373	***29***	0.213	***41***	0.113
6	0.143	***18***	1.003	***30***	0.630	***42***	0.066
7	0.108	***19***	1.383	***31***	0.529	***43***	0.171
8	0.222	***20***	0.393	***32***	0.587	***44***	0.100
9	0.208	***21***	0.151	***33***	0.871	***45***	0.176
10	0.358	***22***	0.475	***34***	0.820		
11	0.617	***23***	0.864	***35***	0.143		
12	0.297	***24***	0.302	***36***	0.643		

[a]Position of accelerometer

[b]Average magnitude of acceleration over 200 ms [measured in m/s^2]

Appendix F Impulse Responses from the PRBS System Identification Experiments

The impulse responses shown here were obtained by calculating the inverse fast Fourier transform of the cross-correlation sequence (refer to Appendix D) from each experiment conducted in Section 5.5.

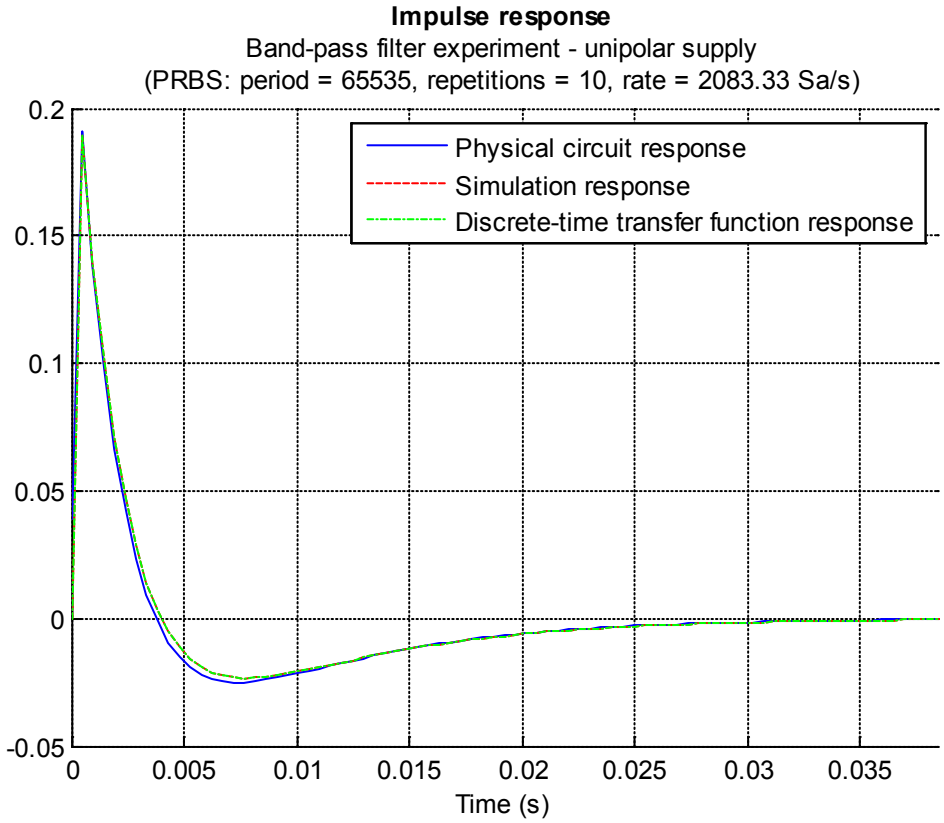

Figure F.1: The impulse response from the band-pass filter PRBS system identification experiment (Section 5.5.1).

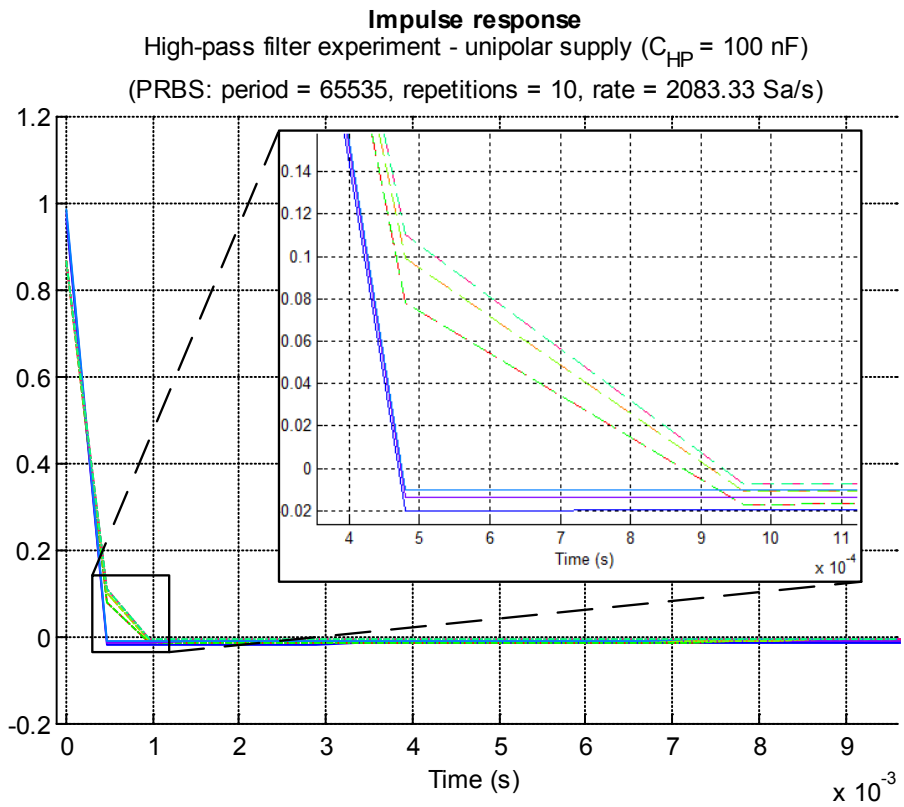

Figure F.2: The impulse response from the high-pass filter PRBS system identification experiment (Section 5.5.2). The line styles match those in Figure 5.27.

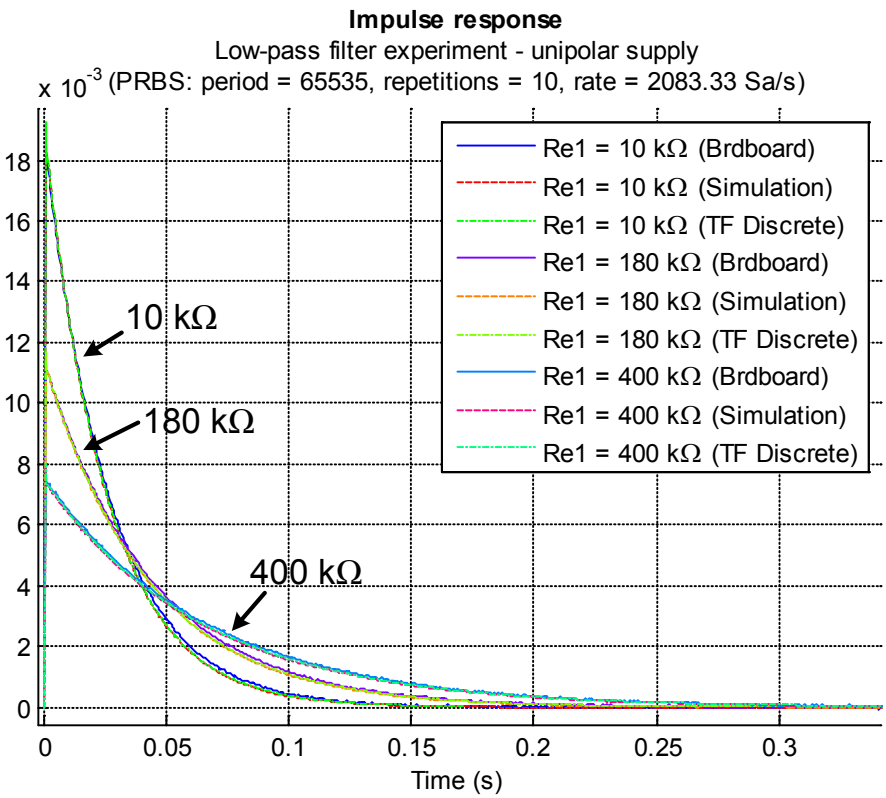

Figure F.3: The impulse response from the low-pass filter PRBS system identification experiment (Section 5.5.3).

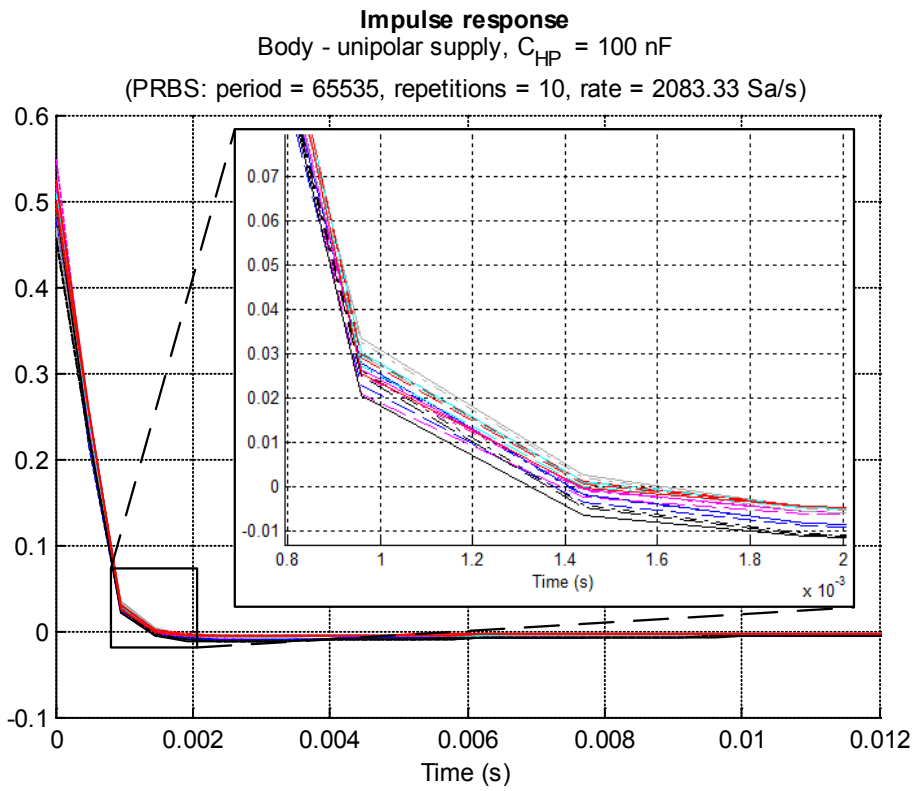

Figure F.4: The impulse response from the first PRBS system identification experiment connected to a human body (Section 5.5.4). The line styles match those in Figure 5.31.

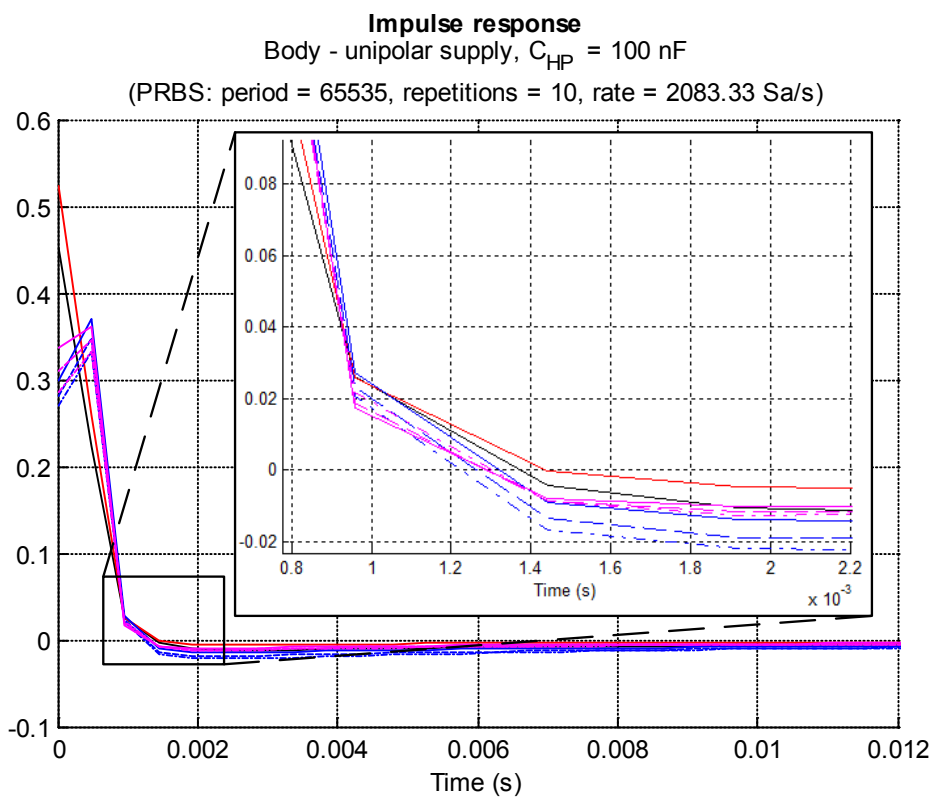

Figure F.5: The impulse response from the second PRBS system identification experiment connected to a human body (Section 5.5.4). The line styles match those in Figure 5.33.

Appendix G Table of WEBS Sampling Rates for Various Configurations (Arduino-based Master)

Table G.1: ***WEBS*** **maximum sampling rate for various slave configurations and settings using an** ***Arduino-based WEBS*** **master. Measured rates are based on a sample data packet recorded by a USBee SX logic analyser at a sampling rate of 16 Msps. Packet duration varies between packets, therefore this table represents the approximate upper limit of** ***WEBS*** **sampling rate for various configurations. Because of the variation, the chosen sampling rate should be set to be approximately 5 % less than the guides values listed here. Using all axes of the master accelerometer and gyroscope adds approximately 0.8 ms/Sa to the sample time and the master magnetometer adds approximately 0.4 ms/Sa. The yellow shaded boxes are estimated values based on the measured values shown and green shaded boxes represent values that are not applicable to their respective settings.**

Configuration	Properties	OSR	LSB TOG	ADC @ 4th sample	4th sample & X axis	4th sample & X + Y axes	4th sample & X + Y + Z axes	With master accel. & gyro.	With master magnet.
				Sa/s	Sa/s	Sa/s	Sa/s	Sa/s	Sa/s
ECG - 3-lead	3 electrodes recording (4 total)	1024	Y	194.55	169.49	161.55	154.32	137.36	129.20
			N	207.47	179.53	170.36	162.87	144.09	135.14
		512	Y	325.73	261.10	242.72	226.76	191.94	176.37
			N	364.96	286.53	263.85	246.31	205.76	187.97
	longest wire length = 118 cm	256	Y	534.76	380.23	342.47	311.53	249.38	223.71
			N	584.80	406.50	362.32	330.03	261.10	233.10
		128	Y	740.74	473.93	416.67	371.75	286.53	253.16
			N	840.34	515.46	446.43	398.41	302.11	265.25
	I2C clock = 400 kHz	64	Y	917.43	540.54	467.29	411.52	309.60	271.00
			N	1075.63	595.35	505.13	444.51	327.90	284.93

	(0 V–3.36 V)	32	NA	1260.14	641.03	540.54	467.29	340.14	294.12
		Just accelerometers			980.39	769.23	636.94	NA	NA
ECG - 12-lead	9 electrodes recording (10 total)	1024	Y	145.99	109.53	99.60	92.08	85.76	82.51
			N	170.07	122.70	110.38	101.01	93.46	89.61
		512	Y	209.21	141.64	125.47	113.77	104.28	99.50
			N	262.47	164.47	143.06	127.71	115.87	110.01
	longest wire length = 118 cm	256	Y	306.75	180.51	155.04	137.55	123.92	117.23
			N	359.71	198.02	167.79	147.06	131.58	124.07
		128	Y	363.64	198.81	168.35	147.93	132.28	124.69
			N	442.48	220.75	183.82	159.24	141.24	132.63
	I2C clock = 400 kHz (0 V–3.36 V)	64	Y	401.61	209.64	176.06	153.85	136.99	128.87
			N	500.00	234.19	193.05	166.11	146.63	137.36
		32	NA	531.91	240.96	198.81	169.49	149.25	139.66
		Just accelerometers			346.02	263.16	216.92	NA	NA
EOG	4 electrodes recording (5 total)	1024	Y	184.16	155.28	146.41	138.89	125.00	118.20
			N	200.40	166.39	156.01	147.71	132.10	124.53
		512	Y	298.51	229.36	210.53	195.31	168.92	156.74
			N	342.47	254.45	231.48	213.22	182.15	168.07
	longest wire length = 51 cm	256	Y	478.47	322.58	286.53	259.07	214.59	195.31
			N	531.91	346.02	304.88	273.97	224.72	203.67
		128	Y	632.91	386.10	335.57	298.51	240.96	216.92
			N	735.29	421.94	362.32	319.49	254.45	227.79
	I2C clock = 400 kHz (0 V–3.36 V)	64	Y	757.58	429.18	367.65	323.62	257.07	229.89
			N	900.90	471.70	398.41	347.22	271.74	241.55
		32	NA	1029.07	505.05	418.41	364.96	282.49	250.00
		Just accelerometers			757.58	581.40	480.77	NA	NA
Single Electrode Test (half breadboard)	1 electrodes recording (2 total)	1024	Y	218.82	207.04	203.67	200.00	172.41	159.74
			N	224.22	212.31	207.90	204.50	175.75	162.60
		512	Y	401.61	363.64	353.36	342.47	268.82	239.23
			N	418.41	377.36	366.30	354.61	276.24	245.10
	longest wire length = 20 cm	256	Y	709.22	598.80	571.43	543.48	378.79	322.58
			N	746.27	625.00	595.24	564.97	389.11	330.03
		128	Y	1136.52	877.29	819.75	763.43	473.96	389.12
			N	1216.46	924.16	860.54	798.68	487.32	398.08
	I2C clock = 400 kHz (0 V–3.36 V)	64	Y	1613.87	1136.84	1042.07	952.72	540.65	432.97
			N	1759.60	1207.28	1100.95	1001.69	556.08	442.81
		32	NA	2307.82	1456.66	1292.41	1152.66	599.68	470.02
		Just accelerometer			2610.56	2037.70	1787.92	NA	NA

VEP	3 electrodes recording (2 biopotenital, 1 trigger) (4 total)	1024	Y	194.55	NA	NA	NA	NA	NA
			N	207.47	NA	NA	NA	NA	NA
		512	Y	326.80	NA	NA	NA	NA	NA
			N	364.96	NA	NA	NA	NA	NA
	longest wire length = 118 cm	256	Y	537.63	NA	NA	NA	NA	NA
			N	588.24	NA	NA	NA	NA	NA
		128	Y	740.74	NA	NA	NA	NA	NA
	I2C clock = 400 kHz (0 V–3.36 V)		N	847.46	NA	NA	NA	NA	NA
		64	Y	917.43	NA	NA	NA	NA	NA
			N	1089.17	NA	NA	NA	NA	NA
		32	NA	1261.34	NA	NA	NA	NA	NA
PRBS (breadboard)	1 electrodes recording (2 total with no accel.)	1024	Y	218.29	NA	NA	NA	NA	NA
			N	223.21	NA	NA	NA	NA	NA
		512	Y	399.36	NA	NA	NA	NA	NA
			N	417.71	NA	NA	NA	NA	NA
	longest wire length = 10 cm	256	Y	709.42	NA	NA	NA	NA	NA
			N	737.14	NA	NA	NA	NA	NA
		128	Y	1115.30	NA	NA	NA	NA	NA
	I2C clock = 400 kHz (0 V–3.36 V)		N	1187.47	NA	NA	NA	NA	NA
		64	Y	1573.42	NA	NA	NA	NA	NA
			N	1714.53	NA	NA	NA	NA	NA
		32	NA	2209.31	NA	NA	NA	NA	NA

Appendix H Proposed circuit board designs for future WEBS Implementations

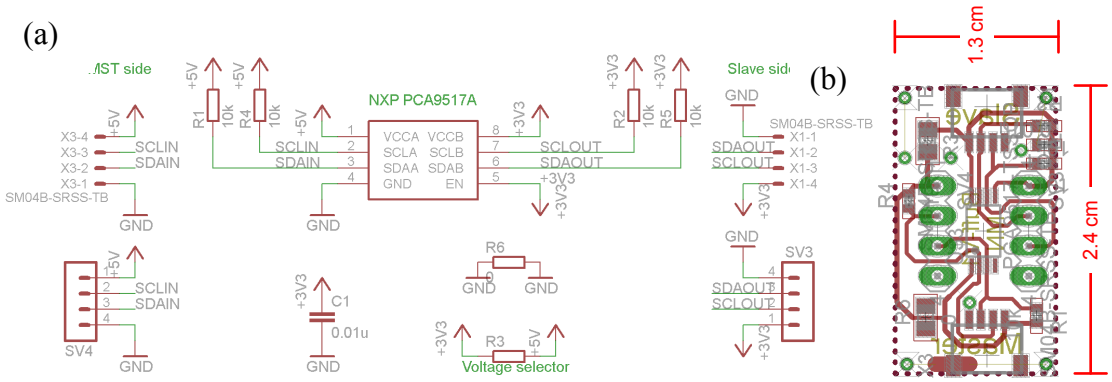

Figure H.1: A (a) schematic and (b) circuit board design for an I²C-bus repeater for the *WEBS* system. This design features the NXP PCA9517A repeater and two surface mount JST-SH sockets for easy connection into the existing *WEBS* system.

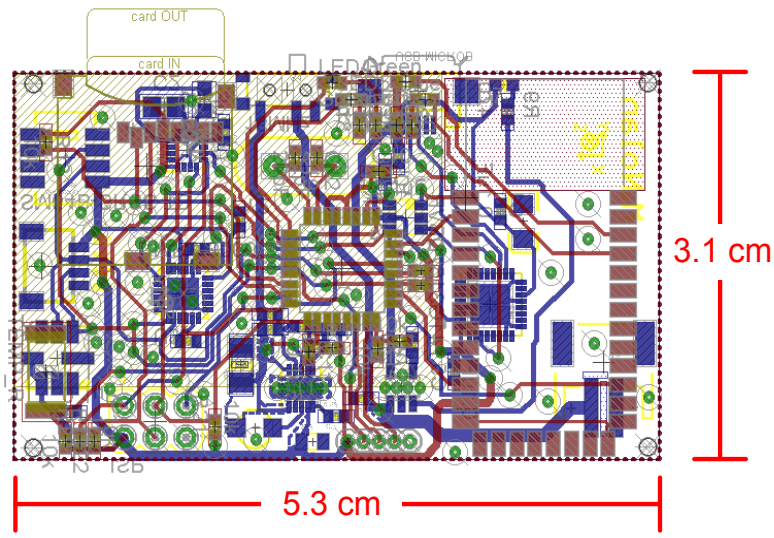

Figure H.2: A circuit board design of a possible next generation of the *WEBS* master. This design contains the same features as the existing *WEBS* master but with the addition of, an on-board microSD card socket; Arduino microcontroller with USB-to-serial programming ability; barometric pressure sensor; electret microphone; and a light-dependent resistor.

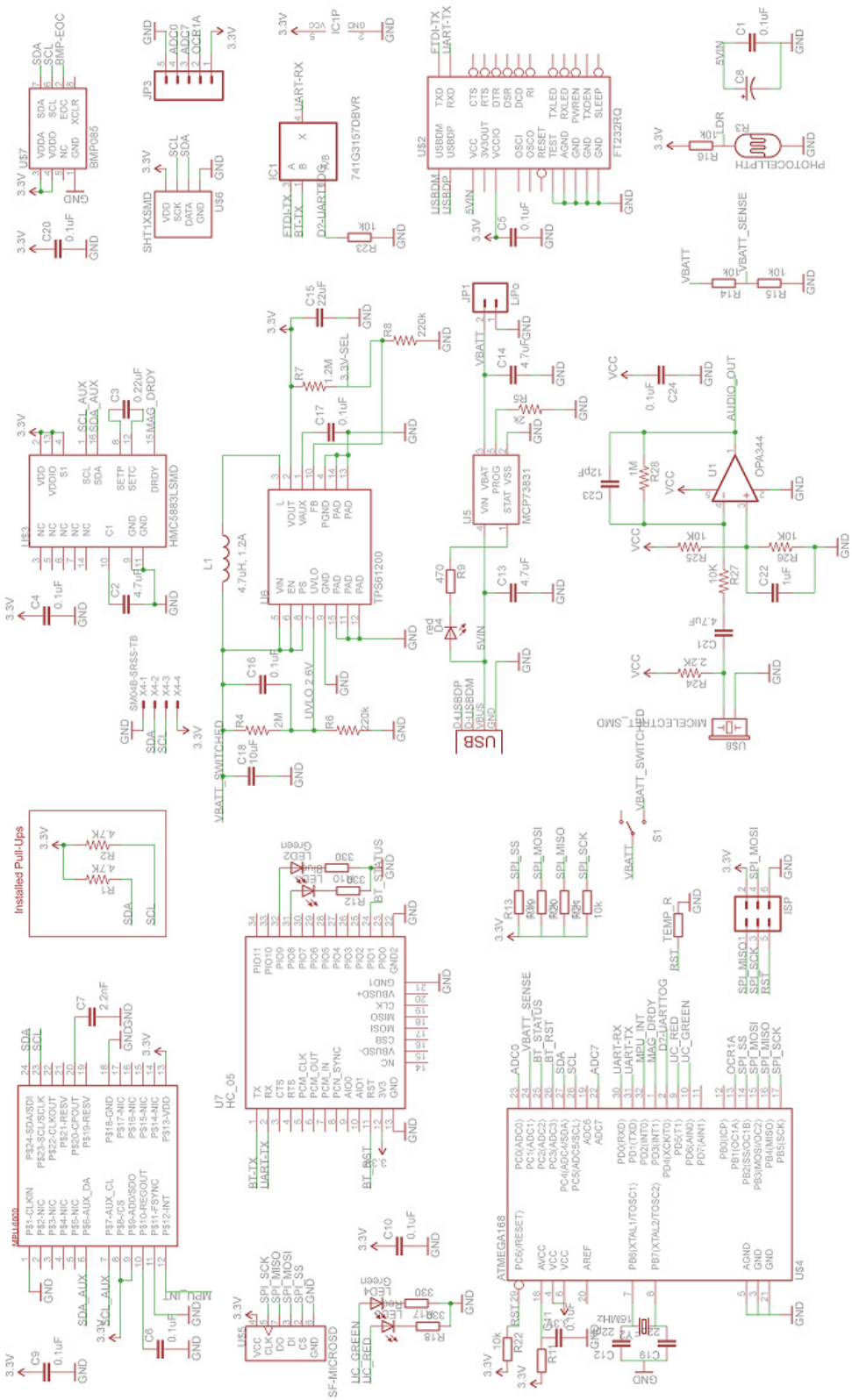

Figure H.3: A schematic of a possible next generation of the *WEBS* master. This design contains the same features as the existing *WEBS* master but with the addition of, an on-board microSD card socket; Arduino microcontroller with USB-to-serial programming ability; barometric pressure sensor; electret microphone; and a light-dependent resistor. The schematic design of the sensors and power supply features are modified from (SparkFun 2012).

Publications Arising from this Thesis (all peer reviewed).

M. Nolan, T. Burke, E. Coyle. (2012) A Wireless and Digital Electrode Bus Topology for Biopotential Measurement. *23rd IET Irish Signals and Systems Conference*. Maynooth, Ireland. 70-73.

M. Nolan, T. Burke, E. Coyle. (2011) Novel Bioelectric Measurement using a Digital Biopotential Monode. *Bioengineering in Ireland*. Galway, Ireland. 100.

B. Madden, **M. Nolan**, T. Burke, J. Condron, E. Coyle. (2011) Intelligibility of Electrolarynx Speech using a Novel Hands-Free Actuator. *4th International Joint Conference on Biomedical Engineering Systems and Technologies*. Rome, Italy. 265-269.

B. Madden, **M. Nolan**, T. Burke, J. Condron, E. Coyle. (2010) Intelligibility of Electrolarynx Speech using a Novel Actuator. *21st IET Irish Signals and Systems Conference*. Cork, Ireland. 158-162.

M. Nolan, B. Madden, T. Burke. (2009) Accelerometer based Measurement for the Mapping of Neck Surface Vibrations during Vocalized Speech. *IEEE Engineering in Medicine and Biology Society, EMBC*. Minneapolis, Minnesota, USA. 4453-4456.

M. Nolan, T. Burke, F. Duignan. (2009) Accelerometer based Measurement of Body Movement for Communication, Play, and Creative Expression. *4th European Conference of the International Federation for Medical and Biological Engineering*. Antwerp, Belgium. 1835-1838.